Probing the stability of halide perovskite films using electron spectroscopy techniques.

Udit Tiwari

A thesis submitted in partial fulfilment for the requirements for the degree of Doctor of Philosophy at the University of Central Lancashire.

November 2023

RESEARCH STUDENT DECLARATION FORM

Type of Award Doctor of Philosophy

School Engineering and Computing

1 Concurrent registration for two or more academic awards

I declare that while registered as a candidate for the research degree, I have not been a registered candidate or enrolled student for another award of the University or other academic or professional institution.

2 Material submitted for another award

I declare that no material contained in the thesis has been used in any other submission for an academic award and is solely my own work.

3 Collaboration

Where a candidate's research programme is part of a collaborative project, the thesis must indicate in addition clearly the candidate's individual contribution and the extent of the collaboration. Please state below:

Experiments at external facilities were carried out with some help from beamline/facility scientists.

_____

4 Use of a Proof-reader

No proof-reading service was used in the compilation of this thesis.

Signature of Candidate 

Print name: _____Udit Tiwari_____

Abstract

Halide perovskites have attracted considerable attention from the photovoltaic research community due to the rapid advancements in reported device efficiencies. This attention is also fuelled by their easy solution processability compared to the extensive and costly crystallisation process required for traditional silicon solar cells. However, the structural instability of perovskites, particularly under high-temperature and high-humidity conditions, hampers their potential for commercialisation. This thesis attempts to explore the underlying mechanisms responsible for this instability and aims to address it through modification of the perovskite with additives.

The response of two halide perovskites, $CH_3NH_3PbI_3$ and $CH_3NH_3PbBr_3$, to high-temperature exposure is initially discussed utilising X-ray Photoelectron Spectroscopy (XPS). The primary objective is to understand the role of halide ions in the structural stability of perovskites. Analysis reveals that $CH_3NH_3PbBr_3$ exhibits greater resistance to heating compared to $CH_3NH_3PbI_3$, and a proposed degradation mechanism explains this difference in thermal stabilities. The incorporation of ionic liquids (ILs) $BMIMBF_4$ and BMIMCl into a mixed-halide perovskite is investigated, employing a range of analytical techniques such as XPS, work function measurements, Near Edge X-ray Absorption Fine Structure (NEXAFS), Angle-resolved Hard X-ray Photoelectron Spectroscopy (Ar-HAXPES), and Near-Ambient Pressure XPS (NAP-XPS) to study the thermal and moisture resistance of the films. The role of the incorporated ILs, as well as the addition of a SnO_2 electron transport layer (ETL), is investigated. Results indicate that the combined effect of ILs and SnO_2 enhances the stability of the perovskite against heat and moisture. Finally, an investigation into perovskite modification using the two zwitterionic methylamines, TMAO and betaine, utilising XPS, Ar-HAXPES, and NAP-XPS is presented. The study demonstrates that TMAO-modified samples exhibit notable heat tolerance, while betaine-modified samples showcase superior moisture endurance.

Overall, this thesis provides new insights into the intrinsic mechanisms governing the degradation of perovskites and the role of additives in stabilising perovskite materials. These results could inform the future design of perovskite solar cells.

Table of Contents

Acknowledgements

I extend my deepest gratitude to my supervisor, Karen, whose guidance, and unwavering support have been invaluable throughout my research journey. Her mentorship and encouragement made this journey enjoyable and stress-free. I also extend my thanks to my second supervisor, Joe, for all our discussions on science and politics. I wish you all the best for your future!

The DTA3/COFUND Marie Skłodowska-Curie PhD Fellowship programme deserves sincere acknowledgment for generously funding my research and conference travels. I am grateful to our collaborators at the Henry Royce Institute, Manchester, and Aarhus University, Denmark, for their invaluable contributions to our work on the beamline.

I express my appreciation to Jordan for patiently addressing all my questions over the years. To my dear friends in Preston – Maria, Ranbir, Swarnim, Elisa, Ricky, Spyros, and Jonny – your presence has added immeasurable joy to my life during my time in the UK.

My heartfelt thanks go to my family for their unwavering support in all my endeavours. Finally, I want to express my deepest gratitude to my beloved girlfriend, Sushma. During my hardest time, your encouragement shined light to my world. No word can describe how important you are to my life.

List of Figures

List of Tables

Chapter 1. Introduction

1.1. Overview and Motivation

The colossal emission of greenhouse gases caused by the rapid industrialisation of the world economy has led to global warming [1]. A concerted global push towards renewable energy sources is urgently needed to halt the climate change crisis before it makes life unsustainable on Earth [2]. Of all the available renewable energy sources, solar power is the most abundant. The amount of solar energy received by Earth in a year is estimated to be over a hundred times the energy of the total known fossil fuel reserves on Earth [3]. Therefore, developing devices to capture solar energy could be an important step towards building a more sustainable energy future. Figure 1.1 displays the electromagnetic radiation that comes from the sun. Photovoltaic devices provide the most efficient way to harness this energy by converting sunlight directly into electricity. Although solar energy is not the cheapest renewable energy source, it is a technology where the costs are dropping rapidly.

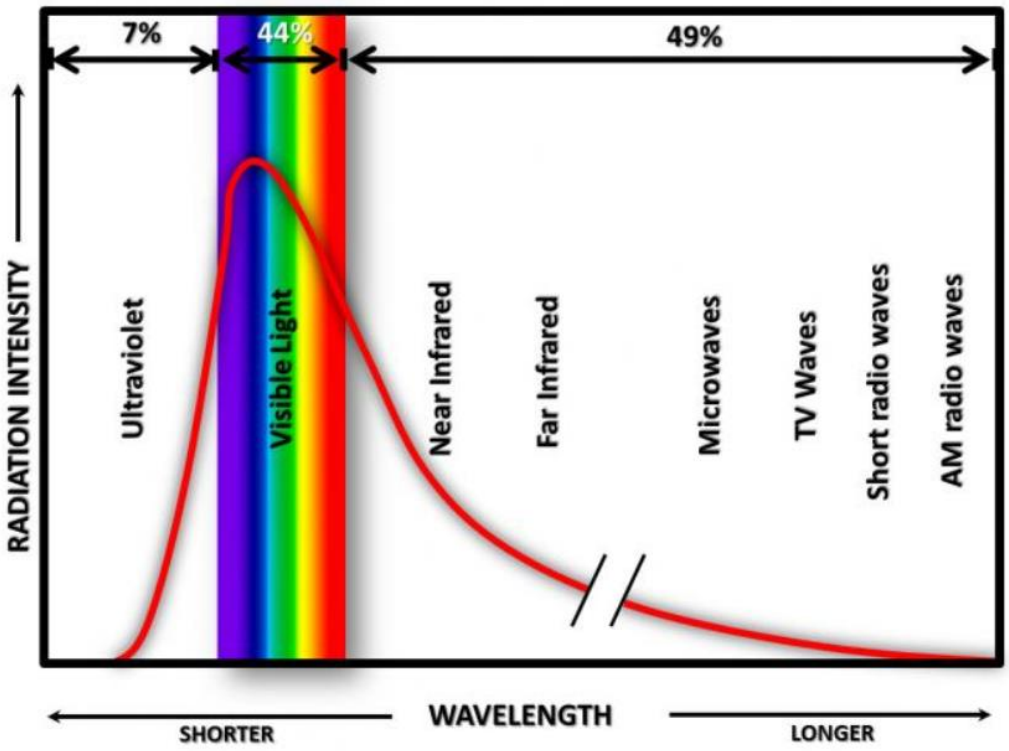

Figure 1.1 Sun's electromagnetic radiation.

Tremendous progress has been made in the field of organic optoelectronics in recent years, with commercial devices ranging from flexible sensors to solar cells becoming commonplace in our day-to-day lives. There are certain advantages of organic semiconductors over more conventional inorganic semiconductors such as silicon which make them extremely attractive for commercial applications. Firstly, most organic semiconductors are soluble in simple organic solvents like chlorobenzene or toluene. This makes the fabrication of high-quality thin films possible via spin coating or blade-coating as opposed to more complicated processes like crystal growth or evaporation deposition.

The crystallisation of silicon is a highly energy-intensive process and takes place at temperatures exceeding 1000 °C while organic semiconductor-based thin films can be formed at room temperatures and can be deposited on flexible substrates, which, combined with their solution processability makes their roll-to-roll mass production a low-cost energy efficient process. Finally, organic semiconductors being carbon-based molecules, allow structural modifications, which gives the possibility of developing structures with a diverse range of properties that can be tailored to any specific application. Despite their superior processability, flexibility, tuneability and low cost, their wide-scale use in the photovoltaic sector remains limited owing to their high instability under atmospheric conditions such as high temperature, moisture, and oxygen. Hybrid perovskites have quickly risen to dominate optoelectronic research as they are solution processable, cheap, tuneable and competitive with monocrystalline silicon solar cells in outright performance.

Perovskite solar cells (PSCs) have shown remarkable progress in recent years with rapid increases in power conversion efficiencies (PCEs) from 3% in 2009 to over 32.5% today, making it the fastest advancing technology in material science [4-7]. Figure 1.2 shows the evolution in the efficiencies of PV technologies over the years. The instability of interlayers in PSCs, electrode corrosion and intrinsic instabilities of perovskite materials continue to present significant challenges to achieving 25 years of operational lifetime [6]. Multiple environmental stresses, such as moisture, heat, bias, oxygen, and light,

have been identified as possible causes of perovskite degradation, limiting the operational lifetime of unencapsulated PSCs.

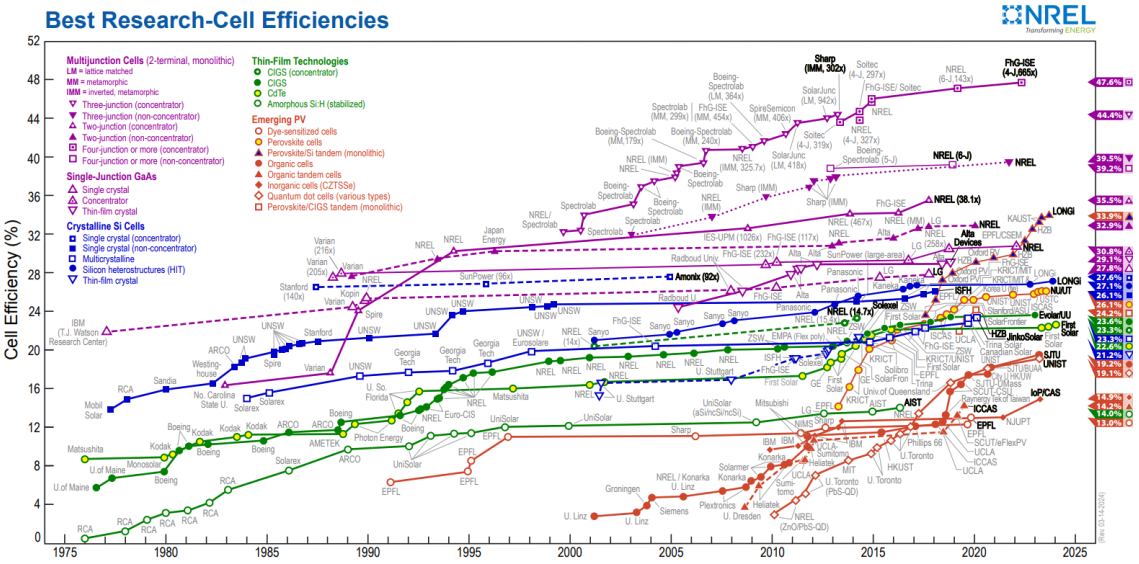

Figure 1.2 NREL photovoltaic efficiency chart until 01/04/2024. The most recent world record for each technology is highlighted along the right edge in a flag that contains the efficiency and the symbol of the technology. The company or group that fabricated the device for each most-recent record is bolded on the plot. This plot is courtesy of the National Renewable Energy Laboratory, Golden, CO. [8].

This thesis aims to elucidate the degradation mechanism of perovskites and investigate strategies for enhancing its structural stability. Chapter 1 presents a brief history of solar cells and discusses in detail the structure, advances and issues facing them. A general background knowledge of the physics of solar cells, delving deeper into the working principle of PSCs and related research about the stability of the devices is also discussed. In Chapter 2 the characterisation methods employed in the investigation of our samples are presented in detail.

Chapter 3 delves into understanding the role of halide ions in the structural integrity of perovskites. An X-ray Photoelectron Spectroscopy (XPS) study was carried out on two different perovskites: methylammonium lead iodide ($CH_3NH_3PbI_3$ often written as $MAPbI_3$) and methylammonium lead bromide ($CH_3NH_3PbBr_3$ often written as $MAPbBr_3$).

(Note: this experiment was carried out at MAX-lab synchrotron in 2015 by Syres et al. and this previously unused data has been analysed for this chapter of the thesis). This investigation sheds light on how the electronegativity of halide ions influences the degradation of the perovskite lattice. Notably, the higher electronegativity of bromine compared to iodine renders $MAPbBr_3$ more thermally stable due to the strengthened Pb-X bond (where X represents the halide).

Chapter 4 introduces ionic liquids into the perovskite films with an aim to improve their stability. The ionic liquids (ILs) 1-Butyl-3-methylimidazolium tetrafluoroborate ($BMIMBF_4$) and 1-Butyl-3-methylimidazolium chloride (BMIMCl) were introduced into a mixed halide perovskite, $CH_3NH_3PbI_{3-x}Cl_x$ ($MAPbI_{3-x}Cl_x$). Employing various analytical techniques—XPS, Work-Function measurements, Near-Edge X-ray Absorption Fine Structure (NEXAFS), Angle-Resolved Hard X-ray Photoelectron Spectroscopy (AR-HAXPES), and Near-Ambient Pressure X-ray Photoelectron Spectroscopy (NAP-XPS)—we assessed the stability of the resulting IL-modified perovskite thin films against the environmental stressors of high temperature and moisture. The observed stability improvements are attributed to the interaction between the ionic liquids and the perovskite.

Building on the idea that charged species may enhance perovskite stability, Chapter 5 focuses on additive engineering of mixed halide perovskites using two zwitterionic species: Trimethylamine N-oxide (TMAO) and Trimethyl glycine (Betaine). Through XPS, AR-HAXPES, and NAP-XPS analyses, we examined the interaction between these zwitterionic molecules and the perovskite. Our findings revealed that TMAO-modified perovskite films exhibit superior thermal stability, while Betaine-modified samples demonstrate enhanced moisture resistance. The stability enhancement is due to the interaction between charged species and the perovskite.

1.2. A Brief History of Solar Cells

The discovery of the photovoltaic effect in 1839 by A.E Becquerel by immersing an electrode in a conductive solution while exposing the system to light led to the beginning of solar cell technology [9]. The first solar cell was developed from selenium by Charles Fritts in 1883 [10]. In 1918 Jan Czochralski prepared the first single-crystal silicon, which kick-started the age of silicon wafers [11].

Fabrication of the first commercial crystalline silicon solar cell was carried out by the Bell Lab USA team in 1954 [12]. This cell had an efficiency of 6% and was followed by a period of intense research in crystalline silicon-based solar cells. This led to an increase in the efficiency of the cells, however, the cost and the time taken for the total savings and revenue streams from the solar cells to cover the total cost of the installation (payback time) did not decrease. Therefore, a new device fabrication technology was launched known as thin film technology.

The first thin film solar cell was developed from Cu_2S/CdS at the University of Delaware in 1980 [13]. However, this technology failed to reduce the price and the payback time. The first dye-sensitized solar cell (DSSC) was fabricated in École Polytechnique fédérale de Lausanne (EPFL) in Lausanne, Switzerland, by Michael Grätzel and Brian O'Regen who used mesoporous TiO_2 electrodes prepared from colloidal TiO_2 nanoparticles [14]. DSSCs acted as a precursor in the development of hybrid perovskite solar cells, which started a new era in photovoltaic technology.

The progress of solar cell technology can be divided into three generations of fabrication methodologies in terms of their efficiencies and costs, presented in Figure 1.3.

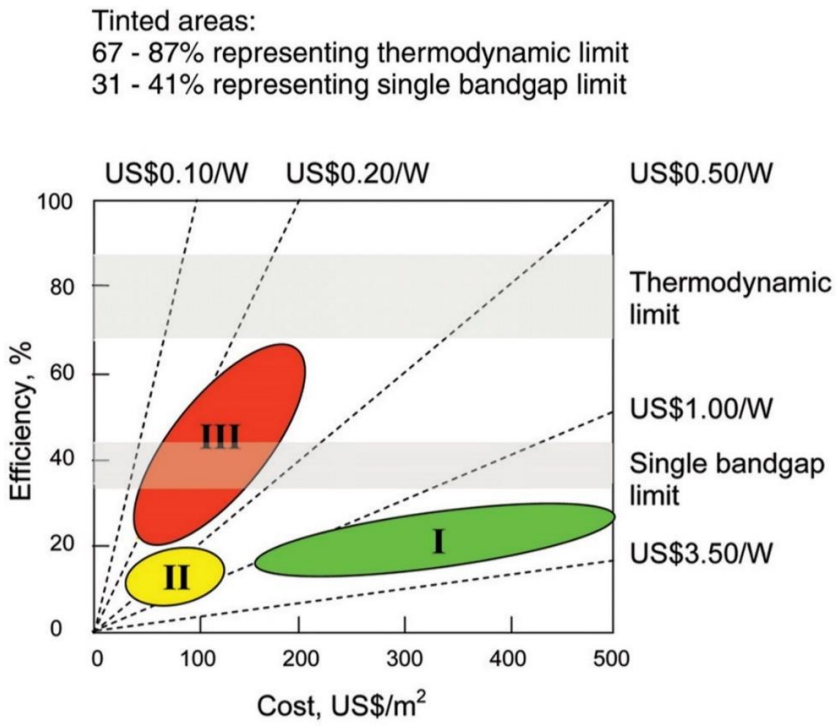

Figure 1.3 Efficiency and cost projections for first–I (high efficiency, high costs), second–II (low efficiency, low costs), and third–III generation (low costs, high efficiency) PV technologies. Reproduced from [15].

1.2.1. First-generation solar cells

First-generation cells are characterised by high costs but also high efficiency. Similar to computers in their manufacturing process, they utilise exceptionally pure silicon and employ a single junction to extract energy from photons. These cells boast impressive efficiency, nearing their theoretical maximum of 33%. Initially dominant in commercial production, accounting for 89.6% in 2007, their market share has since declined. The manufacturing processes involved are inherently expensive, resulting in prolonged periods for these cells to offset their purchasing costs. It is unlikely that first-generation cells will surpass fossil fuels in cost-effectiveness.

Crystalline silicon solar cell

Crystalline silicon solar cells are the oldest and, currently, the most dominant technology of solar cells, constituting about 90% of photovoltaic production worldwide. However, the energy-intensive and complicated fabrication (Czochralski process) makes it an

expensive technology with a long payback time [16]. In a monocrystalline silicon solar cell, each cell is a single crystal of silicon, providing a high extraction of charge carriers. Polycrystalline silicon solar cells consist of more than one crystal resulting in a very high number of grain boundaries, thereby increasing the recombination of the photo-generated electrons with the positively charged holes (created by the excitation of electrons). Therefore, monocrystalline silicon solar cells are much more efficient than polycrystalline silicon solar cells. The highest efficiency of a single junction crystalline silicon solar cell at the module level design stands at 26.8% [17].

1.2.2. Second-generation solar cells

Second-generation cells, primarily developed during the 1990s and early 2000s, are low-cost with lower efficiency. Commonly thin film solar cells, they utilise minimal materials and inexpensive manufacturing methods. Materials such as copper indium gallium selenide, cadmium telluride (CdTe), amorphous silicon, and micromorphous silicon are frequently employed. Nanosolar's solar panel production exemplifies this generation, using a specialised machine for rapid solar cell printing [18]. Despite a lower conversion efficiency of 10-15%, their reduced cost compensates for this drawback. Second-generation cells are more economical than first generation solar cells [19].

Cadmium telluride (CdTe)

Second-generation solar cells are based on thin film technology, where a small amount of the active photo absorber material, such as cadmium telluride (CdTe), is deposited onto a substrate to create a thin film. This approach reduces the amount of materials and production costs compared to crystalline silicon solar cells, however, they cannot match the high efficiencies of silicon solar cells. The maximum lab efficiency of CdTe is just above 22% [20]. In addition to their low cost, the main advantage of CdTe solar cells lies in their optimum direct band gap (1.45 eV), which results in a high optical absorption coefficient. The absorption coefficient determines how far into a material light of a particular wavelength can penetrate before it is absorbed. A material with a higher absorption coefficient means that the material absorbs more light per thickness. CdTe

solar cells do have some disadvantages. The primary concerns include cadmium toxicity and the requirement of a high production temperature (600 °C) [21].

Copper zinc tin sulphide (CZTS)

Copper zinc tin sulphide solar cells address the major limitations of toxicity and rarity associated with CdTe-type solar cells by relying on abundant and eco-friendly materials. CZTS solar cells also exhibit an optimum and direct band gap, resulting in high optical absorption. However, they offer lower efficiency compared to CdTe solar cells, with the lab-recorded solar cell efficiency standing at 12.6% [22].

1.2.3. Third-generation solar cells

Third-generation solar cells are emerging photovoltaic technologies that are currently the focus of intense research. The aim is to create low-cost, high-efficiency cells, likely thin-film cells targeting efficiencies ranging from 30-60%. Technologies linked with third-generation products involve multijunction photovoltaic cells, tandem cells and nanostructured cells to enhance light absorption, and harness excess thermal generation to improve voltages or carrier collection.

Organic solar cells

Organic solar cells can be synthesised at room temperature using solution-based earth-abundant materials. This makes them promising candidates for future solar cells. The typical device structure consists of an electron donor material and an electron acceptor material, which can be polymers or small organic molecules. When light is absorbed by the electron donor material, it leads to the generation of electron-hole pairs. These electrons and holes then dissociate at the interface between the two materials and are collected through an external circuit by two electrodes. These solar cells offer efficiencies as high as 16% [23, 24].

Dye-sensitised solar cells (DSSCs)

DSSCs were invented in 1988 by Brian O'Regan and Michael Grätzel by coating an organic dye on a thin film of TiO_2 nanoparticles [14]. The photo-absorber dye was used

to sensitise the film with light-harvesting characteristics and yielded an overall conversion efficiency of 7.9% in simulated solar light. Figure 1.4 shows the working of a DSSC. The efficiency of DSSCs improved from 7.9% in 1991 to 15% in 2015 [14, 25]. They offer low production costs and ease of fabrication. However, these cells suffer from poor long-term stability.

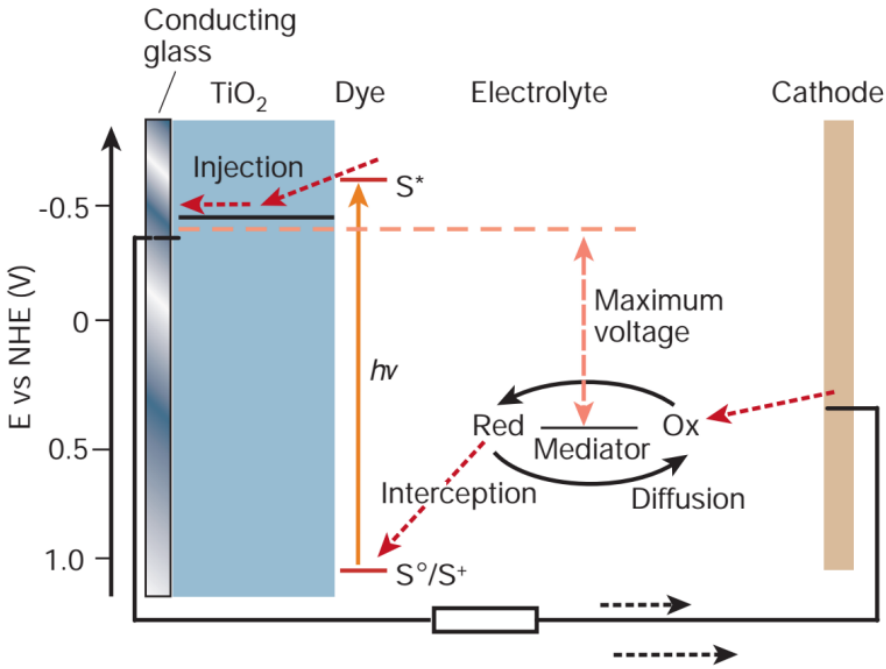

Figure 1.4 Schematic diagram of the working of a dye-sensitised solar cell. The photoanode, composed of a mesoporous dye-sensitised semiconductor, receives electrons from the photo-excited dye, which is thereby oxidised, and which in turn oxidises the mediator, a redox species dissolved in the electrolyte. The mediator is regenerated by reduction at the cathode by the electrons circulated through the external circuit. Adapted from [26].

1.3. Perovskite solar cells

Perovskite solar cells combine the advantages of inorganic solar cells, like long diffusion length, weak exciton binding energy, long lifetime of charge carriers, and high carrier mobility, with that of organic solar cells, such as high optical absorption coefficient, solution processability and low cost of production [27-30]. PSCs have made remarkable progress in recent years and are the fastest-growing solar-cell technologies in the world.

Since the first use of perovskites in 2009, the efficiency of perovskite-based solar cells has shot up from 3.81% to 32.5% [31, 32].

1.3.1. Structure of perovskites

The term perovskite refers to the crystal structure of the mineral calcium titanium oxide ($CaTiO_3$), discovered in the Ural Mountains in Russia by Gustav Rose. The term perovskite was later adopted to refer to materials that possess the perovskite structure, which is the same crystal structure as $CaTiO_3$. The perovskite structure (see Figure 1.5) can be represented by the formula ABX_3, where A site is a monovalent cation ($CH_3NH_3^+$, $(CH(NH_2)_2)^+$, Cs^+), B site is a divalent cation (Pb^{+2}, Sn^{+2}) and X site is a halogen (Cl^-, Br^-, I^-) [33, 34].

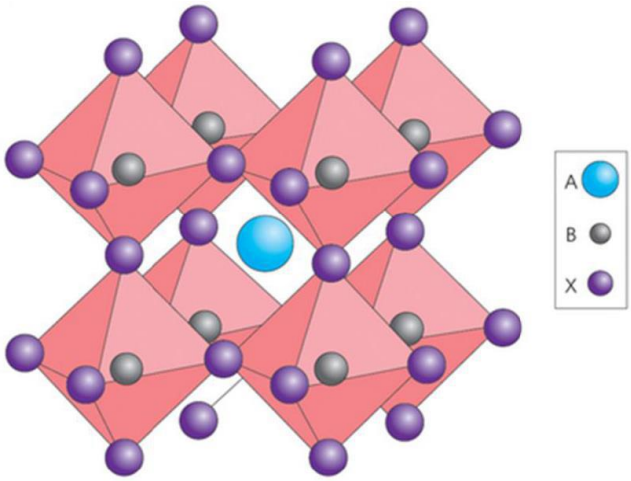

Figure 1.5 Perovskite crystal structure.

Commonly, two requirements that must be met to complete the perovskite formation are electroneutrality and ionic radii.

Electroneutrality: Perovskite's formula must have a neutral balanced charge; therefore, the sum of the addition of the charges of A and B ions should be equivalent to the total charge of the halide ions. For example, in $CH_3NH_3PbI_3$, the sum of the charges on $CH_3NH_3^+$ and Pb^{+2} (1+2 = 3) is equal to the total charge of the three iodide ions I^- (-1 × 3 = -3).

Ionic radii requirements: To achieve a stable cubic perovskite structure, certain requirements must be met concerning the size of ions. These criteria are determined by the tolerance factor, denoted as Γ in Equation 1.1, which must fall within the range of $0.813 < \Gamma < 1.107$.

$$\Gamma = \frac{(r_A + r_X)}{\sqrt{2}(r_B + r_X)} \quad 1.1$$

Here, r_A, r_B, and r_X stand for the effective ionic radii of A, B, and X ions, respectively. For solar cell applications, the widely used perovskite is the organoammonium lead (or tin) halide perovskite, such as $CH_3NH_3PbI_3$. The tolerance factor for this compound is determined to be 0.83 [35, 36]. Larger (>1) or smaller (<0.8) values of tolerance factor usually result in non-perovskite structures. For example, $CH(NH_2)_2PbI_3$, also known as $FAPbI_3$, can be found in the perovskite α-phase, which has strong photovoltaic properties and appears black. However, it shows higher stability in the yellow hexagonal δ_H-phase due to a larger tolerance factor, with a transition temperature from δ_H to α phase higher than room temperature. Conversely, $CsPbI_3$ maintains an orthorhombic structure, known as the δ_O-phase, at room temperature because of its smaller tolerance factor [37].

1.3.2. Advances in perovskite solar cells

Perovskite solar cells were first reported in 2009 and evolved from the dye sensitised solar cell (DSSC) technology [14]. In 2009, Miyasaka and co-workers demonstrated the use of $MAPbI_3$ and $MAPbBr_3$ nanocrystals as light absorbers in a DSSC with a liquid electrolyte to deliver PCEs of 3.8% and 3.1%, respectively [38]. Since then, $MAPbI_3$ has become a prototype for perovskite solar cells, attracting a large body of early-stage research due to its higher initial efficiency than $MAPbBr_3$ and more suitable band gap (1.55 eV). The efficiency was increased to 6.54% after the optimisation of the film thickness of the TiO_2 electron transport layer (ETL) in 2011 [39]. However, the device

showed poor stability and degraded under constant illumination as the $MAPbI_3$ dissolved in the liquid electrolyte.

A year later, the same research group led by Park made the first breakthrough in the efficiency and stability of PSCs by introducing a hole transport layer (HTL) composed of 2,2,7,7-tetrakis(N,N-p-dimethoxyphenylamino)-9,90-spirobifluorene (spiro-OMeTAD) [40]. The solar cell used $MAPbI_3$ as the photo absorber material deposited on a 0.6 µm mesoporous-TiO_2 layer (ETL) with spiro-MeOTAD (HTL) deposited on top of the $MAPbI_3$ layer (see Figure 1.6). The replacement of the liquid electrolyte with this solid state HTL solved the problem of dissolution of perovskite in the electrolyte and therefore improved the device stability. The device showed a power conversion efficiency (PCE) of 9.7%.

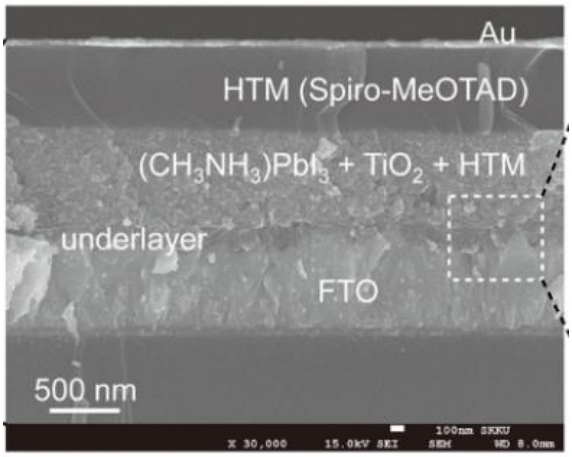

Figure 1.6 Cross-sectional structure of the device fabricated by Park et al. Reproduced from [40].

Around the same time, Snaith and colleagues achieved a breakthrough in perovskite solar cell technology by using a mixed-halide $MAPbI_{3-x}Cl_x$ perovskite with the same device structure as employed by Park et al. and achieved a PCE (power conversion efficiency) of ~8% [41]. They also made a device by substituting the mesoporous n-type TiO_2 layer with mesoporous Al_2O_3. Al_2O_3, known for its insulating properties with a band-gap of 7-9 eV, was an unexpected choice as it lacks electron conductivity. However, to everyone's surprise, the device continued to function effectively, and it was discovered that electron transport within the Al_2O_3-based device was even faster than in the TiO_2-

based device. Additionally, the introduction of the insulating Al_2O_3 scaffold led to an increase of several hundred millivolts in the V_{OC} (open-circuit voltage), resulting in an impressive PCE of 10.9% [41]. These results indicate that the perovskite layer can also transport electrons out of the device.

In the same year, a group led by Grätzel reported a mesoscopic $MAPbI_3/TiO_2$ heterojunction solar cell without a hole transporting material (HTM) layer which showed a PCE of 5.5%, demonstrating that perovskite can also work as an HTM in a heterojunction solar cell [42]. In 2013, Seok's group achieved a power-conversion efficiency of about 12.3% using a mix-halide perovskite $MAPb(I_{1-x}Br_x)_3$ [43]. Again in 2013, Grätzel's group reported achieving a PCE of more than 15% [44]. They employed a sequential deposition route to perovskite synthesis. PbI_2 was first absorbed into a nanoporous TiO_2 film and then exposed to a solution of CH_3NH_3I to form the perovskite. This method permitted a much better control over perovskite morphology and hence gave a higher PCE. In the same year, Snaith's group was the first to deposit perovskite using vapor deposition [45].

Snaith developed a device consisting of a planar FTO/compact-TiO_2/$MAPbI_{3-x}Cl_x$/spiro-OMeTAD/Ag configuration, notable for its absence of a mesoporous layer. This was made possible by employing a highly consistent $MAPbI_{3-x}Cl_x$ layer synthesised using a dual-source vapour deposition technique. The resulting perovskite films displayed exceptional uniformity, free from any pinholes. Consequently, direct contact between the spiro-OMeTAD and compact-TiO_2 layers, which could potentially create shunting paths and compromise cell performance, was avoided. This innovative approach yielded an impressive efficiency exceeding 15%, accompanied by a V_{OC} of 1.07 V. Soon after that several groups reported to achieve a power-conversion efficiency more than 20% [46-48].

The mixed halide perovskite $MAPbI_{3-x}Cl_x$ exhibited superior performance compared to the pure iodide perovskite $MAPbI_3$ [49-51]. The addition of chlorine is believed to enhance the uniformity of perovskite films and increase the carrier lifetime and diffusion length. In 2014, Gratzel's group developed a mixed cation perovskite by incorporating

FA (formamidinium) cations into the perovskite lattice. They reported that the band-gap of perovskite can be altered by adjusting the FA content in the $(MA)_x(FA)_{1-x}PbI_3$ mixed cation perovskite composition [52]. As the FA content increased, the absorption onset experienced a red shift, indicating a smaller optical band-gap. However, this also led to a decrease in the light-absorbing ability. The highest efficiency of 14.9% was obtained from $MA_{0.6}FA_{0.4}PbI_3$.

In 2016, Saliba and colleagues further introduced a small amount of Cs into the binary mixed cations, forming a triple cation configuration $Cs_x(MA_{0.17}FA_{0.83})_{(100-x)}Pb(I_{0.83}Br_{0.17})_3$, which delivered stabilised PCEs up to 21.1% [53]. The triple cation configuration retains an efficiency of 18% even after continuous aging for 250 hours under operational conditions, and it currently stands as the most efficient perovskite family configuration. The following year (2017), the Korea Research Institute of Chemical Technology (KRICT) reported a 22.7% efficiency in the NREL chart [54]. They developed a double-layered halide architecture (DHA) using Poly(3-hexylthiophene) (P3HT) as an HTM without any dopants. An ultrathin layer of a wide-bandgap halide (WBH) was stacked onto the $(FAPbI_3)_{0.95}(MAPbBr_3)_{0.05}$ perovskite layer (narrow-bandgap halide) before depositing the HTM layer. The WBH layer was formed by simply reacting *n*-hexyl trimethyl ammonium bromide (HTAB) on the perovskite surface. The WBH layer effectively reduced recombination at the perovskite/P3HT interface.

In 2018, a team at the Institute of Semiconductors, Chinese Academy of Sciences (ISCAS), also reported that depositing a layer of an organic halide salt phenethylammonium iodide (PEAI) can reduce surface defects and suppress nonradiative recombination. Their device $ITO/SnO_2/FA_{1-x}MA_xPbI_3/PEAI/Spiro\text{-}OMeTAD/Au$ achieved an efficiency of 23.3%. The following year in 2019, two updates (24.2%, and 25.2%) to the efficiency were reported to the NREL chart by KRICT [55]. In 2021, Seok etal. reported a PSC with a certified PCE of 25.8% [56]. A coherent interface was developed between the ETL and the perovskite layer to minimise interface defects by coupling Cl-bonded SnO_2 with a Cl-containing perovskite precursor.

1.3.3. Stability issues

Organolead halide perovskites offer great promise as photoelectrode materials thanks to their low cost, easy processability, high efficiency [57, 58], tuneable band-gap [43, 59], ambipolar charge transport [27], long carrier lifetimes [29], and long charge diffusion lengths [30, 60]. The immense potential of these materials is evident from the rapid improvement in their power conversion efficiencies making it the fastest growing technology in the history of photovoltaics [38, 56]. Despite the tremendous promise shown by these materials, their poor stability in ambient conditions is hampering their wide-scale commercialisation. The Gibbs free energy change for the decomposition reaction (Equation 1.2) at 300 K is ΔG^{o}_{300K} = 0.16 eV per formula unit [61].

$$MAPbI_3 \rightleftharpoons PbI_2 + MAI \qquad 1.2$$

The small magnitude of ΔG^{o}_{300K} indicates that the chemical stability is very fragile and can be easily shifted by the presence of extrinsic agents like moisture. Due to its high solubility in water, MAI's saturation concentration in water for preventing the decomposition of $MAPbI_3$ is estimated to be approximately 8 g/L [61]. This implies that even a small quantity of water can cause significant degradation of the perovskite phase. In a study by Niu et al. [62], it was discovered that when exposed to air with a humidity of 60% at 35°C for 18 hours, $MAPbI_3$ completely degraded into PbI_2. Therefore, for the long-term stability of perovskite solar cells, it is essential to optimise the device architecture and improve encapsulation.

Knop et al. were the first to isolate and characterise the dihydrate phase $(CH_3NH_3)_4PbI_6 \bullet 2H_2O$ formed as result of the interaction of water with perovskites [63]. Barnes et al. showed that in fact moisture exposure to perovskites first results in a monohydrate phase which stays in equilibrium with a dihydrate phase depending upon the intensity and duration of water exposure [64]. Equation 1.3 and Figure 1.7 show the decomposition mechanism proposed by Barnes et al.

$$4CH_3NH_3PbI_3 + 4H_2O \leftrightarrow 4(CH_3NH_3PbI_3 \cdot H_2O) \leftrightarrow (CH_3NH_3)_4PbI_6 \cdot 2H_2O + 3PbI_2 + 2H_2O \quad (1.3)$$

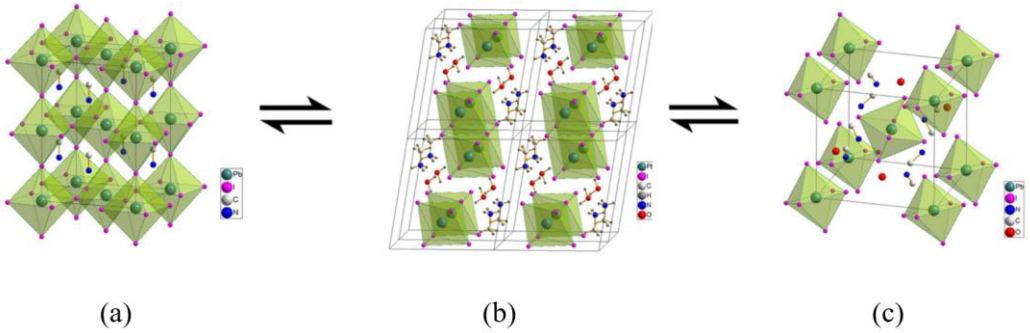

Figure 1.7 Depiction of the (a) cubic (b) monohydrate and (c) dihydrate phases of $MAPbI_3$ as proposed by Barnes et al. Reprinted from ref [64].

An important observation was the reversibility of the hydration reaction on exposure to dry air. However, as degradation progresses with time and more of the dihydrate phase is formed, the formation and phase segregation of PbI_2 limits the reversibility of the hydration reaction. Furthermore, a combination of moisture and heat really accelerates the decomposition reaction leading to the loss of organic components and the generation of PbI_2 [65, 66]. Such recovery of perovskites during periods of rest between cycles of continuous testing has been observed in other studies as well [67, 68]. The pathways of degradation proposed by E. J. Juarez-Perez et al. for $MAPbI_3$ are depicted through Equations 1.4 to 1.8 [67].

$$CH_3NH_3PbI_3 \leftrightarrow CH_3NH_3I + PbI_2 \quad (1.4)$$

$$PbI_2 \leftrightarrow Pb(0) + I_2 \quad (1.5)$$

$$CH_3NH_3I \leftrightarrow CH_3NH_2 + HI \quad (1.6)$$

$$4HI + O_2 \leftrightarrow 2I_2 + 2H_2O \quad (1.7)$$

$$2HI \leftrightarrow H_2 + I_2 \quad (1.8)$$

Li et al looked at the moisture induced degradation of $MAPbI_3$ by exposing the films to up to 20 mbar of water vapour pressure in the XPS preparation chamber [69]. They

found that water molecules acted as n-type dopants even before the onset of severe degradation. Upon exposure to higher pressures, there was complete loss of nitrogen and a partial loss of iodine from the structure. The concentration of carbon remained constant with the transformations from C-N to C-H. Equation 1.9 below shows the decomposition pathway proposed by them.

$$CH_3NH_3PbI_3(s) \xrightarrow{H_2O} (-CH_2-) + NH_3(g) + HI(g) + PbI_2(s) \quad 1.9$$

However, this degradation route differs from the widely accepted route as shown in Equation 1.10 [49].

$$CH_3NH_3PbI_3 \xrightarrow{H_2O} CH_3NH_3I + PbI_2 \quad 1.10$$

Philippe and co-workers employed a different approach to water exposure [49]. They added a water droplet directly on the surface of $MAPbI_3$ films and observed a loss in nitrogen as well carbon moieties of $MAPbI_3$, thereby suggesting that the MAI formed as a result of the degradation process was washed away by water.

Several approaches have been reported to improve the resistance of perovskites to moisture ingress, including compositional engineering and interlayer modification [70, 71]. Noh et al. and Pont et al. found that increasing the Br ratio in $MAPb(I_{1-x}Br_x)_3$ enhances its moisture resistance, likely due to the Br incorporation shrinking the perovskite crystal lattice and changing its phase from tetragonal to cubic, which is less susceptible to moisture incorporation [43, 70]. Substituting iodide with thiocyanate (SCN) is another reported method that makes perovskite less prone to hydration due to the stronger bonding of SCN to Pb^{2+} compared to I^- [72]. Introducing hydrophobic interlayers on top of the perovskite is another technique for improving moisture stability. For instance, Cao et al inserted thiols at the perovskite/HTL interface in negative-intrinsic-positive (n-i-p) structured PSCs [73], while Bai et al. replaced 6,6-phenyl-C_{61}-butyric acid methyl ester (PCBM) with a cross-linkable silane-functionalised fullerene as the ETL, which blocks the pathway for moisture diffusion [71].

The different phases of the perovskite structure (orthorhombic, tetragonal and cubic) can influence their optoelectronic properties significantly [74]. These structural transitions are very sensitive to temperature which makes it paramount for the devices to be thermally stable over a wide range of operational temperatures [75]. At approximately 330 K, the structure of $MAPbI_3$ alters from tetragonal to cubic, resulting in a slight decrease in band gap and an acentric configuration with ferroelectric properties [76, 77]. In contrast, FA perovskites are more resistant to thermal degradation and discoloration, even when subjected to temperatures of approximately 400 K. $FAPbI_3$ maintains its ideal tetragonal black phase up to about 430 K, but this phase is vulnerable to high humidity levels. In such conditions, the black phase is unstable and converts to a yellow hexagonal perovskite with linear chains of PbI_6, exhibiting a large optical band gap and inadequate charge separation and transfer. However, this FA phase transition can be reversed by re-annealing a perovskite film to restore the optimal FA black phase [58, 78].

Conings and co-workers studied the thermal degradation of $MAPbI_3$ films by subjecting them to a temperature of 85 °C *ex-situ* in different environments (air, N_2 and O_2) [79]. A gradual loss of nitrogen was observed in all the environments with the generation of metallic lead showing the intrinsic thermal instability of $MAPbI_3$. The *in-vacuo* thermal degradation of $MAPbI_3$ was studied by Huang et al. who reported a complete loss of nitrogen between 100 °C and 150 °C and the formation of metallic lead above 150 °C [80].

Some studies have reported that adding bulky cations or surface ligands can stabilise the photoactive phase of $FAPbI_3$ and $CsPbI_3$ [81-84]. Another approach towards improving their thermal stability has been compositional engineering where A, B and X site cations are mixed in various ratios to tune their tolerance factor and has proven to be an effective strategy towards stabilising their structure [37, 85]. Furthermore, an increase in temperature has also shown to accelerate the diffusion of ions into the adjacent interlayers leading to the creation of defects and unwanted reaction with the interlayers [86].

1.4. Theoretical background

1.4.1. Semiconductors

Photovoltaic devices usually employ a semiconductor material for light absorption. The electronic conductivity of semiconductors lies between conductors and insulators. According to the band theory of solids, the discrete energy levels of individual atoms in a solid overlap to form allowed energy bands where electrons may be found. For a solid to be conductive, it must have a partially occupied energy band. Insulators are non-conductive because the energy gap (band gap, E_g) between their highest occupied energy band (valence band, VB) and the next higher band (conduction band, CB) is very wide, making the excitation of electrons from VB to CB nearly impossible. The overlap of the VB and CB is responsible for the conductivity of metals while semiconductors usually have a narrower band gap which makes the excitation of electrons from VB to CB possible.

The band gap signifies the minimal energy needed to excite an electron within a semiconductor to a higher energy level. Only photons possessing energy equal to or surpassing the band gap of a material are capable of absorption. A solar cell generates power, denoted as the product of current and voltage. Larger band gaps yield higher maximum attainable voltages, albeit diminishing sunlight absorption and consequentially reducing current. This inherent compromise signifies that only a limited subset of materials, featuring band gaps within an optimal range, exhibit potential in photovoltaics. As depicted in Figure 1.8, this trade-off in efficiency is illustrated for single-junction photovoltaics (referred to as the Shockley–Queisser limit), along with the existing highest efficiencies achieved in various lab-scale (1 cm^2 or larger) solar cell technologies. The ideally suited photovoltaic material boasts a band gap falling within the range of 1–1.8 eV [87, 88].

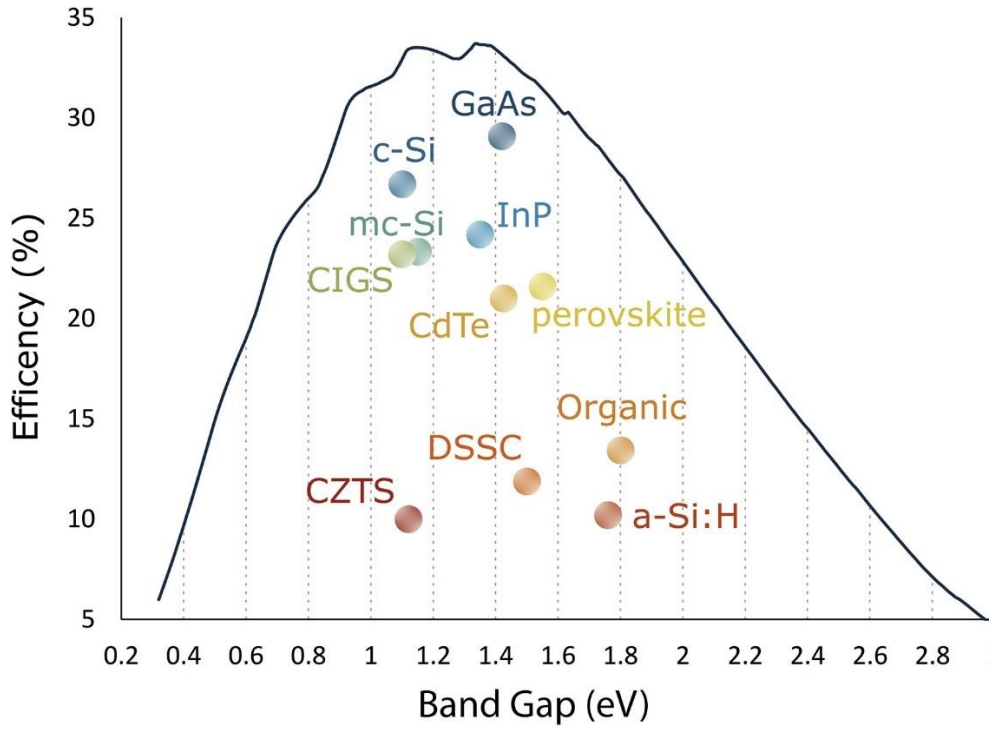

Figure 1.8 Efficiency comparison of diverse band gap materials. The continuous line denotes the theoretical limit of radiative power conversion efficiency for single-junction photovoltaics under AM 1.5 illumination, following the Shockley–Queisser limit. The circles depict the current recorded efficiencies for different types of solar cells with active areas equal to or greater than 1 cm^2. Reproduced from [87].

The property of a semiconductor depends on the position of the Fermi level. The Fermi level (E_F) is a hypothetical energy level where the probability of occupancy by an electron is 50%. Figure 1.9 shows the position of the Fermi level in metals, semiconductors and insulators. For metals at absolute temperature (0 K), the Fermi level is the energy of the highest occupied electronic states (valence band maxima, VBM) which overlaps with the energy of the lowest unoccupied energy states (conduction band minima, CBM).

For an intrinsic semiconductor, the Fermi level lies exactly between the VBM and CBM while for an extrinsic semiconductor, the Fermi level can either be close to the VBM (*p*-type) or CBM (*n*-type). The shift in the Fermi level in extrinsic semiconductors occurs due to the addition of impurities/dopants. A dopant can provide an extra electron (*n*-type) or a hole (*p*-type) to an intrinsic semiconductor leading to the generation of an

additional donor level (close to CBM) or acceptor level (close to VBM), respectively. The addition of a donor/acceptor level facilitates the movement of charge carriers (from donor level to CB or from VB to acceptor level) through an extrinsic semiconductor, thereby decreasing the effective band gap [89].

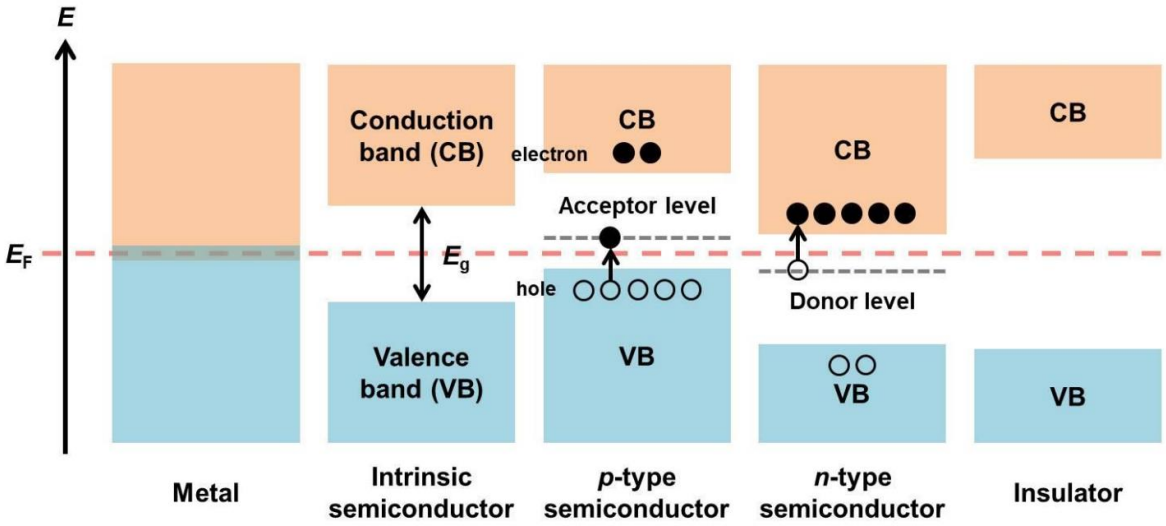

Figure 1.9 Energy band diagram for metals, semiconductors and insulators.

1.4.2. Photovoltaic device physics

When *p*-type and *n*-type semiconductors are placed in contact, a *p*-*n* junction is formed due to the migration of electrons from *n*-type to *p*-type and of holes from *p*-type to *n*-type and the fermi level reaches an equilibrium position as shown in Figure 1.10 below. E_{vac} is the vacuum energy level.

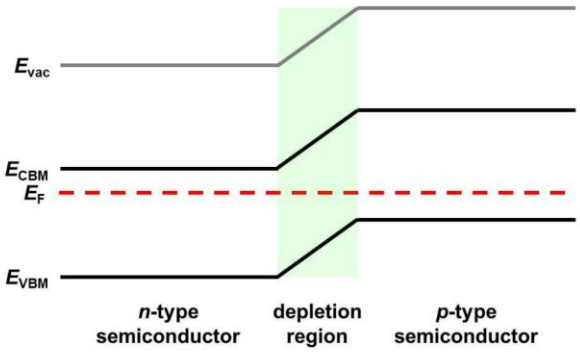

Figure 1.10 Formation of a p-n junction

The recombination of charge carriers generates a depletion region and leads to the charging of the two semiconductors (*p*-type becomes negatively charged and *n*-type becomes positively charged), forming a 'built-in' voltage. The *p*-*n* junction is said to be in forward bias when the *p*-type region is connected to a positive terminal and *n*-type is connected to a negative terminal. This forces the electrons from the *n*-side and the holes from the *p*-side to keep moving towards the *p*-side and *n*-side, respectively as minority carriers, counteracting the built-in voltage. On the contrary, reverse bias is applied when the *p*-side is connected to a negative terminal and the *n*-side to a positive terminal. This pulls the holes in the *p*-type and the electrons in the *n*-type away from the junction increasing the barrier voltage and minimising the current flow across the *p*-*n* junction. The current density (j) voltage (V) characteristic of a *p*-*n* junction under bias can be described as

$$j = j_s \left[exp\left(\frac{eV}{kT}\right) - 1 \right] \qquad 1.11$$

where j_s is called the reverse saturation current. When the *p*-*n* junction is exposed to solar radiation, electron-hole pairs can be generated by the absorption of photons with sufficient energy to excite across the band gap. The built-in electric field separates the electron and hole, with the electron moving to the n side and the hole moving to the p side. This increases the concentration of minority charge carriers i.e. holes in the *p*-type and electrons in the *n*-type regions.

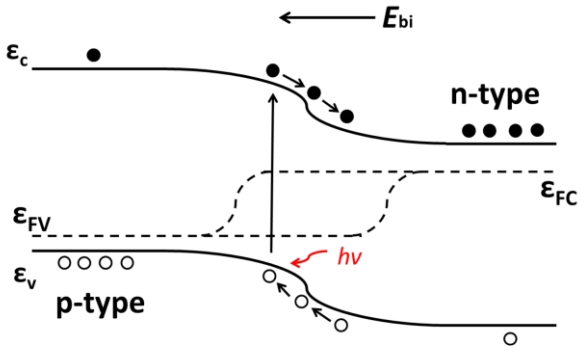

Figure 1.11 A p-n junction absorbing incident photons.

When this *p-n* junction is connected to an external circuit, the photo-generated carriers flow through the circuit giving rise to a photocurrent. Equation 1.1 can then be modified as

$$j = j_s \left[exp\left(\frac{eV}{kT}\right) - 1 \right] + j_{sc} \qquad 1.12$$

where j_{sc} is the short circuit current. This is the current-voltage characteristic for *p-n* junction solar cells. For j=0, we obtain the open circuit voltage V_{OC} as shown in Equation 1.13.

$$V_{OC} = \frac{kT}{e} \ln\left(1 - \frac{j_{SC}}{j_s}\right) \qquad 1.13$$

There is a large temperature difference between the Sun (~5800 K) and the Earth (~300 K). The detailed balance model of an ideal solar cell is based on the exchange of radiation between the sun and the earth. The principle of detailed balance necessitates that each microscopic action within a system maintains equilibrium with its reverse action when the entire system achieves thermodynamic equilibrium. This principle holds significant relevance in photovoltaics as it enables the computation of the maximum achievable efficiency of a specific solar cell. It defines the fundamental loss process as the radiative recombination of electron/hole pairs, succeeded by photon emission. Under equilibrium conditions—specifically, in darkness and without an applied voltage—the absorbed and emitted photon fluxes must be equal, adhering to the principle of detailed balance.

Figure 1.12 depicts the basic device makeup of a *p-n* junction solar cell consisting of a photo absorber material (A) sandwiched between an electron transport and a hole transport material on the left and right side of A, respectively.

When a photon with energy greater than the band gap of the material falls on it, the photon is absorbed, and an electron-hole pair is created. This electron-hole pair rapidly loses energy (process B) to give an electron and a hole with energy approximately equal to the band gap of the material. However, the energy lost by the electron-hole pair is not the free energy which can be extracted to do work in the circuit. The energy per extracted carrier, which can be used to do work in the circuit, is the product of the elementary charge and the voltage at the point of operation which is substantially smaller than the band gap (see Figure 1.12). In a photovoltaic device, there is some built in asymmetry which pulls the excited electrons away (process C) before they can relax and feeds them to an external circuit. The extra energy of the excited electrons generates an electromotive force (e.m.f.) which drives the electrons through a load in the external circuit to do electrical work.

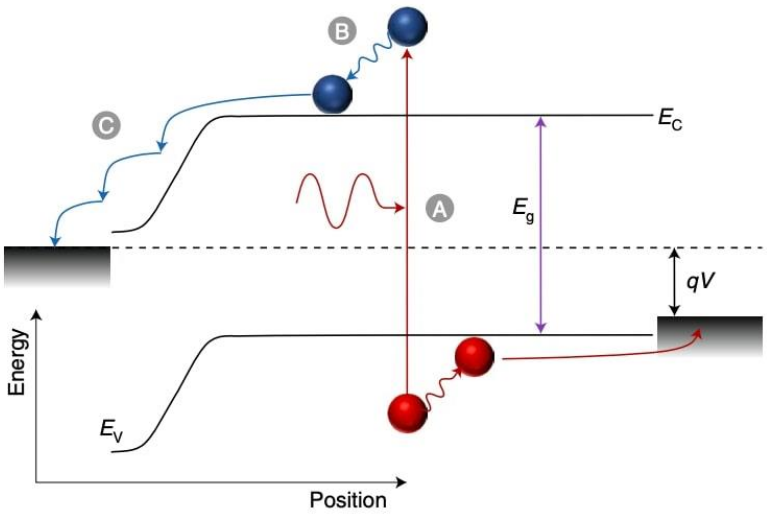

Figure 1.12 Energy band diagram illustrating the solar cell process. A denotes the photoexcitation of the electron, B signifies the thermalization of the electron-hole pair, and C depicts the movement of the excited electron to the electron transport layer."

For any intermediate load resistance R_L the cell develops a voltage between 0 and V_{OC} and delivers a current I such that $V = IR_L$. Since the current is approximately proportional to the illuminated area, the short circuit density J_{SC} is an important quantity for comparison. The power density of the cell at a certain voltage V is given by Equation 1.14,

$$P = JV \tag{1.14}$$

where J is the current density at the voltage V. P reaches a maximum at the cell's maximum power point which occurs at some voltage V_m with a corresponding current density J_m. The optimum load has sheet resistance given by V_m/J_m. The fill factor (Equation 1.15) is defined as the ratio,

$$FF = \frac{J_m V_m}{J_{SC}\, V_{OC}} \tag{1.15}$$

and describes the squareness of the J-V curve. The efficiency η of the cell is the power density delivered at operating point as a fraction of the incident light power density, P_S,

$$\eta = \frac{J_m V_m}{P_S} \tag{1.16}$$

Efficiency is related to J_{SC} and V_{OC} using FF,

$$\eta = \frac{J_{SC} V_{OC} FF}{P_S} \tag{1.17}$$

These four quantities J_{SC}, V_{OC}, FF and η are the key performance characteristics of a solar cell.

Figure 1.13 illustrates the current-voltage (I-V) characteristics of a typical solar cell. The power output from a solar cell is determined by multiplying the current (I) by the voltage (V). This curve demonstrates the presence of a maximum power point located at I_{max} and V_{max}.

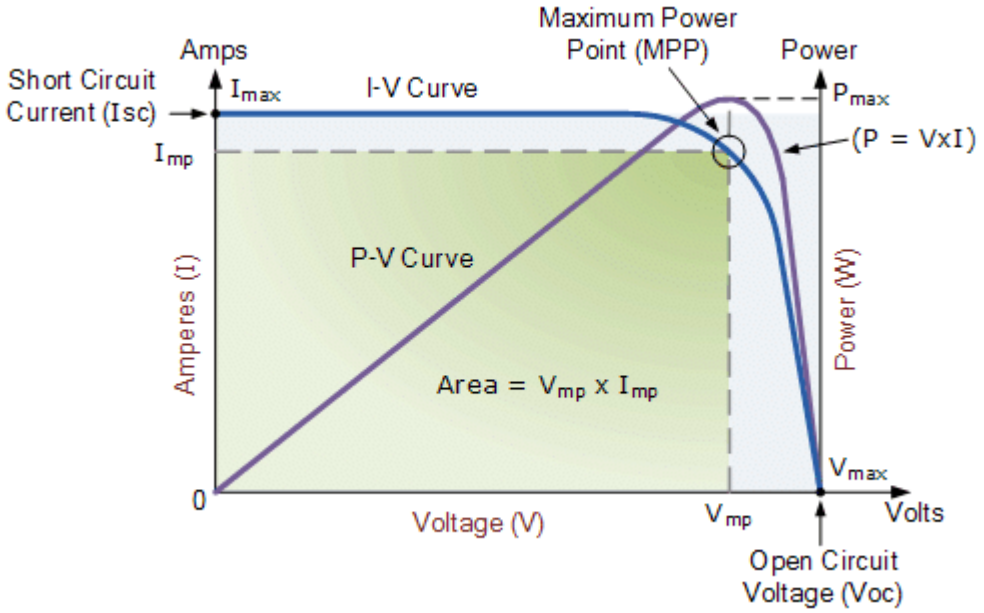

Figure 1.13 Current-Voltage characteristics of a typical solar cell. Adapted from [90]

Upon being excited into conduction bands, electrons may subsequently return to valence bands and recombine with holes, resulting in the release of energy. This process of recombination represents a reversal of the initial excitation and ultimately results in the elimination of charge carriers. Based on the underlying mechanisms, three distinct types of recombination can be identified as depicted in Figure 1.14 below.

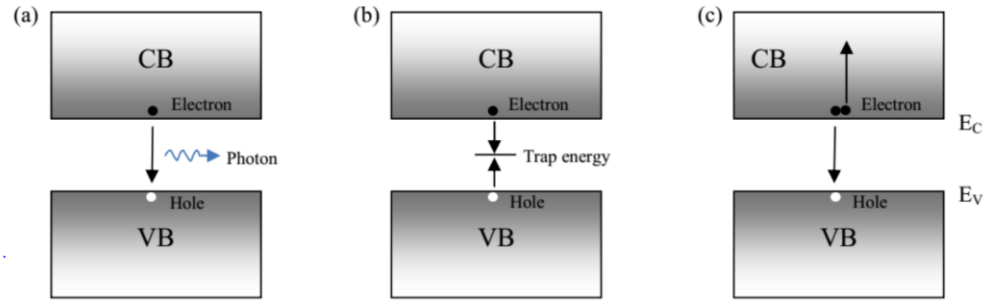

Figure 1.14 Illustration of different recombination mechanisms: (a) radiative recombination, (b) SRH (Shockley-Read-Hall) recombination, and (c) Auger recombination.

Radiative Recombination

This is the opposite of excitation wherein the electron recombines with hole at the valence band resulting in the release of energy in the form of a photon. Since the energy of the photon is roughly equal to the band gap of the semiconductor the photon can only be weakly absorbed and is ejected out of the material.

Shockley-Read-Hall Recombination

This type of recombination occurs due to the presence of defects in the crystal lattice. An electron (or hole) may get trapped in one of these defect sites at an energy level within the forbidden region of the energy bands. The trapped carrier may get released by thermal activation or could recombine with an opposite carrier if the defect site traps another charge carrier before it is released. Since the defect sites are more common at the surfaces and grain boundaries, this type of recombination is more profound in these areas.

Auger Recombination

This type of recombination involves three different charge carriers. An electron in the conduction band combines with a hole in the valence band, and the released energy is absorbed by another electron in the conduction band, which gets excited to a higher energy level. So, unlike radiative recombination, there is no emission of photons. The excited electron finally comes back to the valence band edge as it releases its excess energy thermally. Due to the involvement of three charge carriers, this type of recombination is only prominent when carrier densities are very high like in heavily doped materials, at high temperatures and under strong illumination.

References

1. Graham Mott, C.R.a.R.H. *Carbon emissions anywhere threaten development everywhere*. 2021; Available from: https://unctad.org/news/carbon-emissions-anywhere-threaten-development-everywhere.

2. Wang, F., et al., *Technologies and perspectives for achieving carbon neutrality.* The Innovation, 2021. **2**(4): p. 100180.

3. Sum, T.C. and N. Mathews, *Advancements in perovskite solar cells: photophysics behind the photovoltaics.* Energy & Environmental Science, 2014. **7**(8): p. 2518-2534.

4. Jiang, Q., et al., *Surface passivation of perovskite film for efficient solar cells.* Nature Photonics, 2019. **13**(7): p. 460-466.

5. Meng, L., J. You, and Y. Yang, *Addressing the stability issue of perovskite solar cells for commercial applications.* Nature Communications, 2018. **9**(1): p. 5265.

6. Wang, R., et al., *A Review of Perovskites Solar Cell Stability.* Advanced Functional Materials, 2019. **29**(47): p. 1808843.

7. Green, M.A., et al., *Solar cell efficiency tables (Version 53).* Progress in Photovoltaics: Research and Applications, 2019. **27**(1): p. 3-12.

8. *NREL Best Research-Cell Efficiency Chart*. 2023; Available from: https://www.nrel.gov/pv/cell-efficiency.html.

9. Lameirinhas, R., J.P. Torres, and J. Cunha, *A Photovoltaic Technology Review: History, Fundamentals and Applications.* Energies, 2022. **15**: p. 1823.

10. Fritts, C.E., *On the fritts selenium cells and batteries.* Journal of the Franklin Institute, 1885. **119**(3): p. 221-232.

11. Czochralski, J., *Ein neues Verfahren zur Messung der Kristallisationsgeschwindigkeit der Metalle.* Zeitschrift für Physikalische Chemie, 1918. **92U**(1): p. 219-221.

12. Lab, B. *April 25, 1954: Bell Labs Demonstrates the First Practical Silicon Solar Cell*. 2009; Available from: http://www.aps.org/publications/apsnews/200904/physicshistory.cfm.

13. Rothwarf, A., *The CdS/Cu2S solar cell: Basic operation and anomalous effects.* Solar Cells, 1980. **2**(2): p. 115-140.

14. O'Regan, B. and M. Grätzel, *A low-cost, high-efficiency solar cell based on dye-sensitized colloidal TiO2 films.* Nature, 1991. **353**(6346): p. 737-740.

15. Conibeer, G., *Third-generation photovoltaics.* Materials Today, 2007. **10**(11): p. 42-50.

16. Kazim, S., et al., *Perovskite as Light Harvester: A Game Changer in Photovoltaics.* Angewandte Chemie International Edition, 2014. **53**(11): p. 2812-2824.

17. Green, M.A., et al., *Solar cell efficiency tables (Version 63).* Progress in Photovoltaics: Research and Applications, 2024. **32**(1): p. 3-13.

18. Vidal, J., *Solar energy 'revolution' brings green power closer*, in *The Guardian*. 2007: https://www.theguardian.com/environment/2007/dec/29/solarpower.renewableenergy?CMP=share_btn_url.

19. Lu, K., *Comparison and Evaluation of Different Types of Solar Cells.* Applied and Computational Engineering, 2023. **23**: p. 263-270.

20. Scarpulla, M.A., et al., *CdTe-based thin film photovoltaics: Recent advances, current challenges and future prospects.* Solar Energy Materials and Solar Cells, 2023. **255**: p. 112289.

21. Kanevce, A., et al., *The roles of carrier concentration and interface, bulk, and grain-boundary recombination for 25% efficient CdTe solar cells.* Journal of Applied Physics, 2017. **121**(21).

22. Wang, W., et al., *Device Characteristics of CZTSSe Thin-Film Solar Cells with 12.6% Efficiency.* Advanced Energy Materials, 2014. **4**(7): p. 1301465.

23. García-Valverde, R., J.A. Cherni, and A. Urbina, *Life cycle analysis of organic photovoltaic technologies.* Progress in Photovoltaics: Research and Applications, 2010. **18**(7): p. 535-558.

24. Jean, J., et al., *Pathways for solar photovoltaics.* Energy & Environmental Science, 2015. **8**(4): p. 1200-1219.

25. Kakiage, K., et al., *Highly-efficient dye-sensitized solar cells with collaborative sensitization by silyl-anchor and carboxy-anchor dyes.* Chemical Communications, 2015. **51**(88): p. 15894-15897.

26. Grätzel, M., *Photoelectrochemical cells.* Nature, 2001. **414**(6861): p. 338-344.

27. Bai, S., et al., *High-performance planar heterojunction perovskite solar cells: Preserving long charge carrier diffusion lengths and interfacial engineering.* Nano Research, 2014. **7**(12): p. 1749-1758.

28. Srivastava, P. and M. Bag, *Elucidating tuneable ambipolar charge transport and field induced bleaching at the CH3NH3PbI3/electrolyte interface.* Physical Chemistry Chemical Physics, 2020. **22**(19): p. 11062-11074.

29. Wehrenfennig, C., et al., *High charge carrier mobilities and lifetimes in organolead trihalide perovskites.* Adv Mater, 2014. **26**(10): p. 1584-9.

30. Shi, D., et al., *Low trap-state density and long carrier diffusion in organolead trihalide perovskite single crystals.* Science, 2015. **347**(6221): p. 519.

31. Kojima, A., et al., *Organometal Halide Perovskites as Visible-Light Sensitizers for Photovoltaic Cells.* Journal of the American Chemical Society, 2009. **131**(17): p. 6050-6051.

32. Mariotti, S., et al., *Interface engineering for high-performance, triple-halide perovskite–silicon tandem solar cells.* Science, 2023. **381**(6653): p. 63-69.

33. Antonietta Loi, M. and J.C. Hummelen, *Perovskites under the Sun.* Nature Materials, 2013. **12**(12): p. 1087-1089.

34. Kim, H.-S., S.H. Im, and N.-G. Park, *Organolead Halide Perovskite: New Horizons in Solar Cell Research.* The Journal of Physical Chemistry C, 2014. **118**(11): p. 5615-5625.

35. Li, C., et al., *Formability of ABX3 (X = F, Cl, Br, I) halide perovskites.* Acta Crystallographica Section B, 2008. **64**(6): p. 702-707.

36. Park, N.-G., *Perovskite solar cells: an emerging photovoltaic technology.* Materials Today, 2015. **18**(2): p. 65-72.

37. Li, Z., et al., *Stabilizing Perovskite Structures by Tuning Tolerance Factor: Formation of Formamidinium and Cesium Lead Iodide Solid-State Alloys.* Chemistry of Materials, 2016. **28**(1): p. 284-292.

38. Kojima, A., et al., *Organometal Halide Perovskites as Visible-Light Sensitizers for Photovoltaic Cells.* Journal of the American Chemical Society, 2009.

39. Im, J.-H., et al., *6.5% efficient perovskite quantum-dot-sensitized solar cell.* Nanoscale, 2011. **3**(10): p. 4088-4093.

40. Kim, H.-S., et al., *Lead Iodide Perovskite Sensitized All-Solid-State Submicron Thin Film Mesoscopic Solar Cell with Efficiency Exceeding 9%.* Scientific Reports, 2012. **2**(1): p. 591.

41. Lee, M.M., et al., *Efficient Hybrid Solar Cells Based on Meso-Superstructured Organometal Halide Perovskites.* Science, 2012. **338**(6107): p. 643.

42. Etgar, L., et al., *Mesoscopic CH3NH3PbI3/TiO2 Heterojunction Solar Cells.* Journal of the American Chemical Society, 2012. **134**(42): p. 17396-17399.

43. Noh, J.H., et al., *Chemical Management for Colorful, Efficient, and Stable Inorganic–Organic Hybrid Nanostructured Solar Cells.* Nano Letters, 2013. **13**(4): p. 1764-1769.

44. Burschka, J., et al., *Sequential deposition as a route to high-performance perovskite-sensitized solar cells.* Nature, 2013. **499**(7458): p. 316-319.

45. Liu, M., M.B. Johnston, and H.J. Snaith, *Efficient planar heterojunction perovskite solar cells by vapour deposition.* Nature, 2013. **501**(7467): p. 395-398.

46. Park, N.-G., *Organometal Perovskite Light Absorbers Toward a 20% Efficiency Low-Cost Solid-State Mesoscopic Solar Cell.* The Journal of Physical Chemistry Letters, 2013. **4**(15): p. 2423-2429.

47. Yang, W.S., et al., *High-performance photovoltaic perovskite layers fabricated through intramolecular exchange.* Science, 2015. **348**(6240): p. 1234-1237.

48. Saliba, M., et al., *A molecularly engineered hole-transporting material for efficient perovskite solar cells.* Nature Energy, 2016. **1**(2): p. 15017.

49. Philippe, B., et al., *Chemical and Electronic Structure Characterization of Lead Halide Perovskites and Stability Behavior under Different Exposures—A Photoelectron Spectroscopy Investigation.* Chemistry of Materials, 2015. **27**(5): p. 1720-1731.

50. Hwang, H., et al., *Enhancing performance and stability of perovskite solar cells using hole transport layer of small molecule and conjugated polymer blend.* Journal of Power Sources, 2019. **418**: p. 167-175.

51. Kim, M., et al., *Enhanced solar cell stability by hygroscopic polymer passivation of metal halide perovskite thin film.* Energy & Environmental Science, 2018. **11**(9): p. 2609-2619.

52. Pellet, N., et al., *Mixed-Organic-Cation Perovskite Photovoltaics for Enhanced Solar-Light Harvesting.* Angewandte Chemie (International ed. in English), 2014. **53**.

53. Saliba, M., et al., *Cesium-containing Triple Cation Perovskite Solar Cells: Improved Stability, Reproducibility and High Efficiency.* Energy & Environmental Science, 2016.

54. Jung, E.H., et al., *Efficient, stable and scalable perovskite solar cells using poly(3-hexylthiophene).* Nature, 2019. **567**(7749): p. 511-515.

55. Yoo, J.J., et al., *Efficient perovskite solar cells via improved carrier management.* Nature, 2021. **590**(7847): p. 587-593.

56. Min, H., et al., *Perovskite solar cells with atomically coherent interlayers on SnO2 electrodes.* Nature, 2021. **598**(7881): p. 444-450.

57. Zhou, H., et al., *Photovoltaics. Interface engineering of highly efficient perovskite solar cells.* Science, 2014. **345**(6196): p. 542-6.

58. Jeon, N.J., et al., *Compositional engineering of perovskite materials for high-performance solar cells.* Nature, 2015. **517**(7535): p. 476-480.

59. Zheng, L., et al., *A hydrophobic hole transporting oligothiophene for planar perovskite solar cells with improved stability.* Chemical Communications, 2014. **50**(76): p. 11196-11199.

60. Stranks, S.D., et al., *Electron-Hole Diffusion Lengths Exceeding 1 Micrometer in an Organometal Trihalide Perovskite Absorber.* Science, 2013. **342**(6156): p. 341.

61. Tenuta, E., C. Zheng, and O. Rubel, *Thermodynamic origin of instability in hybrid halide perovskites.* Scientific Reports, 2016. **6**(1): p. 37654.

62. Niu, G., et al., *Study on the stability of CH3NH3PbI3 films and the effect of post-modification by aluminum oxide in all-solid-state hybrid solar cells.* Journal of Materials Chemistry A, 2014. **2**(3): p. 705-710.

63. Vincent, B.R., et al., *Alkylammonium lead halides. Part 1. Isolated PbI64− ions in (CH3NH3)4PbI6•2H2O.* Canadian Journal of Chemistry, 1987. **65**(5): p. 1042-1046.

64. Leguy, A.M.A., et al., *Reversible Hydration of CH3NH3PbI3 in Films, Single Crystals, and Solar Cells.* Chemistry of Materials, 2015. **27**(9): p. 3397-3407.

65. Habisreutinger, S.N., et al., *Carbon Nanotube/Polymer Composites as a Highly Stable Hole Collection Layer in Perovskite Solar Cells.* Nano Letters, 2014. **14**(10): p. 5561-5568.

66. Liu, J., et al., *Employing PEDOT as the p-Type Charge Collection Layer in Regular Organic–Inorganic Perovskite Solar Cells.* The Journal of Physical Chemistry Letters, 2015. **6**(9): p. 1666-1673.

67. Juarez-Perez, E.J., et al., *Photodecomposition and thermal decomposition in methylammonium halide lead perovskites and inferred design principles to increase photovoltaic device stability.* Journal of Materials Chemistry A, 2018. **6**(20): p. 9604-9612.

68. Domanski, K., et al., *Systematic investigation of the impact of operation conditions on the degradation behaviour of perovskite solar cells.* Nature Energy, 2018. **3**(1): p. 61-67.

69. Li, Y., et al., *Degradation by Exposure of Coevaporated CH3NH3PbI3 Thin Films.* The Journal of Physical Chemistry C, 2015. **119**(42): p. 23996-24002.

70. Pont, S., et al., *Tuning CH3NH3Pb(I1−xBrx)3 perovskite oxygen stability in thin films and solar cells.* Journal of Materials Chemistry A, 2017. **5**(20): p. 9553-9560.

71. Bai, Y., et al., *Enhancing stability and efficiency of perovskite solar cells with crosslinkable silane-functionalized and doped fullerene.* Nature Communications, 2016. **7**(1): p. 12806.

72. Jiang, Q., et al., *Pseudohalide-Induced Moisture Tolerance in Perovskite CH3NH3Pb(SCN)2I Thin Films.* Angewandte Chemie International Edition, 2015. **54**(26): p. 7617-7620.

73. Cao, J., et al., *Thiols as interfacial modifiers to enhance the performance and stability of perovskite solar cells.* Nanoscale, 2015. **7**(21): p. 9443-9447.

74. Han, Q., et al., *Single Crystal Formamidinium Lead Iodide (FAPbI3): Insight into the Structural, Optical, and Electrical Properties.* Advanced Materials, 2016. **28**(11): p. 2253-2258.

75. Quarti, C., et al., *Structural and optical properties of methylammonium lead iodide across the tetragonal to cubic phase transition: implications for perovskite solar cells.* Energy & Environmental Science, 2016. **9**(1): p. 155-163.

76. Wu, K., et al., *Temperature-dependent excitonic photoluminescence of hybrid organometal halide perovskite films.* Physical Chemistry Chemical Physics, 2014. **16**(41): p. 22476-22481.

77. Poglitsch, A. and D. Weber, *Dynamic disorder in methylammoniumtrihalogenoplumbates (II) observed by millimeter-wave spectroscopy.* The Journal of Chemical Physics, 1987. **87**(11): p. 6373-6378.

78. Binek, A., et al., *Stabilization of the Trigonal High-Temperature Phase of Formamidinium Lead Iodide.* The Journal of Physical Chemistry Letters, 2015. **6**(7): p. 1249-1253.

79. Conings, B., et al., *Intrinsic Thermal Instability of Methylammonium Lead Trihalide Perovskite.* Advanced Energy Materials, 2015. **5**(15): p. 1500477.

80. Huang, W., S. Sadhu, and S. Ptasinska, *Heat- and Gas-Induced Transformation in CH3NH3PbI3 Perovskites and Its Effect on the Efficiency of Solar Cells.* Chemistry of Materials, 2017. **29**(19): p. 8478-8485.

81. Fu, Y., et al., *Stabilization of the Metastable Lead Iodide Perovskite Phase via Surface Functionalization.* Nano Letters, 2017. **17**(7): p. 4405-4414.

82. Fan, W., et al., *Ligand exchange engineering of FAPbI3 perovskite quantum dots for solar cells.* Frontiers of Optoelectronics, 2022. **15**(1): p. 39.

83. Lee, J.-W., et al., *2D perovskite stabilized phase-pure formamidinium perovskite solar cells.* Nature Communications, 2018. **9**(1): p. 3021.

84. Wang, K., et al., *All-inorganic cesium lead iodide perovskite solar cells with stabilized efficiency beyond 15%.* Nature Communications, 2018. **9**(1): p. 4544.

85. Bhachu, D.S., et al., *Scalable route to CH3NH3PbI3 perovskite thin films by aerosol assisted chemical vapour deposition.* Journal of Materials Chemistry A, 2015. **3**(17): p. 9071-9073.

86. Kato, Y., et al., *Silver Iodide Formation in Methyl Ammonium Lead Iodide Perovskite Solar Cells with Silver Top Electrodes.* Advanced Materials Interfaces, 2015. **2**(13): p. 1500195.

87. Sutherland, B.R., *Solar Materials Find Their Band Gap.* Joule, 2020. **4**(5): p. 984-985.

88. Shockley, W. and H.J. Queisser, *Detailed Balance Limit of Efficiency of p-n Junction Solar Cells.* Journal of Applied Physics, 2004. **32**(3): p. 510-519.

89. *Physics and Properties of Semiconductors—A Review*, in *Physics of Semiconductor Devices*. 2006. p. 5-75.

90. Alanbary, J., *Design and Construction of a Tracking Device for Solar Electrical Systems.* The Journal of Scientific and Engineering Research, 2018. **5**: p. 225-236.

Chapter 2. Characterisation Techniques and Theory

2.1. X-ray Photoelectron Spectroscopy (XPS)

X-ray photoelectron spectroscopy is a non-destructive, surface-sensitive analytical technique that utilises the photoemission of electrons using soft X-rays to provide qualitative and quantitative information about the electronic structure of any solid [1, 2]. Soft X-rays are electromagnetic radiation (ER) with energies in the region 200 eV – 2000 eV. XPS is widely used to investigate the elemental composition, electronic states, and surface chemistry of a large range of materials.

2.1.1. Theory

XPS functions on the principle of the photoelectric effect, first observed by the German physicist Heinrich Rudolf Hertz in 1887. Albert Einstein further provided a quantum-mechanical explanation to this phenomenon in 1905. He postulated that light comprises discrete packets of energy called photons, each carrying an amount of energy, or quantum (hv), determined by the light's frequency.

Core electrons are bound to an atom's nucleus in discrete energy levels known as orbitals. These orbital energies are unique to each element and are susceptible to alterations based on the chemical environment surrounding the element. When a sample interacts with photons of a defined energy (hv), this interaction leads to the excitation and subsequent ejection of these core-level electrons, a process depicted in Figure 2.1. In XPS, the photoemission of core-level electrons occurs due to the absorption of soft X-rays.

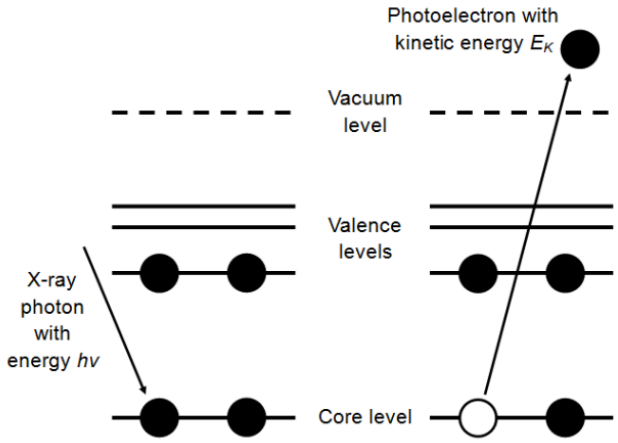

Figure 2.1 Energy level diagram illustrating the X-ray photoemission process.

The kinetic energy (E_K) of the emitted photoelectron depends on its binding energy (BE) within the atom from which it was expelled. Each element exhibits a distinctive BE for its respective orbitals. Consequently, through the assessment of kinetic energy, we indirectly gauge the BE of the electrons, thereby acquiring insights into the chemical environment from which the electron has been discharged. BE of the emitted electrons can be determined by invoking the law of conservation of energy for the photoemission process,

$$BE = h\nu - E_K - \phi_{spec} \qquad 2.1$$

where *hv* represents the X-ray photon energy and ϕ_{spec} represents the work function of the spectrophotometer. Work function can be defined as the energy required to remove an electron from the fermi level to the vacuum level as shown in Figure 2.2. In XPS, the work function of the spectrometer is measured and not the work function of the sample as it is in electrical contact with the spectrometer. A common practice involves calibrating the spectrometer by referencing the spectrophotometer to known energy levels (e.g., Au $4f_{7/2}$ – 84 eV).

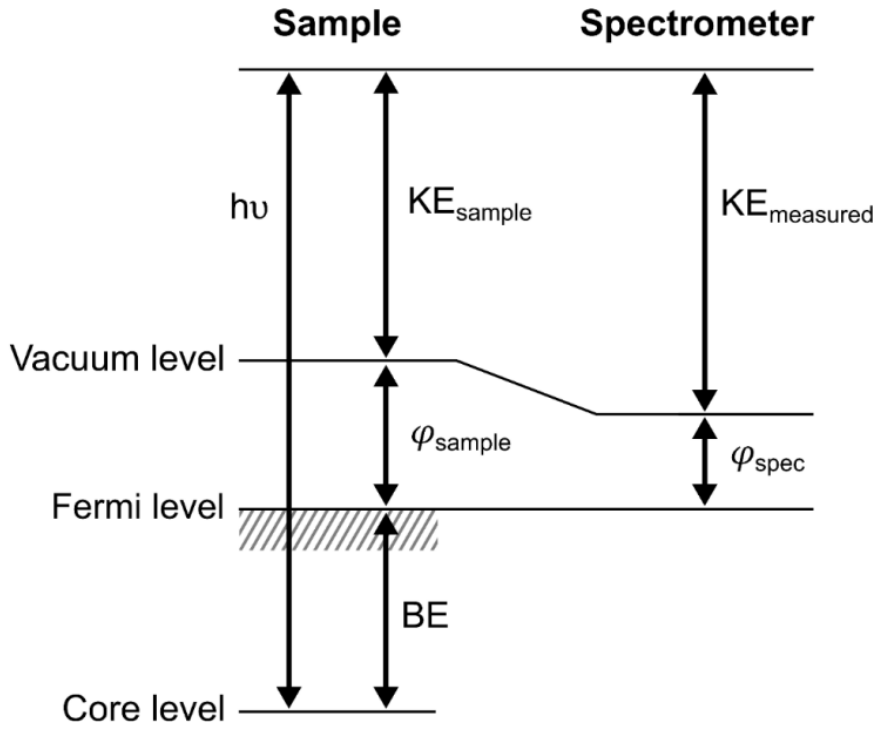

Figure 2.2 Schematic representation of the energy level diagram of a core level electron in a sample electrically connected to the spectrometer. Adapted from [3]

In laboratory based XPS, the utilisation of distinct X-ray sources, such as Al Kα and Mg Kα, generates photons with fixed energies, at 1486.6 eV for Al Kα and 1254.6 eV for Mg Kα. This characteristic sets XPS apart from alternative photoemission techniques like ultraviolet photoelectron spectroscopy (UPS), which relies on lower energy light to probe valence electrons. Synchrotron sources allow the X-ray energy to be varied and will be described in section 2.5.

When electrons are emitted during the photoemission process, core holes are created by the vacancy of the emitted electrons. Generally, this results in the re-arrangement of the energy level of the non-photoemitting electrons leading to a change in the kinetic energy of the emitted photoelectrons. This slight change in energy levels in response to the creation of core holes is known as the relaxation energy [4]. In theory, the relaxation is only significant for valence electrons, and it is assumed that the core hole left behind by the emitted photoelectron is not immediately filled by another electron. This approximation known as Koopman's theorem means that the energies required to

remove the electrons from their orbits are representative of the energy of the orbitals from which they were ejected [5].

XPS Depth Profiling

XPS is known for its surface sensitivity, attributable to its shallow sampling depth, typically within the range of 1 to 10 nanometres. At synchrotron facilities, altering the photon energy modifies the sampling depth. Synchrotron beamlines employed for XPS experiments offer tuneable photon energies within a range of approximately 45 to 2800 eV [6]. Higher photon energies result in higher E_K for emitted electrons from a particular orbital, increasing their λ and consequently expanding the sampling depth.

The attenuation of electrons within a material is elucidated by the Beer-Lambert Law:

$$I = I_o exp\left(\frac{-x}{\lambda\ sin\theta}\right) \qquad 2.2$$

Where I_o represents the original intensity while I denote the measured intensity after travelling a distance x through the material.

Another crucial parameter describing XPS signal intensity is the photoelectric cross-section, σ. This parameter signifies the likelihood of exciting a core-level electron from a specific element with a photon of a specific energy. These cross-sections vary with the atomic number (Z) and the electron orbital being excited (e.g., 1s, 2s, 2p, etc.). The excitation cross-section attains its peak when the photon energy aligns approximately with the core level BE.

Although photoelectrons can be generated a few microns beneath the sample surface, they undergo substantial energy losses due to inelastic scattering. This scattering phenomenon is quantified by the inelastic mean free path (IMFP), denoted as λ, representing the average distance an electron travels between two successive inelastic collisions, as a function of its kinetic energy E_K. The IMFP curve, depicted in Figure 2.3, exhibits a minimum (less than 1 nm) when E_K lies approximately between 20 and 200 eV. In solids, photoelectrons possess extremely small mean free paths, allowing only

those generated within a few nanometres of the surface to escape without considerable energy dissipation. 95% of the XPS signal intensity comes from a depth of 3λ.

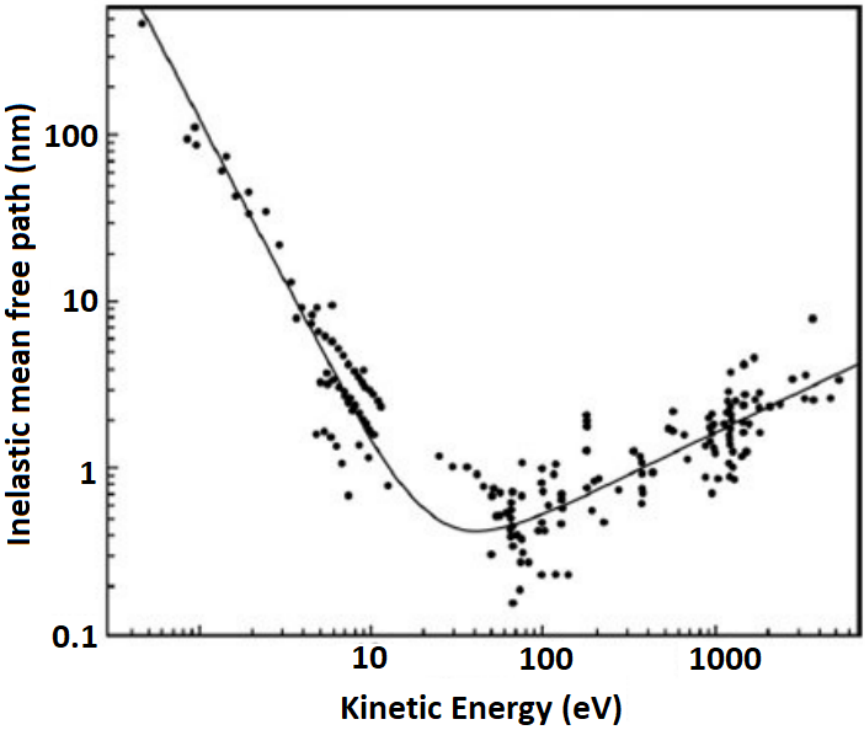

Figure 2.3 The universal curve of inelastic mean free path (IMFP) for the elements as a function of their kinetic energy as calculated by Seah & Dench [7]

The sampling depth, expressed as *d*, is determined by the equation:

$$d = 3\lambda sin\,\theta \qquad 2.3$$

where θ signifies the emission angle of the photoelectron relative to the sample surface, as illustrated in Figure 2.4. The probing depth of the sample is modified by tuning the energy of the incident photon or changing the photoelectron emission angle [1]. The sampling depth can be decreased by increasing the angle between the surface normal and the analyser, keeping the position of the X-ray source and analyser fixed as illustrated in Figure 2.4 below.

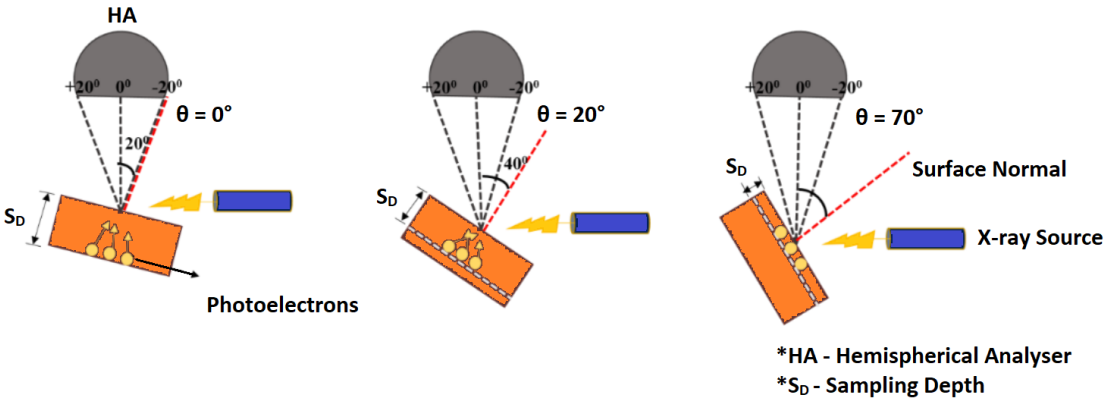

Figure 2.4 Schematic illustration depicting the measurement of photoelectrons originating from various emission angles (ϑ). When the sample is rotated with respect to the analyser while keeping the X-ray source and detector fixed, the effective sampling depth diminishes proportionally by the cosine of ϑ. The depicted analyser's acceptance angle remains approximately 20°.

By manipulating the sample orientation, the electron energy analyser can detect surface-sensitive electrons in what is termed as grazing emission (GE). Conversely, electrons escaping perpendicular to the surface, detected in normal emission (NE), provide insights into distinct chemical and elemental states at the deeper layers of the sample. These depth-profiling measurements are instrumental in characterising surface contaminants, adsorbates, and oxidation on the sample surface.

Photoemission Spectra

A photoemission spectrum typically illustrates the relationship between photoelectron intensity (measured in counts per second) and their binding energy. While it's feasible to plot the spectrum using kinetic energy, the convention predominantly utilises binding energies owing to their relevance in providing insights into the chemistry and structure of a material's surface. BE encapsulates valuable information about a material's surface chemistry and structural composition.

Spin orbit Splitting

In XPS, the detection of core level electrons stems from distinct atomic orbitals—s, p, d, and f. Describing a core level requires a set of four quantum numbers. The principal quantum number, denoted as *n*, assumes integer values, starting from 1 and signifying the shell from which the electron was expelled. The total angular momentum quantum number, *j*, is determined by $j = l \pm s$ and encompasses integer values bounded by $|l - s| \leq j \leq |l + s|$. Here, the angular momentum quantum number, *l*, is correlated with the orbital, adopting values of 0, 1, 2, and 3 for the s, p, d, and f orbitals, respectively. The spin angular momentum number, *s*, assumes values of ±1/2, depending upon whether the electron's spin aligns parallel or antiparallel to the orbital angular momentum.

For s orbitals, $j = 1/2$, contributing to a singular peak in XPS spectra. Conversely, excitation from higher orbitals where $l > 0$ leads to spin orbit splitting, resulting in two sublevels possessing a degeneracy of $2j + 1$. This divergence is observed as a split peak or a doublet, as illustrated in the Cl 2p spectra shown in Figure 2.5.

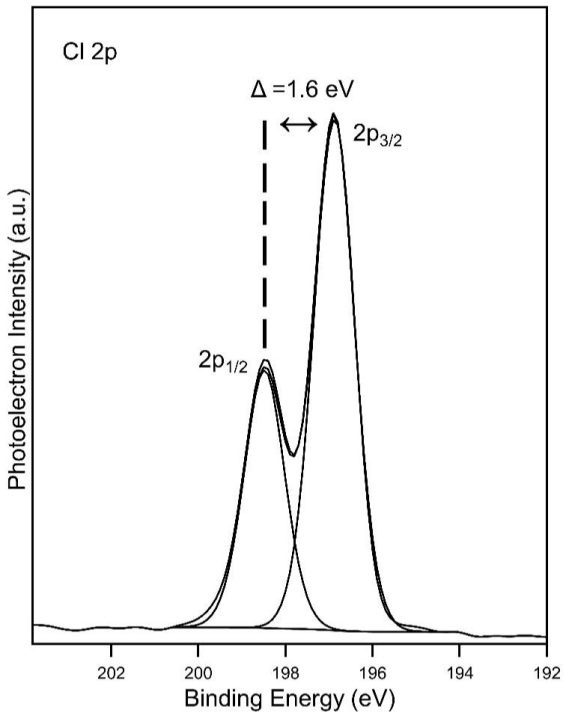

Figure 2.5 Cl 2p doublet from a BMIMCl-modified perovskite thin film surface. The two peaks $2p_{1/2}$ and $2p_{3/2}$ have the same full width at half maximum (1.1 eV), a spin orbit separation of 1.6 eV and an area ratio of 1:2.

The two spin orbit peaks within a p doublet are labelled as $p_{1/2}$ and $p_{3/2}$, with the $p_{1/2}$ peak positioned at a higher BE. The separation in BE of these spin orbit doublet peaks is constant and specific to the orbital and element. The ratio of the areas under these peaks is expressed as $(2j^- + 1)/(2j^+ + 1)$. In the case of p orbitals, where $j^- = 1/2$ and $j^+ = 3/2$, the area ratio between $p_{1/2}$ and $p_{3/2}$ peaks is 1:2 (See Table 2.1). This spin orbit splitting phenomenon, shown by the Cl 2p spectra in Figure 2.5, portrays the distinct peaks by their respective element, shell number, orbital, and *j*. A Cl $2p_{3/2}$ peak indicates electrons excited from the 2p orbital of a chlorine atom with $j = 3/2$.

Orbital	*j* values (j^+, j^-)	Area Ratio (j^- : j^+)
s ($l = 0$)	1/2 (singlet)	—
p ($l = 1$)	1/2 , 3/2	1:2
d ($l = 2$)	3/2 , 5/2	2:3
f ($l = 3$)	5/2 , 7/2	3:4

Table 2.1 Spin orbit splitting j values and doublet peak area ratios for s, p, d, and f orbitals.

2.1.2. Peak fitting

The analysis of XPS spectra involves fitting peaks to experimental data. These fitted peaks are termed components within a given spectrum. To generate a component, the data must initially undergo a background correction procedure. This correction yields regions within a spectrum where the background has been subtracted, allowing for the fitting of components. The background signal emerges from the inelastic scattering of electrons within the material, causing a reduction in the kinetic energy of electrons and resulting in a more pronounced background on the high BE side of the peak. Figure 2.6 below illustrates three commonly utilised background correction methods.

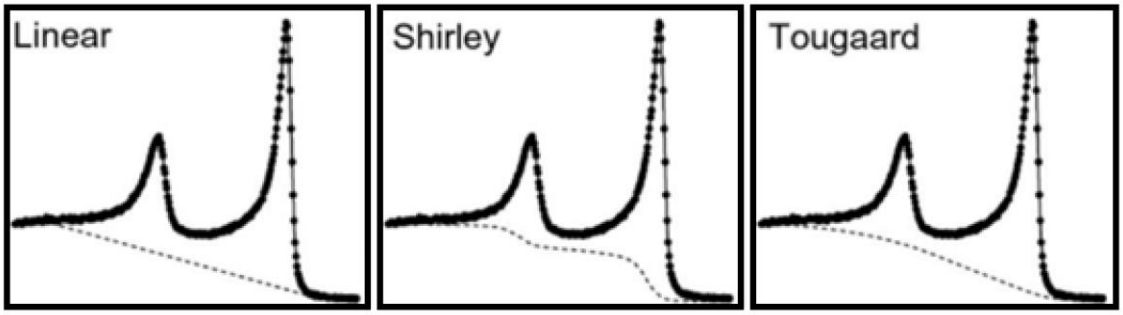

Figure 2.6 Linear, Shirley and Tougaard background correction types for a Fe 2p XPS peak. Figure adapted from [8].

Linear backgrounds serve as a straightforward approximation, particularly valuable when numerous peaks overlap within a dataset. The Tougaard subtraction method addresses background correction by simulating inelastic scattering across an energy range. However, it presents challenges in spectra featuring multiple overlapping peaks. Conversely, the Shirley background algorithm generates an S-shaped background based on the intensity of the initial and final points. This method, widely adopted, stands as the predominant choice for background correction and has been applied within this thesis.

After the subtraction of the background signal, components are fitted to the peaks observed in the core level scans. The creation of these components requires the selection of an appropriate line shape for the peaks. While most peaks exhibit a symmetrical Gaussian-Lorentzian shape, certain peaks like Fe 2p can present complex asymmetric profiles with extended tails at higher binding energies. The natural width of the peak typically adopts a Lorentzian line shape. However, instrumental effects, such as the spread of X-ray energy and the energy resolution of the analyser, further contribute to peak broadening, often following a Gaussian distribution. Consequently, the line shape of an XPS peak is commonly modelled by a combination of Lorentzian and Gaussian components, such as a mixed combination of 30% Lorentzian and 70% Gaussian [9].

Peak fitting generates an envelope that serves as a reliable indicator of the fitting quality. A well-fitting envelope aligns closely with the experimental data. To achieve a

meaningful fit, it's imperative that all components are attributed to a specific chemical species or environment within the sample. Usually, all the components within a peak are constrained to have a similar full width at half maximum (FWHM).

The width of a peak in an XPS spectrum, referred to as FWHM, is influenced by three primary factors: the specific core level being measured, the electron energy analyser, and the photon source [10]. Mathematically, the FWHM can be expressed as follows:

$$FWHM = \Delta E = \sqrt{\Delta E_n^2 + \Delta E_p^2 + \Delta E_a^2} \quad 2.2$$

Here, ΔE_n represents the natural width of the peak, reliant on the lifetime of the core hole generated during photoemission. ΔE_p corresponds to the width due to the photon source, while ΔE_a denotes the energy resolution of the analyser. The natural width attributed to the lifetime of the core level adheres to the Heisenberg uncertainty principle:

$$\Gamma = \frac{h}{\tau} \quad 2.3$$

In equation 2.3, h signifies the Planck constant in eV s, τ denotes the lifetime of the core hole in seconds, and Γ represents the width of the core level peak in eV. The lifetime of the core hole tends to be shorter for deeper core levels, owing to the ease with which outer shell electrons can transition downward to occupy the core hole. This phenomenon contributes to increased peak width. Additionally, elements with higher atomic numbers exhibit broader peak widths due to the heightened electron density, increasing the likelihood of core hole filling during the photoemission process.

Sample Charging and Charge Correction

In cases where the sample under XPS analysis demonstrates low electrical conductivity or lacks direct electrical contact with the spectrometer, the core holes formed by photoemitted electrons face a delay in recombination with the electrons. As a result, a positive charge accumulates on the sample surface, causing a shift in the photoemission peak toward higher binding energies. This shift occurs due to the altered energies of

emitted photoelectrons resulting from the accumulated positive charge, known as sample charging. Consequently, referencing binding energies becomes essential for an accurate examination of the sample's chemical environments.

To mitigate or eradicate the accumulated charge on the sample surface during measurement, a method involves exposing the sample to low-energy electrons (typically <20 eV) via an electron gun. This process aligns the vacuum level of the sample with the energy of the electrons, posing challenges for the absolute measurement of binding energies. In such scenarios, binding energies are often charge-corrected against the adventitious C 1s peak.

Shake up and Shake-off Satellite Peaks

In XPS spectra, apart from the core level peaks, additional features known as satellite peaks may occasionally arise due to atomic relaxation. When emitted photoelectrons undergo inelastic scattering, losing energy within their mean free path, these interactions can lead to the emergence of shake-up and shake-off satellite peaks positioned at higher binding energies.

Throughout the photoemission process, as the outgoing photoelectron interacts with the outermost electron (valence state) of the atom, there's a partial transfer of energy. This energy transfer can excite the valence electron to the continuum band, comprising unfilled energy states situated above the Fermi level. In metallic samples, a continuous range of energies is available, resulting in asymmetric peak broadening on the higher BE side of the core level features. These broadened peaks are termed 'shake-up' features.

Alternatively, if the outgoing photoelectron ionises a valence electron into a free continuum state, this contributes to the broadening of the core-level peaks or contributes to the background signal. These features are referred to as 'shake-off' features. The interplay of these interactions during the photoemission process contributes to the complexity and diverse features observed in XPS spectra.

Auger Emission

Following the photoemission process, when a photoelectron leaves an orbital, it creates a vacancy referred to as a core hole. Consequently, the remaining electrons within the atom rearrange themselves to occupy this vacancy. Figure 2.7 illustrates the Auger emission process, which primarily involves the transition of outer shell electrons to shield the core hole.

The excess energy released during this transition can be released in two ways: through the emission of photons, leading to X-ray fluorescence, or via Auger emission [11]. Auger emission occurs when an electron is excited from another core level, typically denoted by a notation such as KL_2L_3, indicating the participating electron shells in the Auger process. The energy linked to this specific transition can be calculated using the equation:

$$E_{Auger} = E_B - E_{L2} - E_{L3} \qquad 2.4$$

Here, E_B represents the BE of the K shell electron, while E_{L2} and E_{L3} correspond to the BEs of the 2p level (L_2 and L_3 shells). The kinetic energy of the emitted Auger electron relies on the energy difference between these levels within the sample, thus remaining independent of the incident X-ray energy source. This characteristic makes Auger emission a valuable tool for investigating electronic transitions within materials.

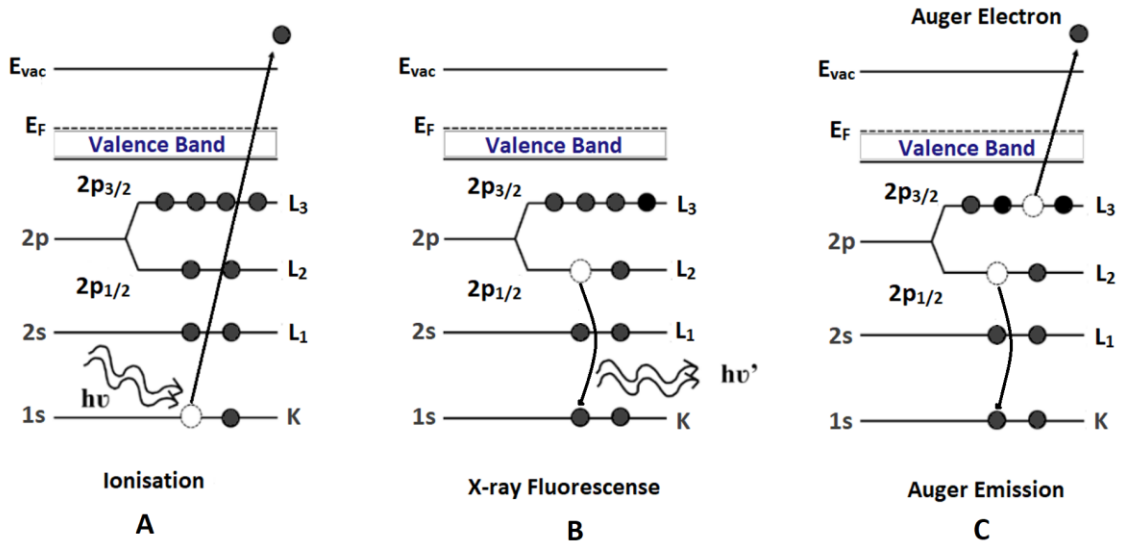

Figure 2.7 Schematic of KL_2L_3 Auger emission: A - An incoming X-ray photon ejects a K shell electron, creating a hole (ionisation). B - An electron from the L_2 level fills the hole, leading to either photon emission (X-ray fluorescence) or C - energy transfer to a third electron at the L_3 level (Auger emission). Transitions are labelled by energy levels: K denotes ionisation, L_2 indicates the origin of the second electron, and L_3 denotes the emitting level of the Auger electron. Adapted from [10].

2.1.3. XPS Instrumentation

Conventional XPS instruments are specifically engineered to function within ultra-high vacuum (UHV) conditions, typically exceeding 10^{-9} mbar. This stringent vacuum environment is crucial for accurate photoelectron measurement. The necessity for UHV in electron spectroscopy is primarily driven by several critical factors:

Preventing Scattering of Photoelectrons: UHV conditions prevent photoelectrons from scattering due to interactions with gas molecules before reaching the electron energy analyser.

Sustaining Instrument Components: Certain elements within the XPS setup, such as X-ray sources, require UHV conditions to sustain operational efficiency or extend their lifespan.

Mitigating Surface Contamination: Maintaining UHV helps prevent gas molecules from adsorbing onto the sample surface. Even a monolayer of contamination could significantly impact a surface science experiment.

Typically, XPS measurements occur within an analysis chamber, where a small load-lock chamber is horizontally linked to the analysis chamber, separated by valves. The purpose of this load-lock chamber is to facilitate sample changes without exposing the entire chamber to atmospheric conditions, thus, preserving the UHV environment.

The fundamental components essential for designing an XPS or ESCA (Electron Spectroscopy for Chemical Analysis) spectrometer comprise a vacuum system, an X-ray source, and an electron energy analyser coupled with a detector. Each of these elements plays a pivotal role in ensuring the precision and reliability of XPS measurements.

Vacuum System

Achieving UHV conditions in an XPS system involves employing various pumps designed to reduce the chamber pressure from atmospheric levels. The process begins rapidly but slows due to the desorption rate of gas molecules absorbed on the chamber walls, a phenomenon termed outgassing. This rate is temperature-dependent and cannot typically reach UHV levels at room temperature. The outgassing rate can be accelerated through a technique called 'baking out.' This involves heating the entire system to temperatures ranging from 100 °C to 200 °C for an extended period, causing the desorption of gas molecules from the chamber walls and filaments, ultimately achieving UHV conditions. However, materials used in the spectrometer need to withstand these temperatures, as certain materials like brass and elastomers might decompose and produce volatile substances in the UHV chamber. Copper O ring gaskets are commonly used as sealing material for knife-edge flange connections in UHV systems.

Various types of pumps are integrated into UHV instruments, each operating on distinct principles and handling specific pressure ranges:

Roughing Pump: In UHV setups, roughing pumps serve as "forepumps" for systems reliant on rough vacuum conditions. The prevalent types of roughing pumps include

rotary pumps and scroll pumps. Rotary pumps operate by extracting gas within a chamber using vanes attached to a rotor. These vanes oscillate, generating movement that collects and compresses gas within the pump's interior. Subsequently, the confined gas is discharged through an exhaust valve into the atmosphere.
In contrast, scroll pumps eliminate gas by employing two interlocking Archimedean screws. These screws are crafted by affixing spiral-shaped walls onto a circular base plate, forming individual scrolls. As these scrolls revolve, they trap gas between the spiral walls. The ongoing rotation propels the confined gas through the pump, directing it toward the outlet and eventually releasing it into the atmosphere.

Turbomolecular Pump (Turbo-pump): In the pressure range of 10^{-3} to 10^{-4} mbar within a chamber, a turbomolecular pump, often referred to simply as a turbo-pump (refer to Figure 2.8 for a schematic representation), is employed. This pump aims to decrease the pressure to approximately 10^{-6} mbar and lower by utilising rapidly spinning rotor blades, capable of achieving speeds up to 3×10^{4} revolutions per minute. Gas molecules remaining in the chamber travel downwards toward the pump's lower section. The blade configuration is designed to impart momentum to these molecules in a downward trajectory upon impact. Subsequently, the gas undergoes compression in the lower section before being expelled to an auxiliary pump. In numerous setups, the combination of turbomolecular pumps, supported by roughing pumps, effectively reduces the pressure to the range of 10^{-9} to 10^{-10} mbar. Nonetheless, to achieve even lower pressures within a chamber, entrapment pumps can be employed.

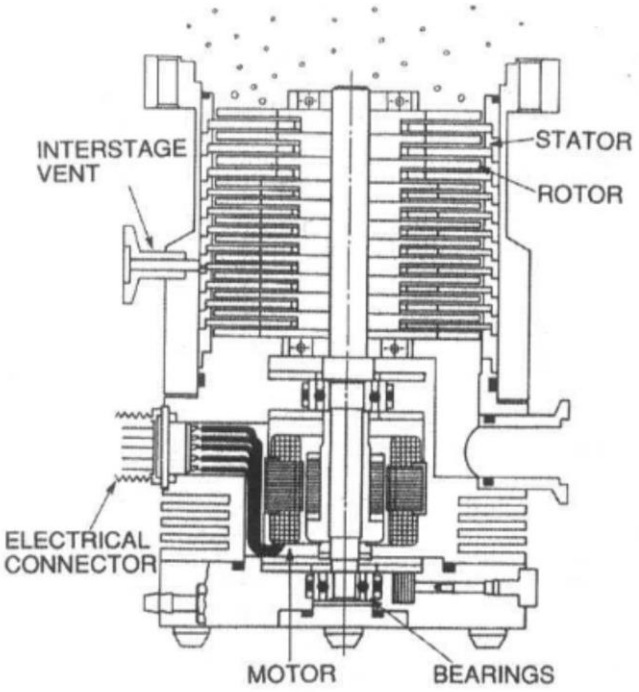

Figure 2.8 Schematic of a turbomolecular pump. Reprinted from [12]

Entrapment Pump: Lowering the pressure from below 10^{-10} mbar to approximately 10^{-12} mbar requires the use of an entrapment pump. These pumps function by effectively 'trapping' residual molecules through various mechanisms. Commonly employed entrapment pumps include cryopumps, sputter ion pumps, and titanium sublimation pumps. Cryopumps, capture molecules on surfaces chilled to temperatures below -150 °C, where gas molecules adhere via Van der Waals forces. In a sputter ion pump, gas undergoes ionisation between a Ti cathode and a stainless-steel anode, generating a robust electric field (typically several kilovolts) between them. The resulting gaseous ions are propelled toward the cathode by this intense electric field, causing sputtering of Ti atoms. This process forms a Ti film on the pump's inner walls (illustrated in Figure 2.9), reacting with residual chamber gases like oxygen, nitrogen, and hydrogen. The gases or compounds formed from these reactions are then confined beneath layers of additional sputtered Ti. A Ti sublimation pump combines cryopump and sputter ion pump technology, evaporating or sublimating Ti from a filament onto cooled surfaces, where gases condense due to the low temperatures. Subsequent reactions between the gases and Ti lead to irreversible entrapment of the gases. Entrapment pumps have the capability to reduce the pressure to as low as 10^{-11} mbar.

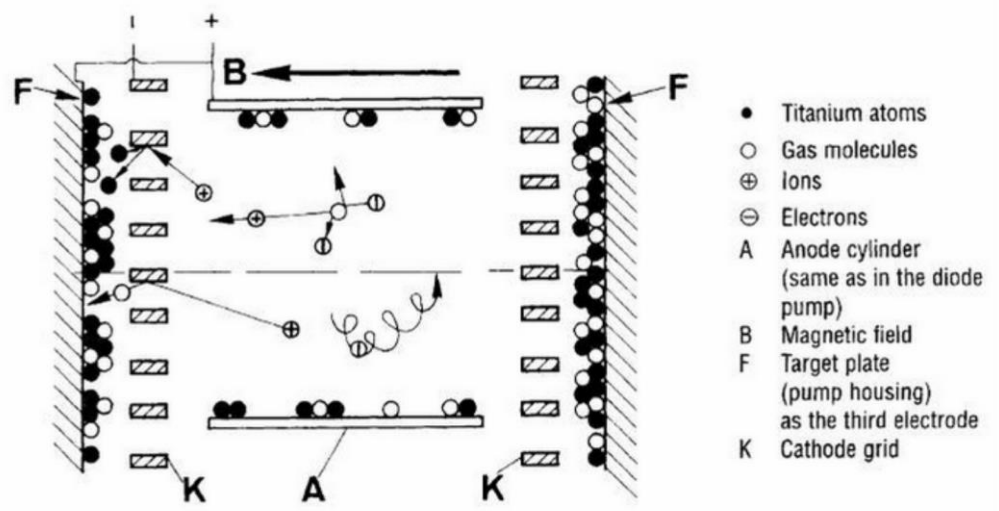

Figure 2.9 A schematic diagram demonstrating the internal elements of a sputter-ion pump and the method of ionising and capturing dispersed gas molecules to uphold UHV conditions. Reproduced from [13]

These pumps collectively contribute to establishing and maintaining the ultra-high vacuum conditions required for precise XPS analysis.

Lab X-ray Sources

Laboratory-based X-ray sources differ from synchrotron radiation sources in that they have fixed energy, dependent on the materials used as anodes. Most modern XPS instruments utilise 'dual anode' X-ray sources, commonly aluminium (Al) and magnesium (Mg), generating X-rays at energies of 1486.6 eV and 1253.6 eV, respectively. These X-rays are generated by directing high-energy electrons (around 10-12 keV) onto a metal target, causing the ejection of core-level electrons. Subsequently, the core holes formed in the photoemission process are filled by outer shell electrons, resulting in the emission of characteristic X-rays with specific energies.

The energies of Mg and Al sources, are quite similar, resulting in very few differences in the observed transitions between these two sources. However, few elements exhibit transitions that are exclusively observable with the higher energy Al source. For example, As 2p (1324 and 1359 eV) and Mg 1s (1303 eV) transitions fall within the range accessible only with the higher energy Al source.

When an overlap occurs between an Auger line and a photoelectron line using one source, employing a different X-ray source relocates the Auger peaks, effectively resolving the spectral overlap. For instance, Ga's Auger peak at 281 eV frequently coincides with the C 1s peak when a Mg source is utilised but employing an Al source shifts this Auger peak to 514 eV.

In cases where spectral resolution holds significance and a monochromatic Al source is available, it significantly improves spectral resolution, as depicted in Figure 2.10. On the other hand, if detecting the presence of a trace element takes precedence and spectral resolution is less critical, a nonmonochromatic Mg source can offer increased X-ray flux, thereby enhancing the overall photoemission intensity for trace element detection. Both Al and Mg sources offer a similar probing depth differing only by ~1 nm.

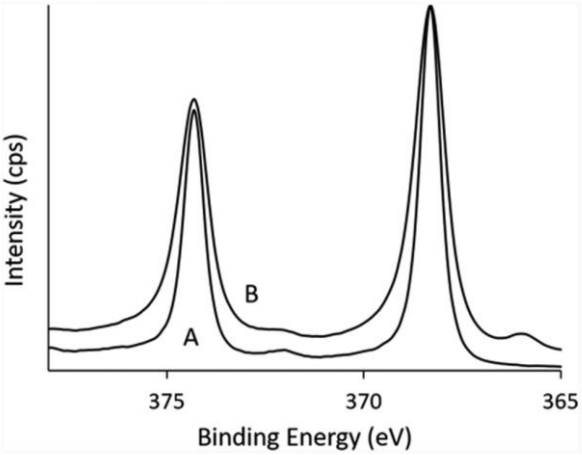

Figure 2.10 High-resolution XPS spectra from a silver sample showing the reduction in Ag 3d linewidth obtained from a monochromatic source (a) compared with a nonmonochromatic Mg source (b).

These characteristic X-ray lines are named based on the principal quantum number (n) of the core hole, denoted by a Greek letter representing the shell from which an electron refills the core hole. For instance, the Kα line emerges from an electron transition between 2p levels in the L shell and the 1s level in the K shell. The Kα line comprises two components, $K\alpha_1$ and $K\alpha_2$, distinguished by different binding energies due to spin-orbit splitting ($2p_{3/2}$ and $2p_{1/2}$).

The bombardment of high-energy electrons heats the target material, shortening its lifespan. To mitigate this, cooling mechanisms, such as circulating cold water around the target material during X-ray generation, are employed to manage heat generation. Additionally, besides the characteristic X-ray lines, high-energy broadband Bremsstrahlung radiation is produced due to electrons decelerating near the target nucleus (see Figure 2.11). To eliminate this radiation from reaching the sample and potentially causing degradation, a thin (~2 µm) transparent Al foil is often positioned between the X-ray source and the sample. This serves to minimise heat and shield the sample from high-energy electrons.

In contemporary XPS instruments, an X-ray monochromator is integrated to further narrow down the X-ray line width. This refinement enhances the signal-to-noise ratio and improves spatial and energy resolution. For Al/Mg Kα sources, this involves utilising backscattering from the (1010) plane of a quartz crystal within the monochromator.

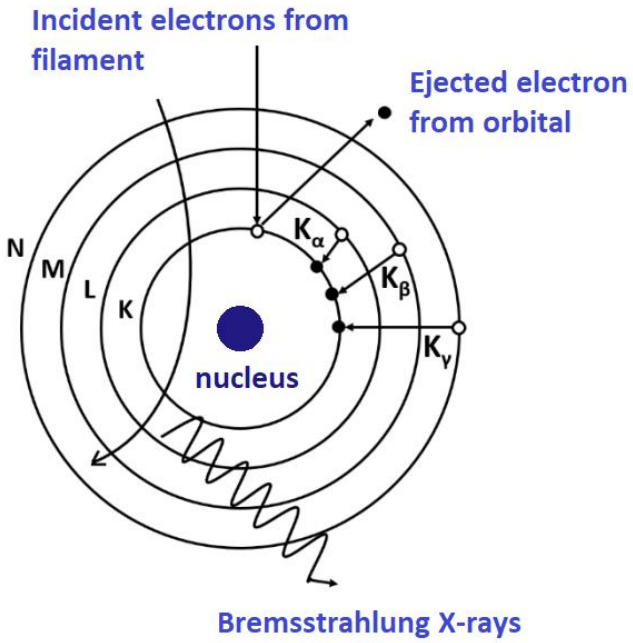

Figure 2.11 Schematic illustration depicting the ionisation and relaxation processes within an atom leading to the generation of Bremsstrahlung and characteristic X-rays.

Monochromator

When emitted from the source, it's crucial to isolate the Kα emission of X-rays from other radiation sources like Bremsstrahlung radiation (generated by electrons slowing down due to interaction with the nucleus) and weaker radiation stemming from different transitions, such as Kβ transitions. This filtering is called 'monochromatization' and the corresponding devices are called monochromators.

Generally, there are two classes of X-ray monochromators: those based on diffraction gratings and those based on crystals. Grating monochromators work well for long wavelength soft X-rays (λ = 6-12 Å) while crystal monochromators are mostly used for shorter wavelength.

A diffraction grating is a surface with a periodic array of geometric features called 'lines' of equal shape that reflect the incident X-rays. The working principle of a diffraction grating is illustrated in Figure 2.12. Two light beams reflected by equivalent points of two adjacent lines are 'in phase' if their overall path difference equals one wavelength or an integer number of wavelengths. However, if the beams experience a slight phase difference, the combined beam intensity diminishes. It reaches zero when they are entirely out of phase. [14].

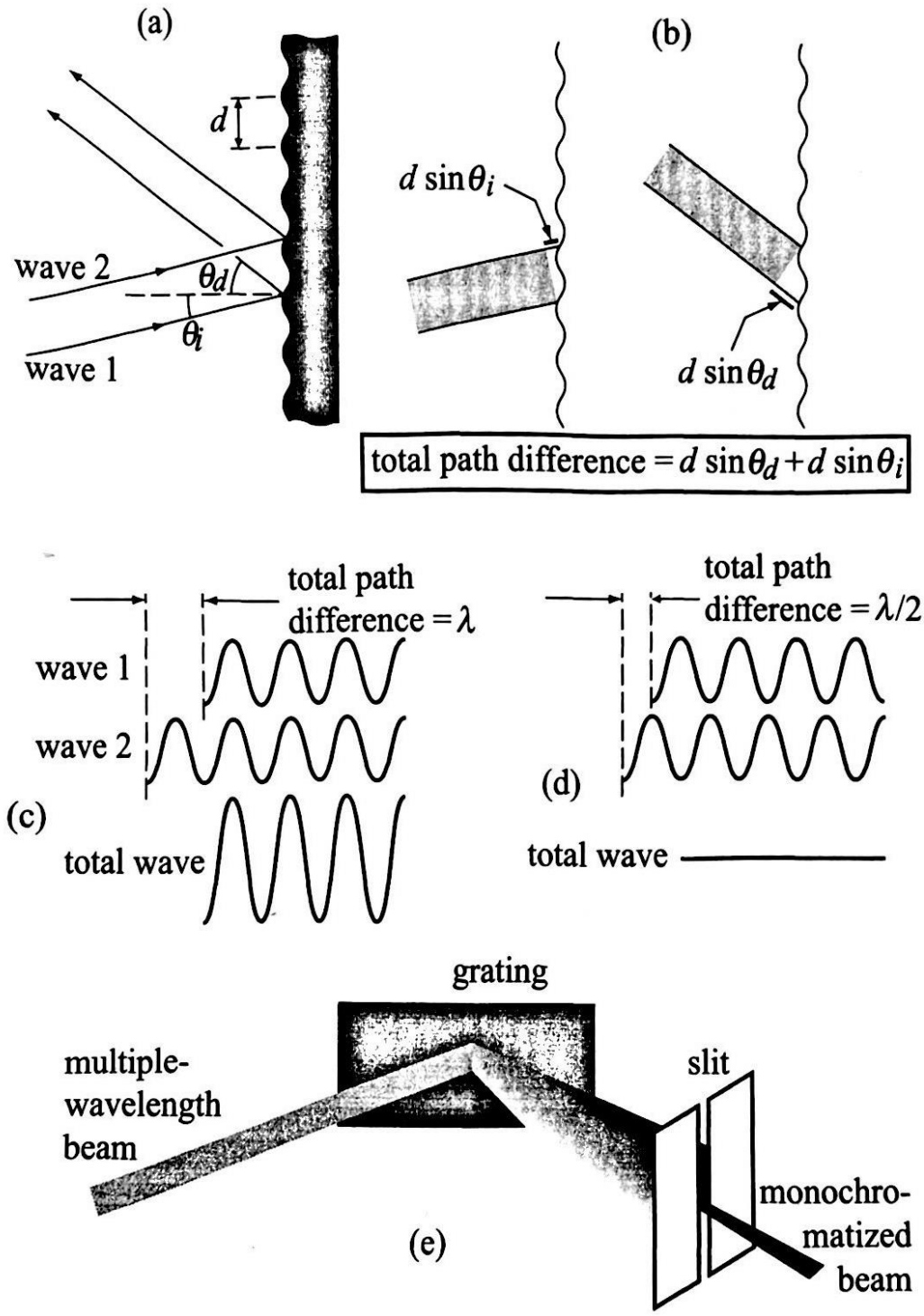

Figure 2.12 Schematic representation of the working of a diffraction grating. (a) Side view of a grating (b) Calculation of the total path difference. (c) If this path difference equals an integer number of λs, then the superposition of the two values produces maximum intensity. (d) If the path difference is an odd multiple of λ/2, then the total wave has zero intensity. (e) The grating, combined with a slit, produces monochromatization [14].

On the other hand, crystal-based monochromators work on the mechanism of crystal diffraction. The basic law for crystal diffraction is the Bragg law shown schematically in Figure 2.13. Consider a beam of X-rays of wavelength λ that reaches a crystal, and assume that the distance between two adjacent atomic planes is d. The two beams reflected by adjacent planes is 2dsinθ. If the difference equals one wavelength, then the superposition of the two waves produces maximum intensity.

$$n\lambda = 2dsin\theta \qquad 2.5$$

Positioning the sample strategically allows for the refocusing of diffracted X-rays—specifically those characteristic of the Al Kα or Mg Kα transition. This refocusing happens at a designated point on a Rowland circle, which is a circle whose diameter matches the radius of curvature of the grating (assuming the X-ray source is also situated on this Rowland circle). This arrangement ensures precise manipulation of the X-rays for optimal analysis [15].

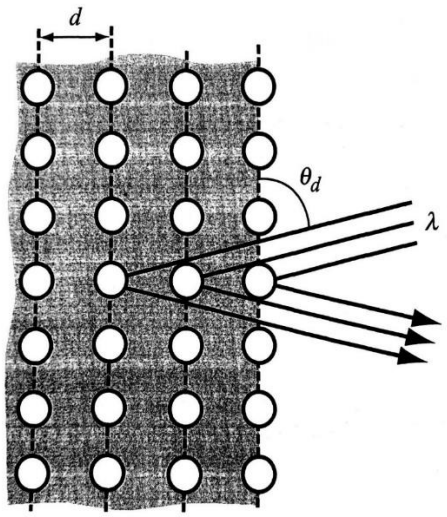

Figure 2.13 Schematic explanation of the Bragg law for crystal diffraction.

Hemispherical Analyser (HSA)

The journey of X-rays from the crystal monochromator to the sample surface involves the generation of photoelectrons with varying kinetic energies. Before reaching the hemispherical analyser, these electrons go through an electrostatic lens (as depicted in

Figure 2.14), strategically designed to reduce their energy to a specific level known as the pass energy. Simultaneously, the lens focuses the electrons, ensuring their dimensions align with the entrance slit of the analyser.

As the electrons pass through the slits, they encounter an electric field generated by the hemispheres (where the outer hemisphere holds a negative voltage while the inner one holds a positive voltage). This field's effect is crucial: electrons with energies higher than the pass energy experience minimal deflection and move towards the outer hemisphere, while those with energies lower than the pass energy encounter increased deflection towards the inner hemisphere. Consequently, only electrons possessing the necessary energy levels reach the exit slits and proceed into the detector, which commonly houses a channeltron or microchannel plate for precise measurement and analysis.

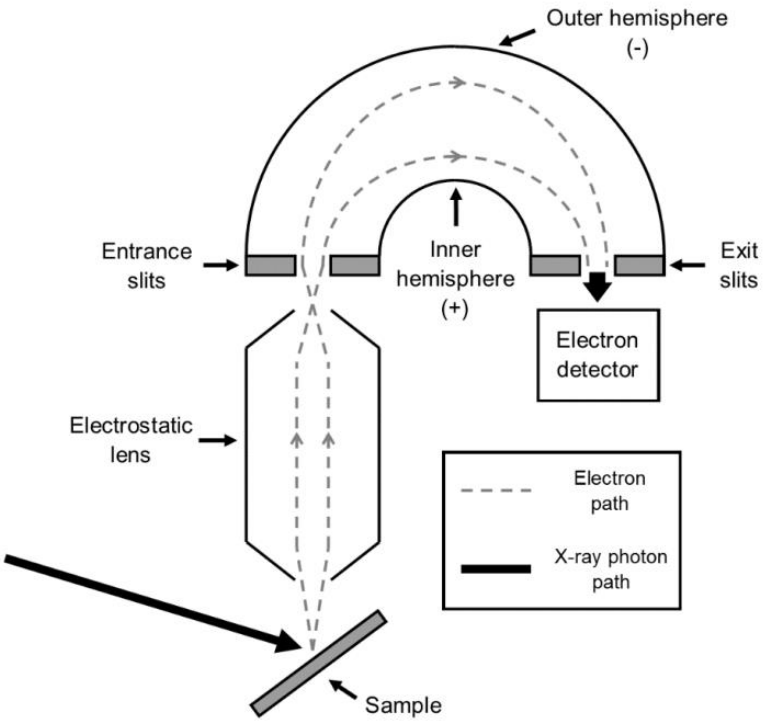

Figure 2.14 Diagram showing the cross-sectional view of a hemispherical electron energy analyser. The electrostatic lens focuses electrons obtained from the sample, while dashed lines indicate the path of electrons diverted by the potential variance between the two hemispherical electrodes prior to reaching the detector Reproduced from [15].

2.2. Hard X-ray Photoelectron Spectroscopy (HAXPES)

In the 1950s, the pioneering X-ray spectroscopic measurements conducted by Siegbahn and colleagues operated within the photon energy range of 5 to 8 keV. However, the pursuit of enhancing spectroscopic resolution and a growing scientific interest in material surface properties initiated a transition to lower energies, where surface sensitivity is most pronounced, typically around 1 to 2 nms. This surface region, exhibiting structural or electronic distinctions from the bulk material, can extend to several monolayers—equivalent to the photoelectron escape depth ranging approximately between 30 to 2000 eV. Consequently, deductions made regarding a sample's chemistry or electronic structure using photoelectron spectroscopy within this energy span might not truly reflect the bulk properties.

Experiments aimed at probing bulk properties or embedded regions beyond a few monolayers require employing photoelectrons with greater escape depths. This requirement suggests a shift to higher X-ray energies, a proposition initially proposed by Lindau et al. in 1974 [16]. However, this notion wasn't actively pursued for a considerable time due to concerns about potentially low photoelectron intensities. Additionally, the sensitivity of the electron-energy analyser diminishes as E^{-1}. Consequently, the photoemission signal intensity for experiments employing photons with energies significantly exceeding the BE of the target quantum state becomes exceedingly small [17].

X-ray photoelectron spectroscopy, employing X-ray energies surpassing 2 keV, falls under the classification of hard X-rays. This variant is capable of prompting electrons from deeper core levels, thereby extending the probing depth to approximately 10 nm and beyond. This technique not only facilitates the exploration of the fundamental electronic structure of solids but also allows for non-destructive depth profiling and examination of concealed layers and interfaces.

Most hard X-ray sources are presently situated within synchrotron radiation facilities due to the necessity for an intense source to counteract the significant reduction in

photoionisation cross-section as X-ray energy increases. Traditionally, hard X-ray energies were predominantly generated through the emission of Bremsstrahlung or characteristic line radiation resulting from decelerating keV electrons in a solid target anode or rotating anode materials. However, the conversion efficiency from electron beam energy to X-ray energy typically ranges below 1%, with approximately 99% of the kinetic energy of the electron beam transforming into heat. Consequently, this limitation constrains both the brightness and X-ray flux, leading to adversely affecting the image quality. The brightness of the produced X-rays is directly linked to the power density of the electron beam at the anode. However, in electron-impact sources, there are constraints imposed by their thermal characteristics, requiring limitations on the electron-beam power density at the anode to prevent damage or reduced lifespan. Hence, an anode configuration with high electron-beam capacity becomes essential to enhance X-ray brightness.

Recent advancements in the design of liquid-metal-jet anodes have led to a remarkable increase in brightness—approximately three orders of magnitude higher than current solid anode types—by operating at elevated electron-beam power densities. The distinctive thermal properties of these regenerative liquid-metal jet anodes allow for a considerably higher thermal load per unit area, making them less susceptible to damage compared to conventional solid anode sources [18].

2.3. Near-ambient Pressure X-ray Photoelectron Spectroscopy (NAP-XPS)

Fundamentally, near-ambient pressure XPS (NAP-XPS) and XPS conducted in UHV operate based on identical physical principles. Both methods involve X-rays interacting with a sample surface, leading to the emission of photoelectrons. However, in NAP-XPS, this process no longer requires vacuum conditions for measurement. Although the concept of NAP-XPS has existed for several decades, its practical implementation became feasible only due to the relatively recent advancement of transfer optics, enabling NAP-XPS hemispherical analysers to capture viable electron signals in non-vacuum environments.

The primary distinctions between XPS conducted in UHV and XPS under near-ambient pressure (NAP) conditions are rooted in the experimental setup. The critical components enabling NAP-XPS are the NAP cell and the transfer optics. These elements facilitate the execution of XPS measurements in environments that deviate from high-vacuum conditions.

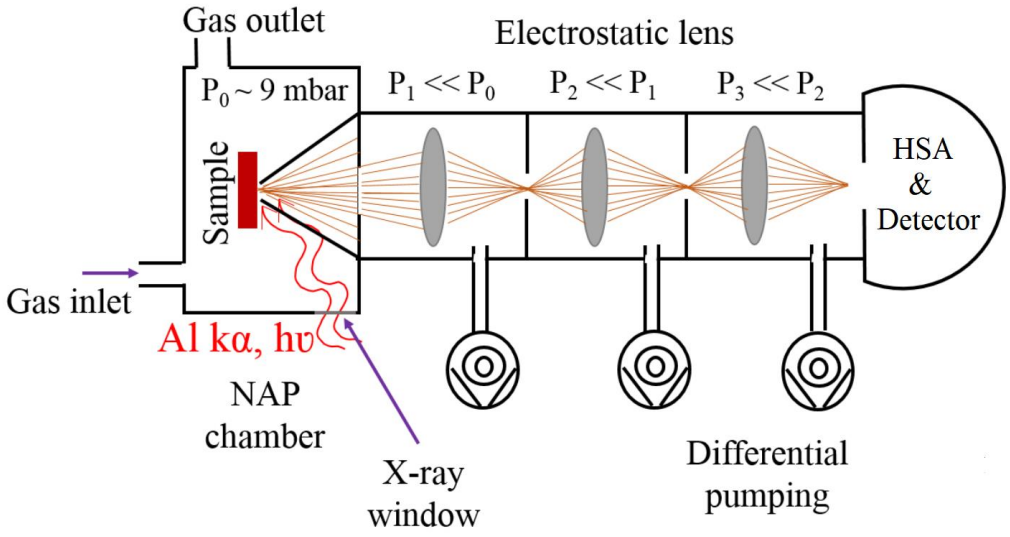

Figure 2.15 A schematic diagram of a NAP cell and differential pumping system combined with a series of electrostatic lens. Adapted from [10]

The NAP cell constitutes a crucial component for conducting NAPXPS measurements. Within this cell, the sample resides in an environment surrounded by near-ambient pressure gas, as depicted in Figure 2.15. Incident X-rays penetrate the NAP cell through an X-ray window typically coated with a Si_3N_4 membrane, either 50 µm or 100 µm thick. This membrane functions to prevent gas leakage from the NAP cell to the X-ray source, operating under UHV. The X-ray housing, positioned on bellows with the X-ray window situated at the end of the bellows, offers ease of alignment. Normally, the source is placed approximately 10 mm away from the sample.

As photoelectrons emitted from the sample travel through the gas, they encounter both elastic and inelastic collisions with gas molecules. The mean free path of these photoelectrons is directly proportional to their kinetic energy and inversely proportional to the gas pressure inside the NAP cell. Consequently, the first aperture must be

optimally positioned at a suitable distance from the sample to maximise the photoelectron yield, typically within the range of tens of μm. This first aperture, conically shaped and often available in various diameters (1 mm or less), facilitates the passage of photoelectrons that successfully exit the NAP cell.

Once the photoelectrons pass through the first aperture, they navigate through a sequence of differentially pumped chambers. The transfer optics play a pivotal role in the process. In the first two chambers subsequent to exiting the NAP cell, the photoelectrons are focussed by two sets of electrostatic lenses, directing them into the third chamber. Both the first and second chambers are rapidly depressurised by turbomolecular pumps to achieve lower pressures. The second chamber, as depicted in Figure 2.15, maintains a lower pressure compared to the first.

Within the third chamber, a quadrupole guides the photoelectrons toward the entrance of the hemispherical analyser. This third chamber is pumped by an ion pump, further reducing the pressure to the extremely low levels required by the analyser, operating under UHV conditions. This differential pumping mechanism allows the NAP cell to maintain relatively higher pressures while ensuring that the analyser operates within the stringent conditions of UHV.

In NAPXPS, the counts per second recorded are notably lower compared to ordinary XPS due to the short mean free path of electrons within high-pressure environments. This leads to a fraction of electrons being lost before they even enter the first aperture. However, the presence of electrostatic lenses between the apertures serves to concentrate and optimise the photoelectron yield. Despite this, the diminished number of electrons reaching the detector directly translates to lower counts in measurements, consequently yielding spectra with a reduced signal-to-noise ratio [15].

2.4. Near-edge X-ray Absorption Fine Structure (NEXAFS)

Near-edge X-ray absorption fine structure (NEXAFS), also known as X-ray absorption near-edge structure (XANES), serves as a complementary technique to XPS. While XPS

probes occupied core level states, NEXAFS provides insights into the electronic structure of unoccupied molecular orbitals. Additionally, NEXAFS proves useful in characterising bonding types and determining molecular orientations on surfaces.

X-ray Absorption

X-ray absorption spectroscopies (XAS) involve exciting core level electrons using X-rays. As X-rays pass through an absorber material, their intensity diminishes according to the Beer-Lambert law:

$$I = I_o e^{-\mu t} \qquad 2.6$$

Here, I_o represents the initial X-ray intensity, I is the intensity after travelling a material of thickness t, and μ stands for the absorption coefficient. In XAS, a significant increase in X-ray absorption occurs when the photon energy approximately matches the BE of the atom's inner shell (typically denoted using X-ray notation K, L, M, etc.). This substantial absorption edge appears at varying photon energies, dependent upon the element—for instance, 285 eV for the carbon K-edge.

NEXAFS primarily investigates the K-edge, signifying X-rays absorbed within the innermost K shell of the atom. This technique probes into the fine structure situated roughly 30 eV above the X-ray absorption edge. This region exhibits multiple sharp resonance peaks highly sensitive to bonding and electronic states. The higher energy region is termed the extended X-ray absorption fine structure (EXAFS). Figure 2.16(b) illustrates an XAS spectrum's absorption edge, emphasising the NEXAFS and EXAFS regions. Upon X-ray absorption, the excited electron can either transition into the continuum of free states above the vacuum level (EXAFS) or occupy an unoccupied molecular orbital (NEXAFS), as depicted in Figure 2.16(a).

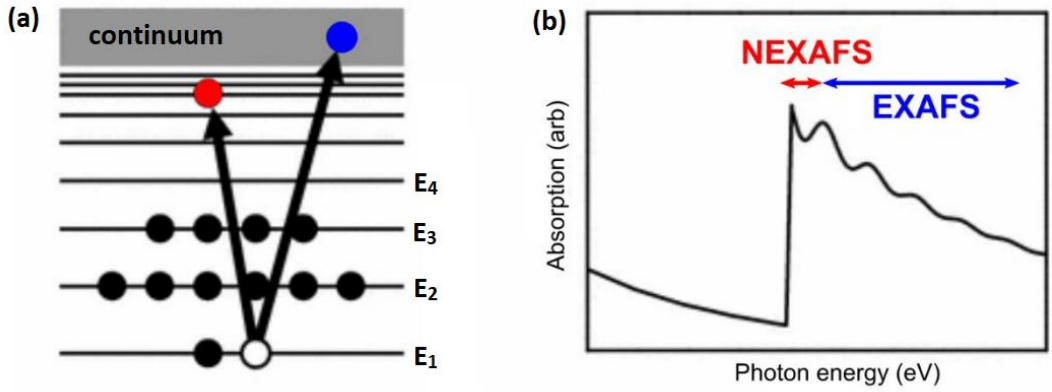

Figure 2.16 Diagram (a) illustrates an energy level diagram showcasing the excitation of a core level electron into either an unoccupied molecular orbital (NEXAFS) or the continuum of free states (EXAFS). The regions adjacent to the absorption edge for NEXAFS and EXAFS are highlighted in diagram (b). Adapted from [19].

Molecular orbitals

In diatomic molecules, molecular orbitals (MOs) can be explained as the result of interactions among atomic orbitals. When adjacent atomic orbitals interact with in-phase orbital amplitudes, they form bonding molecular orbitals, while those with out-of-phase orbital amplitudes create antibonding molecular orbitals (denoted by an asterisk). Bonding orbitals possess lower energy compared to the constituent atomic orbitals, whereas antibonding orbitals exhibit higher energy levels. For instance, π orbitals (or π bonding) arise from interactions between p_x-p_x or p_y-p_y atomic orbitals, while σ orbitals involve interactions like s-s or p_z-p_z atomic orbitals (where subscripts indicate the axis of symmetry). Figure 2.17 depicts an instance illustrating the development of π and σ bonding as well as antibonding molecular orbitals from the interaction of 2p atomic orbitals.

In NEXAFS, the permissible transitions of K shell electrons to unoccupied MOs adhere to the dipole selection rules. To qualify as allowed, a transition must satisfy the condition given by $\Delta l = \pm 1$ where l denotes the orbital angular momentum [20]. This criterion dictates that an electron originating from the 1s initial state with $l = 0$ can exclusively transition into a final state featuring an atomic p orbital component. Given that all

bonding orbitals are already occupied, electrons from the 1s level undergo excitation into antibonding π* and σ* MOs in the context of NEXAFS.

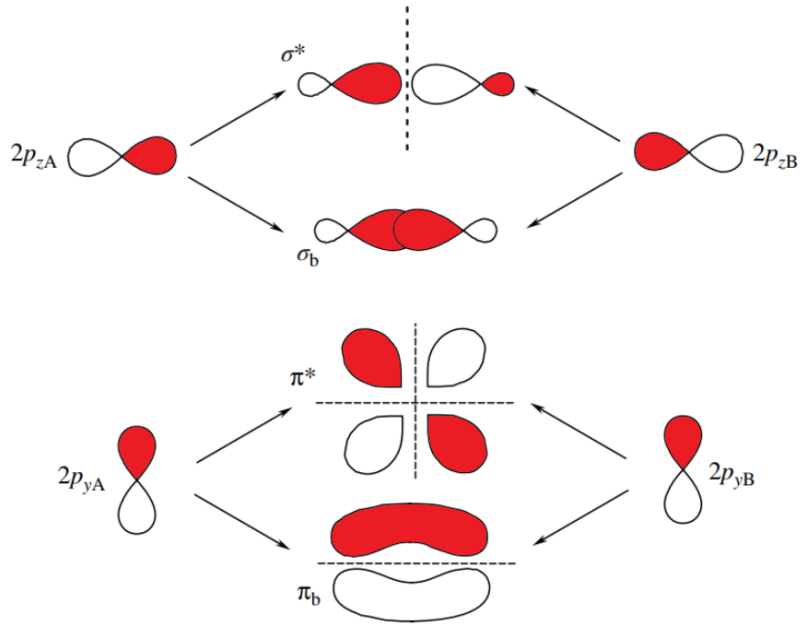

Figure 2.17 Molecular orbitals depicting σ and π bonding and their respective antibonding (*) counterparts formed through the interaction of 2p atomic orbitals within a diatomic molecule.

The π* antibonding MO represents the lowest unoccupied molecular orbital (LUMO), while σ* MOs appear at higher energies. Despite NEXAFS primarily exploring unoccupied states, these transitions still offer valuable insights into a molecule's electronic structure. Transitions from 1s to π* states are only exhibited by materials with π-bonding. Consequently, π* resonances serve as indicators signifying the existence of double/triple bonds or aromatic structures within the molecule [21].

The NEXAFS signal of a core-level electron exhibits sharp bound features, corresponding to unoccupied bound states just below the ionisation threshold and broad features up to 30 or 40 eV above the IP as shown in Figure 2.18. The sharp resonance peak arises from 1s → π* transitions. Following this sharp peak, a step-like structure is located roughly 2 eV below the vacuum level, signifying the ionisation potential of the material.

The IP signifies the energy necessary to excite a core level electron into the continuum of free states, positioned above the vacuum level. Beyond the IP, a broad high-energy peak emerges, attributed to σ* transitions.

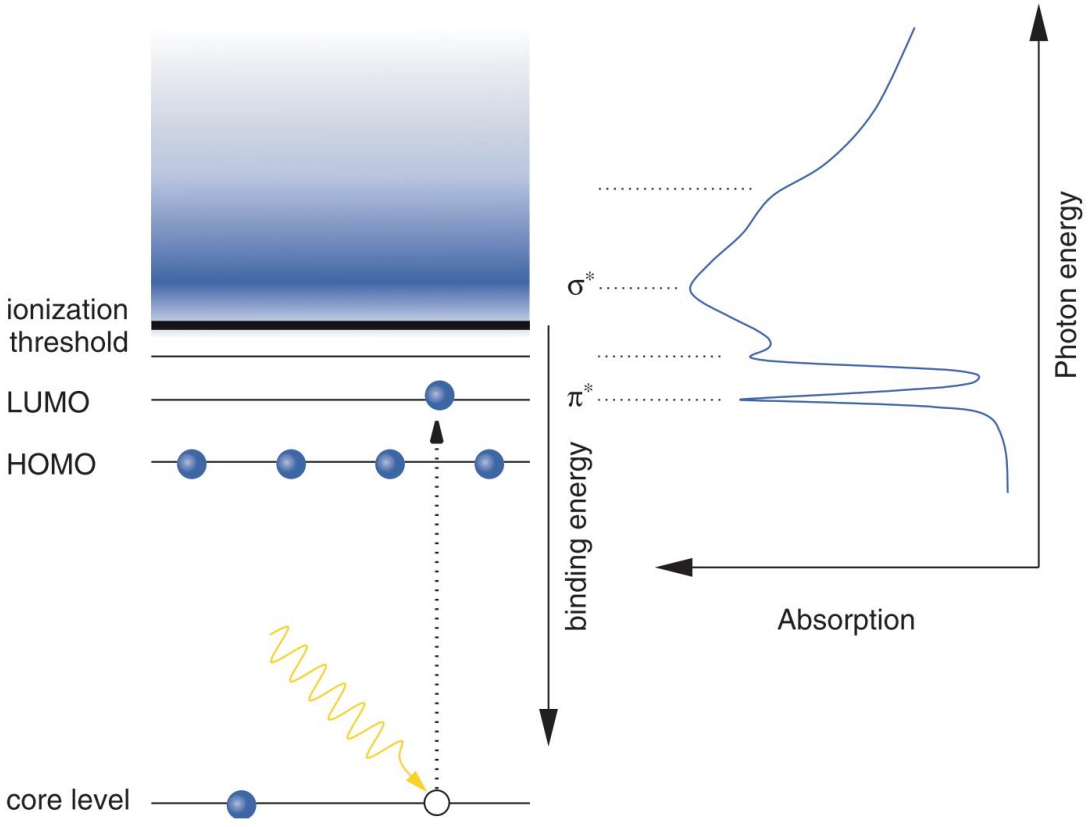

Figure 2.18 Schematic illustration of the energy band diagram of a core electron ejection process along with the corresponding NEXAFS profile it generates.

The width of NEXAFS resonances is dictated by the duration of the excited state's existence. In the case of 1s → π* transitions, the core hole lingers for a prolonged period before decaying through the de-excitation of the excited electron. This leads to the emergence of sharp and narrow π* resonances. However, as an electron travels through the continuum of free states, its probability of decay rises, resulting in the broadening of σ* peaks as their energy increases.

Given that σ* bonds align along the internuclear axis between two atoms, the positions of σ* peaks demonstrate high sensitivity to the internuclear distance. Consequently,

vibrational motion of the molecule further broadens σ* peaks. Generally, the energy width of a NEXAFS peak enlarges with higher photon energy.

Prior to photoexcitation, both the π* and σ* MOs reside above the vacuum level. However, the formation of a core hole escalates the Coulomb potential between the nucleus and remaining electrons. This amplifies the binding energy of the outermost levels, effectively shifting the 1s → π* transition energy below the vacuum level.

The background against which these resonances sit may stem from various sources, including signals originating from the substrate, experimental losses, interferences, and impurities on the sample surface. Addressing these involves background corrections, typically executed by normalising the experimental spectrum using a clean substrate signal or the X-ray photon flux derived from a reference grid covering the same area.

Electron yield in NEXAFS can be measured in three primary methods: Auger electron yield (AEY), partial electron yield (PEY), and total electron yield (TEY). AEY is focused on a narrow detector window around the energy of the Auger peak of interest. In PEY, a minimum pass energy, Ep, is introduced to prevent electrons with low kinetic energy to reach the detector. Adjusting Ep can eliminate substrate photoemission peaks from the spectrum, although the higher count rate in PEY comes at the expense of reduced signal-to-noise ratio.

TEY, on the other hand, captures all electrons via drain current measurements with an ammeter. This method results in a dominant inelastic 'tail,' a convolution of signals from low-energy electrons (< 20 eV kinetic energy), which significantly influences the obtained spectrum. Despite the high-count rates in TEY spectra, their signal-to-background ratios are typically minimal. Compared to AEY and PEY, TEY is less surface-sensitive due to its broad range of electron energies, making it less selective in probing surface-specific information.

2.5. Synchrotron Radiation

Synchrotron radiation (SR) is electromagnetic radiation produced by accelerating high energy charged particles close to the speed of light around curved paths. Third-generation synchrotrons are characterised by their ability to produce highly parallel and narrow beams of x-rays with high intensity. (4). These properties can be expressed in a single parameter called 'brilliance'. Brilliance describes the photon density which is equal to the number of photons (ph) per second (s) per unit solid angle ($mrad^2$) per unit source size (mm^2) per 0.1 % bandwidth of X-ray energy (0.1 % BW). The energy of the electrons which generate the X-rays within the storage ring of the synchrotrons determines the range of photon energies a particular facility can produce. The most important parameters of a selection of third-generation facilities are listed in Table 2.2.

Facility, Country	Storage-ring energy (GeV)	Current (mA)	Circumference (m)	Brilliance (ph/s/$mrad^2$/mm^2 /0.1% BW)
BESSY II, Germany	1.7	100	240	5×10^{18}
ALS, US	1.9	400	198	3×10^{18}
Elettra, Italy	2-2.4	320	260	1×10^{19}
SLS, Switzerland	2.4	400	288	4×10^{19}
Anka, Germany	2.5	200	110	1×10^{18}
Soleil, France	2.75	500	354	1×10^{20}
Diamond, England	3.0	300	562	3×10^{20}
ESRF, France	6.0	300	846	8×10^{20}
APS, US	7.0	100	1104	8×10^{19}
Spring8, Japan	8.0	100	1436	2×10^{21}
Petra-III, Germany	6.0	100	2304	2×10^{21}
MAX-IV, Sweden	3.0	500	528	2.2×10^{21}
NSLS-II, US	3.0	500	792	3×10^{21}
Astrid-2, Denmark	0.58	200	45.7	1×10^{17}

Table 2.2 Important properties of selected third-generation synchrotron facilities [22, 23].

Figure 2.19 depicts the most important elements of a contemporary synchrotron source. Initially, electrons originate from a source, such as a heated filament within an electron gun. These electrons undergo acceleration within a linear accelerator (linac) and progress into an evacuated booster ring, where further acceleration occurs. Subsequently, they are introduced into the storage ring, where their trajectory is maintained along a closed path using bending magnets at arc sections. Downstream, aligned with the emission axis, beamlines utilise the emitted radiation from insertion devices (wigglers or undulators) and bending magnets. Synchrotron light radiation from electrons is compensated for by a radio frequency (RF) supply, replenishing the energy lost during emission.

A synchrotron has five main components as depicted in Figure 2.19 [22]:

1. **An electron source**: Usually made by heating a filament to emit electrons in an electron gun. These electrons get accelerated to about 100 MeV using a linear accelerator (linac). To keep the machine running, a steady supply of electrons is needed because they are lost when they hit gas particles in the storage ring.
2. **A booster ring**: The electrons from the linac are fed into a booster ring where they are further accelerated. They can either reach the same energy level as the storage ring electrons or sometimes a bit lower. These electrons are regularly added to the storage ring to maintain the desired current. This addition happens when the current in the storage ring drops to about 70%.
3. **The storage ring**: This holds and guides electrons using an arrangement of magnets known as the 'magnet lattice.' There are three main types of magnets: Bending magnets, Quadrupole magnets and Sextupole magnets. Bending magnets alter the electron path, ensuring they follow a closed loop. Quadrupole magnets focus the electron beam and counteract the repulsion between electrons. Sextupole magnets correct any chromatic aberrations caused by the focusing of the quadrupoles.

The electrons in the ring have very high kinetic energies measured in GeV, and they move at velocities extremely close to the speed of light, making them highly relativistic. The ring structure comprises curved sections with bending magnets and straight sections housing insertion devices (IDs) that produce intense synchrotron radiation. While bending magnets guide electrons around curved sections, they also generate some radiation, though not as brilliant as that from IDs. Even when the bending-magnet radiation is made monochromatic, it is still significantly more intense than what standard laboratory-based sources can produce.

4. **A radio frequency (RF) supply**: Electrons lose energy by emitting synchrotron radiation. To prevent them from spiralling into the inner walls and being lost, this lost energy needs to be replaced. A radio frequency (RF) supply fulfils this by providing the electrons with precisely the right amount of extra energy each time they pass through it.
5. **Beamline:** Beamline can be divided into three main parts-

   The front end: It separates the beamline vacuum from the storage ring's vacuum, tracks the photon beam's position, determines the synchrotron radiation's angular acceptance, and shields against harmful radiation.

   The optics hutch: The beam typically undergoes focusing and/or monochromation in the optics hutch before reaching the experimental hutch.

   The experimental hutch: For high-energy X-ray-generating beamlines, the hutches are shielded with lead-lined concrete walls to safeguard users from X-rays, gamma rays, and high-energy neutrons produced in the storage ring collisions. Such radiation, reaching energies of a few GeV, requires thick lead blocks for effective shielding, allowing remote operation of experiments outside the radiation zone.

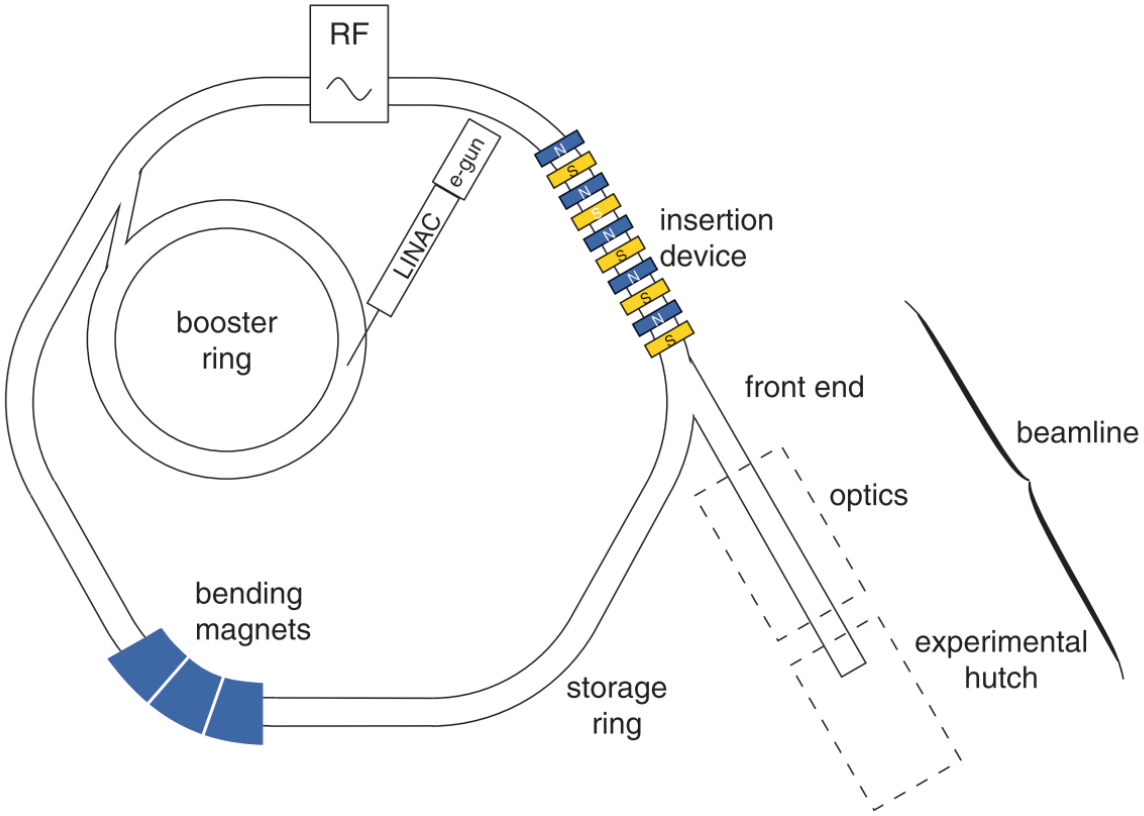

Figure 2.19 Components of a modern synchrotron source. Adapted from [22].

An accelerated charged particle moving with a small fraction of the speed of light generates an isotropic electromagnetic radiation. However, when a charged particle is accelerated to a velocity comparable with the speed of light it starts emitting a sharp needle like electromagnetic radiation in the direction of its motion. This characteristics of this sharp radiation is dependent on two factors: the number of radians turned by the electrons per second i.e., its angular frequency (ω_0) and the energy of the electrons in the storage ring given by the Lorentz factor:

$$\gamma = \frac{E}{mc^2} \qquad 2.7$$

where mc^2 is the rest mass energy of the electron, equal to 511 keV. This can be simplified in terms of the storage ring energy in GeV as:

$$\gamma = 1957\ \mathrm{E(GeV)} \qquad 2.8$$

Bending Magnets

Bending magnets steer electron beams in the storage ring along a closed path, generating radiation in a wide cone due to the electron path change. These magnets, with typical strengths around a Tesla, can accommodate multiple 'bending-magnet beamlines' using various apertures. The critical energy and emitted power depend on the storage-ring energy and magnetic field strength, limiting the X-ray spectrum in some facilities.

Insertion Devices

Insertion devices are periodic arrays of magnets placed in the straight sections of the storage ring. They're designed to oscillate the electron trajectories, typically causing radial movements due to magnets positioned perpendicular to the ring's plane. Two main types exist: undulators and wigglers (see Figure 2.20) which only differ from each other in the degree to which they force the deviation in the straight path of the moving electrons.

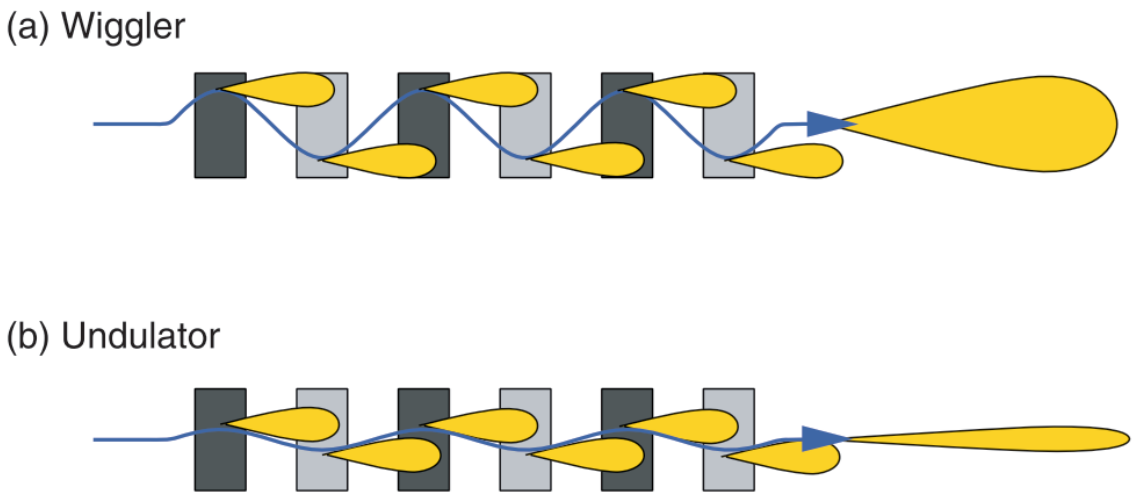

Figure 2.20 The angular excursions forced on the straight path of the moving electrons by the insertion devices.

This subtle difference between the deviation in the path of the electrons can have a profound impact on the nature of the radiation produced by them. Wigglers produce larger excursions such that the radiation cones from each wiggle do not overlap and the

intensities are added up. Undulators on the other hand cause a much gentler excursion (of the order of γ^{-1}) leading to the overlapping of the radiation cones. This results in a much higher intensity at those wavelengths where the interference is constructive.

Monochromators

Synchrotron radiation possesses a continuous range of energies, requiring the use of a monochromator to select a specific photon energy. This device comprises a curved quartz crystal diffracting incident X-rays based on Bragg's Law. Adjusting the crystal's rotation and θ angle results in transmitted light within a narrow wavelength range of around λ. Both the entry and exit slits of the equipment align on a Rowland circle (illustrated in Figure 2.21) matching the quartz crystal's curvature radius. This arrangement ensures that the diffracted beam is refocused before reaching the sample.

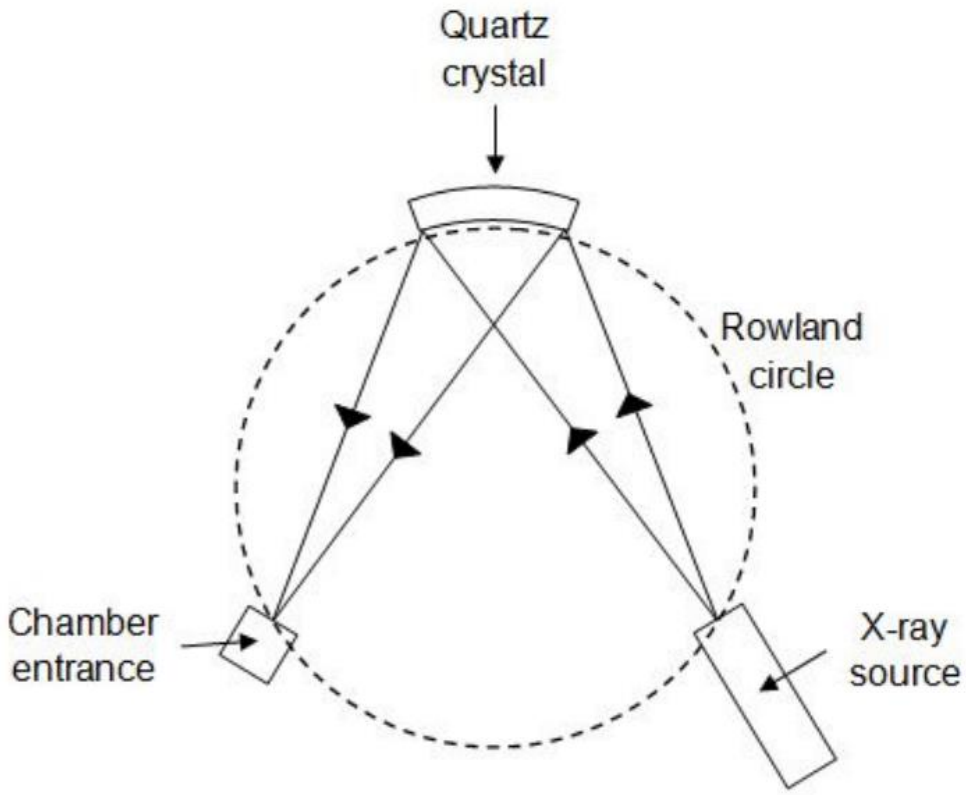

Figure 2.21 Schematic Diagram demonstrating the configuration for generating monochromatic X-rays, with the X-ray source, concave quartz crystal, and entrance to the target chamber aligned along a Rowland circle. Adapted from [15]

2.6. Beamline D1011 at MAX-lab

The experimental data for $MAPbI_3$ and $MAPbBr_3$ as presented in the third chapter of this thesis were acquired at Beamline D1011 situated in MAX-lab (the data was recorded in 2015, before MAX-lab was closed to make way for MAX IV). The 3rd generation synchrotron MAX-II at Lund University, Sweden. The MAX-II storage ring spanned a circumference of 90 m, operating with an electron energy of 1.5 GeV and a current of 200 mA.

Beamline D1011, a bending magnet beamline, covered an energy spectrum ranging from 30 to 1500 eV. It incorporated a modified SX-700 monochromator equipped with 360 lines/mm and 1220 lines/mm gratings, along with a plane-elliptical focusing mirror. This beamline delivered an energy resolution between $1.5x10^3$ and $1.3x10^4$ and a photon flux ranging from 10^{10} to 10^{11} photons per second.

The beamline consisted of two end stations as shown in Figure 2.22 the front station positioned directly after the monochromator and the back station farther along the beamline after two refocusing mirrors. The front station catered to XPS and XAFS techniques, aligning with the focus of the work in this thesis. In the front chamber, the sample's spot size was approximately 1 mm vertically by 3 mm horizontally.

Within the front chamber, analyser and preparation chambers are depicted in Figure 2.23. The preparation chamber, located above the analysis chamber and separated by a valve, allowed independent baking. A sample transfer system was attached to the preparation chamber. The station featured a 600 mm-travel Omniax™ manipulator with motorized z motion, facilitating movement between the preparation and analysis chambers.

The analyser chamber was outfitted with a SCIENTA SES200 200 mm mean radius hemispherical electron energy analyser and a microchannel plate detector tailored for electron yield measurements, specifically the partial electron yield technique. The preparation chamber housed an argon ion sputtering gun, a gas-inlet system, and LEED.

The manipulator was equipped with electron beam sample heating, incorporating a thermocouple in contact with the sample for temperature monitoring. Additionally, the manipulator allowed for sample plate cooling via liquid nitrogen [24].

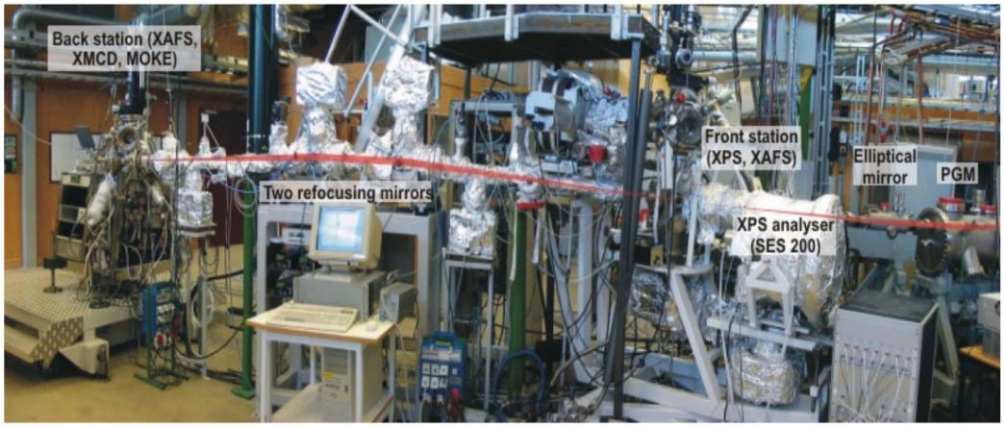

Figure 2.22 Photograph of beamline D1011 showing front and end stations. Reprinted from [24]

Figure 2.23 Photograph showing the positions of the preparation chamber, analysis chamber and manipulator at beamline D1011. Reprinted from [24]

2.7. Astrid-2, Aarhus

The AU-MATline (Aarhus University Material Science Beamline) operates within the 3rd generation synchrotron ASTRID2, part of ISA, situated in Denmark. The main parameters of the Astrid-2 synchrotron facility are listed in Table 2.3 and a schematic layout of the storage ring is shown in Figure 2.24. As a wiggler beamline, AU-MATline offers a photon energy span ranging from 20 eV to 700 eV, yielding a standard photon flux of 1×10^{11} per second. The end station (depicted in Figure 2.25) is equipped with a SX-700 monochromator and a Scienta hemispherical analyser. This setup facilitates various techniques such as XPS, low-energy electron diffraction (LEED), UPS, NEXAFS, and photoelectron diffraction.

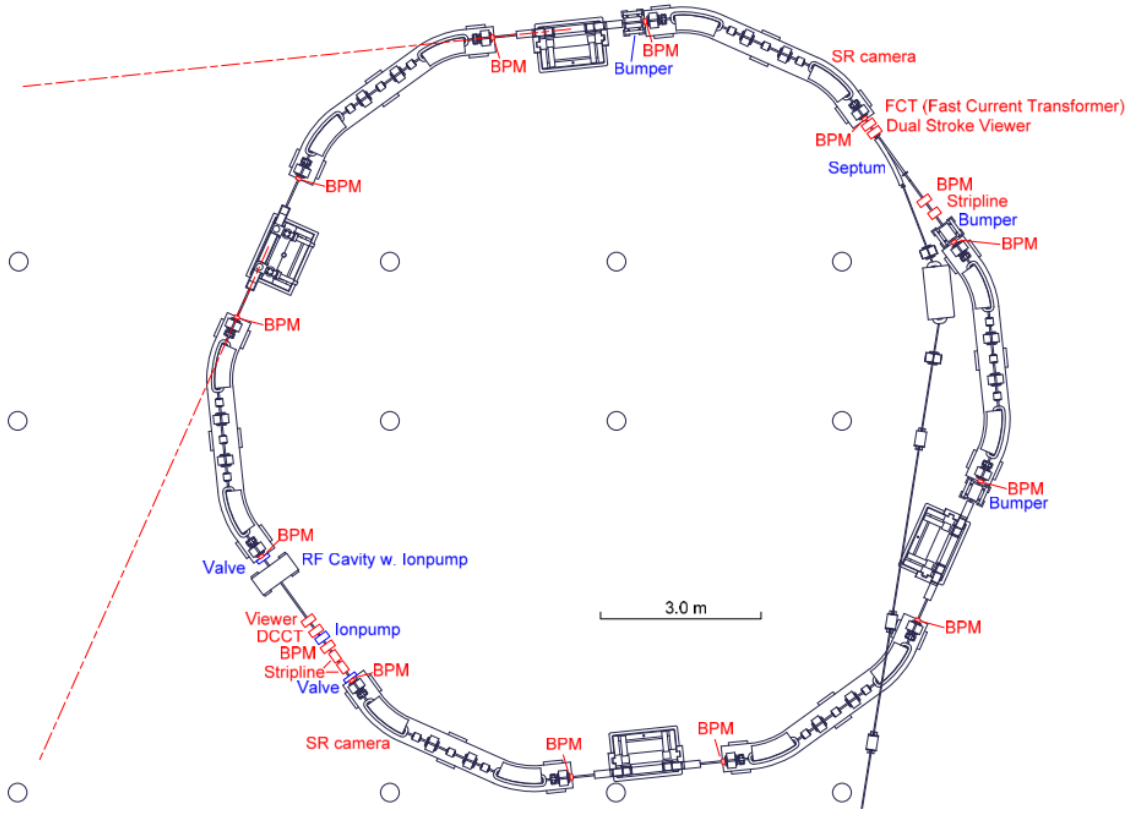

Figure 2.24 An overview of the ASTRID2 storage ring showing the locations of diagnostic elements. The small circles are pillars in the building. Adapted from [25].

Energy (MeV)	580
Circumference (m)	45.704
Current (mA)	200
Revolution time (ns)	152.45
Length of straight sections (m)	2.7
Number of straight sections	4
Horizontal tune	5.23
Vertical tune	2.23
Natural emittance (nm)	13

Table 2.3 Main parameters of the ASTRID2 storage ring facility.

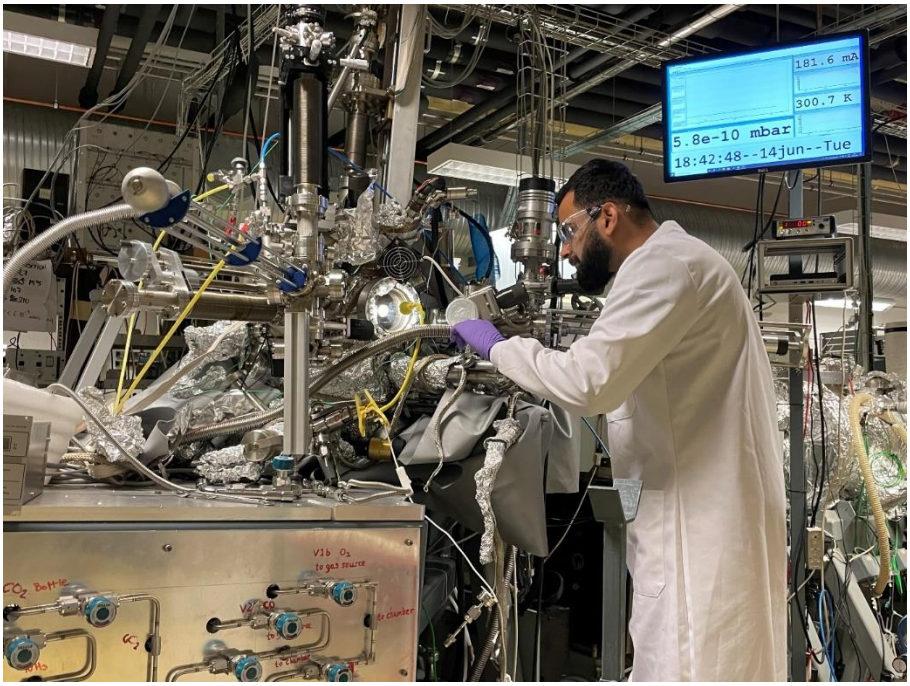

Figure 2.25 ASTRID-2 beamline end station.

2.8. HAXPES, University Manchester

The first commercially available high-throughput hard X-ray photoelectron spectrometer, situated at the Photon Science Institute of The University of Manchester, utilises an X-ray source fabricated by Excillum (MetalJet D2 + 70 kV). This source employs a gallium liquid metal jet anode, depicted schematically in Figure 2.26. The process

involves containing liquid gallium within a stainless-steel pressure tank, subjected to an IR-radiation heater to elevate the temperature to around ~50 °C (the melting point of gallium is approximately ~29.8 °C). The entire assembly is housed within a vacuum chamber, typically evacuated to 10^{-4} mbar.

The molten gallium is expelled as a liquid jet into the vacuum chamber via a tapered glass capillary, utilising a 200 mbar nitrogen backing pressure connected to the pressure tank. An electron beam, featuring an 80 × 20 µm² spot size and an intensity of 250 W, is generated by an acceleration voltage of 70 kV in the electron-beam system. This beam is directed towards the gallium jet to generate an X-ray spot, as illustrated in Figure 2.26.

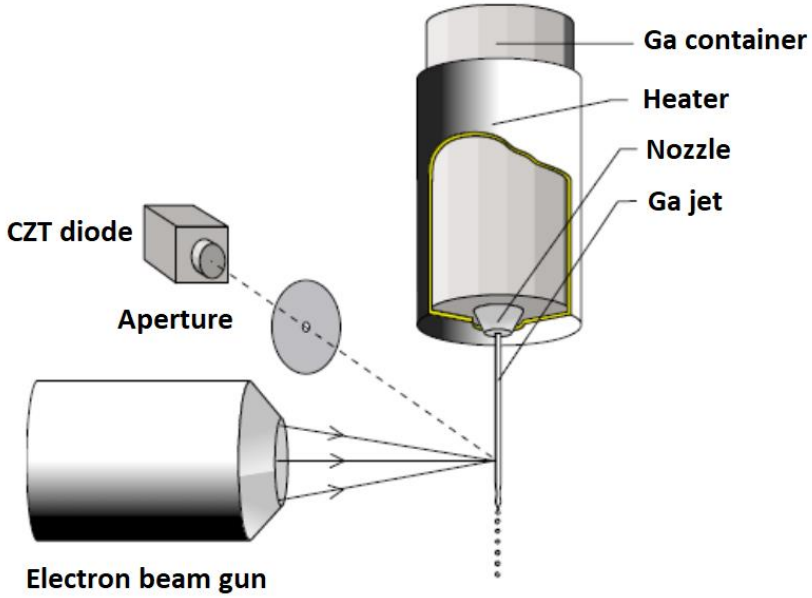

Figure 2.26 The experimental set up of liquid-gallium metal jet anode source. Adapted from [18]

The produced X-rays undergo monochromation and focusing by a bent Si crystal, utilising a 550 mm Rowland circle, resulting in a flux of approximately 6.8×10^8 photons per second. To ensure long-term stability and optimal performance, which includes high spectral resolution and intensity, the Si crystal is maintained at a constant elevated temperature. An X-ray detector, employing a diode setup and positioned perpendicular to both the electron beam and the metal jet, serves for the quantitative spectral characterisation of the X-ray source.

In the HAXPES setup, a Scienta Omicron EW4000 electron energy analyser is employed, featuring a wide acceptance angle of 60° and capable of measuring a maximum kinetic energy of 12 keV. The 2D detector setup comprises a microchannel plate (MCP), a phosphor screen, and a CCD camera, allowing for angle-resolved XPS and ensuring a high signal-to-noise ratio in the measurements.

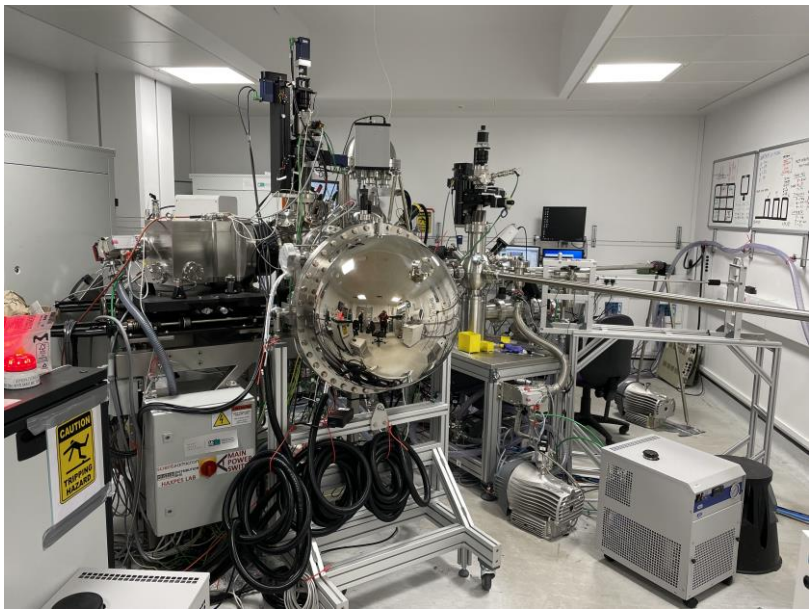

Figure 2.27 Photograph of the HAXPES kit at the Henry Royce Facility, UK.

THE HAXPES lab also has a standard Kratos system with Al Kα source where the XPS experiments were performed. The Al kα X-ray source emits photons at an energy level of 1486.6 eV, alongside a hemispherical analyser.

2.9. NAP-XPS, University of Manchester

The near-ambient pressure X-ray photoelectron spectroscope is located at the Henry Royce Institute at the University of Manchester (see Figure 2.28). It is a custom-built SPECS system and comprises of a monochromated Al Kα X-ray source (of photon energy 1486.6 eV) and PHOIBOS 150 NAP hemispherical analyser. The system is equipped with a load lock chamber, preparation chamber, analysis chamber, and NAP cell. The load lock chamber is equipped with a transfer arm for sample transfers from the load lock chamber to the preparation chamber.

Inside the preparation chamber is a sample manipulator to transfer samples between the preparation chamber and the analysis chamber. The sample manipulator is equipped with a k-type thermocouple attached to the sample holder, and spans a sample temperature range of -150 °C to 800 °C. The analysis chamber is equipped to perform a variety of measurements on a sample including regular (UHV) XPS, UPS, mass spectrometry and Low Energy Electron Diffraction (LEED).

The NAP cell is brought into the analysis chamber using the sample manipulator and 'docks' with the PHOIBOS 150 NAP analyser. The wobble stick is used to open the cell initially before taking the sample from the manipulator and placing it inside the NAP cell. Once the sample is securely inside, the NAP cell is then closed up and sealed. The PHOIBOS 150 NAP analyser has a mean radius of 150 mm, a nozzle with a half-angle of 35° and post-lens apertures of radius 0.4 mm. The lenses, analyser and detector are coated in μ-metal to screen external magnetic fields. The NAP-XPS system can achieve up to 25 mbar in pressure, and available gases include H_2O, O_2, CO, CO_2, and NH_3.

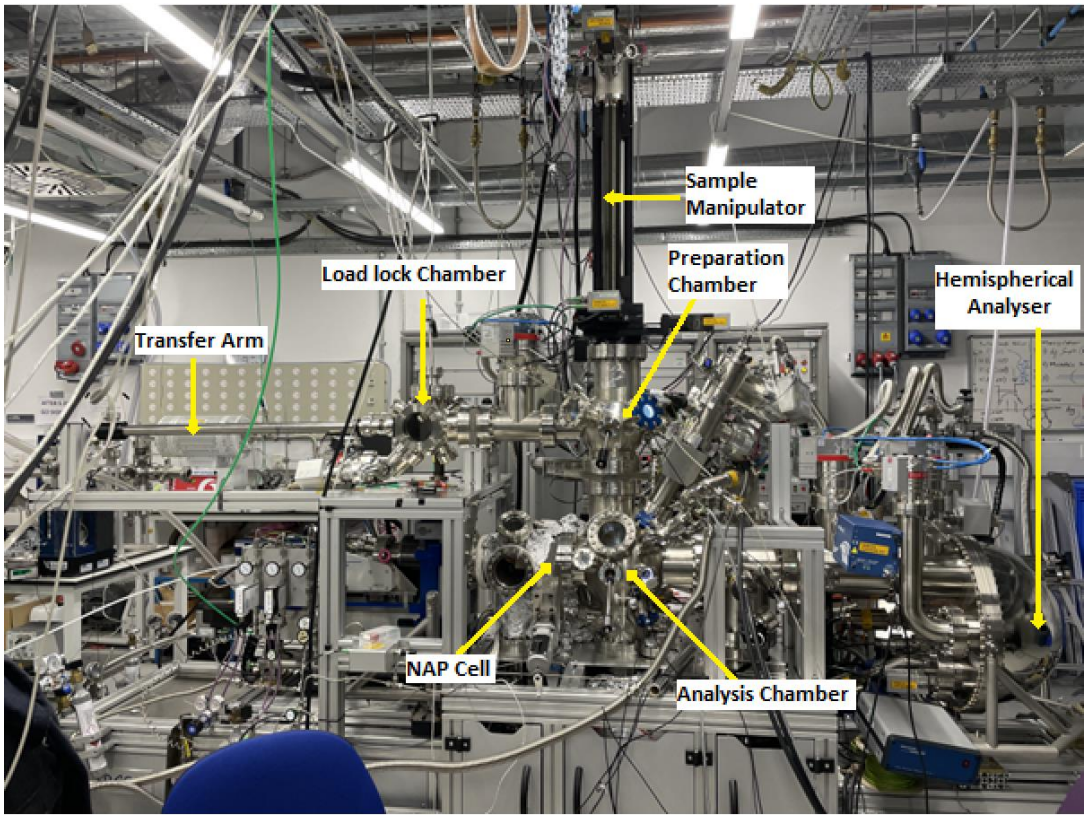

Figure 2.28 Photograph of the NAP-XPS kit at the Henry Royce Facility, UK.

References

1. Ratner, B.D. and D.G. Castner, *Electron Spectroscopy for Chemical Analysis*, in *Surface Analysis – The Principal Techniques*. 2009. p. 47-112.

2. Seah, M.P., *The quantitative analysis of surfaces by XPS: A review.* Surface and Interface Analysis, 1980. **2**(6): p. 222-239.

3. Stevie, F.A. and C.L. Donley, *Introduction to x-ray photoelectron spectroscopy.* Journal of Vacuum Science & Technology A, 2020. **38**(6): p. 063204.

4. Eland, J.H.D., *1 - Principles of photoelectron spectroscopy*, in *Photoelectron Spectroscopy (Second Edition)*, J.H.D. Eland, Editor. 1984, Butterworth-Heinemann. p. 1-29.

5. Band, Y.B. and Y. Avishai, *7 - Approximation Methods*, in *Quantum Mechanics with Applications to Nanotechnology and Information Science*, Y.B. Band and Y. Avishai, Editors. 2013, Academic Press: Amsterdam. p. 303-366.

6. Held, G., et al., *Ambient-pressure endstation of the Versatile Soft X-ray (VerSoX) beamline at Diamond Light Source.* Journal of Synchrotron Radiation, 2020. **27**(5): p. 1153-1166.

7. Seah, M.P. and W.A. Dench, *Quantitative electron spectroscopy of surfaces.* Surface and Interface Analysis, 1979. **1**(1): p. 2-11.

8. Heide, P.v.d., *Data Collection and Quantification*, in *X-Ray Photoelectron Spectroscopy*. 2011. p. 61-99; https://doi.org/10.1002/9781118162897.ch4.

9. Jain, V., M.C. Biesinger, and M.R. Linford, *The Gaussian-Lorentzian Sum, Product, and Convolution (Voigt) functions in the context of peak fitting X-ray*

photoelectron spectroscopy (XPS) narrow scans. Applied Surface Science, 2018. **447**: p. 548-553.

10. Maniyarasu, S., *PhD Thesis - The Effect of Additives on the Stability of Mixed-Cation Perovskites Studied by Electron Spectroscopy.* 2023; https://pure.manchester.ac.uk/ws/portalfiles/portal/250505017/FULL_TEXT.PDF.

11. Weightman, P., *X-ray-excited Auger and photoelectron spectroscopy.* Reports on Progress in Physics, 2000. **45**: p. 753.

12. Ohring, M., *Materials Science of Thin Films (Second Edition)*. 2002: Academic Press: https://doi.org/10.1016/B978-0-12-524975-1.X5000-9.

13. Hucknall, D.J. and A. Morris, *Vacuum Technology: Calculations in Chemistry*. 2003: Royal Society of Chemistry; https://books.google.com.na/books?id=HJLG-DtMYEEC.

14. Margaritondo, G., *Elements of Synchrotron Light: for Biology, Chemistry, and Medical Research*. 2002: Oxford University Press: https://doi.org/10.1093/oso/9780198509301.001.0001.

15. Henderson, Z., *Understanding Surface Structure and Interactions of Ionic Liquids for Energy Applications*, in *School of Physical Sciences and Computing*. 2019, University of Central Lancashire: https://clok.uclan.ac.uk/30852/.

16. Lindau, I., et al., *X-ray photoemission spectroscopy.* Nature, 1974. **250**(5463): p. 214-215.

17. *Spectroscopic Techniques*, in *An Introduction to Synchrotron Radiation*. 2011. p. 223-302.

18. Otendal, M., et al., *A 9keV electron-impact liquid-gallium-jet x-ray source.* Review of Scientific Instruments, 2008. **79**(1): p. 016102.

19. Schnohr, C.S. and M.C. Ridgway, *Introduction to X-Ray Absorption Spectroscopy*, in *X-Ray Absorption Spectroscopy of Semiconductors*. 2015, Springer Berlin Heidelberg: Berlin, Heidelberg. p. 1-26: https://doi.org/10.1007/978-3-662-44362-0_1.

20. Mewe, R., *A. Thorne, U. Litzen and S. Johansson, Spectrophysics Principles and Applications.* Space Science Reviews, 1999. **90**(3): p. 525-525.

21. Nefedov, A. and C. Wöll, *Advanced Applications of NEXAFS Spectroscopy for Functionalized Surfaces*. 2013. p. 277-303.

22. *Synchrotron Physics*, in *An Introduction to Synchrotron Radiation*. 2011. p. 39-86.

23. Niels Hertel, S.P.M.a.J.S.N. *ASTRID2 – the UV and soft x-ray synchrotron light source with the ultimate brilliance*. 2009; Available from: https://www.isa.au.dk/facilities/astrid2/docs/astrid2-preliminarydesign-report-august2009.pdf.

24. Syres, K., *Molecular Adsorption on TiO_2 Surfaces: Modelling Potential Biomedical and Photovoltaic Devices*, in *School of Physics & Astronomy*. 2010, University of Manchester: https://pure.manchester.ac.uk/ws/portalfiles/portal/60828299/FULL_TEXT.PDF .

25. J.S. Nielsen, N.H., S.P. Møller *An overview of the proposed beam diagnostic for Astrid2*. 2009; Available from: https://www.isa.au.dk/facilities/astrid2/docs/MOPD24-DIPAC2009-Article.pdf.

Chapter 3. A comparison of thermal stabilities of $MAPbI_3$ and $MAPbBr_3$ perovskites using X-ray photoelectron spectroscopy

3.1. Introduction

Tremendous progress has been made in the field of hybrid organic-inorganic perovskites in recent years, with thin film solar cell efficiency reaching over 26% [1, 2]. Although they have efficiencies competitive with monocrystalline silicon, the advantages of flexibility, low cost, and easy processing make them superior candidates over conventional inorganic solar cells [3].

Perovskite materials are distinguished by their unique optoelectronic properties, such as tuneable bandgap, high absorption coefficients, ambipolar charge transport [4], long carrier lifetimes [5], and long charge diffusion lengths [6]. The major obstacle facing perovskite solar cells (PSCs) is their limited-service life under operating conditions owing to the deterioration of the absorber material in contact with humidity, oxygen, and exposure to UV light and heat [7-9].

Understanding the degradation mechanism in perovskites is of crucial importance for device design and optimisation. Although the degradation induced by humidity and high temperature is more severe than other factors [10-12], more work is needed to fully understand the temperature-induced degradation of the material. Most studies have focused on tackling the moisture instability of PSCs by suggesting better device encapsulation, modification of the hole transport layer (HTL) and a more suitable electron transport layer (ETL) [13-17].

Conings et al. demonstrated the intrinsic thermal instability of $MAPbI_3$, showing that the degradation process starts right at the annealing stage (85 °C), even in an inert

atmosphere [8]. In the case of PSCs, various pathways of the thermal degradation process have been reported, such as diffusion of iodine into the HTL [18], migration of gold through HTL into perovskite material [19], and precipitation of metallic lead [20, 21]. Some studies have suggested that the degradation might be a result of the crystallisation [22] or oxidation of the spiroOMeTAD [23]. However, a thorough study of the thermal degradation mechanism is significant for understanding the basic decomposition reaction chemistry.

In this study, we compare the thermal degradation mechanism of the two main lead halide perovskites: $MAPbI_3$ and $MAPbBr_3$, using X-ray photoelectron spectroscopy. The samples were subjected to thermal stress of 200 °C and the XPS data was recorded pre- and post-heating. The $MAPbBr_3$ sample was found to be more thermally stable than the $MAPbI_3$ sample. To explain this difference in thermal stabilities in the two lead halide perovskites, we suggest a three-step thermal degradation mechanism. The degradation mechanism can be used to understand the role of halide ions in the structural stability of perovskites.

3.2. Experimental Section

The perovskite samples, $MAPbI_3$ and $MAPbBr_3$, were synthesized using the aerosol-assisted chemical vapour deposition (AACVD) method by colleagues at the University of Manchester (David Lewis *et al.*). For AACVD deposition of perovskites, a precursor solution is prepared in N,N-dimethylformamide (DMF) by stirring equimolar amounts of PbI_2 and MAI for $MAPbI_3$, and equimolar amounts of $PbBr_2$ and MABr for $MAPbBr_3$. Stirring was carried out at 70 °C for 20 mins. Subsequently, an ultrasonic humidifier was employed to generate an aerosol mist from this solution. The resulting mist was then transported into a hot wall reactor maintained at a temperature of 150 °C. Within the reactor, single crystal rutile TiO_2 substrates were present, onto which the mist was deposited [24].

Experimental measurements were carried out at beamline D1011 ($30 \leq h\nu \leq 1500$ eV) at the MAX-lab synchrotron facility in Sweden. The D1011 end station was equipped with

a SCIENTA SES200 200 mm mean radius hemispherical electron energy analyser. XPS spectra were used to probe the chemical bonding and electronic structure of the photo-absorber material. Quantification was carried out using CasaXPS. XPS peaks have been fitted using a Gaussian-Lorentzian product line shape (GL(30)) and a Shirley background. The binding energy scale is charge-corrected to adventitious carbon at 284.5 eV, and fitted peaks are quoted to ±0.1 eV binding energy.

3.3. Results and Discussion

To ascertain the decomposition pathway of the halide two perovskites, XPS survey spectra (refer to Figure 3.1 & Table 3.1) of the samples were analysed, and the relative atomic concentrations were calculated from the peak areas and the relative sensitivity factors (RSFs) to track changes in the chemical composition. In the $MAPbI_3$ sample, a decrease in the concentration of iodine from 12.0% to 6.1% and nitrogen from 2.8% to 2.3% after heating points to the outgassing of iodine (I_2) and ammonia (NH_3), as shown in the degradation pathway below. The precipitation of metallic lead following the degradation of lead iodide results in an increase in the metallic lead concentration (4.1% to 4.2%). In contrast, in the $MAPbBr_3$ sample, only a slight decrease in bromine (17.8% to 17.0%) and nitrogen (2.6% to 2.4%) concentrations is observed in the survey spectrum.

The halide/Pb concentration ratios of the two perovskites (see Figure 3.2) indicates the change in stoichiometry following the thermal degradation of the perovskites. Before heating $MAPbI_3$, the I/Pb ratio was 3.0, indicating a stoichiometric composition consistent with the perovskite. However, after heating, the I/Pb ratio decreased to 1.5. This decrease in the I/Pb ratio suggests that the thermal degradation process caused the decomposition of lead iodide, leading to the release of iodine and the formation of metallic lead. The bromide perovskite, $MAPbBr_3$, also exhibited a decreasing trend, albeit not as pronounced. The Br/Pb ratio was 3.0 before heating, indicating a stoichiometric ratio consistent with the presence of perovskite. After heating, the Br/Pb ratio decreased to 2.2.

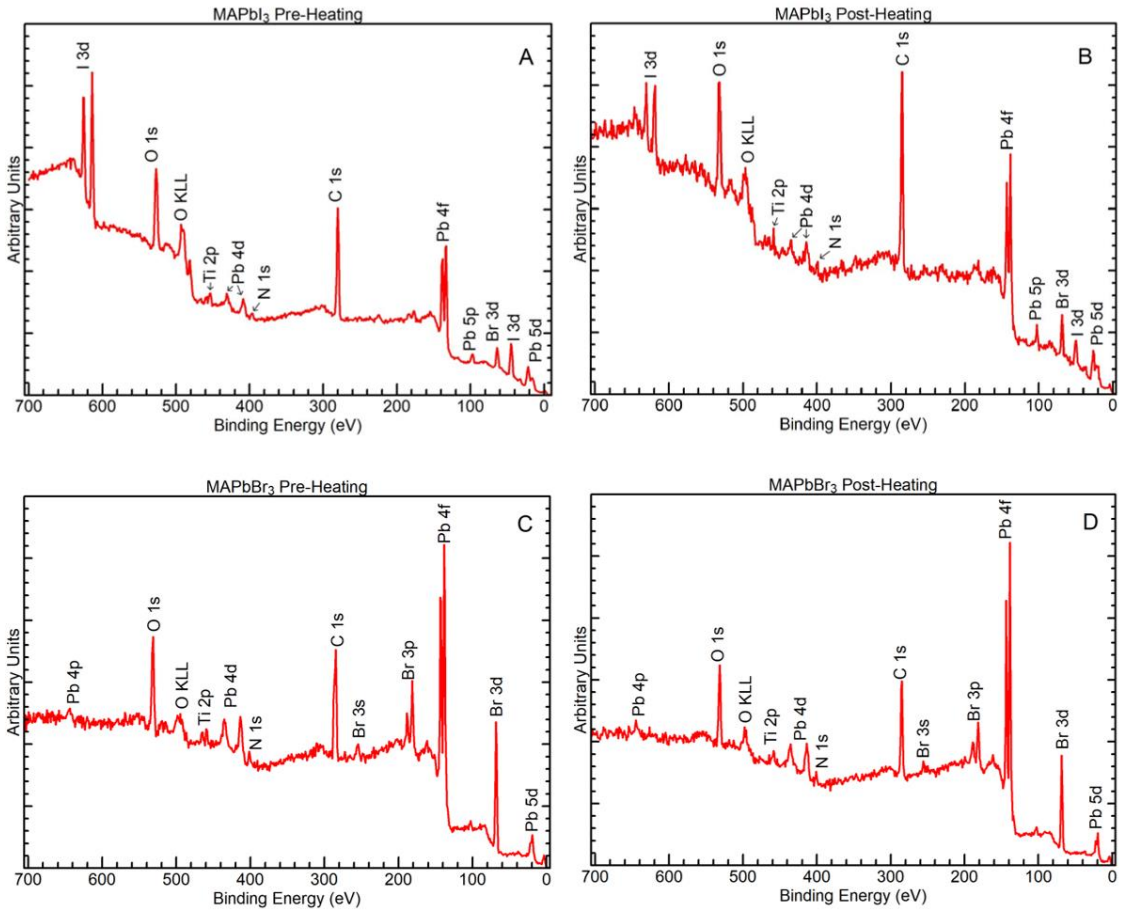

Figure 3.1 XPS survey spectra for $MAPbI_3$ (A & B) and $MAPbBr_3$ (C & D) recorded with an excitation energy of 1000 eV. A & C represent fresh samples, while B & D represent samples post-heating.

$MAPbI_3$	C	Ti	O	N	Pb	I	I/Pb
Before Heating	61.0	1.5	18.7	2.8	4.0	12.0	3.0
After Heating	68.5	2.1	16.8	2.3	4.2	6.1	1.5
$MAPbBr_3$	C	Ti	O	N	Pb	Br	Br/Pb
Before Heating	57.4	1.3	14.9	2.6	6.0	17.8	3.0
After Heating	55.6	2.0	15.4	2.4	7.6	17.0	2.2

Table 3.1 Relative composition of the elements before and after heating (in at. %). (Numerical values are reported with an accuracy of ± 0.1)

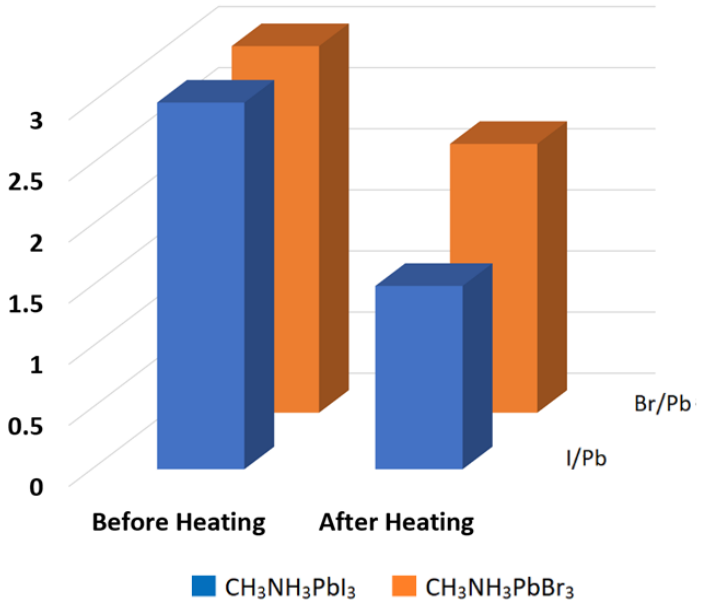

Figure 3.2 Halide/Pb ratios for $MAPbI_3$ (blue) and $MAPbBr_3$ (orange)

It is important to highlight that the peaks at approximately 70 eV in the wide scans of $MAPbI_3$ could not be attributed to any elements present in either the perovskite film or the substrate. The BE of these peaks corresponds with that of the Br 3d peaks and may have originated from residual bromine in the XPS chamber following the heating of the bromide sample.

The C 1s spectra for the two samples, before and after heating, are shown in Figure 3.3. Before heating, the $MAPbI_3$ C 1s spectrum is fitted with three peaks at 284.5 eV, 285.4 eV and 286.5 eV. After heating, the peaks are fitted at 284.5 eV, 285.4 eV and 287.0 eV. The peaks at 284.5 eV are consistent with the sp^3 adventitious carbon, while the peaks at 285.4 eV may be attributed to CH_3I [25]. According to the study by Liu et al., CH_3I drives the phase transition of PbI_2 to PbI_3, which is a crucial starting step in forming the perovskite structure. This results in the incorporation of a secondary carbon species (CH_3I) in $CH_3NH_3PbI_3$, leading to some degree of substitution of CH_3NH_3 with CH_3 [25]. We believe that CH_3I peaks originating pre-heating are part of the CH_3PbI_3 structure, but they may also result from the precursors. The peak at 286.5 eV has been assigned to the carbon of the perovskite ($CH_3NH_3PbI_3$) [25, 26]. After heating, the peak at 286.5 eV shifts to 287.0 eV, indicating the thermal degradation of the perovskite into CH_3NH_3I (MAI),

which is in line with the XPS spectra of MAI reported by Liu et al. [25]. The wide scans reveal a significant presence of oxygen beyond what would typically be attributed to the underlying TiO_2 substrate, suggesting it likely stems from surface hydrocarbon contamination. We were unable to identify any peaks corresponding to C-O bonds in the C 1s spectra of $MAPbI_3$. Nonetheless, we speculate that a portion of the intensity observed in the C-I peak may originate from oxygenated carbon present on the surface.

The $MAPbBr_3$ C 1s spectrum before heating is fitted with four peaks at 284.5 eV, 285.3 eV, 286.5 eV and 288.0 eV. After heating, the peaks are fitted at 284.5 eV, 285.3 eV, 286.5 eV and 287.6 eV. The peaks at 284.5 eV are assigned to sp^3 carbon while the peaks at 285.3 eV demonstrate the presence of CH_3Br, as explained with CH_3I above. The peak at 286.5 eV represents the state of carbon in the perovskite ($CH_3NH_3PbBr_3$) and its presence post-heating suggests that the perovskite phase did not completely degrade during the heating process [27]. The peaks at higher binding energies, 288.0 eV and 287.6 eV, are assigned to C-O bonds from hydrocarbon contamination. The peaks observed at higher binding energies at 288.0 eV and 287.6 eV, are attributed to C-O bonds originating from hydrocarbon contamination. The atomic concentration of oxygen derived from these C-O bonds in the C 1s spectra approximately matches the concentration of oxygen detected in the wide scans once the expected contribution from the TiO_2 substrate is subtracted.

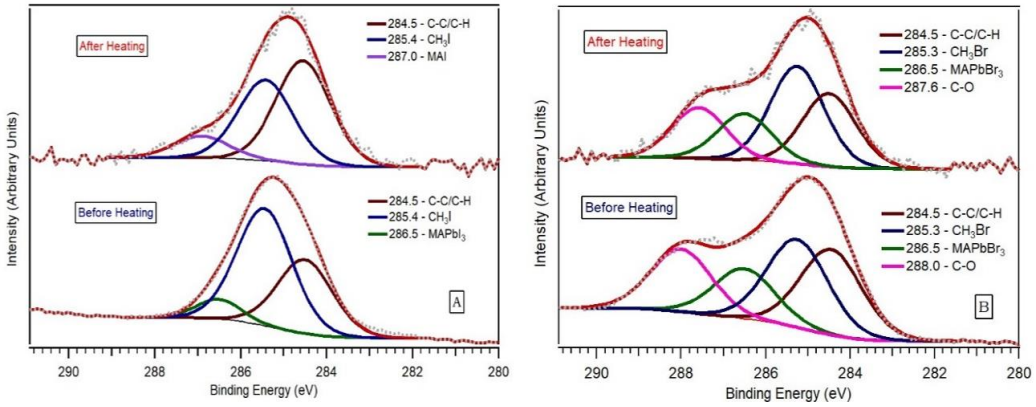

Figure 3.3 C 1s Core level XPS spectra for $MAPbI_3$ (A) and $MAPbBr_3$ (B) recorded with excitation energies of 800 eV (pre-heating) and 1200 eV (post-heating).

The N 1s spectra (depicted in Figure 3.4) for the two perovskites exhibit three peaks at 399.5 eV, 401.2 eV, and 402.6 eV prior to heating. After heating, the peaks for the $MAPbI_3$ sample can be identified at 399.5 eV and 401.2 eV, while the $MAPbBr_3$ sample maintains its peaks at 399.5 eV, 401.2 eV, and 402.6 eV. The peaks at 402.6 eV can be assigned to nitrogen in the perovskite lattice [25]. The peaks at 399.5 eV suggests the existence of an amide group, which is attributed to the residual DMF solvent used during the fabrication process.

The intensity of the DMF peak increases post heating which could be resulting from DMF forming a complex with other degradation products such as MAX and PbX_2 (X = I/Br) [27]. The peak at 401.2 eV usually arises from a protonated amine group. Therefore, we attribute it to MAI and MABr, which might have formed due to the degradation of perovskites [28]. While an MAI component was detected in the C1s spectra of $MAPbI_3$, distinguishing the peaks related to MABr in the same spectra proved challenging due to their similarity to the peaks associated with carbon oxidation.

It is evident that while the peak intensities for the bromide sample change, the binding energies can be fitted at the same positions, indicating the persistence of the perovskite peak. This observation underscores the superior thermal stability of $MAPbBr_3$ relative to $MAPbI_3$, where the latter shows a complete loss in the 402.6 eV peak, signifying thermal degradation. Although the intensity of the $MAPbBr_3$ perovskite peak decreased from 3.1% to 2.8% after heating, its presence post-heating suggests that the perovskite phase did not fully degrade. This is in line with the observation made from the C 1s spectra of the bromide sample, where a peak corresponding to the perovskite phase ($CH_3NH_3PbBr_3$) can be seen post-heating.

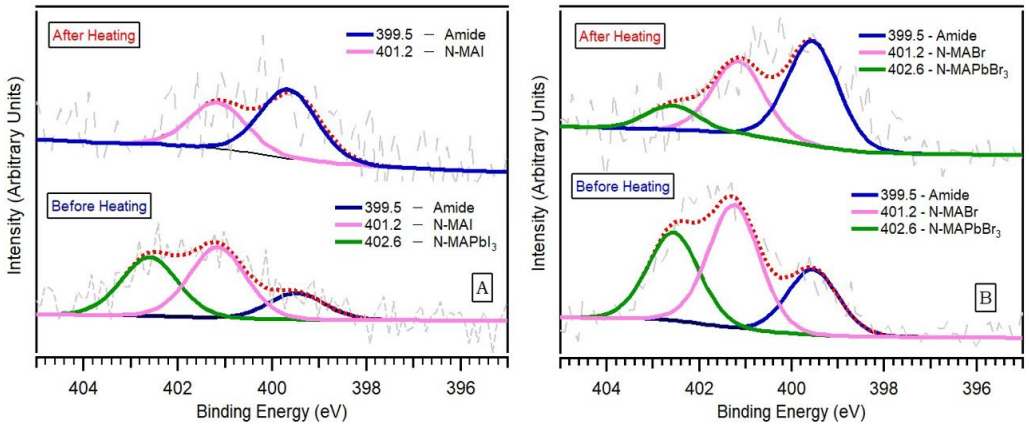

Figure 3.4 N 1s Core level XPS spectra for $MAPbI_3$ (A) and $MAPbBr_3$ (B) recorded with excitation energies of 800 eV (pre-heating) and 1200 eV (post-heating).

The Pb 4*f* spectra consist of two separate contributions: $4f_{7/2}$ and $4f_{5/2}$ peaks with a spin-orbit splitting of 4.88 eV. Each branch (i.e., $4f_{7/2}$ and $4f_{5/2}$) in the spectra can be adequately fitted with two main Pb 4*f* peaks attributable to Pb in the perovskite structure and metallic Pb. The Pb 4*f* spectra (Figure 3.5) of the as-prepared $MAPbI_3$ sample shows four components at 138.6 eV, 143.5 eV, 136.5 eV and 141.4 eV. After heating, the spectrum is fitted with four peaks at 138.7 eV, 143.6 eV, 136.5 eV and 141.4 eV.

The $MAPbBr_3$ Pb 4*f* spectra are fitted with four peaks at 138.5 eV, 143.4 eV, 136.5 eV and 141.4 eV before heating and at 138.7 eV, 143.6 eV, 136.5 eV and 141.4 eV after heating. The peaks at 138.5 eV, 138.6 eV and 138.7 eV correspond to Pb^{+2} $4f_{7/2}$ state, while the peaks at 143.4 eV, 143.5 eV and 143.6 eV represent Pb^{+2} $4f_{5/2}$ state. These peaks can be attributed to Pb in the perovskite structure. The smaller components in each spectrum at 136.5 eV and 141.4 eV are consistent with the binding energy of metallic lead (Pb^0) [29]. The atomic concentration of metallic lead after heating increases from 4.1% to 4.6% and 5.8% to 7.7% in the case of $MAPbI_3$ and $MAPbBr_3$, respectively (see Table 3.1). The increase in the intensity of metallic lead peaks after heating indicates the decomposition of PbI_2 and $PbBr_2$ and the corresponding loss of I_2 and Br_2 from the surface [21].

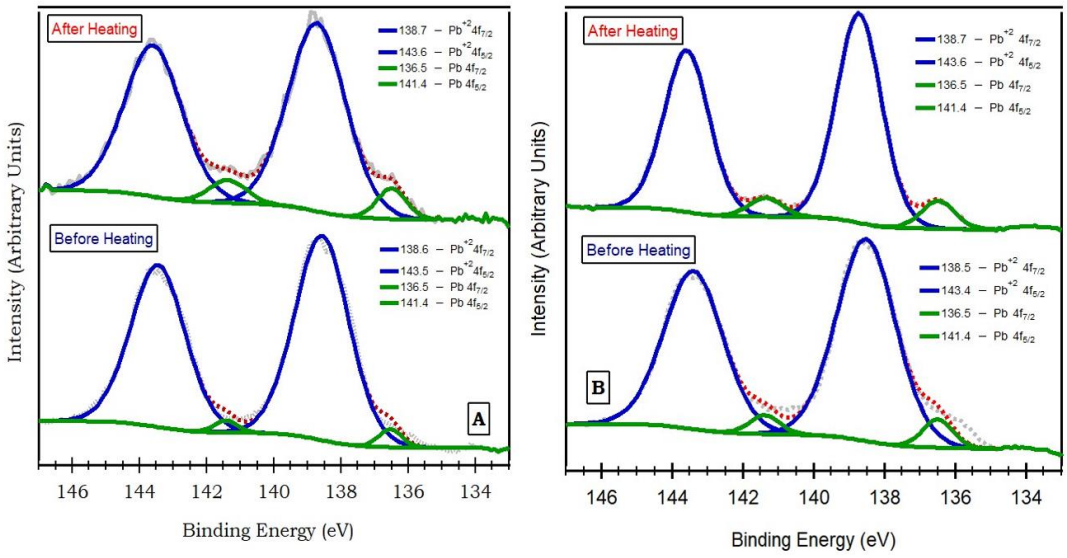

Figure 3.5 Pb 4f Core level XPS spectra for $MAPbI_3$ (A) and $MAPbBr_3$ (B) recorded with excitation energies of 800 eV (pre-heating) and 1200 eV (post-heating).

The I 3*d* spectra (Figure 3.6) of the as-prepared sample are fitted with two peaks at 619.2 eV and 630.7 eV. After heating, the peaks are fitted at 619.2 eV, 630.7 eV, 620.7 eV and 632.2 eV. The 619.2 eV and 630.7 eV peaks correspond to I $3d_{5/2}$ and I $3d_{3/2}$ states in the perovskite. The other components at 620.7 eV and 632.2 eV are particularly interesting as it lends credence to our initial proposition that a secondary carbon species (CH_3I) might have been produced in the perovskite by heating.

The Br 3*p* spectrum before heating is shown in Figure 3.6 and is fitted with two peaks at 181.7 eV and 188.5 eV. After heating, the peaks are fitted at 181.8 eV and 188.7 eV. The peaks at 181.7 eV and 181.8 eV represent the Br $3p_{3/2}$ state, while the peaks at 188.5 eV and 188.7 eV represent the Br $3p_{1/2}$ state in the perovskite. We observe an unusual shoulder in the Br 3p scan post heating at ~191 eV, however, there is no corresponding spin-orbit split component at lower energy. We suggest this feature could be due to some instability on the beamline during data acquisition.

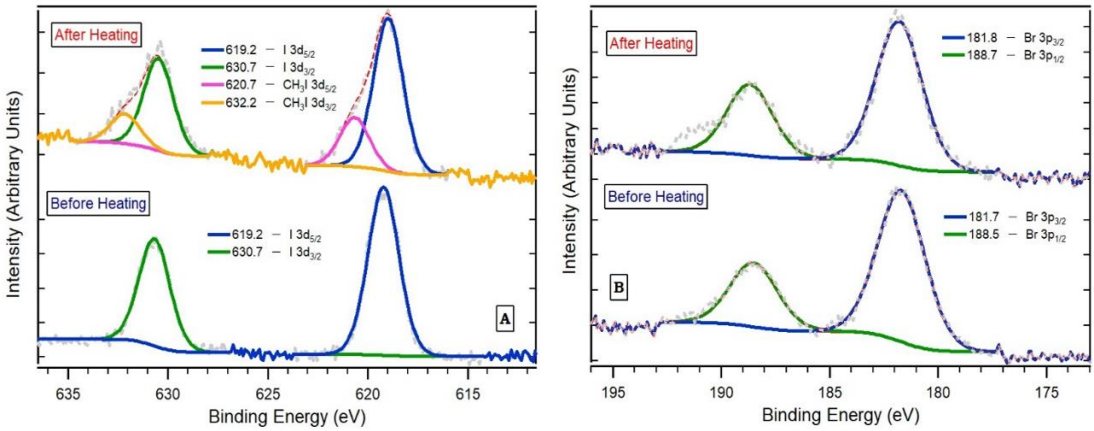

Figure 3.6 I 3d & Br 3p Core level XPS spectra for $MAPbI_3$ (A) and $MAPbBr_3$ (B) respectively recorded with excitation energies of 800 eV (pre-heating) and 1200 eV (post-heating).

It's important to note that all high-resolution spectra acquired before heating utilized 800 eV photons, while those obtained after heating were acquired using 1200 eV photons. This variance in photon energy results in a difference in the kinetic energy of emitted photoelectrons and subsequently affects the inelastic mean free path for measurements conducted before and after heating. Consequently, there may be a slight variation in probing depths pre- and post-heating.

Table 3.2 provides the XPS binding energy values for $MAPbI_3$ and $MAPbBr_3$, along with the assigned components in the XPS spectra.

SPECTRA	HEATING	IODIDE SAMPLE	BROMIDE SAMPLE
C 1*s*	BEFORE Δ	284.5 – C-C/C-H	284.5 – C-C/C-H
		285.4 – C-I in CH_3I	285.3 – C-Br in CH_3Br
		286.5 – C-N in $CH_3NH_3PbI_3$	286.5 – C-N in $CH_3NH_3PbBr_3$
			288.0 – C-O
	AFTER Δ	284.5 – C-C/C-H	284.5 – C-C/C-H
		285.4 – C-I in CH_3I	285.3 – C-Br in CH_3Br
		287.0 – C-N in CH_3NH_3I	286.5 – C-N in $CH_3NH_3PbBr_3$
			287.6 – C-O
N 1*s*	BEFORE Δ	399.5 – Amide (solvent)	399.5 - Amide (solvent)
		401.2 – N in CH_3NH_3I	401.2 – N in CH_3NH_3Br
		402.6 – N in $CH_3NH_3PbI_3$	402.6 – N in $CH_3NH_3PbBr_3$
	AFTER Δ	399.5 – Amide (solvent)	399.5 - Amide (solvent)
		401.2 – N in CH_3NH_3I	401.2 – N in CH_3NH_3Br
			402.6 – N in $CH_3NH_3PbBr_3$
Pb 4*f*	BEFORE Δ	138.6 – Pb^{+2} $4f_{7/2}$	138.5 – Pb^{+2} $4f_{7/2}$
		143.5 – Pb^{+2} $4f_{5/2}$	143.4 – Pb^{+2} $4f_{5/2}$
		136.5 – Pb $4f_{7/2}$	136.5 – Pb $4f_{7/2}$
		141.4 – Pb $4f_{5/2}$	141.4 – Pb $4f_{5/2}$
	AFTER Δ	138.7 – Pb^{+2} $4f_{7/2}$	138.7 – Pb^{+2} $4f_{7/2}$
		143.6 – Pb^{+2} $4f_{5/2}$	143.6 – Pb^{+2} $4f_{5/2}$
		136.5 – Pb $4f_{7/2}$	136.5 – Pb $4f_{7/2}$
		141.4 - Pb $4f_{5/2}$	141.4 – Pb $4f_{5/2}$
I 3*d* & Br 3*p*	BEFORE Δ	619.2 - I $3d_{5/2}$ ($CH_3NH_3PbI_3$)	181.7 – Br $3p_{3/2}$ ($CH_3NH_3PbBr_3$)
		630.7 - I $3d_{3/2}$ ($CH_3NH_3PbI_3$)	188.5 – Br $3p_{1/2}$ ($CH_3NH_3PbBr_3$)
	AFTER Δ	619.2 - I$3d_{5/2}$ ($CH_3NH_3PbI_3$)	181.8 – Br $3p_{3/2}$ ($CH_3NH_3PbBr_3$)
		630.7 - I $3d_{3/2}$ ($CH_3NH_3PbI_3$)	188.7 – Br $3p_{1/2}$ ($CH_3NH_3PbBr_3$)
		620.7 - I $3d_{5/2}$ (CH_3I)	
		632.2 - I $3d_{3/2}$ (CH_3I)	

Table 3.2 XPS binding energy values for $MAPbI_3$ & $MAPbBr_3$

Based on the observations above, it is proposed that the thermal degradation of methylammonium lead iodide proceeds as:

$$CH_3NH_3PbI_3 \xrightarrow{\Delta} CH_3NH_3I + PbI_2 \quad 3.1$$

$$CH_3NH_3I \xrightarrow{\Delta} CH_3I + NH_3 \uparrow \quad 3.2$$

$$PbI_2 \xrightarrow{\Delta} Pb + I_2 \uparrow \quad 3.3$$

The decomposition of $MAPbI_3$ into MAI in the first step is supported by the simultaneous disappearance of the perovskite peak and the appearance MAI peak in the C 1*s* spectra post-heating. Similarly, the disappearance of the perovskite peak in the N 1s spectra after heating, supports the decomposition of $MAPbI_3$ into MAI. Furthermore, the presence of CH_3I in the perovskite samples would suggest the dissociation of MAI (CH_3NH_3I) into CH_3I and NH_3 rather than forming CH_3NH_2 and HI. The distinct appearance of the metallic lead peaks in the Pb 4*f* spectra can be attributed to step 3 of the degradation mechanism above, leading to the precipitation of lead [30].

The decomposition mechanism stated above also helps us understand the better stability of $MAPbBr_3$ over $MAPbI_3$. Equation 3.4 shows the movement of electrons in the degradation of MAI in the second step of the reaction mechanism. The electron density of the iodide ion attacks the sp^3 hybridised carbon atom, acting as a nucleophile. This attack is simultaneously followed by the movement of the electron pair (forming the C-N bond) towards the positively charged nitrogen atom, which subsequently acts as an electrophile. Thus, the decomposition proceeds via the simultaneous breaking of the C-N bond and forming a C-I bond, as shown below (Equation 3.4).

$$(H_3N^+ — CH_3 \cdots I^-) \rightarrow NH_3 \uparrow + CH_3I \uparrow \quad 3.4$$

The lone pair of electrons on the larger, less basic iodide ion are held less tightly by its nucleus and are able to attack the electrophile more easily as compared to the smaller, more basic bromide ion whose lone pair electrons are more firmly held by its nucleus.

The higher electronegativity of the bromine stabilizes the electron pair on the bromide ion, decreasing its nucleophilic strength and making the degradation of $MAPbBr_3$ more difficult.

3.4. Conclusion

The thermal degradation behaviour of $MAPbI_3$ and $MAPbBr_3$ perovskite materials was investigated using X-ray photoelectron spectroscopy. XPS data was acquired both prior to and following heating, with the samples subjected to temperatures of approximately 200 °C. The results obtained demonstrate that $MAPbBr_3$ exhibits higher thermal stability compared to $MAPbI_3$. This conclusion is supported by the disappearance of characteristic peaks of the perovskite phase in the post-heating spectra (C 1s & N 1s) of $MAPbI_3$, whereas these peaks remained observable in the corresponding spectra of $MAPbBr_3$ before and after heating.

The high-resolution C 1s spectra and survey spectra suggest some oxidation on the surface of the samples. Additionally, the Pb 4f XPS spectra indicated the presence of metallic lead species in both samples, with intensified peaks observed after heating. The $MAPbI_3$ sample exhibited a significant reduction in nitrogen and halide concentration, accompanied by an increase in lead concentration. In contrast, the concentration changes in $MAPbBr_3$ were less pronounced.

These findings provide insights into the role of halide ions in the structural stability of perovskites and are consistent with the proposed three-step degradation mechanism. The comparative analysis reveals the superior stability of $MAPbBr_3$ compared to $MAPbI_3$, which can be attributed to the lower nucleophilic strength of bromide ions and the higher electronegativity of bromine. This research contributes to the understanding of the degradation mechanisms in perovskite materials and provides insights for the development of more stable and reliable perovskite-based devices.

References

1. Jeong, J., et al., *Pseudo-halide anion engineering for α-FAPbI3 perovskite solar cells.* Nature, 2021. **592**(7854): p. 381-385.

2. Yoo, J.J., et al., *Efficient perovskite solar cells via improved carrier management.* Nature, 2021. **590**(7847): p. 587-593.

3. Liu, Y., et al., *Flexible Lead Bromide Perovskite Solar Cells.* ACS Applied Energy Materials, 2020. **3**(10): p. 9817-9823.

4. Srivastava, P. and M. Bag, *Elucidating tuneable ambipolar charge transport and field induced bleaching at the CH3NH3PbI3/electrolyte interface.* Physical Chemistry Chemical Physics, 2020. **22**(19): p. 11062-11074.

5. Wehrenfennig, C., et al., *High charge carrier mobilities and lifetimes in organolead trihalide perovskites.* Adv Mater, 2014. **26**(10): p. 1584-9.

6. Stranks, S.D., et al., *Electron-Hole Diffusion Lengths Exceeding 1 Micrometer in an Organometal Trihalide Perovskite Absorber.* Science, 2013. **342**(6156): p. 341.

7. m, n., Zubair, et al., *Instability in CH3NH3PbI3 perovskite solar cells due to elemental migration and chemical composition changes.* Scientific Reports, 2017. **7**(1): p. 15406.

8. Conings, B., et al., *Intrinsic Thermal Instability of Methylammonium Lead Trihalide Perovskite.* Advanced Energy Materials, 2015. **5**(15): p. 1500477.

9. Tiwari, U. and S. Dass. *Moisture Stable Soot Coated Methylammonium Lead Iodide Perovskite Photoelectrodes for Hydrogen Production in Water*. in *Energy and Sustainable Futures*. 2021. Cham: Springer International Publishing.

10. Yang, J., et al., *Investigation of CH3NH3PbI3 Degradation Rates and Mechanisms in Controlled Humidity Environments Using in Situ Techniques.* ACS Nano, 2015. **9**(2): p. 1955-1963.

11. Jena, A.K., et al., *Role of spiro-OMeTAD in performance deterioration of perovskite solar cells at high temperature and reuse of the perovskite films to avoid Pb-waste.* Journal of Materials Chemistry A, 2018. **6**(5): p. 2219-2230.

12. Maniyarasu, S., et al., *Role of Alkali Cations in Stabilizing Mixed-Cation Perovskites to Thermal Stress and Moisture Conditions.* ACS Applied Materials & Interfaces, 2021. **13**(36): p. 43573-43586.

13. You, J., et al., *Improved air stability of perovskite solar cells via solution-processed metal oxide transport layers.* Nature Nanotechnology, 2016. **11**(1): p. 75-81.

14. Wu, S., et al., *A chemically inert bismuth interlayer enhances long-term stability of inverted perovskite solar cells.* Nature Communications, 2019. **10**(1): p. 1161.

15. Zheng, L., et al., *A hydrophobic hole transporting oligothiophene for planar perovskite solar cells with improved stability.* Chemical Communications, 2014. **50**(76): p. 11196-11199.

16. Jeon, N.J., et al., *A fluorene-terminated hole-transporting material for highly efficient and stable perovskite solar cells.* Nature Energy, 2018. **3**(8): p. 682-+.

17. Cao, J., et al., *Thiols as interfacial modifiers to enhance the performance and stability of perovskite solar cells.* Nanoscale, 2015. **7**(21): p. 9443-9447.

18. Divitini, G., et al., *In situ observation of heat-induced degradation of perovskite solar cells.* Nature Energy, 2016. **1**(2): p. 15012.

19. Domanski, K., et al., *Not All That Glitters Is Gold: Metal-Migration-Induced Degradation in Perovskite Solar Cells.* ACS Nano, 2016. **10**(6): p. 6306-6314.

20. Sadoughi, G., et al., *Observation and Mediation of the Presence of Metallic Lead in Organic–Inorganic Perovskite Films.* ACS Applied Materials & Interfaces, 2015. **7**(24): p. 13440-13444.

21. Das, C., et al., *In situ XPS study of the surface chemistry of MAPI solar cells under operating conditions in vacuum.* Physical Chemistry Chemical Physics, 2018. **20**(25): p. 17180-17187.

22. Zhao, X., et al., *Effect of Selective Contacts on the Thermal Stability of Perovskite Solar Cells.* ACS Applied Materials & Interfaces, 2017. **9**(8): p. 7148-7153.

23. Sanchez, R.S. and E. Mas-Marza, *Light-induced effects on Spiro-OMeTAD films and hybrid lead halide perovskite solar cells.* Solar Energy Materials and Solar Cells, 2016. **158**: p. 189-194.

24. Alam, F. and D.J. Lewis, *Thin films of formamidinium lead iodide (FAPI) deposited using aerosol assisted chemical vapour deposition (AACVD).* Scientific Reports, 2020. **10**(1): p. 22245.

25. Liu, L., et al., *Tracking the formation of methylammonium lead triiodide perovskite.* Applied Physics Letters, 2015. **107**(6): p. 061904.

26. Philippe, B., et al., *Chemical and Electronic Structure Characterization of Lead Halide Perovskites and Stability Behavior under Different Exposures—A Photoelectron Spectroscopy Investigation.* Chemistry of Materials, 2015. **27**(5): p. 1720-1731.

27. Guo, X., et al., *Identification and characterization of the intermediate phase in hybrid organic–inorganic MAPbI3 perovskite.* Dalton Transactions, 2016. **45**(9): p. 3806-3813.

28. Park, B.-w., et al., *Stabilization of formamidinium lead triiodide α-phase with isopropylammonium chloride for perovskite solar cells.* Nature Energy, 2021. **6**(4): p. 419-428.

29. Bai, S., et al., *Planar perovskite solar cells with long-term stability using ionic liquid additives.* Nature, 2019. **571**(7764): p. 245-250.

30. Juarez-Perez, E.J., et al., *Thermal degradation of CH3NH3PbI3 perovskite into NH3 and CH3I gases observed by coupled thermogravimetry–mass spectrometry analysis.* Energy & Environmental Science, 2016. **9**(11): p. 3406-3410.

Chapter 4. A study of ionic liquid-modified mixed-halide perovskite thin films

4.1. Introduction

The heat and water resistance of perovskites is crucial for the large-scale deployment of these materials in photovoltaic devices around the world. A good indicator of the operational lifetime of perovskite-based solar cell devices is the surface stability of the perovskite-based thin films. This chapter demonstrates an approach to studying the surfaces of ionic liquid-modified (IL-modified) perovskite thin films. We investigate the role of ionic liquids as additives in perovskite materials.

As mentioned in previous chapters, numerous approaches have been utilised to enhance the stability of perovskite materials such as additive engineering, integrating a superoxide scavenger, introducing hydrophobic interlayers and halide substitution into the perovskite, etc. [1-4]. Additive engineering of perovskites has shown great promise in stabilising the perovskite structure and passivating defects [3, 5, 6].

In this work, we incorporate the ionic liquids – BMIMCl (1-Butyl-3-methylimidazolium chloride) and $BMIMBF_4$ (1-Butyl-3-methylimidazolium tetrafluoroborate) (see Figure 4.1) into a mixed halide perovskite $CH_3NH_3PbI_{3-x}Cl_x$ ($MAPbI_{3-x}Cl_x$) precursor solution prior to thin film deposition via spin-coating. We utilise X-ray Photoelectron Spectroscopy (XPS), Near-ambient Pressure X-ray Photoelectron Spectroscopy (NAP-XPS), Near-edge X-ray Absorption Fine Structure (NEXAFS), and Angle-resolved Hard X-ray Photoelectron Spectroscopy (AR-HAXPES) to study these IL-modified perovskite thin films. The objective of this ionic liquid additive engineering of perovskites is primarily two-fold. One is to improve the film quality by altering the crystallisation process and the other is to increase the tolerance of the perovskite material to environmental stresses such as high temperature and moisture by introducing functional ligands that could potentially create a protective cascade around the perovskite through a network of stronger coordinate bonds.

Ionic liquids (ILs), which are a category of molten salts retaining their liquid state at ambient temperature (below 100 °C), have emerged as promising candidates for enhancing perovskite solar cells [7, 8]. They generally consist of a large organic cation paired with an organic or inorganic anion. Cations can be chosen from a variety of options, including but not limited to pyridinium [9], imidazolium [10], and quaternary ammonium [11] or their derivatives. Anions can encompass halides [12], formate ($HCOO^-$) [13] , phosphate (PF_6^-) [14], and tetrafluoroborate (BF^-_4) [15], to name a few. Differing from conventional inorganic salts (for example, NaCl), ionic liquids exhibit a significant disparity in size between their cations and anions. This size difference results in weaker electrostatic forces of attraction and, consequently, lower melting points, typically below room temperature. Another noteworthy aspect of ionic liquids is their environmentally friendly nature, often characterised as "green solvents," primarily due to their non-volatile properties [16].

Their environmentally friendly quality gain particular significance when contrasting these materials with traditional organic solvents, additives, and passivators commonly employed in perovskite solar cells. In light of concerns regarding the metal (Pb) content in conventional perovskite solar cells, this concept has been adopted to replace toxic organic solvents in these materials. Moreover, ionic liquids have shown the potential to occupy halogen defects resulting from halogen ion migration within perovskite structures due to their high electron density, indicating their ability to inhibit ion migration within perovskite materials [17].

Ionic liquids offer numerous advantages, including a wide liquid temperature range, high carrier mobility, and notably, thermal and electrochemical stability. By utilising the structure of ionic liquids, opportunities emerge for interactions between different functional groups of ILs (such as hydrogen bonding, coordination, and electrostatic interactions) with perovskite materials. These interactions, in turn, can significantly enhance the crystallization tendency, leading to the production of high-quality films with reduced defects. This, combined with the hydrophobic properties inherent in designed ionic liquids, can contribute to improving the water resistance of the resulting films.

Ionic liquids have attracted significant attention in the area of energy storage technologies, primarily attributed to their exceptional properties in terms of ionic conductivity and thermal resilience [18]. While the uses of ionic liquids are almost too numerous to list comprehensively, many of the popular applications are in separations, battery electrolyte development, electrocatalysis, CO_2 gas capture and lubrication. Within the area of PSCs, ionic liquids have found application as additives aimed at enhancing device efficiency and operational stability [1, 7, 15, 19, 20]. Ionic liquids have been previously integrated into perovskite solar cells and have shown to improve device performance [21, 22]. The enhancement has been attributed to either the creation of halide complexes [21] or a favourable alignment of energy levels at the n-type interface between the charge-extraction layer and the perovskite [22]. Snaith et al. have proposed that $BMIM^+$ cations can effectively bind to surface sites vulnerable to heat and moisture-induced degradation, thus enhancing the stability of PSCs [15]. In their study, they fabricated devices containing varying concentrations of $BMIMBF_4$ (ranging from 0.15 to 0.9 mol% relative to lead atoms) by directly incorporating this ionic liquid into the perovskite precursor solution. Their findings showed that the device containing 0.3 mol% of the ionic liquid exhibited the highest efficiency, with a power conversion efficiency (PCE) of 19.8%.

In our current investigation, we probe deeper into these high-performing 0.3 mol% ionic liquid-modified perovskite films. However, unlike Snaith et al.'s work, our primary focus is to gain more comprehensive insights into the stability of the IL-modified perovskite films when subjected to environmental stressors such as heat and moisture.

The motivation for our study of the ionic liquid $BMIMBF_4$ also stems from various studies showing that compositional engineering by integrating BF_4^- ions into the perovskite lattice can significantly improve the device performance of PSCs [23, 24]. For instance, Zhang et al. demonstrated that the incorporation of BF_4^- ions into a mixed-ion perovskite crystal structure can lead to substantial improvements in device performance [23]. According to their findings, BF_4^- ions play a pivotal role in inducing lattice relaxation, consequently extending the photoluminescence lifetime, enhancing resistance to recombination, and significantly reducing trap density in the fabricated perovskite films

and the resulting solar cells. This reduction in trap density is of the order of one to two magnitudes, further underscoring the potential benefits of incorporating BF_4^- ions in perovskite materials. Another study by Yang et al. found that doping BF_4^- ions into $MAPbBr_3$ perovskite can lead to an increase in charge carrier lifetime and a decrease in the rate of recombination in perovskite thin films [24]. Their findings indicate a promising future for perovskite materials when BF_4^- substitutions are incorporated.

The role of chlorine in enhancing the optoelectronic performance of $MAPbI_{3-x}Cl_x$ is well-documented, but its incorporation within the mixed halide perovskite $MAPbI_{3-x}Cl_x$ structure is a subject of intense debate. Multiple studies have presented evidence suggesting that Cl ions do not become part of the inorganic PbI_3 lattice. This implies that Cl ions exert an indirect influence on the optoelectronic properties of $MAPbI_{3-x}Cl_x$ perovskites, leading to the proposition of various indirect enhancement mechanisms. For instance, Chen et al. attributed the enhancement in optoelectronic performance to improved charge transport across the heterojunction interfaces, rather than within the perovskite crystals [25]. Lian et al. showed that Cl ion inclusion could enhance the crystallinity of $MAPbI_{3-x}Cl_x$ perovskite materials, subsequently promoting crystal growth, despite the absence of Cl ions within the crystal lattice [26]. Fan et al. proposed that residual $PbCl_2$ passivated defects in $MAPbI_{3-x}Cl_x$ perovskite thin films, thereby enhancing their electrical properties [27]. Hui et al. have similarly emphasized the negligible presence of chlorine within the perovskite structure [28].

On the opposing side of the debate, some studies have provided evidence supporting the notion that Cl ions can indeed be integrated into the inorganic PbI_3 lattice. For instance, Zhang et al. demonstrated the presence of Cl ions within the inorganic lattice of $MAPbI_{3-x}Cl_x$ nanofibers created through a solution-assembly method [29]. They demonstrated the formation of up to 25% of the mixed halide phase by adjusting the chlorine concentration in the precursor solution. Min et al. revealed the introduction of Cl ions into the $FAPbI_3$ ($FA = CH(NH_2)_2^+$) crystal lattice by substituting FA sites with methylenediammonium dichloride ions [30].

In this work we investigate the influence of a chloride-containing ionic liquid, BMIMCl, on the crystallisation process of $MAPbI_{3-x}Cl_x$, particularly regarding the incorporation of chlorine into the perovskite structure. It has been previously reported that Cl^- ions can assist in the controlled release of excess $CH_3NH_3^+$ (MA^+) ions at lower annealing temperatures, thereby slowing down the crystallisation process and enhancing film quality [28]. Given this premise, it is pertinent to explore the effects of an excess of Cl- ions, supplied by the ionic liquid, on the crystallisation process. The comparison of BMIMCl and $BMIMBF_4$, which share the same cation, allows us to ascertain the specific role of the chloride anion. Figure 4.1 depicts the cation and anions comprising the two ionic liquids used in this study.

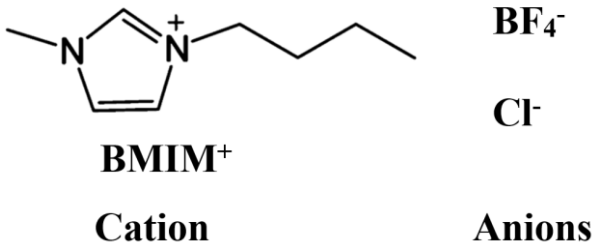

Figure 4.1 Structure and notation of the cation and anions of the ionic liquids $BMIMBF_4$ & BMIMCl

Ensuring the thermal stability of the ILs themselves is vital in safeguarding the perovskite against temperature-induced degradation. ILs exhibit a tendency to undergo decomposition at temperatures lower than their T_{onset} (temperature at which mass loss begins), with a noticeable temperature difference of approximately 100 °C [31]. This observation suggests that utilizing the T_{onset} value may lead to an overestimation of thermal stability. The rationale behind this reasoning is that, during experiments, the temperature increases rapidly at a consistent rate, making it likely to surpass the actual decomposition temperature without recording any significant mass loss. In other words, ILs may degrade at lower temperatures over an extended duration. Table 4.1 shows the T_{onset} and T_{start} (temperature at which decomposition starts) values of the ILs used in this study.

ILs	T_{onset} [31]	T_{start} [31]
$BMIMBF_4$	399 °C	316 °C
BMIMCl	257 °C	208 °C

Table 4.1 Thermal decomposition temperatures of the ILs.

Mixed-halide perovskite solar cells, specifically those utilizing $MAPbI_{3-x}Cl_x$, present notable advantages over their pure $MAPbI_3$ counterparts during the fabrication process. This is attributed to the considerably longer charge carrier diffusion length in $MAPbI_{3-x}Cl_x$ mixed-halide perovskite solar cells, which is approximately ten times greater than that of pure $MAPbI_3$ perovskite solar cells. Consequently, the charge collection efficiency and the reproducibility of $MAPbI_{3-x}Cl_x$ mixed-halide perovskite solar cells surpass those of $MAPbI_3$ perovskite solar cells [32]. Traditionally, $MAPbI_3$ is often combined with mesostructured cells to achieve satisfactory device performance. In contrast, $MAPbI_{3-x}Cl_x$ has the potential to deliver high power conversion efficiencies (PCEs) when used in a planar device structure, and this can be accomplished through a straightforward spin-coating or co-evaporation film deposition process [28]. In light of these inherent advantages, we have selected $MAPbI_{3-x}Cl_x$ (see Figure 4.2) as the preferred perovskite material for this study.

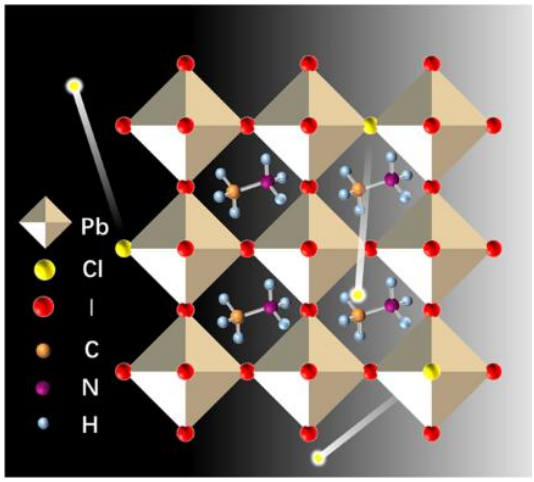

Figure 4.2 Representation of crystal lattice structure of $MAPbI_{3-x}Cl_x$ perovskite. Reproduced from [33]

In this study, we investigate the stability of pristine perovskite thin films, as well as perovskite thin films modified with $BMIMBF_4$ and BMIMCl, deposited on titanium foil substrates, both with and without a SnO_2 coating (see Figure 4.3). SnO_2 has been identified as one of the most promising ETL material owing to its favourable optoelectronic properties, including low light absorption, appropriate energy level alignment with the perovskite, high electron mobility as well as low-temperature processing [34]. The choice of Ti foil as the substrate for sample deposition was made to prevent the charging-up of the films during XPS/NEXAFS measurements. The samples were probed using XPS under UHV both before and after heating in order to assess their thermal stability. To gain a more comprehensive understanding of the chemical composition at the elemental level, we additionally conducted NEXAFS and AR-HAXPES analyses. NEXAFS probes the unoccupied molecular states of a material and provides information about the electronic structure of a material. Moreover, there's very limited literature available on NEXAFS pertaining to IL-modified perovskites. AR-HAXPES was instrumental in providing depth profiling, facilitating the identification of degradation differences from the surface towards the bulk. Furthermore, we employed NAP-XPS technique to study the degradation of samples with moisture. NAP-XPS allows for XPS measurements in more realistic environments, providing insights into the water resistance of the samples. Prior studies in the literature predominantly focus on understanding the influence of ionic liquids on the performance of perovskite-based devices. However, our approach undertakes a fundamental investigation into the structural stability of IL-modified perovskite films, utilising relatively new techniques such as Ar-HAXPES and NAP-XPS.

This combination of techniques reveals differences in the thermal and moisture resistance between the perovskite and IL-modified perovskite samples. Results suggest that the ionic liquid and SnO_2 layer both play an important role in stabilising the films. These results offer valuable insights into the heat and moisture stability of halide perovskites and may contribute to future advancements in perovskite design. Ultimately, this could open the path to the development of highly efficient and stable perovskite solar cell (PSC) devices.

4.2. Experimental

4.2.1. Materials

$MAPbI_{3-x}Cl_x$ perovskite precursor ink (I101) was purchased from Ossila. I101 has been specially formulated in the Ossila laboratories to be deposited by spin coating under ambient conditions. All other chemicals were purchased from Sigma Aldrich, Thermo Scientific Chemicals or Ossila and used as received unless stated otherwise.

4.2.2. Substrate preparation

Samples were fabricated on titanium foil substrates. The substrates underwent a sequential cleaning process involving a 2% Hellmanex solution, deionized water, acetone, and isopropanol. Each step was carried out in an ultrasonic bath for 15 minutes with the substrates immersed in the respective solution. Following the sonication, the substrates were rinsed with isopropanol and dried using a nitrogen gun.

4.2.3. Thin film deposition

Sample fabrication was performed at the University of Central Lancashire, UK. The six substrates were divided into two sets. One set, comprising three substrates, were spin-coated with a layer of SnO_2 prior to perovskite deposition. To achieve this, 50 µl of a 15% SnO_2 solution in H_2O colloidal dispersion was spin-coated onto cleaned substrates at 3000 rpm for 30 seconds. Subsequently, the coated substrates were annealed at 150 °C for 40 minutes on a hotplate.

For the perovskite deposition, the precursor ink (I101, Ossila) was activated by placing it on a hotplate at 70 °C for 2 hours to ensure complete solute re-dissolution. Following this step, two separate solutions were prepared, each containing 0.3 mol% of BMIMCl and $BMIMBF_4$ in the perovskite precursor ink. These solutions were also heated on a hotplate at 70 °C for approximately 10 minutes to facilitate dissolution.

The deposition procedure involved spin-coating, where 50 µl of the inks (both pure and ionic liquid-modified perovskite inks) were spin-coated onto the six titanium foil substrates. Three of these substrates had the SnO_2 layer, and three did not. The spin-coating was carried out at 3000 rpm for 30 seconds. After the spin-coating, the substrates were annealed at 90 °C for 120 minutes and subsequently transferred into a nitrogen-filled glovebox for storage.

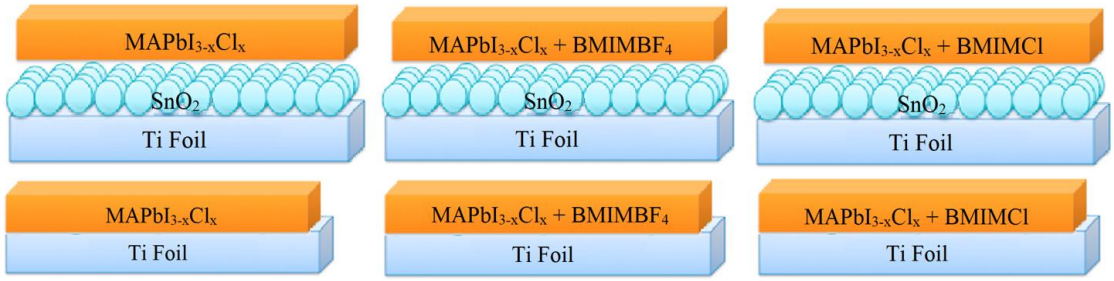

Figure 4.3 A schematic representation of the six samples used in this study. The top three show the perovskite and IL-modified perovskite films deposited on SnO_2-coated Ti foil substrate, while the bottom three show the samples deposited directly onto Ti substrate without a layer of SnO_2.

4.2.4. Storage and transfer of the thin films

The samples were carefully stored in a nitrogen-filled plastic container, placed atop a layer of zeolite molecular sieve beads. This setup was employed to ensure the maintenance of dry conditions to the greatest extent possible. Subsequently, the container was vacuum sealed with paraffin to prevent moisture ingress during transportation to external facilities. The samples were shipped to Denmark, where XPS and NEXAFS studies were conducted at the ASTRID-2 synchrotron facility located within the University of Aarhus. Two fresh batches of samples were prepared and transported to the Henry Royce Facility at the University of Manchester, where AR-HAXPES and NAP-XPS measurements were carried out. At these facilities, the vacuum-sealed sample container was opened in air and the samples were mounted onto sample plates and loaded into a load-lock chamber as quickly as possible to minimise exposure to the atmosphere. The samples were mounted on tantalum sample plates by soldering them

with tantalum strips before being introduced into the Ultra-High Vacuum (UHV) systems for characterization.

4.2.5. XPS measurements

XPS measurements were carried out at the Matline end station at ASTRID-2 synchrotron facility, ISA, Denmark. The AU-Matline is a multi-pole wiggler beamline offering a spectral range of 20-700 eV. The beamline offers a resolving power of 200 to 3,500 with a typical Flux $1x10^{11}$ photons/sec. The UHV chamber (base pressure below 1×10^{-9} Torr) was equipped with a Scienta electron energy analyser and the beam spot size was $\sim 0.7 \times 1$ mm^2. The XPS scans were taken both before and after heating the samples to temperatures of 100 °C, 150 °C and 300 °C. All the core level scans were recorded at normal emission (photoelectron emission angle at 90˚ relative to the sample surface) with a pass energy of 20 eV.

XPS data acquisition commenced once the filament was turned off and the sample temperature had cooled down to approximately room temperature. The sample position was changed at each temperature setting to avoid beam damage as far as possible. Table 4.2 outlines the photon energies used in acquiring the XPS spectra. For synchrotron XPS experiments, the photon energy for each region is often set to approximately 100 eV above the core level binding energy (i.e. the C 1s binding energy is at 280 eV so the photon energy is set to 380 eV). This method probes the top-most layers of the sample and ensures a similar probing depth for each core level spectrum. However, due to the low flux of the beamline at certain energies and the low cross sections for some regions, a trade-off was necessary.

The spectra are charge-corrected with respect to the adventitious carbon at 285.0 eV. Background subtraction was carried out using the Shirley method and a Gaussian-Lorentzian product GL(30) line shape was used to fit the peaks using CasaXPS software. BE values are quoted with an accuracy of ±0.1 eV. The spectral regions and the peak components are normalised by the intensity of C1s peak.

Region	Photon Energy
C 1s	380 eV
Pb 4f	320 eV
I 4d	120 eV
Cl 2p	320 eV

Table 4.2 Photon energies used in acquiring the XPS spectra on the AU-MATline beamline.

4.2.6. NEXAFS measurements

NEXAFS measurements were performed on the MATLINE beamline at the ASTRID-2 synchrotron at the University of Aarhus, Denmark. The carbon K-edge (C K-edge) and nitrogen K-edge (N K-edge) data were acquired by scanning the photon energy from 280-320 eV and 395-420 eV, respectively. The base pressure of the system was ca. 4×10^{-10} mbar. For each sample, spectra were collected with the synchrotron beam incidence at 45°. All scans were taken at 100 eV pass energy. The NEXAFS spectra were recorded by detecting C K-edge and N K-edge Auger electrons at a kinetic energy of 270 eV and 380 eV, respectively in constant final state mode using the hemispherical analyser. NEXAFS spectra were recorded once the samples had cooled back to room temperature. The spectra were analysed using Igor pro software package, version 8.04.

4.2.7. AR-HAXPES measurements

AR-HAXPES was used to study the elemental composition and depth profile of elements in the samples. The experiments were performed in the high-throughput HAXPES instrument (Scienta Omicron GmbH) at the Henry Royce Institute, Manchester. The instrument uses a Ga Kα metal jet X-ray source (Excillum, 9.25 keV) to generate monochromated high energy X-rays which are micro-focussed to a 50 µm spot via Bragg reflection at a silicon crystal. Equipped with an EW-4000 electron energy analyser, the spectrometer can measure photoelectrons with up to 12 keV of kinetic energy (KE), detected at an angle of 90° with respect to the incident X-rays. The HAXPES measurements were recorded using the transmission mode of the analyser at normal

emission (sample at 0° w.r.t the analyser normal) and using the angular mode of the analyser at grazing emission (sample at 40° w.r.t the analyser normal). All the core level spectra were recorded with a pass energy of 200 eV and at a slit width of 0.8 mm. At grazing emission, a series of photoemission spectra were obtained over a range of photoelectron emission angles (θ =20°−60°, w.r.t the surface normal) allowing for the probing of the sample at different sampling depths as illustrated in Figure 4.4 below.

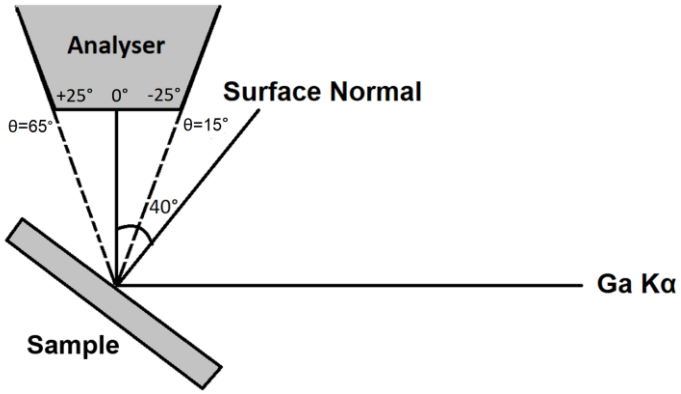

Figure 4.4 Sample configuration for measuring photoelectrons from different photoelectron emission angles (ϑ).

Spectral data at different photoelectron emission angles is gathered by averaging the data over a selected angular range of the analyser. Table 4.3 shows the different angular ranges from which the data was binned for this study along with the corresponding photoelectron emission angles (θ).

Angular Range on analyser (°)	Average Angle (X) (°)	Photoelectron Emission Angle from Surface Normal (θ) (°) = (Sample Tilt Angle – X)	Cos θ
-25 to -20	-22.5	40-(-22.5) = 62.5	cos 62.5 = 0.46
-20 to -15	-17.5	40-(-17.5) = 57.5	cos 62.5 = 0.54
-15 to -10	-12.5	40-(-12.5) = 52.5	cos 52.5 = 0.61
10 to 15	12.5	40-12.5 = 27.5	cos 27.5 = 0.89
15 to 20	17.5	40-17.5 = 22.5	cos 22.5 = 0.92
20 to 25	22.5	40-22.5 = 17.5	cos 17.5 = 0.95

Table 4.3 The photoelectron emission angles employed in depth profiling study.

The sampling depth (d_s) is directly proportional to the cosine of the photoelectron emission angle (θ) (Equation 4.1). Therefore, surface sensitivity increases with the increase in the value of θ.

$$d_s = 3\lambda \cos\theta \quad (4.1)$$

As the sample was rotated, the distance between the surface and analyser entrance slits was maintained (optimised with maximum counts), and a camera was used to maintain the analysis position on the surface ensuring that the X-ray beam was hitting the sample. Atomic concentrations are determined by employing RSFs for individual core levels, which are referenced from the work of Maniyarasu et al., specifically tailored for this HAXPES instrumentation [35]. Background subtraction was carried out using the Shirley model and GL(30) line shape was used to fit components using CasaXPS software.

4.2.8. NAP-XPS measurements

NAP-XPS measurements were carried out at the Henry Royce Facilities at the University of Manchester. The instrument was equipped with a SPECS Focus 500 monochromated Al Kα source with a photon energy of 1486.6 eV. The NAP-XPS kit was equipped with a SPECS 150 mm Phoibos 150 NAP hemispherical electron energy analyser, with a three-stage, differentially pumped electrostatic lens directly connected to the NAP cell. XPS measurements were conducted in two distinct environments: the first being a conventional ultrahigh vacuum (UHV) chamber and the second in a near-ambient pressure (NAP) cell connected to the entrance cone of the analyser lens system.

For the NAP-XPS experiments, the NAP cell was filled with H_2O vapor until it reached a stabilised pressure of approximately 4.5 mbar, which corresponded to a relative humidity (RH) of roughly 15%. The samples were exposed to water vapour for approximately 10 hours in the NAP cell and 25 scans were taken for each core level. These measurements were carried out under standard atmospheric conditions at a temperature of 25 ˚C. XPS spectra were recorded before, during and after exposure to water.

The BE values are charge-corrected with reference to the Sn $3d_{5/2}$ peak at 488.0 eV [36]. Calibrating to C 1s was avoided to counteract the ambiguity posed by the large spread in the BE values of the adventitious carbon. All BE values are reported with a precision of ±0.1 eV. Survey spectra are taken at a pass energy of 60 eV while the core level spectra are recorded at 30 eV pass energy. A Shirley background is subtracted from the data and the core-level spectra are fitted using the CasaXPS software, applying a GL(30) line shape. The built-in CasaXPS sensitivity factors (Kratos) are employed to determine the sample's stoichiometry from the integrated peak areas, both before and after exposure to water.

4.3. Results and Discussion

4.3.1. XPS Results

The C 1s XPS spectra for the two sets of samples (with and without a SnO_2 layer) are shown in Figure 4.6 (perovskite), Figure 4.7 (perovskite + $BMIMBF_4$) and Figure 4.8 (Perovskite + BMIMCl). In all the spectra, peaks fitted at 285.0 eV are attributed to hydrocarbon contamination [37]. The peaks fitted at 286.0 eV correspond to an aliphatic C-N bond. In the perovskite samples this could arise from the unreacted/dissociated precursor CH_3NH_3I (MAI) [38-40]. In the perovskite samples modified with ionic liquids (ILs), the 286.0 eV peak could also originate from the aliphatic C-N bond (C3 in Figure 4.5) within the BMIM group [38].

The peaks at 286.6 eV can be attributed to both the perovskite C-N bond (in the perovskite lattice) and the aromatic C-C-N carbons (labelled C2 in Figure 4.5) in the ionic liquids [41, 42]. The imidazolic N-C-N carbon (labelled C1 in Figure 4.5) exhibits a peak at 287.3 eV [38]. However, in pure perovskite samples, the peaks at 287.3 eV at 300 °C are likely associated with the formation of CH_3NH_2 due to the thermal decomposition of MAI (CH_3NH_3I) and perovskite. The peaks at 287.7 eV can be assigned to C=O groups formed due to surface oxidation of the sample [43]. Similarly, high energy peaks in the range of 288.5 eV to 289.5 eV can be assigned to the O-C=O group, indicating oxidative

decomposition [44-47]. All the peak assignments in the C1s spectra are tabulated in Table 4.4.

To ascertain that the peak assignments to IL and perovskite are not originating from surface hydrocarbon contamination, XPS survey spectra were analysed (see appendix 1). The oxygen concentration assigned to the peaks in the C 1s spectra aligns with the oxygen concentration calculated from these wide scans. Additionally, NEXAFS spectra, discussed later in this chapter (section 4.3.3), distinctly show peaks corresponding to both the IL and perovskite components, providing clear evidence of their presence in the samples. Furthermore, in separate experiments utilising NAPXPS (section 4.3.5), a perovskite peak was identified at a similar BE in freshly prepared perovskite films just prior to their introduction into the XPS chamber.

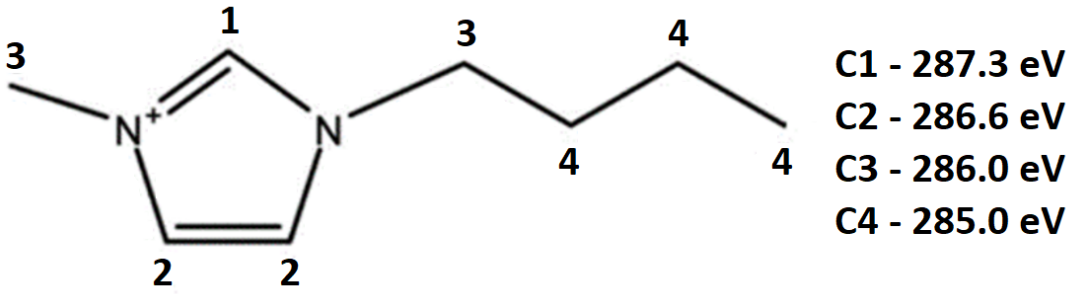

Figure 4.5 Chemical structure of the BMIM cation showing 4 distinct carbon environments labelled 1-4.

Binding Energy (eV)	Peak Assignment
285.0 eV	Adventitious carbon
286.0 eV	C-N in CH_3NH_3I or C3 in BMIM group
286.6 eV	C-N in Perovskite or C2 in BMIM group
287.3 eV	C-N in CH_3NH_2 or C1 in BMIM group
287.7 eV	C=O
288.5-289.5 eV	O-C=O

Table 4.4 C 1s peak assignments.

The C1s XPS spectra of the pure perovskite samples with SnO_2 (SnO_2/Perovskite) and without a SnO_2 layer (Perovskite) are shown in Figure 4.6 (a & b). The spectra before heating and after heating to temperatures of 100 °C and 150 °C are fitted with an adventitious carbon peak at 285 eV, a MAI peak at 286.0 eV, a perovskite C-N peak at 286.6 eV, a C=O peak 287.7 eV and an O-C=O peak at 289.2 eV. The spectra obtained after heating to 300 °C are fitted with an adventitious carbon peak at 285 eV, a MAI peak at 286.0 eV and a CH_3NH_2 peak at 287.3 eV.

As the temperature increases, the intensity of the MAI peak also rises in both samples, indicating the thermal degradation of the perovskite. At 300 °C, most of the hydrocarbon contamination is burnt off, leading to the disappearance of C-O peaks. The perovskite peak vanishes at 300 °C, while a CH_3NH_2 peak emerges at 287.3 eV, demonstrating the decomposition of MAI and perovskite into methylamine. Overall, both samples show very similar behaviour.

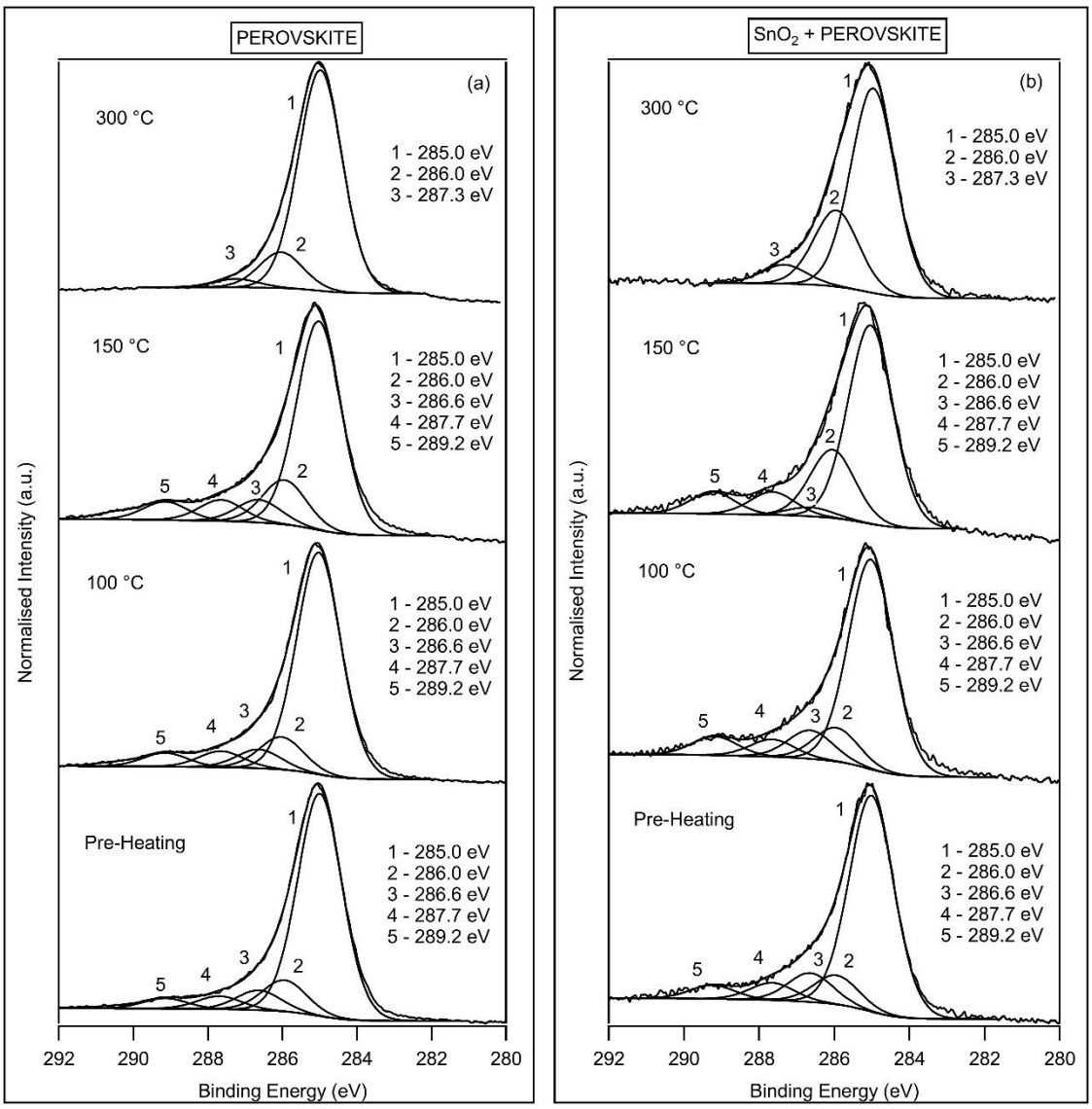

Figure 4.6 High-resolution C 1s core level XPS spectra of the pure perovskite samples deposited on (a) Ti foil (b) SnO_2 coated Ti foil. Peak intensities are normalised to the intensity of the adventitious carbon peak.

The XPS spectra of the $BMIMBF_4$-modified perovskite samples are depicted in Figure 4.7 (a-b). Before any heating, the spectra are characterised by distinct peaks at 285.0 eV, 286.0 eV, 286.6 eV, 287.3 eV, and 289.0 eV. As previously discussed, the 285.0 eV peak corresponds to adventitious carbon or aliphatic carbon originating from ionic liquids. The 286.0 eV peak is likely associated with the aliphatic C-N bond in the ionic liquid or unreacted/dissociated MAI from the perovskite. At 286.6 eV, we observe the perovskite C-N bond, which signifies the presence of perovskite material. Additionally, the 287.3 eV

peak can be attributed to the imidazolic N-C-N bond in the ionic liquid or CH_3NH_2, a product of MAI decomposition or perovskite degradation. Finally, at 289.0 eV, we detect the O-C=O bond, indicating the presence of oxygen-containing functional groups in the sample. The SnO_2/$BMIMBF_4$-Perovskite sample shows a more intense MAI/IL peak (286.0 eV) before heating.

Upon heating the samples to 100 °C, the peaks can still be fitted at the same BE positions. The $BMIMBF_4$-Perovskite sample exhibits a broadening of the spectrum towards the higher BE side. This results in the replacement of the 289.0 eV peak with two distinct peaks at 288.5 eV and 289.7 eV, indicating an increased level of sample oxidation. In contrast the SnO_2/$BMIMBF_4$-Perovskite sample doesn't show any significant change in the spectral shape after heating to 100 °C.

Upon heating the samples to 150 °C, the peaks are still fitted at the same BEs. The SnO_2/$BMIMBF_4$-Perovskite sample shows a broadening in the spectrum and consequently a higher intensity of all the components relative to the adventitious carbon peak while the $BMIMBF_4$-Perovskite sample shows a narrowing of the spectral shape exhibiting a decrease in the intensity of the perovskite peak at 286.6 eV. In contrast, the SnO_2/$BMIMBF_4$-perovskite sample maintains a peak of nearly constant intensity up to 150 °C and even at 300 °C.

When the sample is subjected to a higher temperature of 300 °C, more significant changes become apparent. In the $BMIMBF_4$-Perovskite sample, the perovskite peak at 286.6 eV completely disappears and low BE peaks at 282.3 eV and 283.7 eV emerge. In the SnO_2/$BMIMBF_4$-Perovskite sample, the perovskite peak can still be fitted at 286.6 eV, but a low BE peak is also observed at 282.3 eV (note that these additional low energy peaks at 300 °C change the numbering in Figure 4.7 compared to the other temperatures). These new features are indicative of boron-carbide bonds, suggesting alterations in the chemical structure of the sample under the influence of higher temperatures [48].

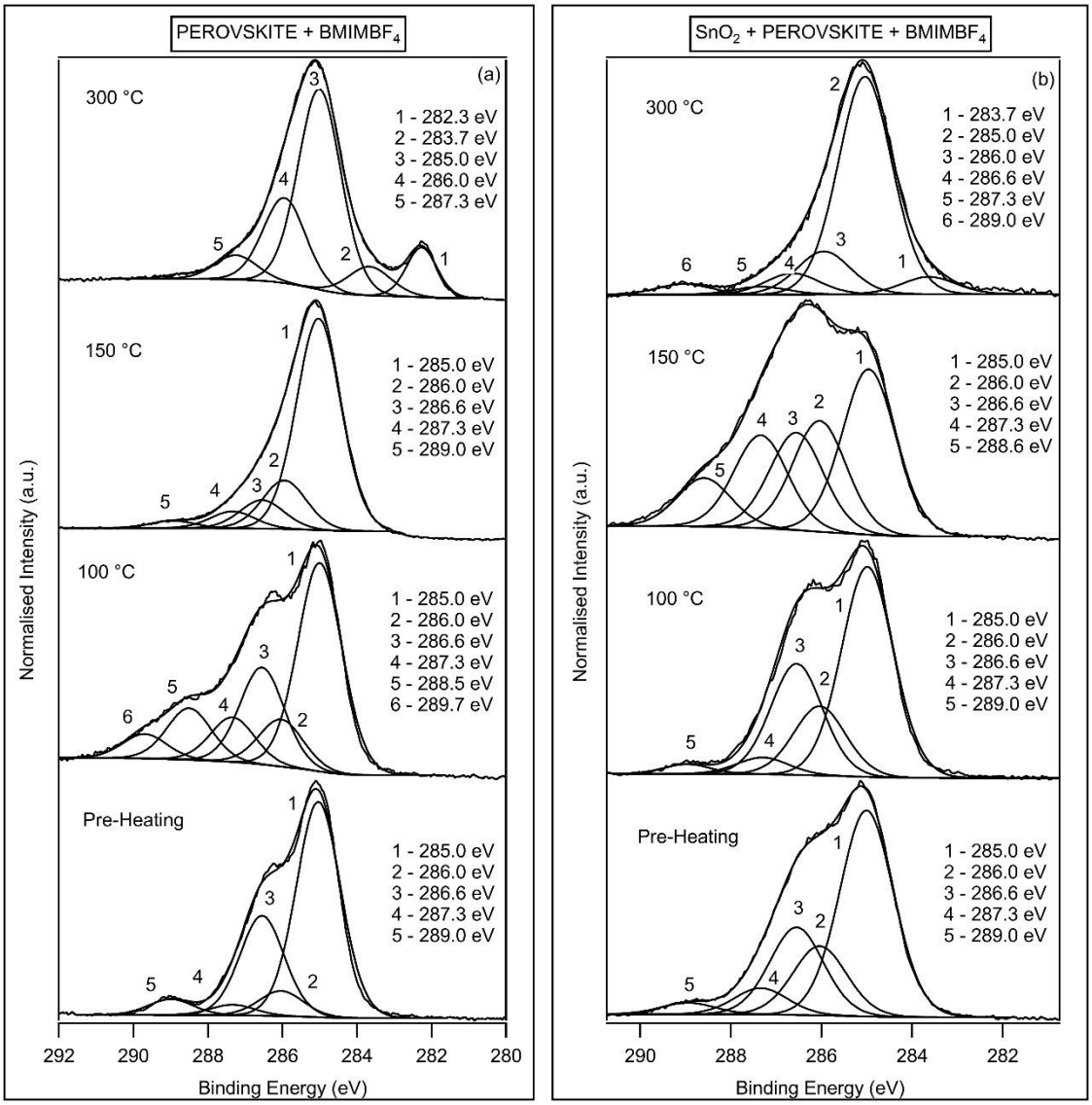

Figure 4.7 High-resolution C 1s core level XPS spectra of the $BMIMBF_4$ perovskite samples deposited on (a) Ti foil (b) SnO_2 coated Ti foil. Peak intensities are normalised to the intensity of the adventitious carbon peak.

The C1s XPS spectra of the BMIMCl-modified perovskite samples are presented in Figure 4.8 (a-b). In the BMIMCl-Perovskite sample, a broad, unresolved peak at higher than expected binding energy is observed before heating. During the synchrotron experiment, several unsuccessful attempts were made to re-measure this spectrum. The pure BMIMCl IL is a crystallised solid at room temperature and we believe this might cause the BMIMCl-Perovskite film to be more susceptible to charging under the X-ray beam. Sample charging of ionic liquids during XPS studies is a problem that has been

previously reported [49]. It is interesting that the SnO_2/BMIMCl-Perovskite sample does not show this charging behaviour before heating which might be indicative of the role played by SnO_2 in preventing the accumulation of charges at the surface by facilitating the incorporation of the ionic liquid into the perovskite matrix.

Upon heating the samples to 100 °C the BMIMCl-Perovskite sample shows a spectrum that can be fitted with peaks at 285.0 eV, 286.0 eV, 286.6 eV, and 287.3 eV. An increase in the temperature appears to solve the sample charging problem. A possible explanation is that heating the sample has aided the incorporation of BMIMCl into the perovskite lattice. The SnO_2/BMIMCl-Perovskite sample shows peaks at 285.0 eV, 286.0 eV, 286.6 eV, and 287.3 eV after heating to 100 °C. All these peaks share the same assignments as those in the $BMIMBF_4$-modified sample. The BMIMCl-Perovskite sample shows a more intense MAI/IL (286.0 eV) peak compared to the SnO_2/BMIMCl-Perovskite sample after heating to 100 °C, possibly showing less incorporation of the IL into the perovskite as compared to the sample with SnO_2.

When the samples are heated to 150 °C, a notable decrease in the intensity of the peak at 286.0 eV is observed in the BMIMCl-Perovskite sample. This reduction potentially signifies the ongoing incorporation of the ionic liquid into the perovskite structure, a process seemingly facilitated by the increasing temperature. In contrast, the SnO_2/BMIMCl-Perovskite sample exhibits an increase in the intensity of the 286.0 eV peak.

The spectra recorded for the BMIMCl-Perovskite sample after heating to 300 ˚C could not be fitted with a peak at 286.6 eV (the shape of the spectrum changes subtly from 150 ˚C and the fit couldn't be reasonably forced in the software).This could signify the degradation of the perovskite under the influence of the elevated temperature. However, all other peaks previously fitted in the spectra at 150 °C remain unchanged in the spectra obtained at this higher temperature. In contrast, the SnO_2/BMIMCl-Perovskite sample spectra could still be fitted with a perovskite peak after heating to 300 ˚C. All other peaks remained consistent with those fitted in the spectra obtained at 150 °C. The presence of the perovskite peak until 300 ˚C in both SnO_2/IL-modified

perovskite samples suggests that the SnO_2 layer may help to preserve the IL-modified perovskite films, even under higher thermal stress.

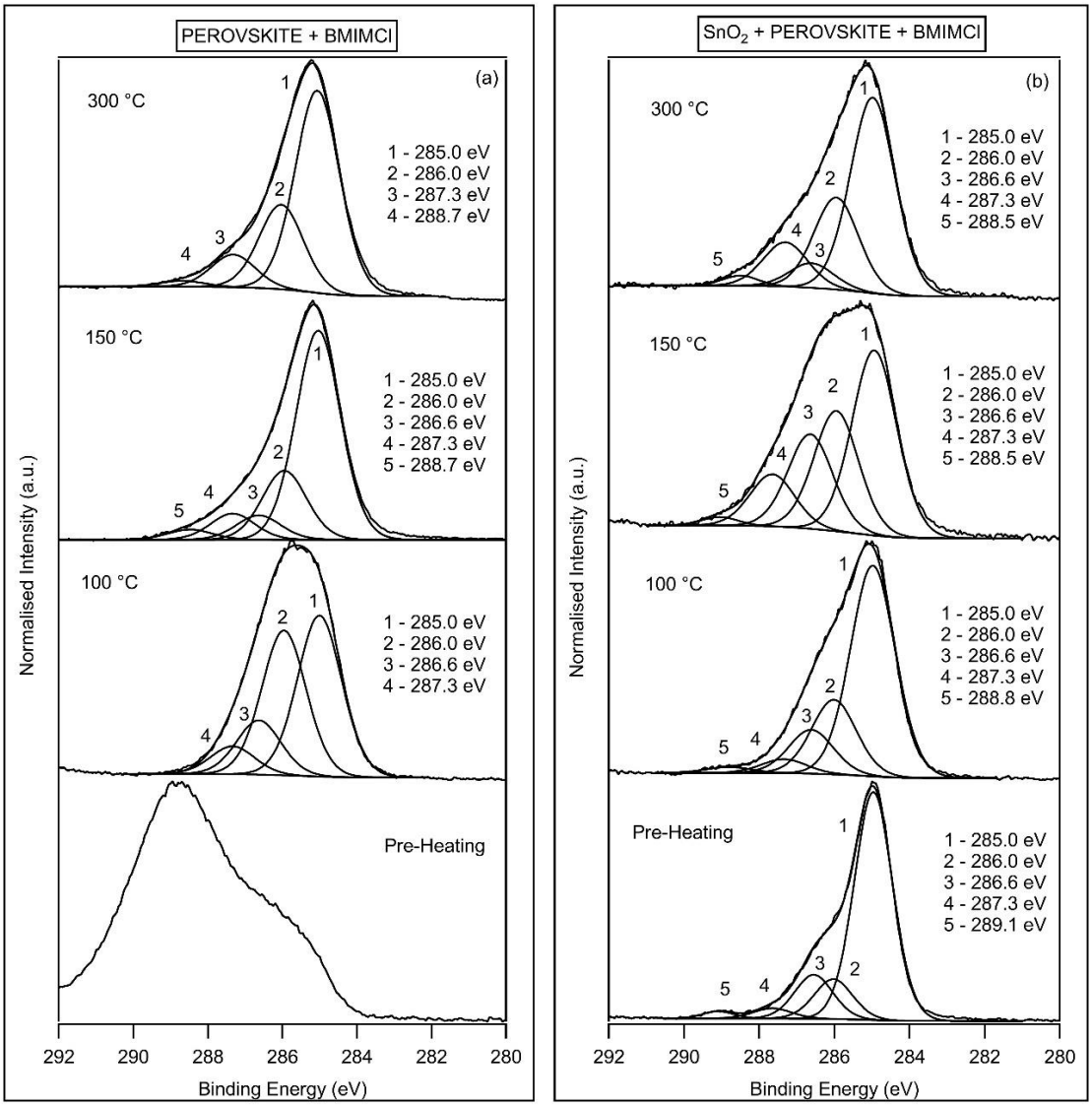

Figure 4.8 High-resolution C 1s core level XPS spectra of the BMIMCl perovskite samples deposited on (a) Ti foil (b) SnO_2 coated Ti foil. Peak intensities are normalised to the intensity of the adventitious carbon peak.

Figure 4.9 (a-f) illustrates the I 4d spectra of the six samples. Each sample graph shows spectra taken at the three temperature settings, which have been overlayed to highlight the temperature-dependent variations. It is important to note that the peak heights have been modified to allow stacking of the axes and do not reflect the peak intensities. The two peaks observed result from the spin−orbit splitting (splitting energy = ~2.0 eV)

of the d orbital and are assigned to I $4d_{3/2}$ and I $4d_{5/2}$. The perovskite I $4d_{5/2}$ peak position has previously been reported at ~49.5 eV [37, 50]. The BE values exhibit relatively stable behaviour as the samples are heated to 100 °C. However, a noticeable, non-uniform shift in the BE values becomes apparent as the temperature is raised to 150 °C, ranging from 48.7 eV to 49.5 eV. In contrast, a clear upward shift in BE values is observed when the temperature is raised to 300 °C.

At 300 °C, the I $4d_{5/2}$ peak position is measured at 50.0 eV for both perovskite samples (a & b), at 50.4 eV for the $BMIMBF_4$-Perovskite sample, at 49.8 eV for the SnO_2/$BMIMBF_4$-Perovskite sample, at 49.9 eV for BMIMCl-Perovskite sample and at 49.7 eV for the SnO_2/BMIMCl-Perovskite sample. These shifts in BE values towards higher energy levels indicate a change in the chemical environment of iodine as it dissociates from the $(PbI_6)^{-4}$ octahedra that constitute the perovskite crystal lattice. Of particular interest is the observation that the SnO_2/IL-modified perovskite samples (d & f) exhibit the smallest increase in BE after heating to 300 °C.

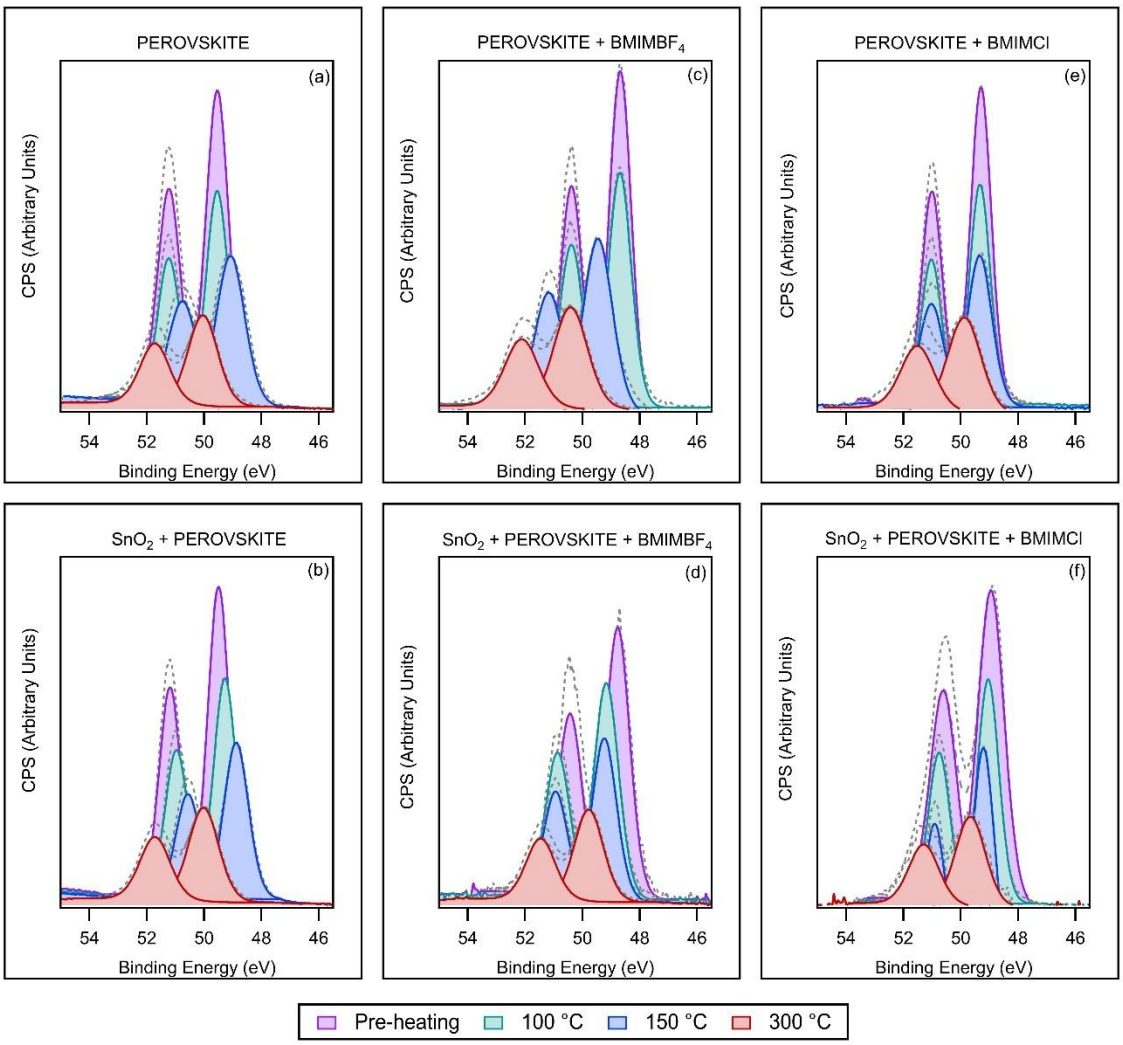

Figure 4.9 High-resolution I 4d core level XPS spectra of pristine (a-b) and ionic liquid-modified perovskite (c-f) samples deposited on Ti foil (a, c & e) and SnO_2 coated Ti foil (b, d &f). The dotted lines represent the raw data and the coloured areas represent the fitted components.

The Pb 4f core level XPS spectra are displayed in Figure 4.10 (a-d)(we were unable to record Pb 4f spectra for all of the samples). These spectra have been fitted with two sets of doublets corresponding to chemical environments Pb^{+2} and Pb^0. The $4f_{7/2}$ & $4f_{5/2}$ components of each doublet have a spin-orbit splitting of approximately 4.87 eV. The Pb^{+2} corresponds to the state of lead in the perovskite while Pb^0 represents metallic lead formed as a result of the degradation of the perovskite. The spectra for the SnO_2/$BMIMBF_4$-Perovskite and BMIMCl-Perovskite samples were very challenging to fit,

primarily due to the broadening of spectra. This could be due to the sample charging under the X-ray beam.

The Pb $4f_{7/2}$ peaks corresponding to the perovskite lattice have been documented in prior studies to fall within the range of 138.5 – 138.9 eV [37, 41, 42, 50-53]. Figure 4.10 (a) shows the Pb 4f spectra for the Perovskite sample. Before heating, the spectrum shows two sharp doublets peaks at 138.7 eV and 143.6 eV, which can be indexed to Pb $4f_{7/2}$ and Pb $4f_{5/2}$ states of Pb^{+2} in the perovskite phase. In addition, weak shoulders can be identified at 136.8 eV and 141.6 eV which are attributed to metallic Pb (Pb^0) [50, 54-56]. Following heating up to 100 °C, these peaks remain essentially unaltered. After further heating to 150 °C, the Pb^{+2} peaks undergo a slight -0.2 eV shift, although they still fall within the previously mentioned perovskite peak range. This downward shift can be attributed to a certain extent of sample oxidation resulting from the increased temperature. After heating to 300 °C, the Pb 4f spectrum has much lower intensity and cannot be easily resolved into distinct peaks.

The Pb 4f core level spectra of the SnO_2/Perovskite sample are shown in Figure 4.10 (b). Prior to heating, the spectrum can be resolved into two well-defined perovskite Pb^{+2} doublet peaks at 138.7 eV and 143.5 eV and smaller, less pronounced doublet peaks at 136.8 eV and 141.7 eV, consistent with the metallic Pb^0 state. Upon increasing the temperature to 100 °C and 150 °C, the Pb^{+2} undergoes a BE shift of -0.2 eV and -0.5 eV, respectively, gradually approaching the Pb-O BE value of 138.0 eV [50]. This shifting in the BE indicates the formation of oxidised products like lead oxide and lead carbonate. Additionally, Pb^0 doublets can be discerned at 136.7 eV and 141.5 eV at both 100 °C and 150 °C. Similarly, to the Perovskite sample, the spectrum at 300 °C could not be easily resolved.

The Pb 4f spectra of the SnO_2/$BMIMBF_4$-Perovskite sample exhibit doublet peaks at 138.7 eV and 143.5 eV accompanied by a weaker contribution at 136.8 eV and 141.6 eV. The more intense doublet is assigned to Pb^{+2} in the perovskite, while the less intense doublet is attributed to Pb^0. With an increase in temperature to 100 °C and 150 °C, the Pb^{+2} doublet experiences a downward shift to 138.5 eV and 143.3 eV, whereas the Pb^0

doublet remains unchanged. Intriguingly, at 300 °C, the Pb^{+2} doublet shifts back very close to its pre-heating position, being identified at 138.8 eV and 143.7 eV, accompanied by the Pb^{0} doublet at the same energy level. These findings align well with the C 1s and I 4d spectra, which also indicate the presence of perovskite at 300 °C in the SnO_2/$BMIMBF_4$-Perovskite sample.

The Pb 4f peaks for the BMIMCl-Perovskite sample are presented in Figure 4.10 (d). The spectrum before heating could not be resolved into distinct components due to broadening that we attribute to sample charging (similarly to the C 1s spectrum for the same sample). However, the spectrum recorded at 100 °C reveal two doublets at 138.9 eV and 143.8 eV, as well as 136.8 eV and 141.7 eV, corresponding to Pb^{+2} (in perovskite) and Pb^{0}, respectively.

Notably, as the temperature is increased to 150 °C, the Pb^{0} doublet experiences a significant reduction in intensity relative to the Pb^{+2} doublet. The Pb^{+2} doublet undergoes a slight binding energy (BE) shift of -0.1 eV. Upon further increasing the temperature to 300 °C, the Pb^{+2} doublet vanishes, leaving only the Pb^{0} doublet, which signifies the complete degradation of the perovskite. This is in good alignment with the observation made in the C 1s spectra where a perovskite peak (286.6 eV) could not be fitted in the spectra of the BMIMCl-Perovskite sample at 300 °C.

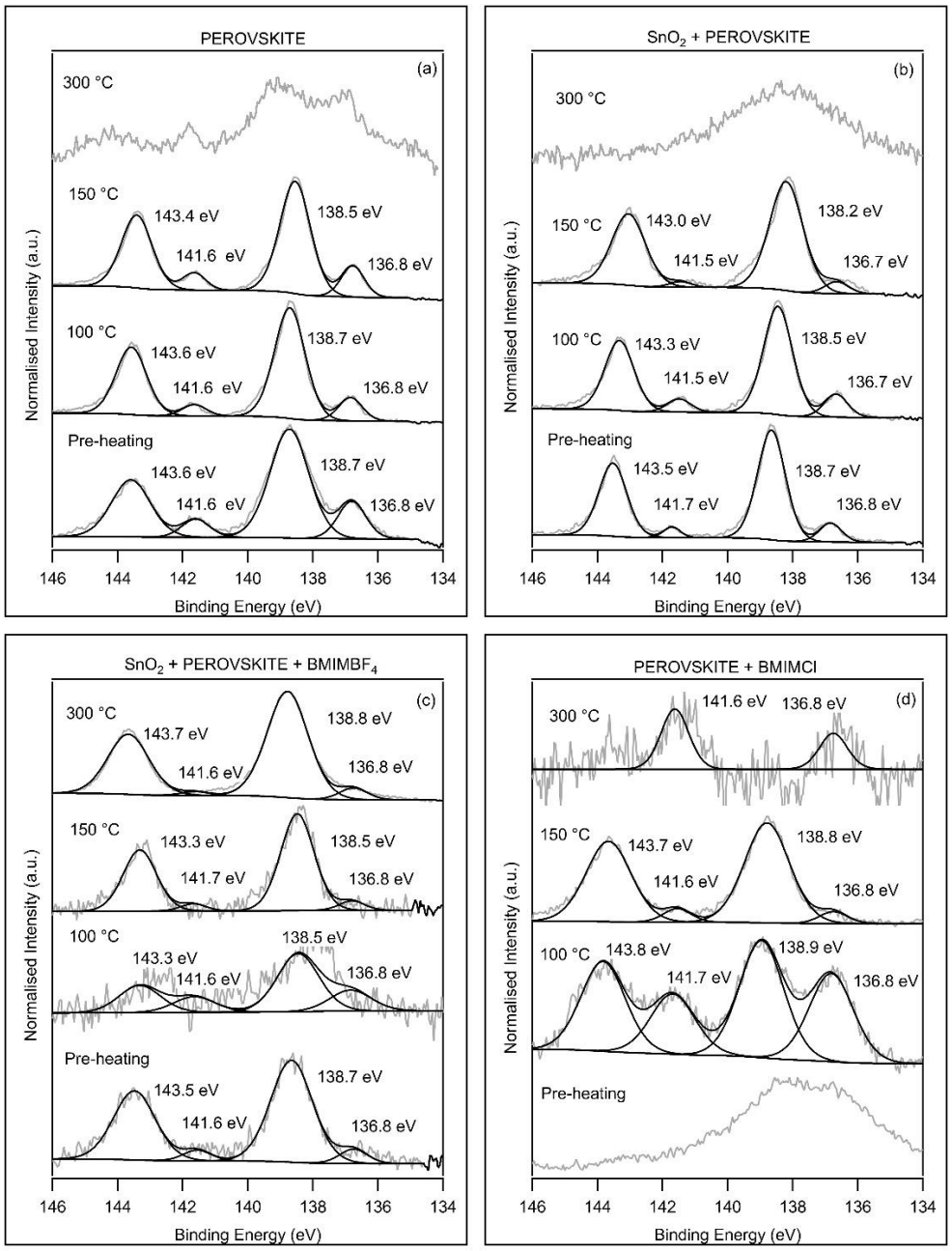

Figure 4.10 High-resolution Pb 4f core level XPS spectra of (a) pristine perovskite on Ti foil (b) pristine perovskite on SnO_2-coated Ti foil (c) $BMIMBF_4$-modified perovskite on SnO_2-coated Ti foil (d)BMIMCL-modified perovskite on Ti foil.

As highlighted in the introduction, an ongoing debate persists regarding the inclusion of chlorine within the perovskite lattice. Numerous studies have put forth the contention that chlorine is not integrated into $MAPbI_3$ [28]. Moreover, even within studies

purporting the presence of chlorine, certain instances failed to detect it using XPS due to the instrument's stringent detection limits [26, 57].

The Cl 2p XPS spectra of our samples are shown in Figure 4.11 a-f. In all the spectra, a discernible Cl 2p peak is unequivocally evident. The Cl 2p XPS spectra reveal a characteristic doublet structure, encompassing Cl $2p_{3/2}$ and Cl $2p_{1/2}$ components with a spin-orbit splitting energy of 1.6 eV.

For reference, Philippe et al. detected the Cl $2p_{3/2}$ component of $MAPbCl_3$ at 198.5 eV and the residual $PbCl_2$ Cl $2p_{3/2}$ at 198.9 eV in their mixed halide perovskite sample [37]. Conversely, other studies have attributed peaks at 196.6 and 197.6 eV to the Cl $2p_{3/2}$ component within the perovskite structure [27, 58]. Two of our samples also contain a chlorine contribution from the ionic liquid BMIMCl. The $Cl2p_{3/2}$ peak for this ionic liquid has previously been observed at approximately 198.8 eV [59].

In our samples, peaks fitted within the range of 197.5 to 198.5 eV have been assigned to the perovskite structure, while peaks in the range of 198.9 to 199.4 eV have been attributed to inorganic chloride (Cl^-). The latter can result from unreacted or decomposed $PbCl_2$, as well as from BMIMCl in the BMIMCl-modified perovskite samples. The range of 199.9 to 200.9 eV corresponds to organic chlorine, which may arise from the formation of CH_3NH_3Cl during the thermal degradation of perovskites.

In Figure 4.11, the doublet assigned to the perovskite structure is depicted by green peaks, the inorganic chloride by red peaks, and the organic chlorine by blue peaks. The $BMIMBF_4$-Perovskite sample also contain boron from the BF_4^- anion. B 1s peaks have a similar BE to the Cl 2p peaks, so the BE window was widened when taking XPS measurements to show both Cl 2p and B 1s in the same spectrum. The B 1s peaks are depicted by yellow peaks in Figure 4.11.

The Perovskite sample (Figure 4.11a) shows distinct Cl 2p doublet peaks (198.4 – 198.5 eV) originating from the perovskite structure up to a temperature of 150 °C. As the temperature rises from 150 °C to 300 °C, these peaks shift to 198.9 eV, indicative of the detachment of chlorine from the perovskite lattice, potentially leading to the formation

of $PbCl_2$. It is worth noting that some studies have put forth evidence for the presence of chlorine anions in the form of porous PbICl, which could also contribute to the inorganic chlorine peaks [27]. In addition to these peaks, a Cl 2p doublet centred at 200.6 eV and 202.2 eV is observed, and this is attributed to the existence of organic chlorine.

Conversely, the SnO_2/Perovskite sample (Figure 4.11b) does not show the presence of organic chlorine in any of the spectra. Much like the Perovskite sample, it displays perovskite peaks up to a temperature of 150 °C, after which these peaks shift to higher binding energies to align with inorganic chloride anion peaks.

The Cl 2p spectra of the BMIMCl-Perovskite sample are presented in Figure 4.11c. Prior to heating, the spectra exhibit a well-defined doublet at 198.1 eV and 199.7 eV, along with a weak shoulder at 198.9 eV and 200.5 eV, which can be attributed to the perovskite and inorganic chloride (from the IL), respectively.

As the temperature increases from 100 °C to 150 °C, the intensity of the perovskite peak decreases, while the inorganic chloride peaks intensify and become the dominant features. Additionally, organic chlorine peaks become noticeable. Upon further raising the temperature to 300 °C, the perovskite peaks vanish completely, the inorganic chloride peaks continue to grow in intensity, and the organic chlorine doublet decreases in intensity. This reduction in organic chlorine is consistent with oxidation at this elevated temperature, which impacts the organic components.

In contrast, the SnO_2/BMIMCl-Perovskite sample (Figure 4.11d) exhibits distinct perovskite doublet peaks up to 150 °C. This is accompanied by a less intense inorganic chloride doublet and a very subtle organic chlorine doublet up to 150 °C. As the temperature rises from 150 °C to 300 °C, the intensity of the inorganic chloride doublet increases, but a lower-intensity perovskite doublet can still be discerned at 300 °C. This observation aligns with the C 1s spectra, where it was possible to identify a perovskite peak at 300 °C.

The Cl 2p and B 1s XPS spectra of the $BMIMBF_4$-Perovskite sample and SnO_2/$BMIMBF_4$-Perovskite sample, are illustrated in Figure 4.11e and Figure 4.11f, respectively. In the

$BMIMBF_4$-Perovskite sample, a distinct B 1s peak at 193.9 eV is evident both before and after heating to 100 °C, with no Cl 2p peaks. This B 1s peak is attributed to the presence of the BF_4^- ion within the ionic liquid.

Notably, as the temperature is increased to 150 °C, the Cl 2p doublet peaks abruptly emerge at 198.5 eV and 200.1 eV, while the B1s peak shifts to a lower binding energy value of 192.1 eV. The appearance of the Cl 2p peaks corresponds to the perovskite structure, and the shift in B 1s suggests a modification in the chemical environment of boron within the sample. With a further temperature increase to 300 °C, the Cl 2p undergoes a BE shift of approximately +0.4 eV, indicative of the release of chlorine in the form of chloride anions.

In the SnO_2/$BMIMBF_4$-Perovskite sample (Figure 4.11f), a sharp B1s peak is discernible up to 150 °C, with no Cl 2p peaks observed up to the same temperature. Upon heating the sample to 300 °C, the B 1s peak broadens and shifts to a lower BE position (192.4 eV), and Cl 2p peaks suddenly emerge. The Cl 2p spectra can be deconvoluted into a higher-intensity inorganic chloride doublet (at 198.9 eV and 200.5 eV) and a lower-intensity perovskite doublet at 198.5 eV and 200.1 eV. This result aligns with the observations in the Pb 4f spectra, where we noted a shift of the peak back to its pre-heating position at 300 °C, suggesting a possible regeneration of the perovskite structure.

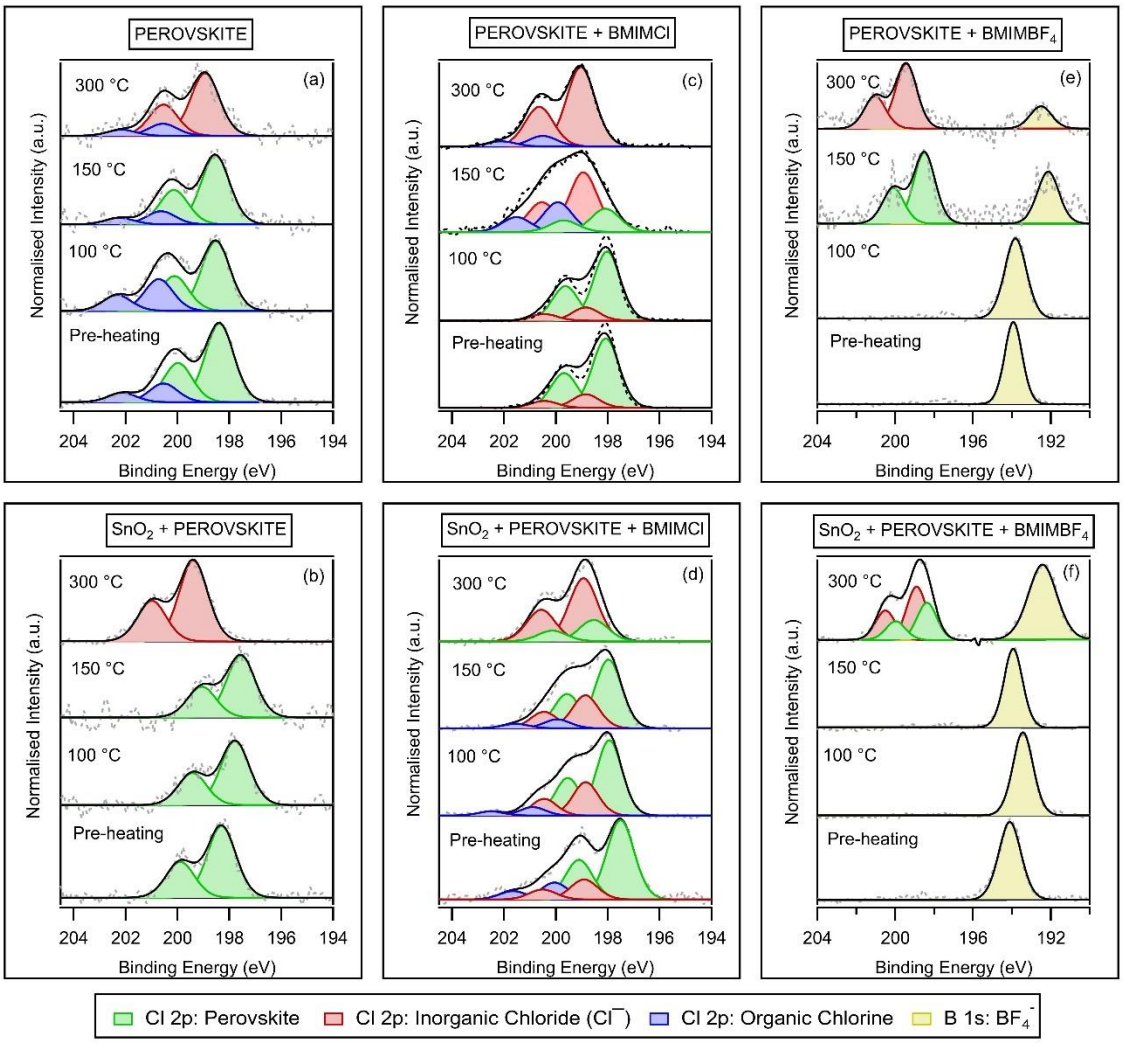

Figure 4.11 High-resolution Cl 2p core level XPS spectra of pristine (a-b) and ionic liquid-modified perovskite (c-f) samples deposited on Ti foil (a, c & e) and SnO_2 coated Ti foil (b, d &f).

The Perovskite and SnO_2/Perovskite samples exhibit similar responses when subjected to thermal stress. Following heating to 300 °C, neither sample displayed a detectable perovskite peak in their C 1s or Cl 2p spectra. Both samples demonstrated a broad unresolved peak in their Pb 4f spectra, accompanied by a corresponding high BE shift in their I 4d spectra after the same heat treatment at 300 °C. The XPS analysis suggests that both samples undergo complete degradation upon heating to 300 °C.

The thermal stability comparison between the SnO_2/BMIMCl-Perovskite sample and the BMIMCl-Perovskite sample reveals a superiority in the sample with a SnO_2 layer. This is evident from the presence of a perovskite peak in both the C 1s (286.6 eV) and Cl 2p spectra (green component in Figure 4.11) after heating the sample to 300 °C. In contrast, neither the C 1s nor the Cl 2p spectra of the BMIMCl-Perovskite sample exhibited identifiable perovskite peaks after heating to 300 °C. Furthermore, a notable shift towards higher BE in the I 4d spectra after heating to 300 °C, can be observed in the BMIMCl-Perovskite sample, which contrasts with the SnO_2/BMIMCl-Perovskite sample. This shift indicates thermal degradation at the elevated temperature in the BMIMCl-Perovskite sample, which is also supported by the presence of only metallic lead peaks in its Pb 4f spectra.

Analysis of the two $BMIMBF_4$-modified samples also suggest the SnO_2/Perovskite-$BMIMBF_4$ shows greater promise in terms of thermal stability. The $BMIMBF_4$/Perovskite sample retains the peak assigned to perovskite until 150 °C but does not exhibit a perovskite peak following heating to 300 °C in the C 1s (286.6 eV) and Cl 2p spectra (green component in Figure 4.11). Additionally, a significant shift occurs in the doublet peaks towards higher BE in the I 4d spectra after the sample is heated to 300 °C, suggesting degradation of the perovskite. In contrast, the SnO_2/Perovskite-$BMIMBF_4$ sample retains a perovskite peak even after being heated to 300 °C, evident in the C 1s (286.6 eV), Pb 4f (138.8 eV and 143.7 eV), and Cl 2p spectra (green component in Figure 4.11).

4.3.2. Work function results

Work function (ϕ) measurements were taken using XPS to further examine the impact of ionic liquids on the electronic properties of the perovskite. The work function of the sample represents the minimum energy required to move an electron from the sample to the vacuum level just above the surface [60]. A material's work function can be determined by analysing the kinetic energy (E_{kin}) distribution of photoelectrons emitted during XPS.

The low E_{kin} region of the XPS spectrum, primarily composed of inelastically scattered electrons (secondary electrons), presents a high-intensity tail with a sharp cut-off. This point of cut-off, known as the Secondary Electron Cut-off (SECO), corresponds to electrons with just enough energy to escape the sample and is vital for work function determination.

Understanding a material's work function is valuable as it provides insight into the absolute energy level of electrons relative to vacuum energy. This knowledge is especially crucial in devices with hetero-structured interfaces, such as solar cells, where energy level discrepancies between materials significantly impact device performance and optimisation. Unlike most other semiconductors, halide perovskites are quite defect tolerant. Defects mostly originate at the grain boundaries and surfaces leading to interfacial recombination at the heterojunctions between the perovskite and other materials in the device [61].

For our measurements, the SECO spectra for the samples were recorded using a 50 eV photon energy X-ray beam while applying a negative bias (~9 V, measured precisely using a multimeter for every work function measurement) to the samples. This bias served two main purposes. Firstly, it provided the additional energy required for electrons to overcome the detector's work function (photoelectrons produced with 0 kinetic energy are pushed out of the sample and into the analyser). Secondly, it helped distinguish the sample's SECO from any additional SECO that might result from electrons emitted by the analyser walls.

The applied bias is subtracted from the measured kinetic energy values, and the SECO spectra are plotted for all samples, as shown in Figure 4.12 (a-f). The subtraction of the applied bias enables the direct extraction of work functions from the SECO spectra, determined by the linear extrapolation of the secondary edge slope to the kinetic energy axis.

The SECO spectra of the SnO_2/Perovskite and Perovskite samples are depicted in Figure 4.12-a & Figure 4.12-b, respectively. The work function values of the perovskite closely

align with the literature-reported value of ~3.90 eV [62]. The SnO_2/Perovskite sample exhibits a ϕ value of 4.1 eV before heating. This value remains constant at 4.1 eV up to 150 °C, then slightly decreases to 4.0 eV after heating the sample to 300 °C. Similarly, the Perovskite sample also maintains a constant ϕ value of 4.0 eV until 150 °C, after which it decreases to 3.7 eV when heated to 300 °C.

This decrease in the ϕ values after heating the samples to 300 °C may be attributed to the thermal decomposition of the perovskite as observed in the XPS analysis. The nearly constant ϕ values in the SnO_2 coated sample suggest that SnO_2 serves as an effective electron transport layer.

Previous studies on the modification of electron transport layers (ETLs) with ionic liquids (ILs) have reported a reduction in the ϕ of ETLs [22, 63, 64]. This reduction is attributed to the introduction of dipoles on the ETL surface by the ILs. Noel et al. reported a reduction in ϕ of both the SnO_2 ETL as well as the perovskite layer due to the doping of $BMIMBF_4$ in SnO_2. However, they associated the reduction in the perovskite ϕ to the shifting of the SnO_2 ϕ and could not identify any change in ϕ without the SnO_2 layer.

The SECO spectra of the BMIMCl-modified perovskite samples are illustrated in Figure 4.12-c and Figure 4.12-d. Prior to heating, the BMIMCl-Perovskite sample has the same ϕ as the pure perovskite sample at 4.0 eV. Upon increasing the temperature to 100 °C, the ϕ reduces to 3.4 eV. This shows that heating is important for the interaction of BMIMCl with the perovskite. The ϕ decreases further to 3.1 eV as the temperature is increased to 150 °C. However, upon increasing the temperature to 300 °C, the ϕ increases slightly to 3.4 eV. The SnO_2/BMIMCl-Perovskite sample demonstrates a lower ϕ of 3.8 eV up to 100 °C, decreasing further to 3.2 eV as the sample is heated to 150 °C, and subsequently rising to 3.5 eV with further heating to 300 °C.

The SECO spectra of the $BMIMBF_4$-modified perovskite samples are shown in Figure 4.12 (e-f). Prior to heating, both samples show a ϕ of 3.7 eV, lower than that measured for the pure perovskite and BMIMCl-modified perovskite samples. For the $BMIMBF_4$-Perovskite sample, the ϕ decreases to 3.4 eV and 3.2 eV after heating the sample to 100

°C and 150 °C, respectively. Upon further increasing the temperature to 300 °C, the ϕ undergoes an upwards shift to 3.6 eV, similarly to the BMIMCl samples. In contrast, the SnO_2/$BMIMBF_4$-Perovskite sample exhibits a consistent ϕ of 3.7 eV up to 100 °C. Beyond this point, the ϕ decreases to 3.4 at 150 °C and subsequently rises to 4.0 eV upon heating the sample to 300°C.

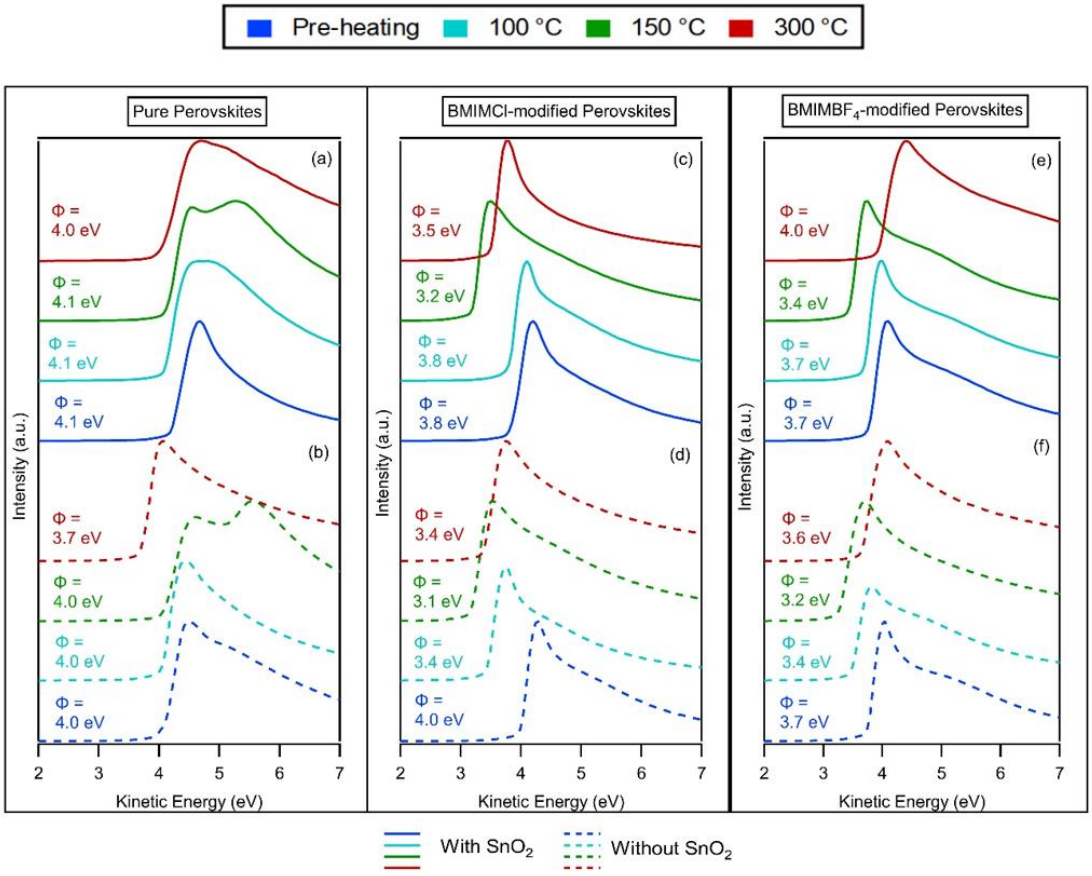

Figure 4.12 SECO spectra and corresponding work function values of samples before and after heating. Solid lines represent the samples with a SnO_2 layer while the dashed lines represent samples without the SnO_2 layer.

We attribute the reduction in work functions to the interaction between the ionic liquids and the perovskite and/or the substrate. In the case of the $BMIMBF_4$-modified samples, the BF_4^- anions can effectively bind to the hydroxyl groups present on the substrate surface, passivating the substrate/perovskite interface, as demonstrated by Zhang et al. in the case of KBF_4 [23]. By doing so, these anions remove some of the under-coordinated sites at the substrate/perovskite interface, which are known to be where

photogenerated charge carriers are often trapped and lost to nonradiative recombination.

We hypothesise that the $BMIM^+$ cations, being relatively large, do not intercalate into the perovskite lattice. Instead, they form a cascade around the perovskite surface, with $BMIM^+$ cations pointing away from the surface. Imidazolium based ILs have been shown to form a layer of cations at the IL-vacuum interface with alkyl chains of the cations facing outwards towards the vacuum [38]. It is well-established that a positive surface dipole decreases the work function [65]. This spontaneous dipolar polarisation, caused by the interaction of the BF_4^- anions with the substrate and the cascading effect of the $BMIM^+$ cations, collectively reduce the effective work function of the $BMIMBF_4$-modified samples.

The thermal energy from heating the samples facilitates the bonding between BF_4^- ions and the substrate. As a result, we observe a decrease in work function as the sample is heated to 150 °C in the $BMIMBF_4$-modified samples. However, as the temperature increases to 300 °C, the BF_4^- ions disassociate from the substrate and diffuse to the surface, neutralising the dipole. This leads to an increase in the work function of the $BMIMBF_4$-modified samples after heating to 300 °C. The sudden appearance of Cl 2p peaks at 150 °C and 300 °C for the $BMIMBF_4$-modified samples stems from this disruption of the $BMIM^+$ overlayer, exposing the chlorine within the perovskite lattice as shown in section 4.3.1.

The migration of BF_4^- ions also explains the shift of the B 1s peaks to a lower binding energy for the $BMIMBF_4$-modified samples after heating to 150 °C and 300 °C in the XPS measurements as shown in section 4.3.1. It requires a much higher temperature for the BF_4^- ions to break free from the SnO_2 surface compared to the Ti substrate due to a stronger interaction with SnO_2 facilitated by its oxygen atoms. As a result, the Cl 2p peaks are only observed after the SnO_2/$BMIMBF_4$-Perovskite sample is heated to 300 °C, whereas they appear at 150 °C in the $BMIMBF_4$-Perovskite sample without SnO_2. The sudden appearance of the low BE boron-carbide peaks at 300 °C in the C 1s spectra of the $BMIMBF_4$-modified samples can also now be better understood. As the BF_4^- ions

detach from the substrate and begin to interact with the $BMIM^+$ cascade, it leads to the formation of bonds between BF_4^- boron atoms and the surface carbon atoms. This results in the appearance of low BE C 1s peaks in the samples modified with $BMIMBF_4$.

In the case of BMIMCl-modified samples, the reduction in work functions could be due to the chemical passivation of the perovskite film itself. This might result from the absence of spontaneous dipole polarisation, as there is poor interaction between Cl^- ions and the substrate, which prevents the formation of a $BMIM^+$ cascade.

We hypothesise that in the BMIMCl-modified samples, the $BMIM^+$ cations diffuse into the perovskite grain boundaries, leading to an improvement in the crystallinity of the perovskite films. This in turn reduces lattice stress and results in a lower work function. This explanation also aligns with the detection of perovskite chlorine peaks in the Cl 2p spectra of the SnO_2/BMIMCl-Perovskite sample at every stage of the heating process.

The work functions of the BMIMCl-modified samples show a similar decreasing trend as the $BMIMBF_4$-modified samples, decreasing up to 150 °C and then rising as the temperature is increased to 300 ˚C. The diffusion of $BMIM^+$ cations into the perovskite grain boundaries is facilitated as the temperature is increased to 150 °C, decreasing the work function. However, heating to 300 °C increases the work function, possibly indicating some thermal degradation. It must be noted that the magnitude of work function increase after heating the samples to 300 °C is smaller in the BMIMCl-modified samples as compared to the $BMIMBF_4$-modified samples. This could be due to the absence of the $BMIM^+$ cascade in the BMIMCl-modified samples. The constant values of work function up to 100 °C in all the samples deposited on SnO_2 shows the effectiveness of SnO_2 in preventing the perovskite lattice stress, which can be induced by the difference in the thermal expansion coefficients of the perovskite and the Ti substrate. These results offer important insights into the stability of perovskite films modified with ionic liquids.

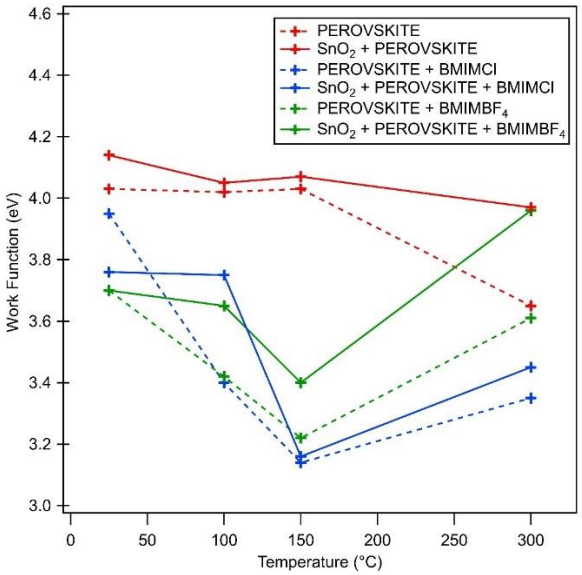

Figure 4.13 Measured work function values of the perovskite, BMIMCl-modified perovskite and $BMIMBF_4$-modified samples as a function of temperature.

4.3.3. NEXAFS results

NEXAFS measurements were performed to gain further understanding of the chemical structure changes occurring at the surface of both the pure and IL-modified perovskite samples. Unlike XPS, which investigates the occupied molecular orbitals, NEXAFS provides information about the electronic structure of the unoccupied molecular orbitals. This information is important in understanding the nature of bonding in molecules. The NEXAFS measurements aimed to confirm and further elucidate the observations discussed above in the XPS and work function measurements.

The C K-edge and N K-edge NEXAFS spectra recorded from a pure $BMIMBF_4$ sample are shown in Figure 4.13a-b. These spectra were recorded in a previous beam run at Max-Lab synchrotron in Sweden and are shown here for comparison with our $BMIMBF_4$-modified perovskite samples. The pure $BMIMBF_4$ sample was made by depositing the IL on a single crystal TiO_2 by physical vapour deposition and is therefore expected to be very clean. This allows us to identify the peaks arising from the BMIM group, to help differentiate them from the perovskite peaks in the ionic liquid-modified perovskite samples. The C K-edge NEXAFS spectrum of $BMIMBF_4$ reveals three main features

(labelled I, II and III in Figure 4.13a) corresponding to the excitation of different carbon atoms in the BMIM group. The spectrum also shows a weak peak located at ~285.0 eV which is attributed to beam damage and adventitious carbon [66]. The first and sharpest feature (I) is a result of core excitation of the three carbon atoms within the imidazolium ring of the BMIM group. This feature is further divided into two sub-peaks at 286.5 eV and 286.7 eV, resulting from the double resonance effect. This effect arises from the distinct chemical environment of one carbon atom (C1) compared to the other two (C2), as depicted in Figure 4.5 above [67]. The sub-peak originating from C1 at 286.7 eV possesses a slightly higher photon energy than the sub-peak emerging from the C2 carbon atoms at 286.5 eV because C1 has two neighbouring electronegative nitrogen atoms, while the C2 carbon atoms have only one. These features are assigned to C 1s $\rightarrow$ π^* transitions, with π^* representing the lowest unoccupied molecular orbital localised on the imidazolium ring.

Features II and III, with resonances at ~289.6 eV and ~294.0 eV, respectively, are induced by the core excitation of the alkyl side chain carbon atoms of the BMIM group. These features (II & III) are attributed to C 1s $\rightarrow$ σ^* transitions contributed by the alkyl side chain carbon atoms of the BMIM group.

The N K-edge NEXAFS spectrum of $BMIMBF_4$ (Figure 4.14) exhibits five distinctive features (I-V) at 401.9 eV, ~403.5 eV, ~405.9 eV, ~408.2 eV, and ~415.4 eV. These features are attributed to the two nitrogen atoms in the imidazolium ring. While both of these ring nitrogen atoms share a similar chemical environment, slight variations arise from the different alkyl side chains. As a result, the contributions of both nitrogen atoms are nearly identical.

The initial feature (I) at 401.9 eV corresponds to N 1s $\rightarrow$ π^* transitions, while feature II at 403.5 eV is associated with N 1s $\rightarrow$ σ^* transitions. Beyond 404 eV, a broad distribution of signals is observed, encompassing Feature III, IV, and V. These signals result from N 1s $\rightarrow$ σ^* transitions. Our measured values are in good agreement with previously reported values for imidazolium ionic liquids [67, 68].

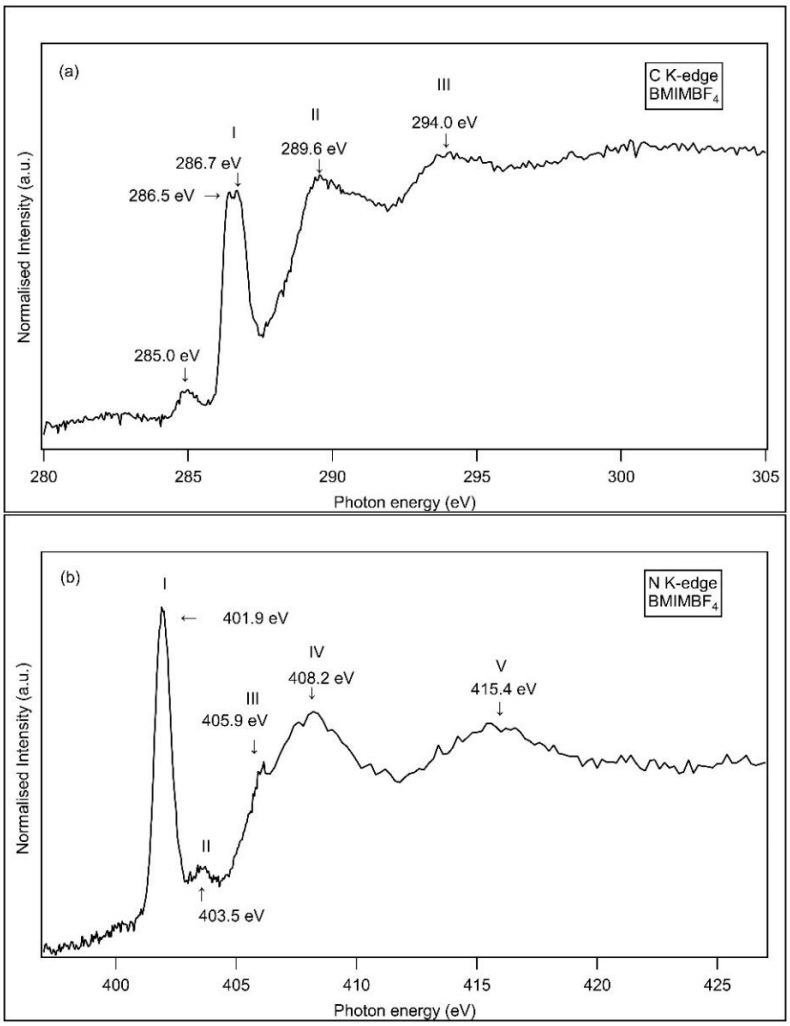

Figure 4.14 C K-edge (a) and N K-edge (b) NEXAFS spectra of $BMIMBF_4$.

There is limited literature available on the NEXAFS of perovskites, and to our knowledge, none exists on IL-modified perovskite samples. The C K-edge NEXAFS spectrum of the Perovskite sample is shown in Figure 4.14a (NEXAFS spectra of the SnO_2/perovskite sample was not measured). The spectrum reveals two distinct signals at 285.0 eV and approximately 289.5 eV, denoted by roman numerals I and III in the Figure 4.14. Feature III is associated with C-N σ* bond transitions, and has been documented in prior NEXAFS studies on perovskites [66, 69]. The perovskite structure does not contain any unsaturated carbon bonds, so no π* peaks are anticipated in the NEXAFS spectra. We therefore consider Feature I at 285.0 eV to arise due to hydrocarbon contamination or X-ray beam damage of the sample. In fact, Feature I has been a subject of debate and has been extensively discussed by Huang et al [66]. In their research, Huang et al. noted

an increase in the intensity of the 285.0 eV signal upon repeated scanning of the same position on the perovskite sample, suggesting that beam damage was causing this feature. However, they did not conclusively attribute this increase to beam damage as they also observed a weak peak at ~285 eV using bulk-sensitive fluorescence yield measurements and described the origin of the peak as uncertain. Some studies have attributed this signal to C-N σ* bond transitions, while others have linked it to transitions to π* orbitals [69, 70]. From our measurements, we suggest the peak at 285 eV could be partly due to beam damage. This conclusion is supported by the observation of a 285 eV peak in the pure $BMIMBF_4$ sample, which cannot be assigned to any carbon atom in the ionic liquid and no contamination is anticipated as it was deposited by physical vapour deposition in UHV on clean single crystal TiO_2 substrate.

The C K-edge NEXAFS spectra of the IL-modified perovskite films reveal three distinct features, denoted as I, II, and III in Figure 4.14-a. Feature I, located at 285.0 eV, corresponds to adventitious carbon or beam damage and is consistent with the previous discussion. Feature III, observed at 289.5 eV, is attributed to C-N σ* transitions within the perovskite structure, as observed in the pure perovskite sample. The second feature (II) is identified at 286.7 eV. This signal is associated with C 1s → π* transitions, which can be attributed to excitation from the carbon atoms within the imidazolium ring. This observation aligns with the signal observed in the pure $BMIMBF_4$ NEXAFS spectrum. It must be pointed out that the double peak structure (observed in the pure $BMIMBF_4$ sample) could not be resolved in the IL-modified perovskite samples.

The two BMIMCl-modified samples exhibit subtle variations in their C K-edge signal intensities, providing valuable insights into the structural characteristics of these films. In the SnO_2/BMIMCl-Perovskite sample, both the perovskite peak (Feature II) and the IL peak (Feature III) have nearly identical intensities, with a minor feature at ~285.0 eV, which is associated with adventitious carbon/beam damage. Conversely, in the BMIMCl-Perovskite sample, the IL peak exhibits the highest intensity, accompanied by a relatively prominent adventitious carbon/beam damage peak. The intensity of the perovskite peak decreases relative to the SnO_2/BMIMCl-Perovskite sample. This observation is consistent with the work function changes discussed in the preceding section 4.3.2.

Specifically, work function values of 3.8 eV and 4.0 eV were recorded (pre-heating) for the SnO_2/BMIMCl-Perovskite and BMIMCl-Perovskite samples, respectively. These findings suggest that SnO_2 facilitates the integration of BMIMCl into the perovskite grain boundaries, resulting in a reduction in work function when compared to the sample without SnO_2. The similar intensities of the perovskite and IL peaks in the SnO_2-coated sample imply a more balanced distribution of these components, highlighting the role of SnO_2 in enhancing the interaction between the ionic liquid and the perovskite material.

On the other hand, the two $BMIMBF_4$-modified samples, which exhibited the same work function value of 3.7 eV before heating, also display very similar C K-edge spectra. In these spectra, Feature I (~285.0 eV) is very small, indicating a higher resistance to beam damage or less adventitious carbon in these samples. The perovskite peak (Feature III) is strong and is comparable in intensity to the IL signal (Feature II).

Figure 4.14-b presents the N K-edge NEXAFS spectra of all the samples. The pure perovskite sample does not exhibit any features, indicating the complete absence of π bonding in the sample, aligning with our initial expectations. A sharp feature at ~401.6 eV is exhibited by all the IL-modified samples and can be assigned to the N 1s → π* transitions corresponding to the two imidazolium ring nitrogen atoms as discussed with pure $BMIMBF_4$ above. Broad σ* features can also be observed at higher photon energies. The N K-edge results confirm the presence of the ionic liquid in all the IL-modified samples.

NEXAFS results have yielded further valuable insights into the structural and electronic attributes of these materials whilst also confirming the findings from XPS and work function measurements.

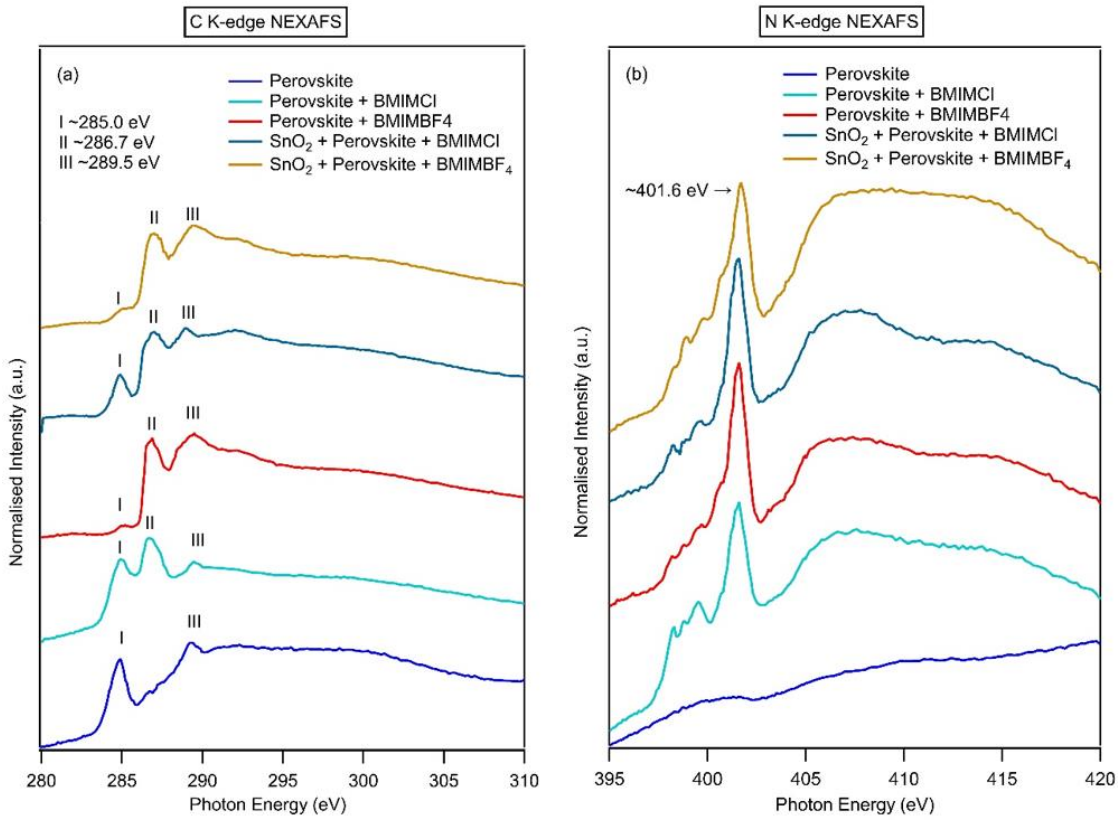

Figure 4.15 (a) C K-edge and (b) N K-edge NEXAFS spectra of pristine and IL-modified perovskite samples.

4.3.4. HAXPES results

The photoemission measurements carried out at ASTRID probed the surface layers of the perovskite samples where we expect decomposition and contamination to be most prominent. HAXPES measurements probe deeper into a sample, allowing a comparison to be made between the surface and bulk composition. The utilisation of higher photon energy in HAXPES leads to the generation of higher-energy photoelectrons with larger Inelastic Mean Free Paths (IMFPs), resulting in deeper probing depths. This advancement allowed us to explore the chemical composition of our samples to depths of several tens of nanometers beneath the surface. Furthermore, the access to and sensitivity of deeper core levels, especially for heavier elements, presented a substantial enhancement in sensitivity in HAXPES compared to conventional XPS.

Thus far, the analysis has indicated that ionic liquid-modified perovskite films deposited on SnO_2-coated Ti substrates exhibit notable promise in terms of stability. Consequently, these samples underwent further investigation via HAXPES to gain insights into their elemental distribution and bulk composition. To provide a comprehensive comparison, the SnO_2/Perovskite sample was also subjected to HAXPES analysis.

The I $2p_{3/2}$ and Pb $3d_{5/2}$ core levels are observed at BE values ~4557 and ~2484 eV, respectively. The integrated peak areas from the I 2p and Pb 3d core level signals were employed to estimate the I/Pb ratios of the samples. In order to estimate the variation in the composition with respect to the sampling depth, the I 2p and Pb 3d core level spectra of the samples were recorded as a function of the photoelectron emission angle. The sampling depth decreases as the emission angle relative to normal emission is increased. Initially, the samples were positioned at a 2° tilt with respect to the analyser's normal, and HAXPES measurements were acquired using the transmission mode of the analyser. The spectra obtained from the transmission mode of the analyser (depicted in Figure 4.16 below) correspond to the deepest probing depth (~31.5 nm) achievable with HAXPES. This depth is crucial for understanding the composition near the bulk of the sample.

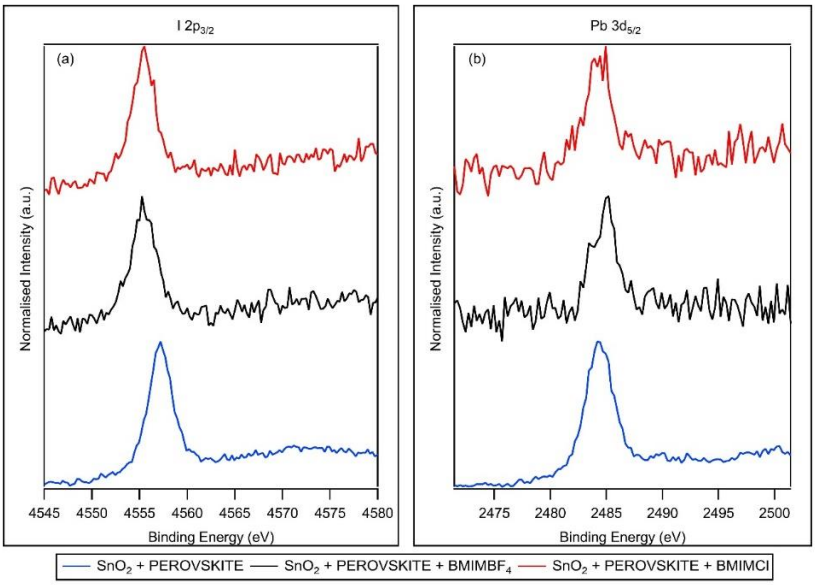

Figure 4.16 High-resolution (a) I $2p_{3/2}$ and (b) Pb $3d_{5/2}$ core-level spectra of the pure and IL-modified perovskite samples measured using the transmission mode of HAXPES. The peaks are intensity normalised with respect to Pb $3d_{5/2}$.

Subsequently, the samples were rotated to a 40° angle with respect to the analyser's normal, and HAXPES measurements were obtained using the angular 45 mode of the analyser. The spectral data collected in this configuration (cos θ values between 0.46 and 0.95) enabled us to generate information from a range of sampling depths, as previously detailed in the experimental section. The calculated I/Pb ratios for the samples, extracted from both the transmission and angular modes of the analyser, are plotted against the cosine of the emission angle (cos (θ)) and illustrated in Figure 4.17. The I/Pb values at different angles are tabulated in Table 4.5. It must be noted that the probing depth is slightly different for I 2p and Pb 3d levels as they emit photoelectrons of different kinetic energies. The average probing depth listed in Table 4.5 is calculated by averaging the probing distance of I 2p and Pb 3d levels.

In the SnO_2/Perovskite sample, the I/Pb ratio is 2.5 at the maximum sampling depth probed using the analyser's transmission mode. This value indicates the presence of perovskite in this depth range. The mixed halide perovskite is expected to display an I/Pb ratio in the range 2.5-2.9. When the emission angle is increased to 17.5°, the I/Pb ratio shows a slight increment to 2.7, which still falls within the range typical of mixed halide perovskite materials. Maintaining this consistency, the ratio remains at 2.7 as the emission angle is further increased to 22.5° and 27.5°. However, with a further increase in the emission angle to 52.5°, 57.5°, and 62.5° (moving to more surface sensitive measurements), the I/Pb ratio progressively decreases to 2.5, 2.4, and eventually 2.0. An I/Pb ratio of 2.0 is characteristic of the I/Pb ratio in PbI_2, signifying surface degradation of the perovskite into lead iodide.

The I/Pb values observed in the ionic liquid-modified perovskite samples consistently fall within the range of 2.7-2.8 throughout the probed depth of the samples. This consistency with the nominal stoichiometry of the mixed halide perovskite indicates the structural integrity and stability of these IL-modified perovskite films. This observation complements our XPS, work function, and NEXAFS analyses, further reinforcing the notion that the incorporation of ionic liquids promotes the formation of more defect-free perovskite material. The stabilisation of the PbI_6^{-2} framework by the ionic liquids suppresses the formation of PbI_2 and the concomitant loss of the vulnerable organic

moiety from the perovskite lattice. The uniform distribution of I/Pb ratios across the sampling depth in the IL-modified samples serves as compelling evidence supporting the enhanced stability of the perovskite material.

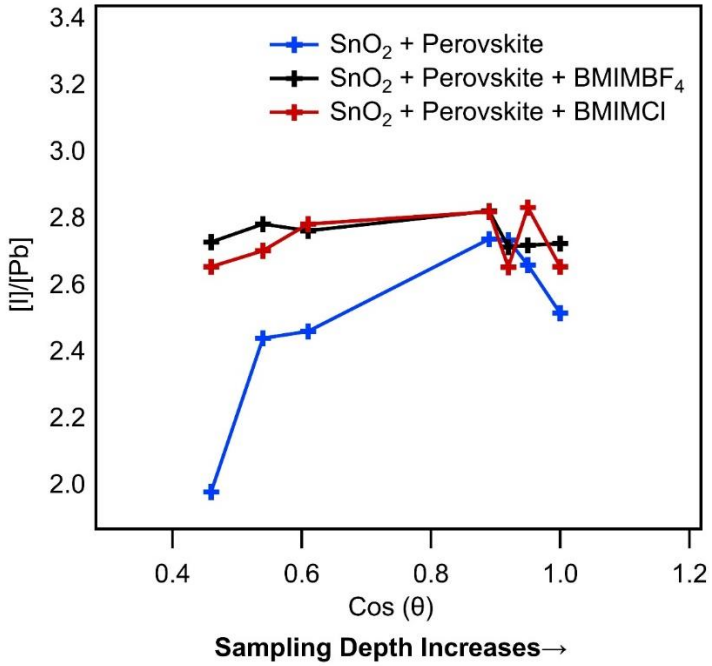

Figure 4.17 I/Pb ratios from HAXPES as a function of cos (ϑ).

Cos θ	d_s for I $2p_{3/2}$ electrons (nm)	d_s for Pb $3d_{5/2}$ electrons (nm)	Average depth probed (nm)	SnO_2 + Perovskite	SnO_2 + Perovskite + $BMIMBF_4$	SnO_2 + Perovskite + BMIMCl
0.46	12.42	16.56	14.5	2.0	2.7	2.7
0.54	14.58	19.44	17.0	2.4	2.8	2.7
0.61	16.47	21.96	19.2	2.5	2.8	2.8
0.89	24.03	32.04	28.0	2.7	2.8	2.8
0.92	24.84	33.12	29.0	2.7	2.7	2.7
0.95	25.65	34.2	29.9	2.7	2.7	2.8
1	27.0	36.0	31.5	2.5	2.7	2.7

Table 4.5 The I/Pb ratios of the samples as a function of the HAXPES probing depth.

Figure 4.18 displays contour plots of the I $2p_{3/2}$ and Pb $3d_{5/2}$ core level spectral intensities with the sampling depth (cos θ = 0.46–0.95). These plots were derived from the angular mode information from the analyser. The I/Pb ratios (for data points taken from angular mode) in Figure 4.17 were calculated from slices of these contour plots (as discussed in the experimental section of this chapter).

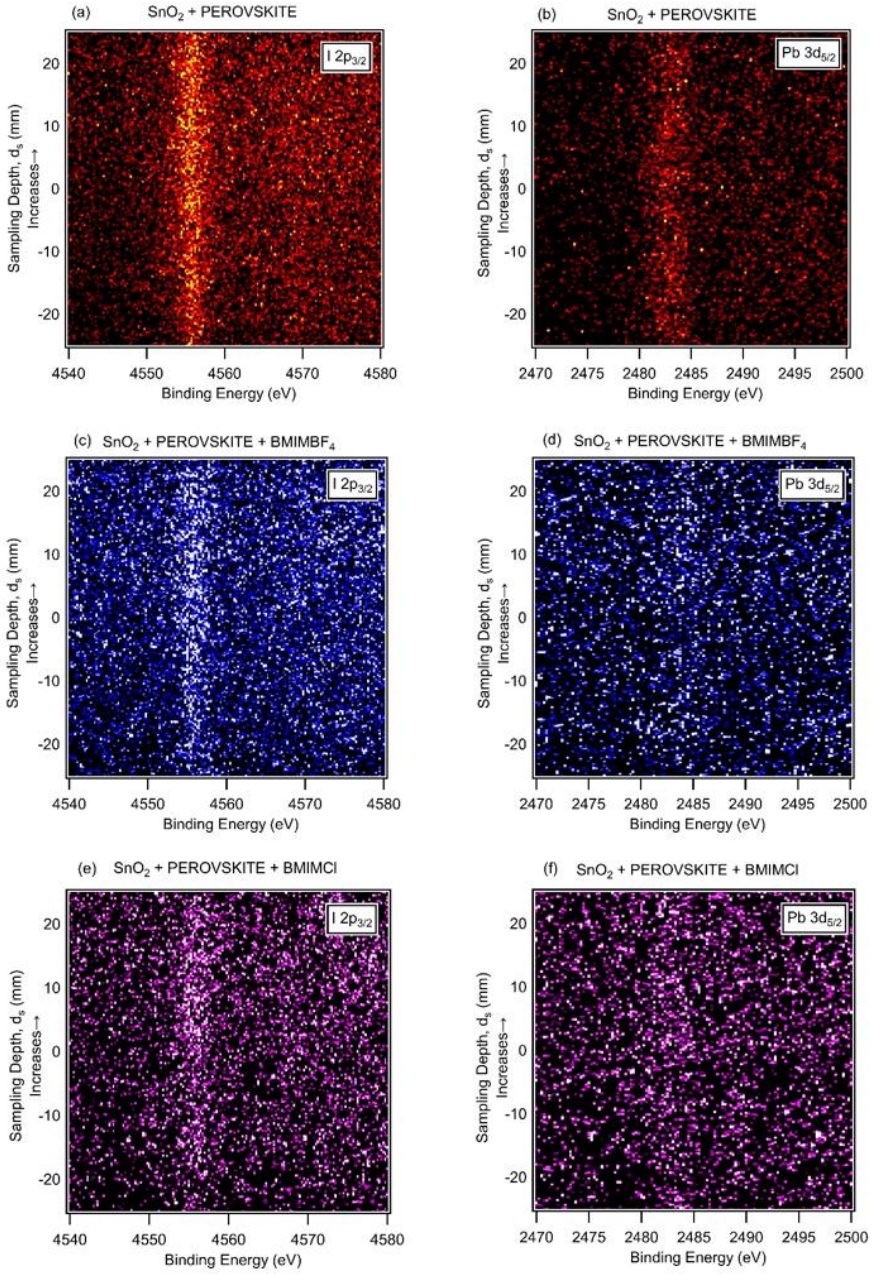

Figure 4.18 The compositional variation of I $2p_{3/2}$ and Pb $3d_{5/2}$ with the sampling depth in the angular mode measurements.

4.3.5. NAP-XPS results

The evaluation of moisture endurance in the pure and IL-modified perovskite samples, deposited on SnO_2-coated Ti substrates, was conducted using laboratory-based Near Ambient Pressure X-ray Photoelectron Spectroscopy (NAP-XPS). In addition to the samples prepared at UCLan (about a week before the NAP-XPS experiment), a fresh perovskite film was prepared in the chemistry laboratory at the Henry Royce Facility. This was spin-coated onto a SnO_2 coated Ti substrate following the same procedure detailed in the experimental section. This newly prepared sample was promptly transferred (within minutes) to the load-lock and subjected to NAP-XPS measurements. Since our previous measurements on the pure perovskite sample showed signs of surface degradation, this fresh sample allowed us to measure the pure perovskite film before surface decomposition occurs. In this section of the results, the pure perovskite sample made at UCLan is referred to as the SnO_2/Aged-Perovskite sample, and the freshly prepared sample made at the Henry Royce Facility is called the SnO_2/Fresh-Perovskite sample.

The investigation into moisture-induced degradation took place in the NAP gas cell, which was filled with water vapor to a pressure of 4.5 mbar, approximately corresponding to a relative humidity of 15% at 25 °C [35]. NAP-XPS is a relatively recent development that enables XPS characterization of samples in a gaseous environment [71]. It is worth noting that there have been limited studies on NAP-XPS of perovskites, and to the best of our knowledge, none have been conducted on the combination of our perovskite and ionic liquid.

In addition to the NAP measurements, we recorded XPS spectra both before and after subjecting the samples to water vapor within a controlled UHV environment. This approach enabled us to capture spectral changes resulting from the water exposure and assess the influence of moisture on our samples. The survey spectra for these samples recorded before, during and after water exposure are attached to Appendix 1 of this thesis. It must be noted that the RSFs are unavailable for the analyser under NAP conditions. Consequently, the percentage concentrations displayed alongside the

survey spectra, calculated using standard RSFs from the Scofield library, only serve as rough estimates of the overall atomic composition. The UHV scans were initiated after NAP exposure from the second sample onwards. As a result, there are no post-NAP scans for the SnO_2/Aged-Perovskite sample, which was the first sample in the investigation.

Figure 4.19 (a-d) presents the C 1s core level spectra for the four samples. The C 1s spectra of the SnO_2/Fresh-Perovskite sample (Figure 4.19a) during water exposure and in UHV before and after water exposure are fitted with peaks at 285.3 eV, 286.0 eV, 286.6 eV, 287.5 eV, and 288.7 eV. The peak at 285.3 eV can be attributed to adventitious carbon contamination, while the peaks at 286.0 eV and 286.6 eV are associated with MAI and the perovskite C-N bond, respectively, as previously discussed in the XPS section. The higher binding energy peaks at 287.5 eV and 288.7 eV are indicative of C=O and O-C=O groups resulting from hydrocarbon oxidation products.

The intensity of the MAI and adventitious carbon peaks increases (relative to the perovskite peak) upon water exposure and subsequently decreases in the UHV scan post NAP. The $CH_3NH_3^+$ (MA^+) group situated at the body centre of the perovskite cubic lattice exhibits high sensitivity to moisture, rendering the perovskite susceptible to instability in moist conditions. The heightened MAI peak intensity during NAP may stem from the release of MA^+ ions from the perovskite lattice upon exposure to water. However, the subsequent reduction in the MAI peak intensity post-NAP is intriguing, suggesting a possible reorganisation of ions that potentially leads to the recovery or regeneration of the perovskite lattice. The perovskite peak consistently maintains the highest intensity across all spectra. The intensity of this peak decreases during water exposure but subsequently recovers in the post-water exposure spectra. This observation underscores the resilience of the perovskite phase, persisting even after prolonged exposure (overnight) to water vapor during the acquisition of the NAP scans.

Figure 4.19-b illustrates the C 1s core level spectra for the SnO_2/Aged-Perovskite sample, which is characterised by peaks at 285.3 eV, 286.0 eV, 286.6 eV, 287.7 eV, and 289.3 eV in the UHV scan conducted before water exposure. In the NAP scan, peaks are observed at 285.3 eV, 286.0 eV, 286.6 eV, 287.6 eV, and 288.7 eV. The peaks at 285.3 eV, 286.0

eV, and 286.6 eV are attributed to adventitious carbon, MAI, and perovskite, respectively. The higher binding energy peaks are consistent with hydrocarbon oxidation products, as discussed previously.

In contrast to the fresh perovskite sample, the peak associated with adventitious carbon contamination has become the most intense peak in the aged perovskite sample, followed by the unreacted/dissociated MAI peak. The intensity of the perovskite C-N peak has significantly reduced in both spectra, but it is still observable. Overall, no relative change in the peak intensities can be observed during water exposure.

The C 1s core level spectra for both the SnO_2/IL-modified perovskite samples (Figure 4.19c-d) reveal peaks at 285.3 eV, 286.0 eV, 286.6 eV, 287.3 eV, and 288.2 eV in both the UHV and NAP scans. Once again, the peaks at 285.3 eV are indicative of hydrocarbon contamination. The peaks fitted at 286.0 eV correspond to an aliphatic C-N bond and may arise from the aliphatic C-N bond within the BMIM group (refer to Figure 4.5) and/or MAI. The peaks at 286.6 eV can be attributed to both the C-N bond within the perovskite lattice and the aromatic C-C-N carbons in the ionic liquids. The imidazolic N-C-N carbon peak is fitted at 287.3 eV. The higher binding energy peaks at 288.2 eV and 290.0 eV are associated with the products of hydrocarbon oxidation.

Overall, both ILs present remarkably similar C 1s spectra. Across all spectra, the peak at 286.0 eV displays the highest intensity, as anticipated, representing contributions from the precursor MAI and the BMIM group within the ILs. With exposure to water vapor, the adventitious carbon peak intensifies, yet the relative intensities of the perovskite and IL peaks remain largely unchanged. This observation suggests that the exposure to water exerts minimal influence on the IL-modified perovskite films. It is important to note that we refrain from drawing extensive conclusions based solely on the presence of the perovskite peak (286.6 eV) in the spectra, as it overlaps with the BE of the aromatic carbon peak within the imidazolium ring.

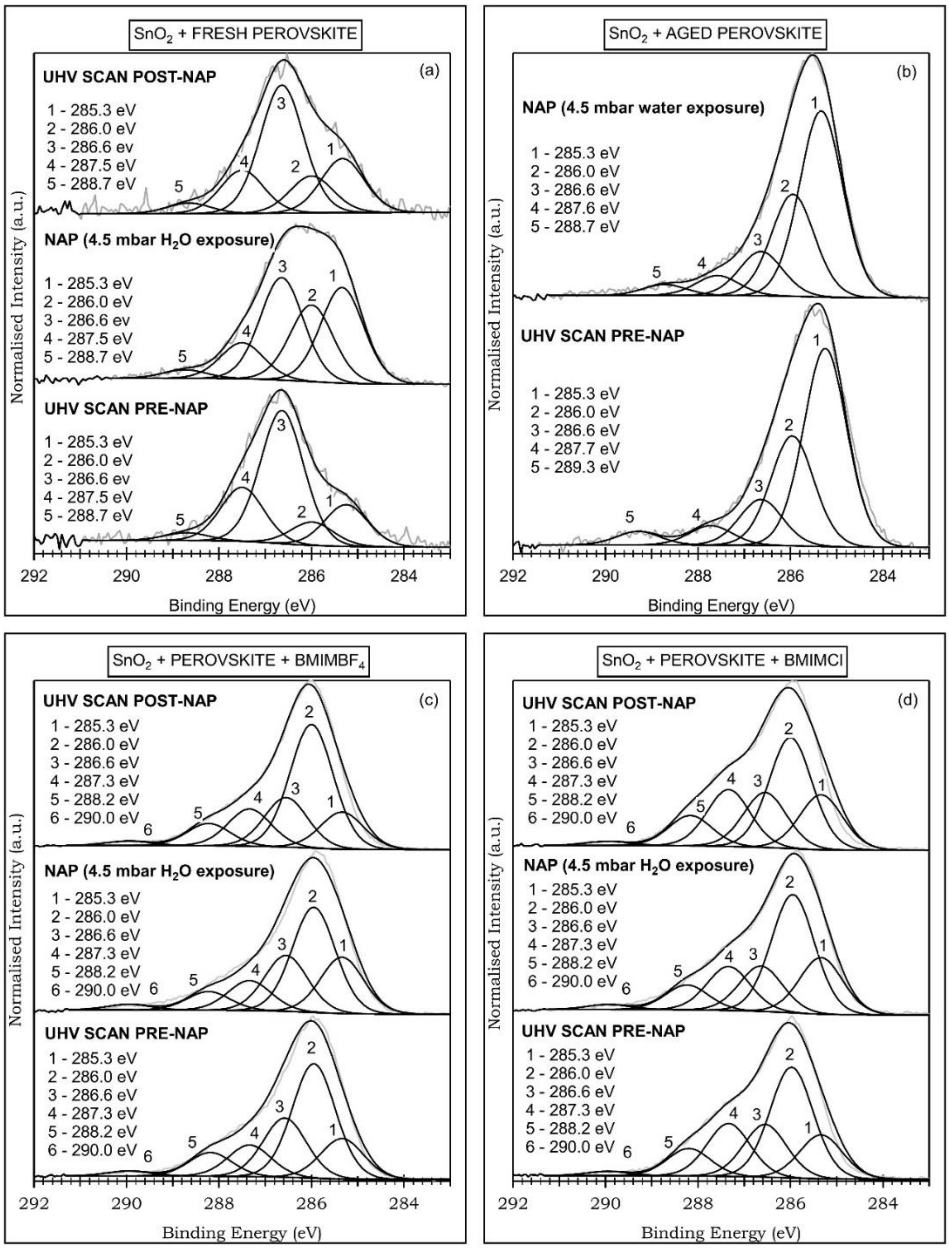

Figure 4.19 High-resolution core level C 1s spectra of pure and IL-modified perovskite samples measured before exposure, during exposure and after exposure to 4.5 mbar water vapour at room temperature. Spectral intensities are normalised to the intensity of the highest peak.

Figure 4.20 (a-d) illustrates the N 1s core level spectra of all the samples. The SnO_2/Fresh-Perovskite sample displays a prominent peak at 402.6 eV and a weaker feature at 400.5 eV in all the spectra recorded before, during and after water exposure. The peak at 402.6 eV is associated with the nitrogen state in the perovskite, while the

feature at 400.5 eV likely arises from unreacted or dissociated MAI [37, 42]. The intensity of the perovskite peak slightly decreases during water exposure but increases again post-exposure.

The N 1s spectra of the SnO_2/Aged-Perovskite sample exhibit a low signal to noise ratio. These spectra are fitted with weak peaks corresponding to the perovskite (402.6 eV) and MAI (400.5 eV) in the scans before and during water exposure. These two peaks are of approximately equal intensity, in contrast to the fresh perovskite sample, where the perovskite peak was much more intense than the MAI peak. This suggests that the aged perovskite sample may have degraded significantly prior to the measurements.

In the N 1s spectra of the SnO_2/$BMIMBF_4$-Perovskite sample, peaks are fitted at 402.9 eV, 401.6 eV, and 400.5 eV before and after water exposure. The NAP spectrum is fitted with peaks at 402.8 eV, 401.6 eV, and 400.5 eV. The less prominent feature at 400.5 eV is attributed to MAI, as discussed in the pure perovskite sample. The peak at 401.6 eV can be assigned to imidazolic nitrogen atoms in the ionic liquid, consistent with prior studies[38, 39, 72]. The peaks at 402.9 eV and 402.8 eV are assigned to the nitrogen state in the perovskite. The upward shift in BE of the perovskite peaks relative to the pure perovskite samples may result from bonding interactions between the IL and the perovskite. However, it is important to note that sample charging in ionic liquids can affect absolute peak positions. Furthermore, the BE values for pure perovskite N 1s core levels have been reported in the range of 402.5 – 402.9 eV, with the -0.1 eV BE shift during water exposure warranting attention [37, 42, 73-77].

The N 1s spectra of the SnO_2/BMIMCl-Perovskite sample, taken before and after NAP measurements, exhibit peaks at 402.8 eV and 401.6 eV. The NAP scan spectra are fitted with peaks at 402.7 eV, 401.6 eV, and 400.5 eV. The peaks at 401.6 eV and 400.5 eV are attributed to nitrogen atoms in the ionic liquid and MAI, respectively, and the peak at 402.8 eV/402.7 eV corresponds to the perovskite. Similar to the $BMIMBF_4$-modified sample, the perovskite peaks show an upward shift of +0.1 eV in BE during water exposure.

The UHV scans recorded before and after water exposure do not show any weak feature corresponding to MAI in the BMIMCl-modified samples. This absence is intriguing and suggests that the BMIMCl incorporation either facilitated the complete conversion of the precursor MAI to the perovskite or prevented its dissociation.

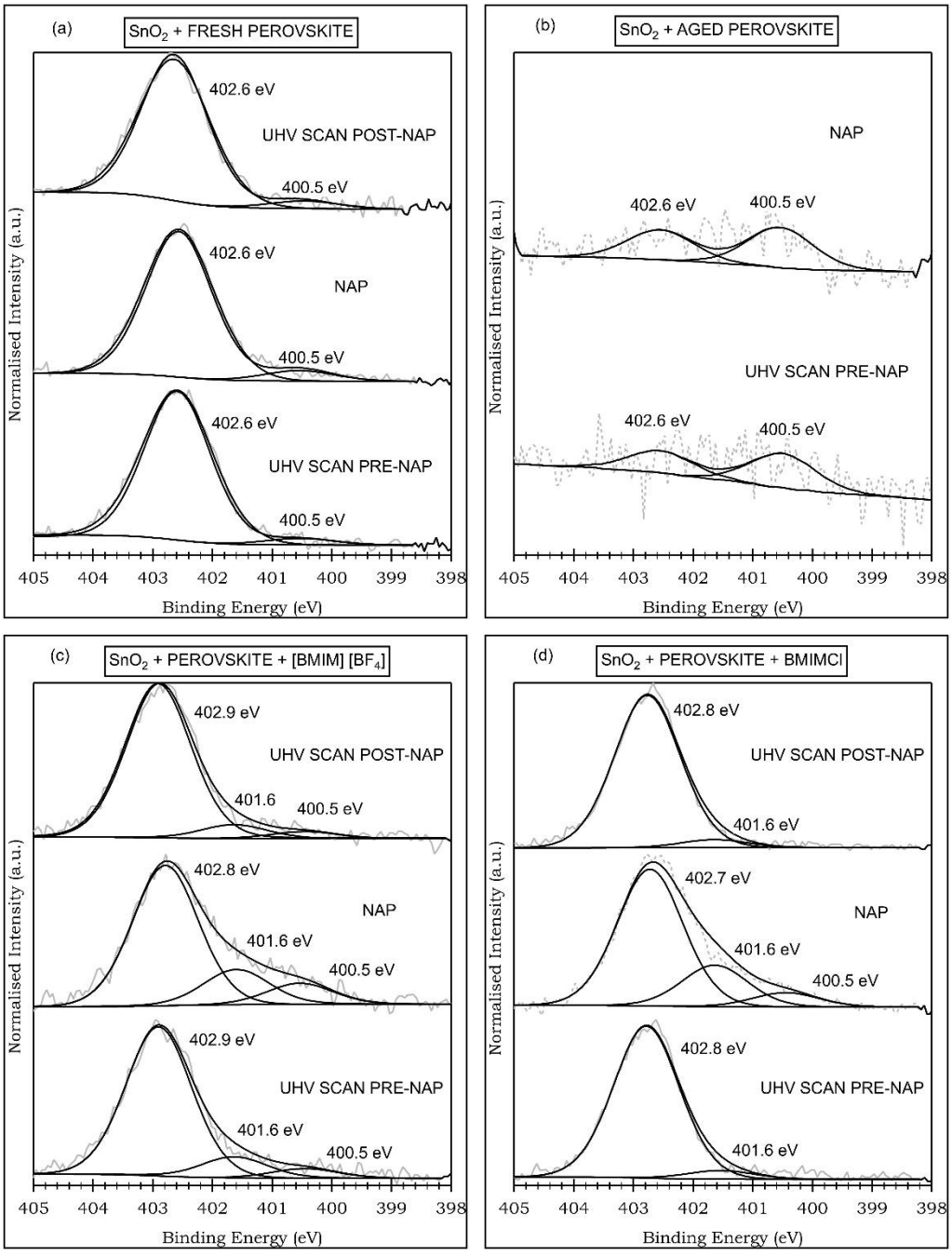

Figure 4.20 High-resolution core level N 1s spectra of pure and IL-modified perovskite samples measured before exposure, during exposure and after exposure to 4.5 mbar water vapour at room temperature.

The Pb 4f core level spectra of the samples are presented in Figure 4.21 (a-d) below. A total of 25 NAP-XPS scans were conducted for each sample, and the first and last NAP scans are displayed alongside the averaged NAP spectra to highlight any BE changes during the water exposure period. The Pb 4f spectra of the UHV scan before water exposure for the SnO_2/Fresh-Perovskite sample exhibit two characteristic peaks at 138.7 eV and 143.6 eV. These peaks are assigned to the two Pb 4f doublet components, Pb $4f_{7/2}$ and Pb $4f_{5/2}$, with a spin-orbit splitting energy of 4.87 ± 0.05 eV and represent the Pb^{+2} state in the perovskite [78]. Over the course of the NAP scans, a +0.2 eV BE shift is identified, with the doublet going from 138.6 eV and 143.5 eV in the first NAP scan to 138.8 eV and 143.7 eV in the last NAP scan. The UHV scan post-water exposure maintains peaks at 138.8 eV and 143.7 eV, consistent with the last NAP scan. This binding energy shift can be attributed to the distortion of the perovskite PbI_6^- octahedra and subsequent formation of lead iodide (PbI_2) (Pb $4f_{7/2}$ BE = 138.9 eV) [37, 44, 73].

In contrast, the Pb 4f doublet in the SnO_2/Aged-Perovskite sample appears at a higher BE, with peaks fitted at 138.9 eV and 143.8 eV in the UHV scan before water exposure, attributed to Pb^{+2} in lead iodide. This shows that the Pb in the aged perovskite had already degraded to lead iodide prior to our XPS measurements. The Pb^{+2} doublet shows no shift in BE across all spectra. However, a weak feature at 137.1 eV and 141.9 eV can be fitted in the averaged and last NAP scans. This weak doublet is consistent with the BE of metallic lead and results from the decomposition of lead halides into metallic lead and halogen gas. As it could only be identified in the averaged and the last NAP scan, the decomposition of lead halides must have only occurred after an extended period of water exposure in the NAP cell.

The Pb 4f core level spectra of the SnO_2/$BMIMBF_4$-Perovskite sample exhibit doublet peaks at 139.7 eV and 144.6 eV in the UHV scans recorded before and after water exposure. As noted earlier in the N 1s spectra, the occurrence of these peaks at a relatively high BE compared to the pure perovskite sample could be a result of the bonding interactions between the IL and the perovskite or could just be an artifact of sample charging, which has been reported as an issue in XPS measurements of ionic liquids. The doublet undergoes a -0.2 eV shift during water exposure, changing from

139.4 eV and 144.3 eV in the first NAP scan to 139.6 eV and 144.5 eV in the last NAP scan during the period of NAP data acquisition.

The SnO_2/BMIMCl-Perovskite sample is fitted with Pb 4f doublet peaks at 139.4 eV and 144.3 eV in the UHV scans before and after water exposure, as well as in the averaged NAP spectra. The first NAP scan exhibits a -0.1 eV BE shift, locating the peaks at 139.3 eV and 144.2 eV. Once again, we attribute these peaks to Pb^{+2} in the perovskite, disregarding absolute peak positions and focusing on the BE changes between scans.

The Pb 4f XPS analysis reveals distinct patterns among the samples. In the two IL-modified samples, the BE values in the UHV scan post NAP precisely return to the peak positions of the UHV scan pre-NAP. However, in the fresh perovskite sample, the final values in the UHV post-NAP exhibit a +0.1 eV shift compared to the pre-NAP values. This observation suggests that the ILs may play a role in facilitating the regeneration of the perovskite [79, 80].

The BMIMCl sample displays nearly constant peak positions, with only a -0.1 eV shift in the first NAP scan. In contrast, the $BMIMBF_4$ sample experiences a more substantial downward shift during water exposure, a phenomenon that will be explored further in subsequent discussions. Notably, none of the samples, except the aged perovskite sample, exhibits the presence of a metallic lead peak. This absence suggests that the lead halide decomposition serves as a clear indication of complete lattice distortion and severe degradation of the perovskite lattice.

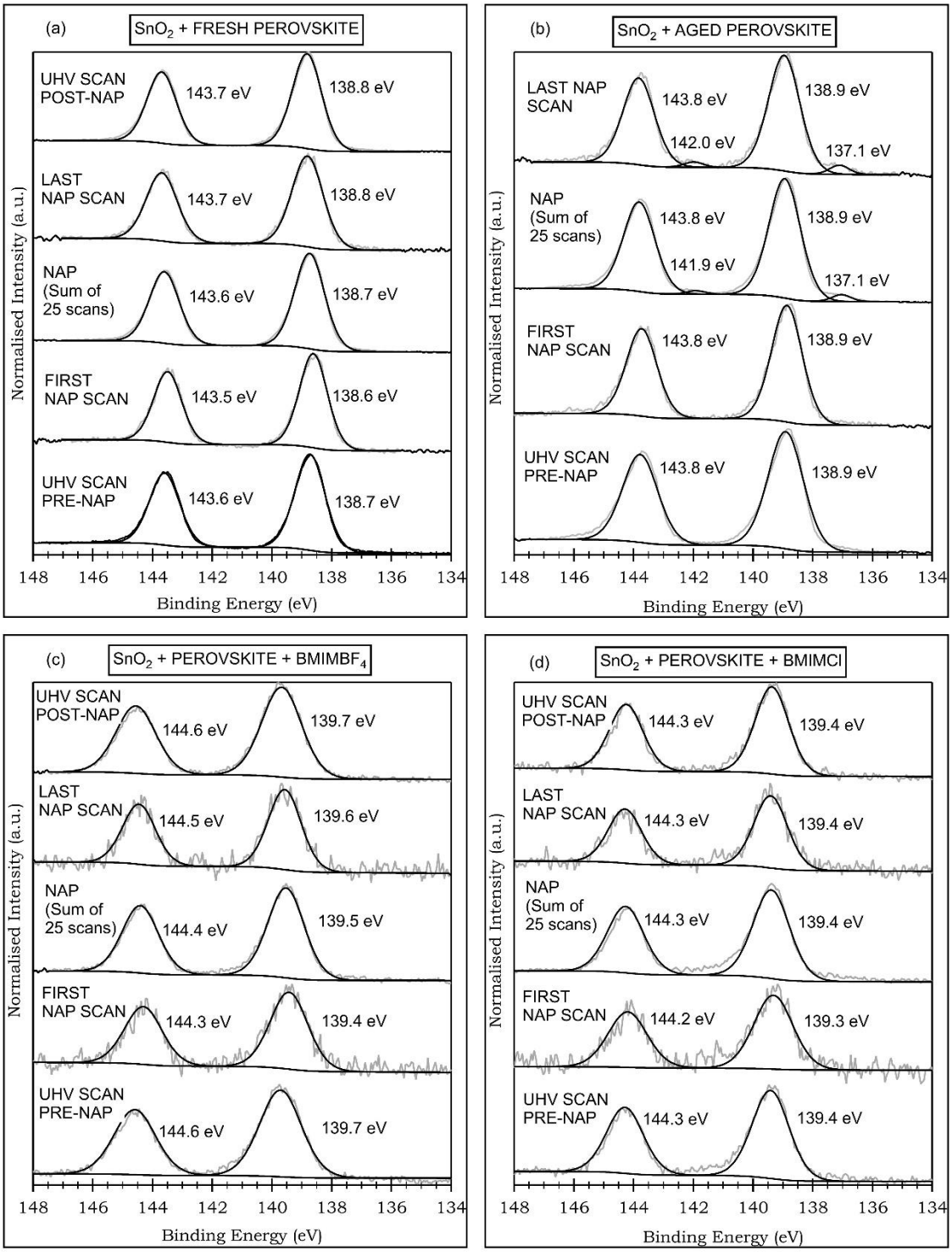

Figure 4.21 High-resolution core level Pb 4f spectra of pure and IL-modified perovskite samples measured before exposure, during exposure and after exposure to 4.5 mbar water vapour at room temperature.

Figure 4.22 (a-d) presents the I 3d core level spectra for the samples. The I 3d XPS spectra, characterised by two components (I $3d_{5/2}$ and I $3d_{3/2}$) with an 11.5 eV doublet splitting, reveal distinctive features. The I 3d spectra of the SnO_2/Fresh-Perovskite sample display peaks at 619.5 eV and 631.0 eV in the UHV scan prior to water exposure. The first NAP scan spectrum is fitted with peaks at 619.4 eV and 630.9 eV, while the last NAP scan shows a +0.2 eV BE shift with peaks at 619.6 eV and 631.0 eV. The UHV scan post-water exposure exhibits peaks at 619.6 eV and 631.0 eV. The characteristic doublet peaks at 619.5 eV and 631.0 eV are attributed to the iodine in the perovskite lattice [75, 78]. Analysis of the first and last NAP scans reveals a +0.2 eV BE shift, mirroring the trend observed in the Pb 4f spectra. This shift is indicative of the formation of PbI_2 as a result of the degradation process (Pb $4f_{7/2}$ BE = 619.8 eV) [53].

The I 3d spectrum of the SnO_2/Aged-Perovskite sample is fitted with doublet peaks at 619.7 eV and 631.2 eV before water exposure. The doublet shows a +0.1 eV shift in the BE going from 619.6 eV and 631.1 eV in the first NAP scan to 619.7 eV and 631.2 eV in the last NAP scan. Again, the Pb 4f BEs suggest that the aged perovskite already suffered a substantial degradation prior to the XPS measurements.

In the UHV scan conducted prior to water exposure for the SnO_2/$BMIMBF_4$-Perovskite sample, peaks are identified at 619.6 eV and 631.1 eV. Subsequent NAP scans unveil a shift in peaks, reaching 620.0 eV and 631.5 eV in the last NAP scan—a +0.4 eV increment from the initial NAP scan, where peaks register at 619.6 eV and 631.1 eV. The UHV scan following water exposure reveals peaks at 619.7 eV and 631.2 eV, demonstrating a -0.3 eV BE shift from the last scan and an overall shift of +0.1 eV compared to the UHV scan pre-NAP. The observed trend of BE shifting during water exposure aligns with findings in the N1s and Pb 4f spectra. The shift of the I $3d_{5/2}$ BE from 619.6 eV (pre-water exposure) to 620.0 eV (last NAP scan) and 619.7 eV (post-water exposure) suggests the distortion and subsequent regeneration of the perovskite lattice.

The SnO_2/BMIMCl-Perovskite sample exhibits doublet peaks at 619.5 eV and 631.0 eV before water exposure, 619.6 eV and 631.1 eV during water exposure (averaged NAP), and 619.4 eV and 630.9 eV after water exposure. Notably, the I $3d_{5/2}$ BE undergoes a

+0.3 eV shift from 619.4 eV (first NAP scan) to 619.7 eV (last NAP scan) during the NAP measurements. The BE values before and after water exposure align with the perovskite BE values. The observed increase in BE during water exposure, consistent with the $BMIMBF_4$-modified sample, suggests lattice distortion due to moisture stress. However, the BE values revert to their initial positions, indicating the regeneration of the perovskite lattice.

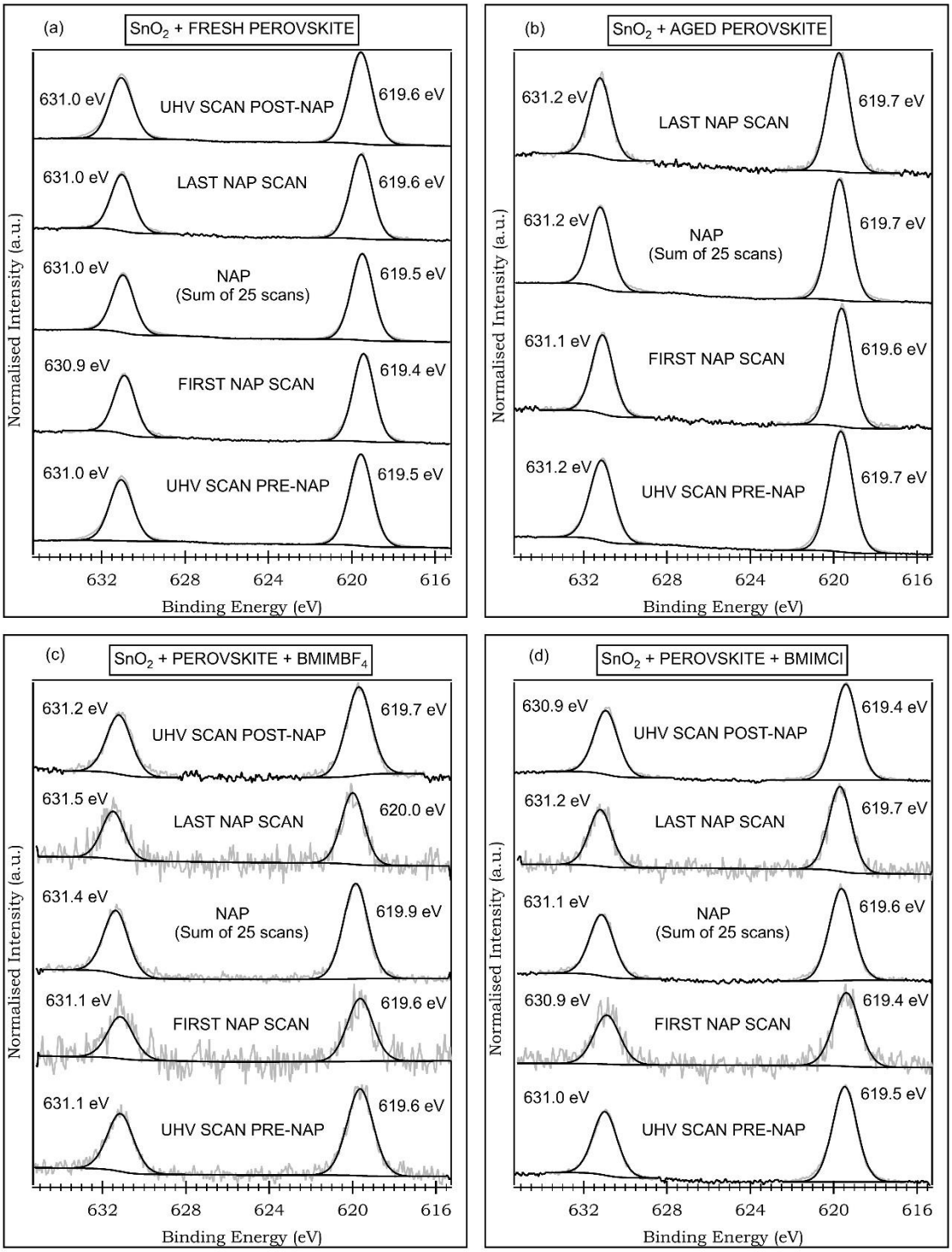

Figure 4.22 High-resolution core level I 3d spectra of pure and IL-modified perovskite samples measured before exposure, during exposure and after exposure to 4.5 mbar water vapour at room temperature.

The NAP-XPS results provide insightful perspectives into the moisture tolerance of IL-modified samples. A comparative analysis of UHV scans before and after exposure to water vapor reveals the BMIMCl sample exhibiting the most promising behaviour in terms of moisture endurance. Notably, the Pb 4f and I 3d spectra of the BMIMCl sample exhibit no upward BE shift, in contrast to the +0.1 eV shift observed in the Pb 4f spectra of the fresh perovskite sample and the +0.1 eV shift in the I 3d spectra of both the fresh perovskite and $BMIMBF_4$ samples.

During UHV scans, the absence of MAI peaks in the N 1s spectra of the BMIMCl sample, coupled with a simultaneous increase in the intensity of the perovskite peak indicates complete regeneration of the perovskite upon removal from the water environment. This observation aligns well with the I 3d and Pb 4f spectra, where BE values return to pre-NAP levels after water exposure. In contrast, both the fresh perovskite and $BMIMBF_4$ samples exhibit a weak MAI feature in both UHV and NAP scans.

The intriguing shifts in Pb 4f, N 1s, and I 3d peaks, initially to lower BE during NAP and then to higher BE in the UHV scan post-NAP, are particularly noteworthy. This phenomenon is more pronounced in the $BMIMBF_4$ sample compared to the BMIMCl sample. These observations can be explained using our initial hypothesis that the incorporation of $BMIMBF_4$ ionic liquid into the perovskite results in the formation of a $BMIM^+$ cascade on the perovskite surface. The strong interaction between $BMIM^+$ cations and I^- ions of the perovskite increases the miscibility of the BMIM group in water, supported by previous findings indicating that halide ions enhance the miscibility of $BMIMBF_4$ in water [81]. This leads to water intercalation with surface BMIM cations, causing an increase in I 3d BE and a decrease in Pb 4f BE. The H-bonding interaction between H^+ ions of water and iodide ions of the perovskite increases the BE of I 3d electrons, weakening the Pb-I bond and decreasing the BE of Pb 4f electrons.

This weakening of Pb-I bonds results in a lowering of N 1s BE of MA^+ cations and facilitates the loss of MA^+ cations from the perovskite lattice, evident in the rising intensity of the MAI peak in NAP spectra. After water exposure, BMIM cations rearrange due to their low solubility in water, leading to the reformation of the BMIM cascade.

This process results in a decrease in I 3d BE, an increase in Pb 4f BE, and a decrease in the N 1s MAI peak intensity.

In the case of BMIMCl sample, the more homogeneous distribution of BMIM cations across the depth of the sample does not favour the intercalation of water molecules. This characteristic proves more efficient in protecting the perovskite from moisture ingress but leaves it more prone to thermal degradation as observed in the XPS analysis.

If our hypothesis holds true, it should be reflected in the relative intensities of peaks, with elemental signals from the perovskite being heavily attenuated in the case of $BMIMBF_4$ due to the effect of the BMIM cascade. To comprehensively compare intensity differences in core levels, the integrated peak areas obtained in the UHV scans before and after water exposure were divided by the smallest area of that core level in all three samples (Fresh and IL-modified). The intensity changes occurring in the I 3d, Pb 4f, and N 1s signals, and the values of the areas are presented in Figure 4.23 below.

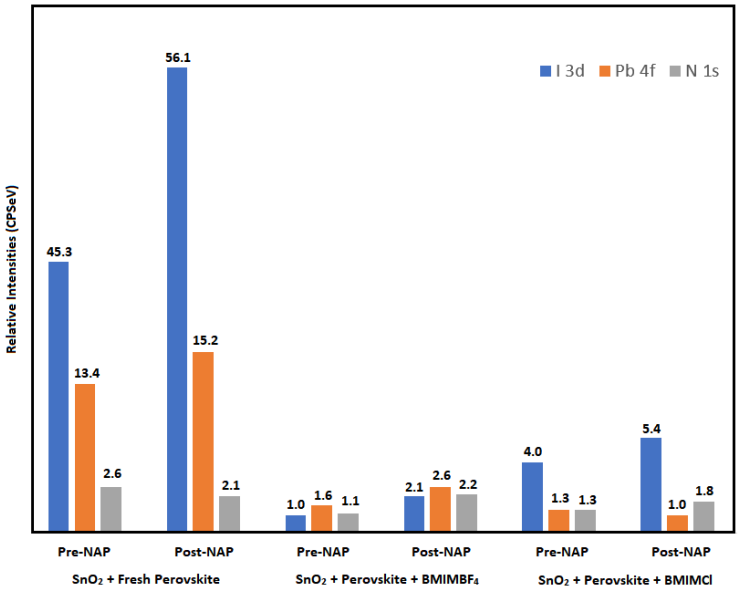

Figure 4.23 The relative peak intensities of I 3d, Pb 4f and N 1s core level signals.

As depicted in Figure 4.23, the Fresh perovskite sample exhibits high intensities of the I 3d and Pb 4f core level signals compared to the IL-modified samples, attributable to the absence of any passivating layer atop the perovskite film. The I 3d signal intensity is

nearly four times in the BMIMCl sample compared to the $BMIMBF_4$ sample, both before and after water exposure. Pre-NAP, the Pb 4f signals show similar intensities in both IL-modified samples. However, post-NAP, the Pb 4f signal intensifies in the $BMIMBF_4$ sample compared to the BMIMCl sample.

The nearly twofold increase in signal intensities of I 3d, Pb 4f, and N 1s core level signals in the UHV scan after water exposure, relative to the signals before water exposure, in the $BMIMBF_4$ sample supports the presence of the BMIM cascade. Disruption of this cascade during water exposure exposes the perovskite layer, leading to an increase in signal intensities post-NAP. The signal intensity increase observed in both the fresh and $BMIMBF_4$ samples from pre-NAP to post-NAP is significantly less than the increase observed in the $BMIMBF_4$ sample.

4.4. Conclusions

The XPS results presented in this chapter indicate that the mixed halide perovskite ink utilised in this study exhibits considerable resistance to thermal degradation up to a temperature of 150 °C. This is evident from the presence of perovskite phase peaks observed in the spectra recorded before and after heating to temperatures of 100 °C and 150 °C across all the studied samples. The XPS analysis further reveals the presence of the perovskite phase in the IL-modified samples deposited on SnO_2-coated Ti substrates even at 300 °C. This underscores the significant role played by both the SnO_2 ETL layer and the ionic liquids BMIMCl and $BMIMBF_4$ in conferring stability to the perovskite even at elevated temperatures of 300 °C.

Work function measurements were conducted on all the samples to probe into the structural changes that affect the enhanced thermal stability and to elucidate the roles played by SnO_2 and the ILs in this observed stability enhancement. The results from the work function measurements aid in comprehending how the two ILs interact with the perovskite, thereby leading to an improvement in the observed thermal stability. The work function results confirm the degradation of the pure perovskite samples upon heating to 300 °C. The reduction in the work function values observed in the IL-modified samples is correlated to the interaction between the IL and the perovskite. The nature

of this interaction is inferred through the changes in the work function values with temperature. We hypothesise that the BMIM cations of $BMIMBF_4$ form a cascade over the perovskite surface, a process facilitated by the documented interaction of the BF_4- ions with the hydroxyl groups on the SnO_2 layer. This hypothesis explains the superior thermal stability of the SnO_2/$BMIMBF_4$-Perovskite sample over the $BMIMBF_4$-Perovskite sample by outlining the role played by SnO_2 in facilitating the formation of the BMIM cascade dipole layer.

In the case of the BMIMCl-modified samples, our hypothesis suggests that the small size and limited interaction of the chloride ions with the SnO_2 layer fail to create the required conditions for the formation of a BMIM cascade. Instead, in the case of BMIMCl, the BMIM cations diffuse into the perovskite grain boundaries, neutralising some of the surface defect sites and enhancing the film's crystallinity. This assertion is supported by the observation of perovskite Cl peaks and the absence of noticeable carbon-boron peaks in the C 1s spectra in the XPS analysis. Constant work function values observed up to 150 °C in all the samples with an underlying SnO_2 layer aid in comprehending the role played by SnO_2 in mitigating lattice stress induced by differences in the thermal expansion coefficients of the perovskite and the Ti substrate.

The interpretations of the work function analysis find further support through NEXAFS measurements of the samples. The NEXAFS results confirm the presence of the perovskite phase in the pure perovskite sample before heat treatment. NEXAFS spectra show individual and distinct features corresponding to the IL and perovskite, which helps with clearer differentiation between them. The changes in NEXAFS peak intensity highlight the significance of SnO_2 and heating in facilitating the incorporation of BMIMCl into the perovskite, thus explaining the difference observed in the work function values between the BMIMCl-Perovskite and SnO_2/BMIMCl-Perovskite samples prior to heating. NEXAFS results confirm the stability of both $BMIMBF_4$-modified perovskite samples, aligning with observations from XPS and work function analyses.

To understand the variations in perovskite degradation with sampling depth, HAXPES measurements were conducted on the samples. The HAXPES findings illustrate that the

observed perovskite degradation in the pure perovskite sample is predominantly a surface phenomenon, with the I/Pb ratio decreasing from the nominal perovskite stoichiometry to the lead halide ratio as the probing depth decreases. Consistent I/Pb ratios obtained from HAXPES measurements for the IL-modified samples across different probing depths further affirm the superior thermal stability of the IL-modified samples across the depth of the sample.

Evaluating the endurance of IL-modified samples against moisture is crucial for understanding their overall stability. The NAP-XPS findings indicate that the IL-modified samples demonstrate favourable stability when exposed to water, evident from the presence of the perovskite peak in the scans. Specifically, the BMIMCl-modified samples show greater resistance to moisture penetration compared to the $BMIMBF_4$-modified samples. The initial hypothesis regarding the interaction mechanism between ILs and perovskite is employed to explain the NAP measurements. Our observations reasonably align with our hypothesis, contributing to a better understanding of the results.

Heat and moisture are key environmental stressors contributing to the instability of perovskite solar cells. Our results show that IL-modified perovskites have increased stability to both. These results are particularly valuable because there is an extensive body of literature discussing the performance of IL-modified perovskites, while there are very few fundamental studies that focus on their structural stability. Our study bridges this gap by providing a deeper understanding of how these modifications affect the structural integrity of perovskite films.

References

1. Liu, D., et al., *Yb-doped SnO2 electron transfer layer assisting the fabrication of high-efficiency and stable perovskite solar cells in air.* RSC Advances, 2022. **12**(23): p. 14631-14638.

2. Bai, Y., et al., *Enhancing stability and efficiency of perovskite solar cells with crosslinkable silane-functionalized and doped fullerene.* Nature Communications, 2016. **7**(1): p. 12806.

3. Grancini, G., et al., *One-Year stable perovskite solar cells by 2D/3D interface engineering.* Nature Communications, 2017. **8**(1): p. 15684.

4. Lin, C.-T., et al., *Passivation against oxygen and light induced degradation by the PCBM electron transport layer in planar perovskite solar cells.* Sustainable Energy & Fuels, 2018. **2**(8): p. 1686-1692.

5. Yang, G., et al., *Stable and low-photovoltage-loss perovskite solar cells by multifunctional passivation.* Nature Photonics, 2021. **15**(9): p. 681-689.

6. Liu, X., et al., *Synergy Effect of a π-Conjugated Ionic Compound: Dual Interfacial Energy Level Regulation and Passivation to Promote Voc and Stability of Planar Perovskite Solar Cells.* Angewandte Chemie International Edition, 2022. **61**(11): p. e202117303.

7. Xia, R., et al., *Retarding Thermal Degradation in Hybrid Perovskites by Ionic Liquid Additives.* Advanced Functional Materials, 2019. **29**(22): p. 1902021.

8. Ghosh, S. and T. Singh, *Role of ionic liquids in organic-inorganic metal halide perovskite solar cells efficiency and stability.* Nano Energy, 2019. **63**: p. 103828.

9. Wan, Y., et al., *Ionic liquid-assisted perovskite crystal film growth for high performance planar heterojunction perovskite solar cells.* RSC Advances, 2016. **6**(100): p. 97848-97852.

10. Luo, C., et al., *Passivation of defects in inverted perovskite solar cells using an imidazolium-based ionic liquid.* Sustainable Energy & Fuels, 2020. **4**(8): p. 3971-3978.

11. Xia, X., et al., *Functionalized Ionic Liquid-Crystal Additive for Perovskite Solar Cells with High Efficiency and Excellent Moisture Stability.* ACS Applied Materials & Interfaces, 2021. **13**(15): p. 17677-17689.

12. Zhang, W., et al., *Interface Engineering of Imidazolium Ionic Liquids toward Efficient and Stable CsPbBr3 Perovskite Solar Cells.* ACS Applied Materials & Interfaces, 2020. **12**(4): p. 4540-4548.

13. Seo, J.-Y., et al., *Ionic Liquid Control Crystal Growth to Enhance Planar Perovskite Solar Cells Efficiency.* Advanced Energy Materials, 2016. **6**(20): p. 1600767.

14. Zhu, X., et al., *High-Efficiency Perovskite Solar Cells with Imidazolium-Based Ionic Liquid for Surface Passivation and Charge Transport.* Angewandte Chemie International Edition, 2021. **60**(8): p. 4238-4244.

15. Bai, S., et al., *Planar perovskite solar cells with long-term stability using ionic liquid additives.* Nature, 2019. **571**(7764): p. 245-250.

16. Wang, F., et al., *Ionic Liquid Engineering in Perovskite Photovoltaics.* ENERGY & ENVIRONMENTAL MATERIALS, 2022. **n/a**(n/a): p. e12435.

17. Du, Y., et al., *Ionic Liquid Treatment for Highest-Efficiency Ambient Printed Stable All-Inorganic CsPbI3 Perovskite Solar Cells.* Advanced Materials, 2022. **34**(10): p. 2106750.

18. Yang, Q., et al., *Ionic liquids and derived materials for lithium and sodium batteries.* Chemical Society Reviews, 2018. **47**(6): p. 2020-2064.

19. Deng, X.Y., et al., *Ionic liquids engineering for high-efficiency and stable perovskite solar cells.* Chemical Engineering Journal, 2020. **398**: p. 17.

20. Lin, Y.-H., et al., *A piperidinium salt stabilizes efficient metal-halide perovskite solar cells.* Science, 2020. **369**(6499): p. 96-102.

21. Zhang, Y., et al., *A Strategy to Produce High Efficiency, High Stability Perovskite Solar Cells Using Functionalized Ionic Liquid-Dopants.* Advanced Materials, 2017. **29**(36): p. 1702157.

22. Yang, D., et al., *Surface optimization to eliminate hysteresis for record efficiency planar perovskite solar cells.* Energy & Environmental Science, 2016. **9**(10): p. 3071-3078.

23. Zhang, J., et al., *Boosting Photovoltaic Performance for Lead Halide Perovskites Solar Cells with BF4− Anion Substitutions.* Advanced Functional Materials, 2019. **29**(47): p. 1808833.

24. Yang, L., et al., *Large-scale synthesis of CH3NH3BF4 crystal and its application on CH3NH3PbBrx(BF4)(3-x) perovskite thin films.* Chemical Physics Letters, 2020. **754**: p. 137638.

25. Chen, Q., et al., *The optoelectronic role of chlorine in CH3NH3PbI3(Cl)-based perovskite solar cells.* Nature Communications, 2015. **6**(1): p. 7269.

26. Lian, Z., et al., *Perovskite CH3NH3PbI3(Cl) Single Crystals: Rapid Solution Growth, Unparalleled Crystalline Quality, and Low Trap Density toward 108 cm–3.* Journal of the American Chemical Society, 2016. **138**(30): p. 9409-9412.

27. Fan, L., et al., *Elucidating the role of chlorine in perovskite solar cells.* Journal of Materials Chemistry A, 2017. **5**(16): p. 7423-7432.

28. Yu, H., et al., *The Role of Chlorine in the Formation Process of "CH3NH3PbI3-xClx" Perovskite.* Advanced Functional Materials, 2014. **24**(45): p. 7102-7108.

29. Zhang, H., et al., *Controlled Substitution of Chlorine for Iodine in Single-Crystal Nanofibers of Mixed Perovskite MAPbI3–xClx.* Small, 2016. **12**(28): p. 3780-3787.

30. Min, H., et al., *Efficient, stable solar cells by using inherent bandgap of α-phase formamidinium lead iodide.* Science, 2019. **366**(6466): p. 749-753.

31. Cao, Y. and T. Mu, *Comprehensive Investigation on the Thermal Stability of 66 Ionic Liquids by Thermogravimetric Analysis.* Industrial & Engineering Chemistry Research, 2014. **53**(20): p. 8651-8664.

32. Colella, S., et al., *MAPbI3-xClx Mixed Halide Perovskite for Hybrid Solar Cells: The Role of Chloride as Dopant on the Transport and Structural Properties.* Chemistry of Materials, 2013. **25**(22): p. 4613-4618.

33. Qiao, W.-C., et al., *Metastable alloying structures in MAPbI3−xClx crystals.* NPG Asia Materials, 2020. **12**(1): p. 68.

34. Eliwi, A.A., et al., *Optimization of SnO2 electron transport layer for efficient planar perovskite solar cells with very low hysteresis.* Materials Advances, 2022. **3**(1): p. 456-466.

35. Maniyarasu, S., et al., *Role of Alkali Cations in Stabilizing Mixed-Cation Perovskites to Thermal Stress and Moisture Conditions.* ACS Applied Materials & Interfaces, 2021. **13**(36): p. 43573-43586.

36. Okejiri, F., et al., *Ultrasound-mediated synthesis of nanoporous fluorite-structured high-entropy oxides toward noble metal stabilization.* iScience, 2022. **25**(5): p. 104214.

37. Philippe, B., et al., *Chemical and Electronic Structure Characterization of Lead Halide Perovskites and Stability Behavior under Different Exposures—A Photoelectron Spectroscopy Investigation.* Chemistry of Materials, 2015. **27**(5): p. 1720-1731.

38. Lockett, V., et al., *Angle-resolved X-ray photoelectron spectroscopy of the surface of imidazolium ionic liquids.* Physical Chemistry Chemical Physics, 2008. **10**(9): p. 1330-1335.

39. Caporali, S., U. Bardi, and A. Lavacchi, *X-ray photoelectron spectroscopy and low energy ion scattering studies on 1-buthyl-3-methyl-imidazolium bis(trifluoromethane) sulfonimide.* Journal of Electron Spectroscopy and Related Phenomena, 2006. **151**(1): p. 4-8.

40. Park, B.-w., et al., *Stabilization of formamidinium lead triiodide α-phase with isopropylammonium chloride for perovskite solar cells.* Nature Energy, 2021. **6**(4): p. 419-428.

41. Calloni, A., et al., *Stability of Organic Cations in Solution-Processed CH3NH3PbI3 Perovskites: Formation of Modified Surface Layers.* The Journal of Physical Chemistry C, 2015. **119**(37): p. 21329-21335.

42. Steirer, K.X., et al., *Defect Tolerance in Methylammonium Lead Triiodide Perovskite.* ACS Energy Letters, 2016. **1**(2): p. 360-366.

43. m, n., Zubair, et al., *Instability in CH3NH3PbI3 perovskite solar cells due to elemental migration and chemical composition changes.* Scientific Reports, 2017. **7**(1): p. 15406.

44. Lee, J.-W., et al., *2D perovskite stabilized phase-pure formamidinium perovskite solar cells.* Nature Communications, 2018. **9**(1): p. 3021.

45. Cao, T., et al., *Interfacial Engineering via Inserting Functionalized Water-soluble Fullerene Derivative Interlayers for Enhancing Performance of Perovskite Solar Cells.* Journal of Materials Chemistry A, 2018. **6**.

46. Chen, P., et al., *In Situ Growth of 2D Perovskite Capping Layer for Stable and Efficient Perovskite Solar Cells.* Advanced Functional Materials, 2018. **28**(17): p. 1706923.

47. Rocks, C., et al., *Understanding surface chemistry during MAPbI3 spray deposition and its effect on photovoltaic performance.* Journal of Materials Chemistry C, 2017. **5**(4): p. 902-916.

48. Matsoso, B., et al., *Synthesis and characterization of boron carbon oxynitride films with tunable composition using methane, boric acid and ammonia.* New J. Chem., 2017. **41**.

49. Ulbrich, A., et al., *Surface Electronic Structure of [XMIm]Cl Probed by Surface-Sensitive Spectroscopy.* ChemPhysChem, 2012. **13**(7): p. 1718-1724.

50. Kot, M., et al., *Room temperature atomic layer deposited Al 2 O 3 on CH 3 NH 3 PbI 3 characterized by synchrotron-based X-ray photoelectron spectroscopy.* 2017.

51. Alberti, A., et al., *Similar Structural Dynamics for the Degradation of CH3NH3PbI3 in Air and in Vacuum.* ChemPhysChem, 2015. **16**(14): p. 3064-3071.

52. Schulz, P., et al., *Interface energetics in organo-metal halide perovskite-based photovoltaic cells.* Energy & Environmental Science, 2014. **7**(4): p. 1377-1381.

53. Lindblad, R., et al., *Electronic Structure of TiO2/CH3NH3PbI3 Perovskite Solar Cell Interfaces.* The Journal of Physical Chemistry Letters, 2014. **5**(4): p. 648-653.

54. Conings, B., et al., *Perovskite-Based Hybrid Solar Cells Exceeding 10% Efficiency with High Reproducibility Using a Thin Film Sandwich Approach.* Advanced Materials, 2014. **26**(13): p. 2041-2046.

55. Sadoughi, G., et al., *Observation and Mediation of the Presence of Metallic Lead in Organic–Inorganic Perovskite Films.* ACS Applied Materials & Interfaces, 2015. **7**(24): p. 13440-13444.

56. McGettrick, J., et al., *Sources of Pb(0) artefacts during XPS analysis of lead halide perovskites.* Materials Letters, 2019. **251**.

57. Williams, S.T., et al., *Role of Chloride in the Morphological Evolution of Organo-Lead Halide Perovskite Thin Films.* ACS Nano, 2014. **8**(10): p. 10640-10654.

58. Heo, J.H., et al., *Highly efficient CH3NH3PbI3−xClx mixed halide perovskite solar cells prepared by re-dissolution and crystal grain growth via spray coating.* Journal of Materials Chemistry A, 2016. **4**(45): p. 17636-17642.

59. Liu, Y., et al., *Enhanced electroluminescent efficiency with ionic liquid doped into PEDOT:PSS hole-injecting layer.* Polymer, 2015. **77**: p. 42-47.

60. Schultz, T., et al., *Reliable Work Function Determination of Multicomponent Surfaces and Interfaces: The Role of Electrostatic Potentials in Ultraviolet Photoelectron Spectroscopy.* Advanced Materials Interfaces, 2017. **4**(19): p. 1700324.

61. Deng, K., Q. Chen, and L. Li, *Modification Engineering in SnO2 Electron Transport Layer toward Perovskite Solar Cells: Efficiency and Stability.* Advanced Functional Materials, 2020. **30**(46): p. 2004209.

62. Caputo, M., et al., *Electronic structure of MAPbI3 and MAPbCl3: importance of band alignment.* Scientific Reports, 2019. **9**(1): p. 15159.

63. Noel, N.K., et al., *Elucidating the Role of a Tetrafluoroborate-Based Ionic Liquid at the n-Type Oxide/Perovskite Interface.* Advanced Energy Materials, 2020. **10**(4): p. 1903231.

64. Zhang, K., et al., *Role of Ionic Liquids in Perovskite Solar Cells.* Solar RRL, 2023. **7**(11): p. 2300115.

65. Jacobs, R., J. Booske, and D. Morgan, *Understanding and Controlling the Work Function of Perovskite Oxides Using Density Functional Theory.* Advanced Functional Materials, 2016. **26**(30): p. 5471-5482.

66. Huang, W., et al., *Probing Molecular and Crystalline Orientation in Solution-Processed Perovskite Solar Cells.* Advanced Functional Materials, 2015. **25**(34): p. 5529-5536.

67. Ehlert, C., et al., *A detailed assignment of NEXAFS resonances of imidazolium based ionic liquids.* Physical Chemistry Chemical Physics, 2016. **18**(12): p. 8654-8661.

68. Wagstaffe, M., et al., *Ionic Liquid Ordering at an Oxide Surface.* ChemPhysChem, 2016. **17**(21): p. 3430-3434.

69. Jung, M.-C., et al., *The presence of CH3NH2 neutral species in organometal halide perovskite films.* Applied Physics Letters, 2016. **108**(7): p. 073901.

70. McLeod, J.A., et al., *Self-Alignment of the Methylammonium Cations in Thin-Film Organometal Perovskites.* The Journal of Physical Chemistry Letters, 2014. **5**(16): p. 2863-2867.

71. Starr, D.E., et al., *Investigation of solid/vapor interfaces using ambient pressure X-ray photoelectron spectroscopy.* Chemical Society Reviews, 2013. **42**(13): p. 5833-5857.

72. Olivares-Xometl, O., et al., *Surface analysis of inhibitor films formed by imidazolines and amides on mild steel in an acidic environment.* Applied Surface Science, 2006. **252**(6): p. 2139-2152.

73. Raninga, R.D., et al., *Strong performance enhancement in lead-halide perovskite solar cells through rapid, atmospheric deposition of n-type buffer layer oxides.* Nano Energy, 2020. **75**: p. 104946.

74. Li, Y., et al., *Degradation by Exposure of Coevaporated CH3NH3PbI3 Thin Films.* The Journal of Physical Chemistry C, 2015. **119**(42): p. 23996-24002.

75. Chun-Ren Ke, J., et al., *In situ investigation of degradation at organometal halide perovskite surfaces by X-ray photoelectron spectroscopy at realistic water vapour pressure.* Chemical Communications, 2017. **53**(37): p. 5231-5234.

76. Liu, L., et al., *Tracking the formation of methylammonium lead triiodide perovskite.* Applied Physics Letters, 2015. **107**(6): p. 061904.

77. Arabpour Roghabadi, F., V. Ahmadi, and K. Oniy Aghmiuni, *Organic–Inorganic Halide Perovskite Formation: In Situ Dissociation of Cation Halide and Metal Halide Complexes during Crystal Formation.* The Journal of Physical Chemistry C, 2017. **121**(25): p. 13532-13538.

78. Maniyarasu, S., et al., *Surface stability of ionic-liquid-passivated mixed-cation perovskite probed with in situ photoelectron spectroscopy.* Journal of Materials Chemistry A, 2022. **10**(35): p. 18206-18217.

79. Seth, C. and D. Khushalani, *Degradation and regeneration of hybrid perovskites.* RSC Advances, 2016. **6**(104): p. 101846-101852.

80. Nishihata, Y., et al., *Self-regeneration of a Pd-perovskite catalyst for automotive emissions control.* Nature, 2002. **418**(6894): p. 164-167.

81. Lin, H.-M., et al., *Solubility of selected dibasic carboxylic acids in water, in ionic liquid of [Bmim][BF4], and in aqueous [Bmim][BF4] solutions.* Fluid Phase Equilibria, 2007. **253**(2): p. 130-136.

Chapter 5. Additive Engineering of Perovskite using Trimethylamine N-oxide and Betaine

5.1. Introduction

In the case of perovskite-based solar cell devices, an inherent instability arises from charge accumulation, a pivotal factor contributing to their degradation. Within the structure of the perovskite thin film, the emergence of defect sites assumes a critical role, serving as focal points for recombination. This interplay often traps charges, causing a pronounced degradation of the device [1-3].

Despite the high defect tolerance intrinsic to perovskites, the efficacy of charge extraction by the electron transport layers (ETLs) remains imperfect [4]. This imperfection results in an accumulation of charges at the interface between the perovskite and the ETLs. The accumulation of charges forms a barrier impeding the transport of electrons, thereby increasing the chances of non-radiative recombination [5].

Numerous strategies have been deployed to mitigate the aggregation of charge carriers and to refine electron extraction techniques. These strategies include the integration of interfacial modification layers; the passivation of ETLs through the incorporation of functional additives; and the introduction of an electrical dipole layer [4, 6-10]. The motivation for introducing electrical dipoles originates from experimental studies which show that subjecting perovskite solar cells (PSCs) to a reverse bias can substantially boost charge extraction, consequently enhancing the stability of these devices [11].

Many previous studies in the literature have concentrated on the insertion of a dipole layer at the interface. However, the study of IL-modified perovskite samples in chapter 4 has provided compelling evidence on the effectiveness of incorporating polar molecules into the perovskite matrix, culminating in the generation of an electric dipole. This reduces the work function and improves the stability of the perovskite.

In this chapter, we explore this approach further. Specifically, we undertake the integration of the two zwitterionic methylamines, namely trimethylamine oxide (TMAO) and betaine, into the perovskite precursor solution. This investigation aims to understand their impact on the structural integrity and stability of the perovskite when subjected to thermal and moisture stresses.

The motivation to use methylamines for our additive engineering of perovskites comes from nature. TMAO and betaine are naturally occurring substances in the metabolism of animals [12, 13]. They have been shown to have a protein stabilising effect in deep sea organisms in an otherwise destabilising aqueous urea environment. Yancey et al. found that the level of methylamines (TMAO and Betaine) increases with depth in the muscles of several deep sea teleost fishes and anemones [14]. It attains notably high concentrations in the deepest-known fish species, *Pseudoliparis swirei*, discovered in the Mariana Trench, at an astounding recorded depth of 8,076 meters. Yancey et al. report that TMAO, and to a lesser extent betaine, play a pivotal role in stabilising proteins against the inhibitory effects of the hydrostatic pressure.

Numerous studies have proposed that TMAO exerts a discernible influence on the water structure. Several experimental approaches have supported the existence of immobilised or stationary water entities within the complexes formed by TMAO and water [15, 16]. Hunger et al. postulated a mechanism involving a water-mediated interaction between TMAO and urea [17]. Central to their proposition are complexes of $TMAO{\cdot}3H_2O$, wherein the hydrated water molecules associated with TMAO effectively establish one or more protective layers, serving as a barrier between TMAO and the donor sites of urea.

Given the documented tendency of TMAO to create protective environments and establish stable complexes with water, the motive for this study is that TMAO and Betaine might offer safeguarding qualities to our perovskite, potentially shielding it from degradation.

Additive engineering of perovskites has shown great promise for passivating defects and governing the crystallisation process, thereby improving the quality of the perovskite film. While most additives exhibit an affinity for either positively or negatively charged defects, the uniqueness of zwitterionic molecules lies in their capacity to effectively passivate both types of defects, owing to their possession of dual positive and negative charges.

These zwitterionic molecules demonstrate a remarkable versatility in their ability to neutralise positively charged undercoordinated Pb^{+2} sites, stemming from the loss of iodide ions (I^-), as well as negatively charged Pb-I antisites, originating from the loss of methylammonium ions (MA^+). Additionally, their efficacy extends to mitigating defects at grain boundaries, comprehensively addressing a spectrum of structural aberrations within the perovskite matrix.

The reduction in trap density, facilitated by the passivation of these defect sites, helps improve the stability of the device. Zwitterionic species based on betaine have shown proficiency in passivating lattice defects and enhancing the stability of the perovskite structure [18]. This shows the potential of betaine-based zwitterionic species as promising candidates for improving perovskite stability through additive engineering methodologies.

A few previous studies have reported that the modification of the ETL with TMAO can modify the work function of the ETL, passivate surface defects within the perovskite, refine the crystallisation process, and curtail charge recombination. These studies have mainly focused on the modification of the ETL itself using TMAO. To the best of our knowledge, there have been no studies exploring the direct incorporation of TMAO or its counterpart, betaine, into the perovskite precursor solution.

The compound TMAO, chemically denoted as $(CH_3)_3NO$, falls within the category of amine oxides. Although this compound does exist in an anhydrous form, it is predominantly encountered in its dihydrate state, which was utilised in our experiments. Both variations, whether anhydrous or hydrated, manifest as white, water-

soluble solids. The 3D representation and the chemical structure of TMAO are depicted in Figure 5.1 below.

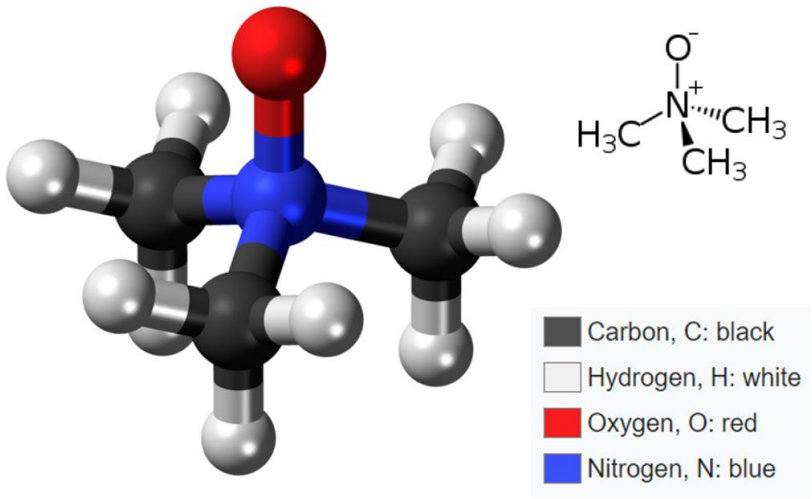

Figure 5.1 The chemical structure of trimethylamine oxide (TMAO).

The experimentally reported dipole moment of TMAO stands at 5.0 Debye [19]. However, when in a complex with water, the effective dipole moment significantly increases to 10.7 Debye [15]. Notably, 90% of TMAO's dipole moment arises from the $N^+—O^-$ component, which characterises the hydrophilicity of the TMAO [20]. The hydrophilic part of TMAO can form very strong hydrogen bonds with water molecules, reducing the number of water molecules available for hydrating a biomolecule [20]. These strong hydrogen bonds are also responsible for the restricted rotation of the OH groups giving rise to the slowing down effect of water molecules near TMAO as discussed above.

In chemistry, a betaine constitutes a neutral chemical compound featuring a positively charged cationic functional group devoid of a hydrogen atom, such as a quaternary ammonium or phosphonium cation, and with a negatively charged functional group, such as a carboxylate group nonadjacent to the cationic site.

Historically, the term "betaine" was originally reserved for trimethylglycine (TMG) or glycine betaine, as it was the first betaine discovered. In this chapter, trimethylglycine is referred to as betaine to avoid any confusion with TMAO. Figure 5.2 depicts the 3D and

chemical structure of betaine, an amphiphilic compound with a hydrophobic positive end and a hydrophilic negative end.

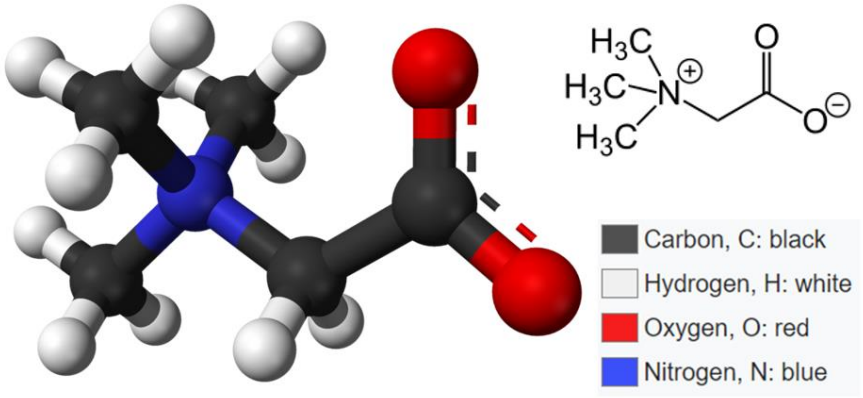

Figure 5.2 The chemical structure of betaine.

5.2. Experimental

5.2.1. Materials

$MAPbI_{3-x}Cl_x$ perovskite precursor ink (I101) was purchased from Ossila. Trimethylamine N-oxide dehydrate (98%) and Tin(IV) oxide, 15% in H_2O colloidal dispersion were purchased from Thermo Fisher Scientific. Betaine was purchased from Fluorochem.

5.2.2. Substrate Preparation

Samples were fabricated on titanium foil substrates. The substrates underwent a sequential cleaning process involving a 2% Hellmanex solution, deionized water, acetone, and isopropanol. Each step was carried out in an ultrasonic bath for 15 minutes with the substrates immersed in the respective solution. Following the sonication, the substrates were rinsed with isopropanol and dried using a nitrogen gun.

5.2.3. Thin Film Deposition

Sample fabrication was performed at the University of Central Lancashire, UK. The substrates were spin-coated with a layer of SnO_2 prior to perovskite deposition. To achieve this, 50 µl of a 15% SnO_2 solution in H_2O colloidal dispersion was spin-coated onto cleaned substrates at 3000 rpm for 30 seconds. Subsequently, the coated substrates were annealed at 150 °C for 40 minutes on a hotplate.

For the perovskite deposition, the precursor ink (I101, Ossila) was activated by placing it on a hotplate at 70 °C for 2 hours to ensure complete solute re-dissolution. Following this step, three separate solutions were prepared, each containing 0.3 mol% of TMAO, 0.3 mol% betaine and 0.15 mol% each of both TMAO and betaine in the perovskite precursor ink. These solutions were also heated on a hotplate at 70 °C for approximately 10 minutes to facilitate dissolution. The TMAO solution turned dark red immediately after placing it on a hot plate as shown in Figure 5.3.

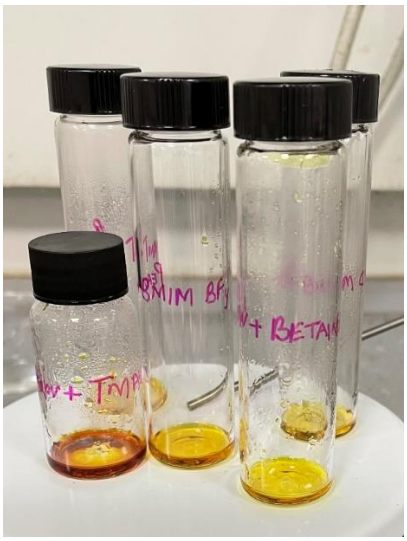

Figure 5.3 Modified perovskite precursor ink solutions.

For deposition, 50 µl of the modified precursor inks were spin-coated onto the SnO_2 coated titanium foil substrates. The spin-coating was carried out at 3000 rpm for 30 seconds. After spin-coating, the substrates were annealed at 90 °C for 120 minutes and subsequently transferred into a nitrogen-filled glovebox for storage.

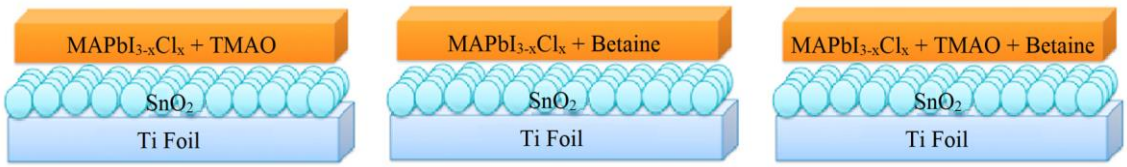

Figure 5.4 A schematic representation of the TMAO/Betaine-modified perovskite samples utilised in this study. The modified perovskite ink is deposited onto a layer of SnO_2-coated Ti foil substrate.

5.2.4. Storage and transfer of the samples

The samples were carefully stored in a nitrogen-filled plastic container, placed atop a layer of zeolite molecular sieve beads. This setup was employed to ensure the maintenance of dry conditions to the greatest extent possible. Subsequently, the container was vacuum sealed with paraffin to prevent moisture ingress during transportation to external facilities.

Two fresh batches of samples were prepared and transported to the Henry Royce Facility within the University of Manchester, where XPS, AR-HAXPES and NAP-XPS measurements were carried out. The samples were briefly exposed to air before they were loaded into the load-lock chamber of the instrument.

The samples were mounted on tantalum sample plates by soldering them with tantalum strips before being introduced into the Ultra-High Vacuum (UHV) systems for characterisation.

5.2.5. XPS measurements

The thermal degradation analysis of the samples in an environment devoid of water vapour was conducted employing an ESCA 2SR X-ray photoelectron spectrometer (Scienta Omicron GmBH), operating under ultrahigh vacuum conditions, below 10^{-8} mbar. This instrument encompasses a monochromatic Al Kα source emitting at 1486.6

eV, delivering 20 mA emission power at 300 W, and an Argus CU hemispherical electron energy analyser.

To mitigate air exposure, the samples were expeditiously loaded from the vacuum desiccator into the load lock chamber and subsequently transferred to the analysis chamber for core level measurements. Heating of the sample plate was carried out using a resistive heating filament fixed to the sample's base plate. The spectral acquisition commenced once the pre-set temperature stabilised and this temperature was maintained throughout the experiment. XPS scans were taken at room temperature, 100 °C and 150 °C.

Survey spectra were acquired at pass energies of 200 eV, providing an overview, while high-resolution core level spectra were obtained at pass energies of 50 eV, enabling core level analysis. All core level spectra were background subtracted using the Shirley background model. Deconvolution of the spectra was conducted using Gaussian/Lorentzian GL(30), employing a composition of 70% Gaussian and 30% Lorentzian line shapes within the CasaXPS software.

Peak intensities were corrected by employing their respective RSFs derived from the Scofield library. The charge correction process posed a significant challenge in the sample analysis. Initial attempts at calibrating to Sn $3d_{5/2}$ yielded inconsistent values for the metallic lead's BE, an unexpected fluctuation within our sample set. Consequently, the spectra were charge-corrected against the metallic lead (Pb^0) Pb $4f_{7/2}$ peak at 137.0 eV. This shift was prompted by the consistent presence of a Pb^0 doublet in all samples.

This charge correction, however, causes a variance in the binding energy of the Sn 3d doublet peaks across the spectra. Thus, interpreting the binding energies requires a cautious approach. We focus on the relative shifts in binding energy and changes in intensity of peaks with increasing temperature. Surface stoichiometries are calculated to offer insights into the composition and behaviour of the samples under thermal degradation.

5.2.6. AR-HAXPES measurements

AR-HAXPES analysis of the samples was conducted to investigate how the elemental composition varies with increasing depth within them. The experiments were conducted at the Henry Royce Institute, Manchester, utilising a Scienta Omicron GmbH high-throughput HAXPES instrument. This instrument has a Ga Kα metal jet X-ray source (Excillum, 9.25 keV) to generate monochromated high-energy X-rays. Focusing these X-rays precisely onto a 50 µm spot occurs through Bragg reflection off a silicon crystal. By employing an EW-4000 electron energy analyser, the spectrometer detects photoelectrons with KEs up to 12 keV, observed at a 90° angle relative to the incident X-rays.

The HAXPES measurements were taken under grazing emission (with the sample at a 40° angle relative to the analyser's normal). The grazing emission setup facilitated obtaining a series of photoemission spectra across various photoelectron emission angles (θ = 20°−60°, relative to the surface normal), allowing investigation into the sample at different depths, as depicted in Figure 4.4 in the preceding chapter.

To obtain data at different photoelectron emission angles, the data over selected angular ranges of the analyser were averaged. Please refer to Table 4.3 in the previous chapter for the specific angular ranges and corresponding photoelectron emission angles (θ) used in this study.

For determining atomic concentrations, RSFs for individual core levels were employed. These RSFs were adapted from Maniyarasu et al.'s work, specifically tailored for this HAXPES instrument [21]. A pass energy of 500 eV and analyser slit widths of 1.5 mm and 0.3 mm were used, resulting in total energy resolutions of 2 eV and approximately 0.5 eV, respectively.

Peak regions were created using the CasaXPS software, and the integrated peak areas were used in the determination of the atomic concentrations. Background subtraction was carried out using the Shirley model.

5.2.7. NAP-XPS measurements

NAP-XPS investigations were conducted at the Henry Royce Facility situated within the University of Manchester. The instrument uses a SPECS Focus 500 monochromated Al Kα source with a photon energy of 1486.6 eV and a SPECS 150 mm Phoibos 150 NAP hemispherical electron energy analyser. This analyser has a three-stage differentially pumped electrostatic lens directly linked to the NAP cell.

The experimental setup involved XPS measurements in two distinctive environments: firstly, within a conventional UHV chamber, and secondly, within a near-ambient pressure (NAP) cell, integrated with the entrance cone of the analyser lens system.

For the NAP-XPS experiments, the NAP cell was filled with H_2O vapor until a stabilised pressure of approximately 4.5 mbar was attained, correlating to a relative humidity (RH) of approximately 15%. These measurements were conducted under standard atmospheric conditions at a temperature of 25 ˚C.

XPS spectra were recorded before, during, and after exposure to water. Charge correction of the BE values was performed with reference to the Sn $3d_{5/2}$ peak at 487.6 eV [22], maintaining a precision of ±0.1 eV for all reported BE values. Survey spectra were measured at a pass energy of 60 eV, while core-level spectra were acquired at 30 eV pass energy. CasaXPS software was used to subtract a Shirley background from the data, and the core-level spectra were fitted using a GL(30) line shape. The inherent RSFs from CasaXPS (Kratos) were utilised to understand the intensity changes of peaks upon exposure to water.

5.3. Results and Discussion

5.3.1. XPS Results

It is important to highlight the limited prior research into perovskites using the NAP-XPS technique. To the best of our knowledge, no previous NAP-XPS studies have been carried out on betaine/TMAO modified perovskites. The C 1s core level spectra of the samples

are presented in Figure 5.5 (a-c) below. As stated in the experimental section, calibrating the BE of these spectra proved challenging. Consequently, the absolute BE values should be interpreted cautiously. Our focus lies in examining the relative shifts in peak intensity and positions with heating. Figure 5.5-a depicts the C 1s spectra of the TMAO-modified sample (SnO_2 + Perovskite + TMAO). Prior to heating, the spectra are fitted with peaks at 285.2 eV, 286.6 eV, 289.3 eV, and 293.7 eV. On heating the sample to 100 ˚C, peaks are fitted at 285.0 eV, 286.5 eV, 289.3 eV, and 293.5 eV. Elevating the sample temperature to 150 ˚C results in peak fits at 285.1 eV, 286.5 eV, 289.3 eV, and 293.6 eV.

The most intense peaks within the range of 285.0-285.2 eV can be attributed to hydrocarbon contamination. Peaks at 286.5 and 286.6 eV overlap with the C-N bond BE found in both the perovskite and the TMAO [23, 24]. The relative intensity of the C-N peak (relative to Pb 4f peaks) exhibits an increment from 19.9% to 25.6% and further to 33.8% as the temperature rises to 100 °C and 150 °C, respectively. Peaks at 289.3 eV may indicate products of hydrocarbon oxidation or result from the interaction of TMAO's O^- with methyl groups within the sample. Notably, an unexpected high BE peak in the range of 293.5-293.7 eV appears in all spectra. This peak appears at a similar binding energy to the potassium K 2p energy level; however, we do not expect any potassium impurities in our samples and no potassium K 2s peaks (at about ~380 eV) are evident in the wide scans of the sample. Therefore, we hypothesise this could be a shake-up satellite peak, which are found at similar binding energies in C 1s spectra.

A shake-up satellite peak typically arises from the interaction of the emitted photoelectron with the valence electrons of the sample. This interaction induces a loss of energy in the outgoing photoelectron, resulting in a peak appearing at a higher BE than the main peak of the spectra. Such shake-ups have been observed as intrinsic properties of certain molecules, even in gas-phase spectra [25]. Considering this, we attribute its presence to the chemical nature of TMAO, as this peak could not be detected in the betaine sample. Additionally, the BE difference between the shake-up satellite peak and the TMAO peak (293.7-286.6 eV ≈ 7eV) roughly corresponds to the bandgap of TMAO, a correlation observed in the case of phthalocyanines by Brena et al.

[26, 27]. The satellite peak intensity initially increases upon heating the sample to 100 °C, followed by a subsequent decrease as the sample is further heated to 150 °C.

This suggests that the increase in the C-N peak intensity with temperature mirrors the behaviour of the perovskite rather than the TMAO. This conclusion is drawn from the fact that despite the decrease in the intensity of the shake-up satellite peak of the TMAO, the C-N peak intensity continues to rise upon heating the sample to 150 °C.

Figure 5.5b illustrates the C 1s spectra of the Betaine-modified sample (SnO_2 + Perovskite + betaine). The spectra are fitted with peaks at 285.3 eV, 286.7 eV, and 289.1 eV before any heating. Subsequently, upon raising the temperature to 100 °C, the peaks are identified at 285.0 eV, 286.5 eV, and 289.1 eV. Further heating to 150 °C revealed peaks at 285.5 eV, 286.9 eV, and 289.4 eV.

The peaks within the range of 285.0—285.5 eV can be attributed to adventitious carbon contamination. The peaks falling within the range of 286.5—286.9 eV are likely associated with the C-N bond, originating from both betaine and the perovskite. The high-energy peaks above 289.1 eV are attributed to the O-C=O bond in betaine and the products of hydrocarbon oxidation. An increase in the intensity of the C-N peak is observed upon heating to 100 °C and then decreases as the sample is heated to 150 °C, respectively.

The C 1s spectra of the TMAO+Betaine-modified sample (SnO_2 + Perovskite + TMAO + Betaine) is depicted in Figure 5.5c. Initially, the spectra are fitted with peaks at 285.2 eV, 286.7 eV, 289.3 eV, and 293.4 eV before any heating. Subsequent heating of the sample at 100 °C reveals peaks fitted at 285.0 eV, 286.6 eV, 289.3 eV, and 293.4 eV. The spectra recorded at 150 °C show peaks at 285.3 eV, 286.8 eV, and 289.3 eV.

The peaks within the range of 285.0–285.3 eV, 286.6–286.8 eV and 289.3 eV are assigned to adventitious carbon, C-N bond and O-C=O bond, respectively as explained in the previous two samples. A shake-up satellite peak at 293.4 eV can be identified in the spectra recorded at room temperature and at 100 °C. Unfortunately, data beyond 293.8 eV was not recorded at 150 °C so this peak cannot be identified. However, the

increase in intensity towards higher BE suggests the likely presence of the satellite peak at 150 °C. The intensity of the C-N peak increases with the increase in temperature.

The XPS survey spectra of the samples (refer to figure S6 in the appendix) exhibited minimal oxygen concentration, affirming that the peak assignments to C-N of the perovskite/methylamine chemistry are unlikely to stem from surface hydrocarbon oxidation products.

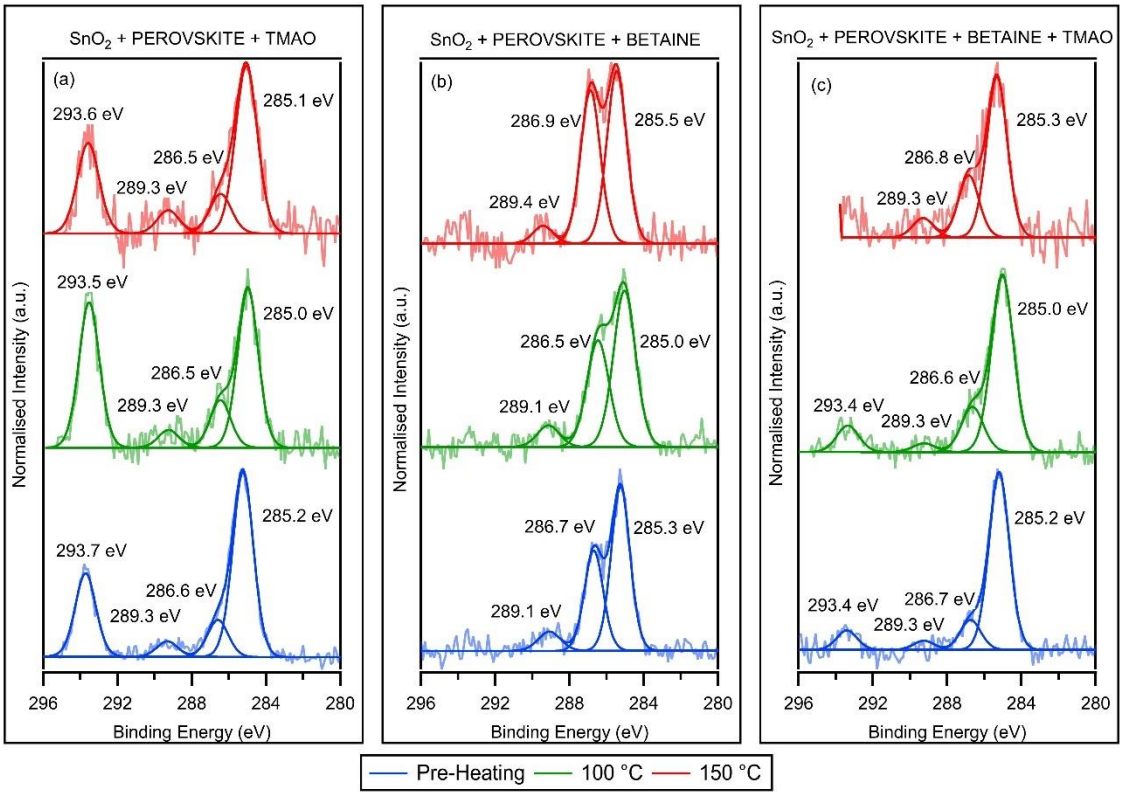

Figure 5.5 High resolution core level C 1s XPS spectra of perovskite modified with (a) TMAO, (b) Betaine, and (c) TMAO & Betaine. The peak intensities are normalised to the intensity of the adventitious carbon peak.

The Pb 4f core level spectra of the three samples are presented in Figure 5.6 (a-c). The Pb 4f spectra of the TMAO-modified sample (Figure 5.6a) display sharp doublet peaks consistently observed at 138.7 eV and 143.5 eV, alongside a weaker doublet consistently appearing at 137.0 eV and 141.9 eV across all temperatures. The peaks observed at 138.7 eV and 143.5 eV can be attributed to the spin-orbit splitting components, Pb $4f_{7/2}$

and Pb $4f_{5/2}$, corresponding to Pb^{+2} within the perovskite structure [28-30]. The doublet peaks at 137.0 eV and 141.9 eV are consistent with the BE of metallic lead Pb^0 [29]. The intensity of the Pb^0 peaks initially increases from 6.1% to 8.8% upon heating to 100 °C, followed by a decrease to 6.4% as the sample is further heated to 150 °C. This trend aligns with the intensity changes observed in the satellite peak of the C 1s spectra.

The Pb 4f spectra of the Betaine-modified sample are shown in Figure 5.6b. The spectra can be resolved into two doublets corresponding to Pb^{+2} in the perovskite and Pb^0 with binding energies identical to those of the doublets in the TMAO-modified sample. Unlike the TMAO-modified sample, the Pb^0 peak intensities exhibit a continuous increase with rising temperature, starting from 2.2% at room temperature, escalating to 8.2% at 100 °C, and further reaching 10.7% at 150 °C.

In Figure 5.6c, the Pb 4f spectra of the TMAO+Betaine-modified sample are presented. Consistently, a doublet at 137.0 eV and 141.9 eV, indicative of Pb^0, is discernible across all spectra. The Pb^{+2} doublet is fitted at 138.6 eV and 143.5 eV in spectra recorded before heating and at 138.7 eV and 143.6 eV when the sample is heated to 100 °C and 150 °C. These Pb^{+2} doublet values align with widely reported binding energy values for Pb in the perovskite. The intensity of the metallic lead peaks exhibits a progressive increase, starting at 2.2% at room temperature and rising to 14.4% and 16.0% as the sample is heated to 100 °C and 150 °C, respectively.

It must be noted that Pb^0 has been previously reported to be produced by X-ray beam irradiation of perovskite samples [31]. While the proportion of metallic lead to the total lead is highest in the TMAO-modified sample before heating, it displays the lowest percentage of metallic lead at 150 °C. Notably, the TMAO-modified sample stands out as the only sample where the percentage of metallic lead initially increases at 100 °C and subsequently decreases upon further heating to 150 °C. Conversely, both the Betaine-modified and the TMAO+Betaine-modified samples consistently demonstrate a continuous rise in metallic lead content as the sample is heated to 100 °C and 150 °C.

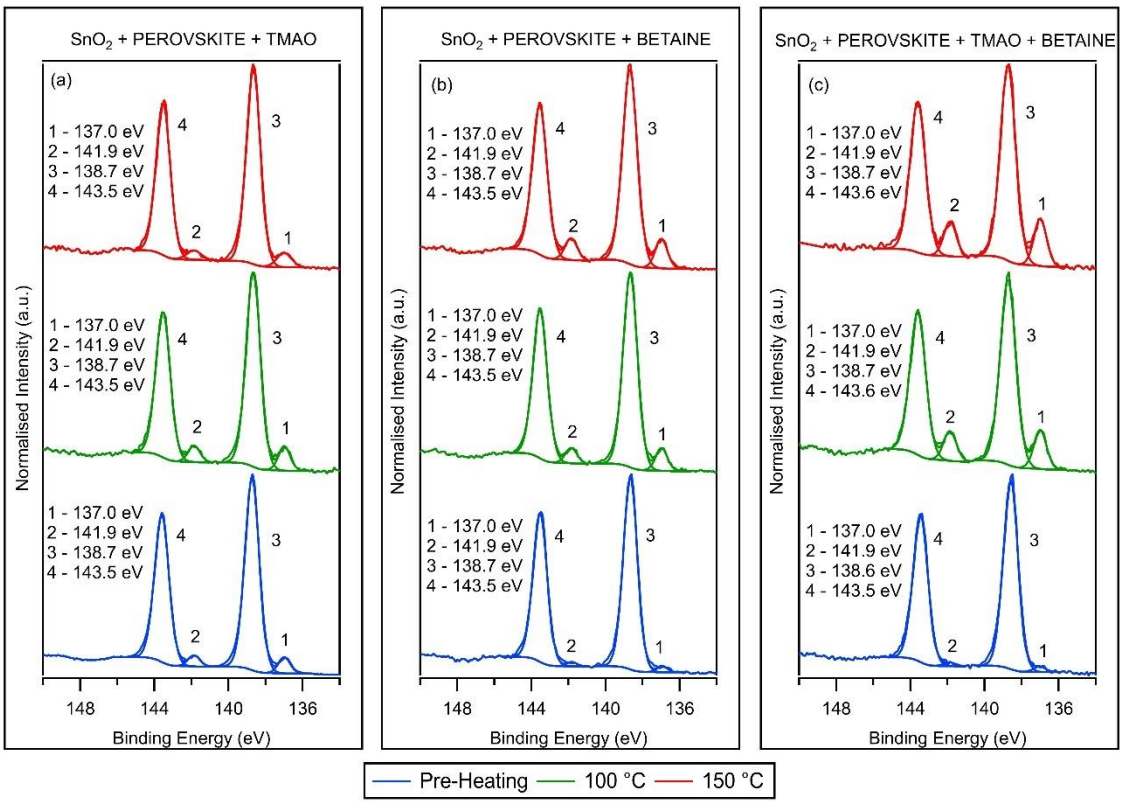

Figure 5.6 High resolution core level Pb 4f XPS spectra of perovskite modified with (a) TMAO, (b) Betaine, and (c) TMAO & Betaine. The peak intensities are normalised to the intensity of the highest peak.

The I 3d core level spectra are presented in Figure 5.7 (a-c). The large shifts observed in the BE values of the I 3d peaks are likely caused by charge correction issues, as previously discussed, rather than indicative changes within the sample. To gain a more comprehensive understanding of these peaks, their intensities are compared, and a further analysis involving the I/Pb atomic ratios is undertaken.

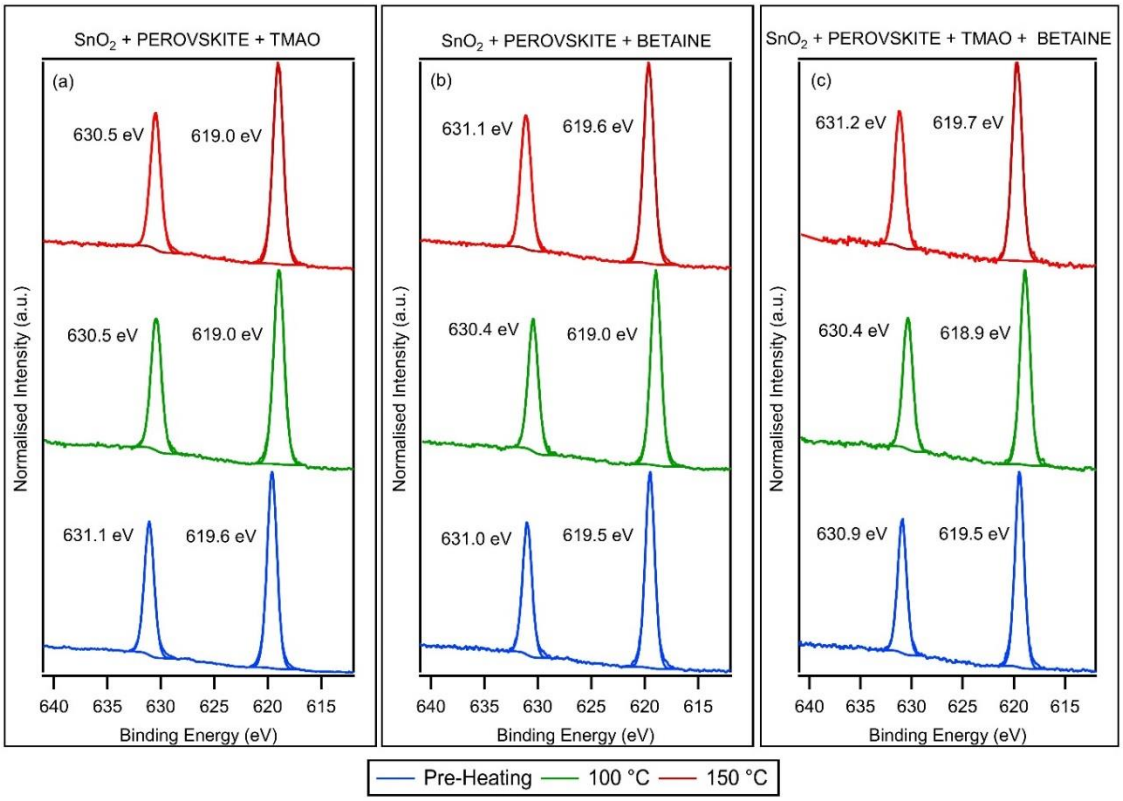

Figure 5.7 High resolution core level I 3d XPS spectra of perovskite modified with (a) TMAO, (b) Betaine, and (c) TMAO & Betaine. The peak intensities are normalised to the intensity of the highest peak.

The I 3d and Pb 4f peak areas served as the basis for calculating the I/Pb^{+2} ratios, as shown in Figure 5.8. The Pb^{+2} component areas were used in the determination of the I/Pb ratios instead of the total Pb areas as Pb^{+2} signals are expected to be coming from the undegraded perovskite phase. The I/Pb^{+2} ratios across all samples closely mirror the nominal stoichiometry of the mixed halide perovskite.

The TMAO-modified and Betaine-modified samples exhibit ratios of 2.7 and 2.6 at room temperature, respectively, with values increasing to 3.0 at 100 °C and 150 °C. In contrast, the TMAO+Betaine-modified sample exhibits a ratio of 2.6 before heating and steadily ascends to 2.7 and 2.9 as the temperature is raised to 100 °C and 150 °C, respectively.

A ratio of 3.0 corresponds to $CH_3NH_3PbI_3$, which suggests that the temperature rise might have prompted the loss of chlorine from the perovskite lattice. The observed rise

in the C-N bond intensity (assigned to the perovskite), as evidenced in the C 1s spectra of the samples, is matched by the increase in the I/Pb^{+2} ratios. This increase implies that both TMAO and betaine play roles in facilitating the incorporation of MAI within the perovskite lattice.

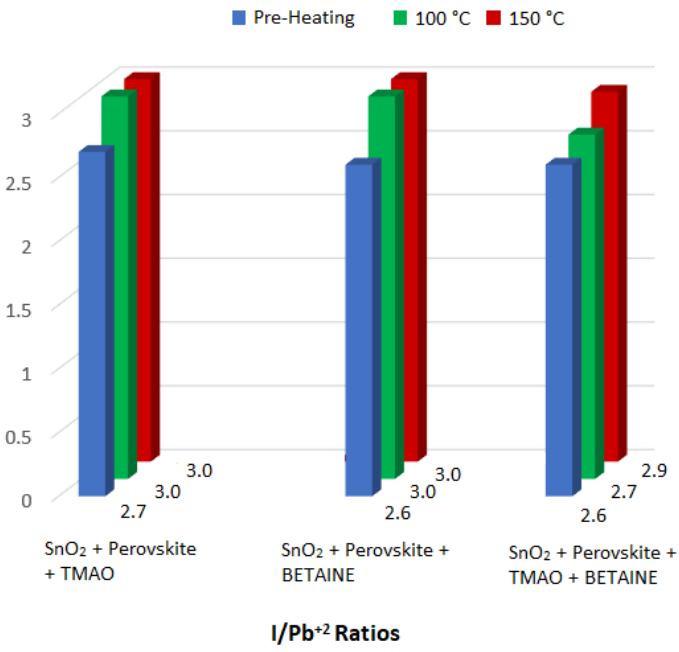

Figure 5.8 I/Pb^{+2} ratios of the samples at different temperatures.

5.3.2. HAXPES results

The investigation using XPS targeted the surface layers of the perovskite samples, where decomposition and contamination is likely to be more prominent. Transitioning to HAXPES, we venture beyond surface analysis. By using a higher photon energy, HAXPES generated photoelectrons have an increased kinetic energy and substantially larger Inelastic Mean Free Paths (IMFPs). This allows a deeper examination of our samples to tens of nanometers below the surface and allows a comparison between surface and bulk composition.

In HAXPES spectra, the Pb and I peaks with the highest intensities are the I 2p and the Pb 3d levels (rather than the I 3d and Pb 4f in standard XPS spectra). The core levels I $2p_{3/2}$ and Pb $3d_{5/2}$ exhibited BE values around ~4557 and ~2484 eV, respectively. Utilising

the integrated peak areas of these core level signals, the I/Pb ratios for the samples were derived. To explore variations in composition with sampling depth, the I 2p and Pb 3d core levels were recorded as a function of the photoelectron emission angle.

The samples were rotated to a 40° angle with respect to the analyser's normal. Employing the angular 45 mode of the analyser during HAXPES measurements enabled data collection across a range of sampling depths, as discussed in section 4.2.7. The data acquired in this configuration is characterised by cosine θ values ranging between 0.46 and 0.95. The relationship between cos θ and the sampling depth have been detailed in the previous chapter.

The calculated I/Pb ratios for the samples are extrapolated from the angular modes of the analyser and plotted against the cosine of the emission angle (cos (θ)).

Figure 5.9 shows contour plots (binding energy vs sampling depth) illustrating the intensities of the I $2p_{3/2}$ and Pb $3d_{5/2}$ core levels with sampling depth (cos θ = 0.46—0.95). These plots were generated based on data obtained from the angular mode of the analyser. The I/Pb ratios, extracted from data points acquired in the angular mode, are tabulated in Table 5.1. These ratios were calculated from slices of the contour plots, a method detailed in the experimental section of Chapter 3. The angular mode scans were taken both before and after heating the samples (after taking XPS scans). Regrettably, due to time constraints, post-heating HAXPES measurements could not be conducted for the Betaine-modified sample.

In Table 5.1, the I/Pb ratios for the TMAO-modified samples pre- and post-heating are detailed, while their corresponding contour plots are illustrated in Figure 5.9. The I/Pb ratios obtained before and after heating for the TMAO-modified sample align closely with the anticipated stoichiometry of the mixed halide perovskite (2.5-2.9).

Figure 5.10 and Table 5.1 present the I/Pb ratios with depth in the Betaine-modified sample. These ratios exhibit values slightly above nominal stoichiometric levels, ranging between 3.1 and 3.3. In contrast, the ratios derived from the TMAO+Betaine-modified

sample (Figure 5.11) consistently align with the nominal values both before and after heating.

TMAO-modified sample			
Cos θ	Average Sampling Depth	I/Pb Pre-heating	I/Pb Post-heating
0.46	14.5 nm	2.8	2.7
0.54	17.0 nm	2.8	2.7
0.61	19.2 nm	2.8	2.7
0.89	28.0 nm	2.8	2.8
0.92	29.0 nm	2.8	2.8
0.95	29.9 nm	2.8	2.9
Betaine-modified sample			
Cos θ	Average Sampling Depth	I/Pb Pre-heating	
0.46	14.5 nm	3.1	
0.54	17.0 nm	3.1	
0.61	19.2 nm	3.2	
0.89	28.0 nm	3.2	
0.92	29.0 nm	3.3	
0.95	29.9 nm	3.1	
TMAO+Betaine-modified sample			
Cos θ	Average Sampling Depth	I/Pb Pre-heating	I/Pb Post-heating
0.46	14.5 nm	1.9	2.7
0.54	17.0 nm	2.7	2.7
0.61	19.2 nm	2.7	2.7
0.89	28.0 nm	2.6	2.9
0.92	29.0 nm	2.6	2.9
0.95	29.9 nm	2.8	2.9

Table 5.1 The I/Pb ratios of the samples plotted against the HAXPES probing depth. Cos θ denotes the cosine of the photoelectron emission angle measured from the surface normal.

The observed ratios consistently mirror the anticipated perovskite stoichiometry, indicating the that both TMAO and betaine may be effective in preventing the thermal degradation of the perovskite. The typical dissociation of perovskite into PbI_2 often results in iodine outgassing into the UHV, subsequently decreasing the I/Pb ratio. The absence of any decrease in the ratio post-heating suggests the suppression of lead iodide formation, attributed to the incorporation of TMAO and betaine into the perovskite lattice.

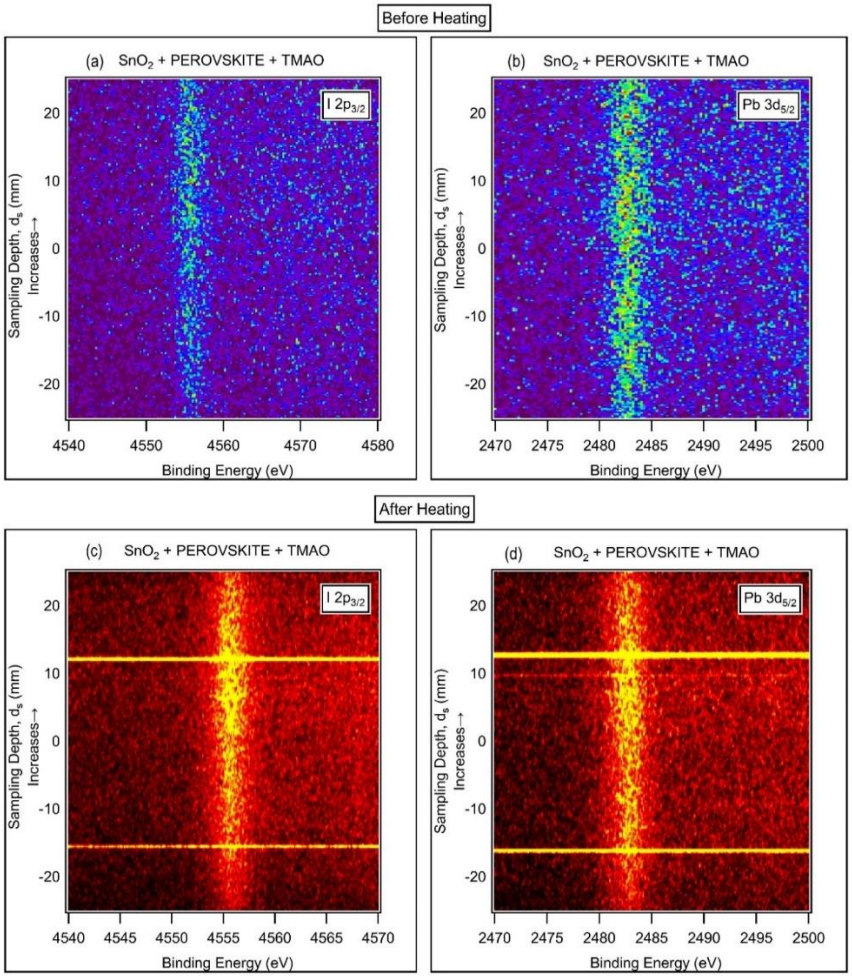

Figure 5.9 Contour plots (Binding energy vs Sampling depth) of I $2p_{3/2}$ and Pb $3d_{5/2}$ from angular mode measurements in the TMAO-modified perovskite sample. Note: the intense lines across the contours are artefacts from the analyser.

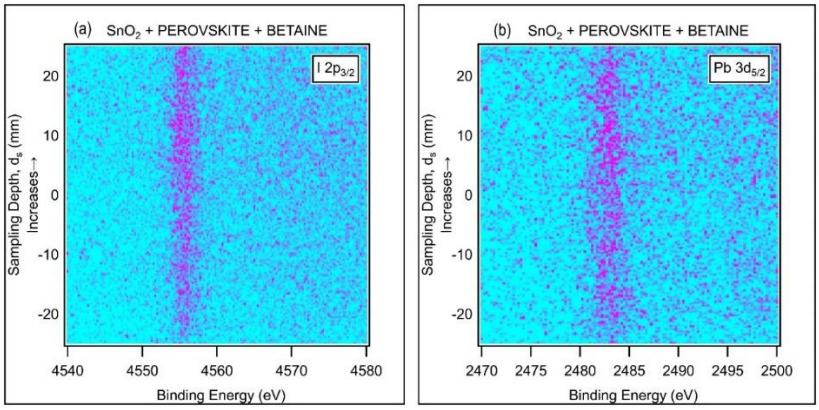

Figure 5.10 Contour plots (Binding energy vs Sampling depth) of I $2p_{3/2}$ and Pb $3d_{5/2}$ from angular mode measurements in the Betaine-modified perovskite sample.

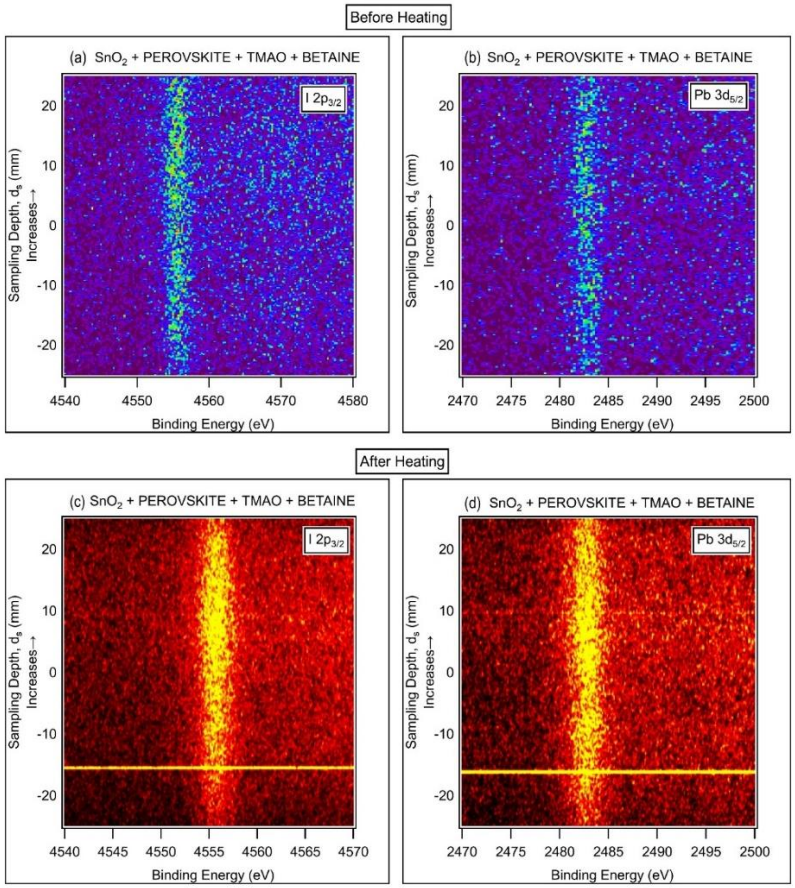

Figure 5.11 Contour plots (Binding energy vs Sampling depth) of I $2p_{3/2}$ and Pb $3d_{5/2}$ from angular mode measurements in the TMAO+Betaine-modified perovskite sample. Note: the intense lines across the contours are artefacts from the analyser.

5.3.3. NAP-XPS results

NAP-XPS was used to evaluate the moisture endurance of the samples. This investigation was carried out within the NAP gas cell, where the introduction of water vapor elevated the pressure to 4.5 mbar, roughly equating to a relative humidity of 15% at 25 °C.

To complement the NAP measurements, XPS was conducted both pre- and post-exposure of the samples to water vapor within a controlled UHV environment. This methodology allows any changes that are induced by water exposure to be observed and allows a thorough assessment of the influence of moisture on the samples.

The survey spectra of the samples are included in the appendix of this thesis (please see figures S7 – S9). As noted in Chapter 4, the RSF values have not been calibrated for the analyser under NAP conditions. Consequently, the atomic concentrations presented alongside the survey spectra (computed using standard RSFs) are provided solely as a rough approximation of the sample composition and should be interpreted with caution. The C 1s core level spectra of the samples—before, during, and after water exposure—are depicted in Figure 5.12 (a-c) below. Within these spectra, three distinct components labelled 1, 2, and 3 are fitted. The primary and most prominent component (1) across all spectra is attributed to adventitious carbon contamination.

The second component (2) is linked to the C-N bond, likely originating from constituents within the perovskite, TMAO, and betaine present in the respective samples, which will all occur at similar binding energies. This shared assignment complicates the data analysis. However, the previous XPS analysis in section 5.3.1 suggests that the observed intensity change predominantly reflects alterations within the perovskite rather than the additives. The third component (3) is associated with carbon bonded to oxygen. This could arise from oxidised hydrocarbons within the sample, potential interactions between TMAO's oxygen and methyl groups, or the O-C=O group for the betaine sample. This multifaceted nature makes it challenging to definitively assign this peak to a single environment.

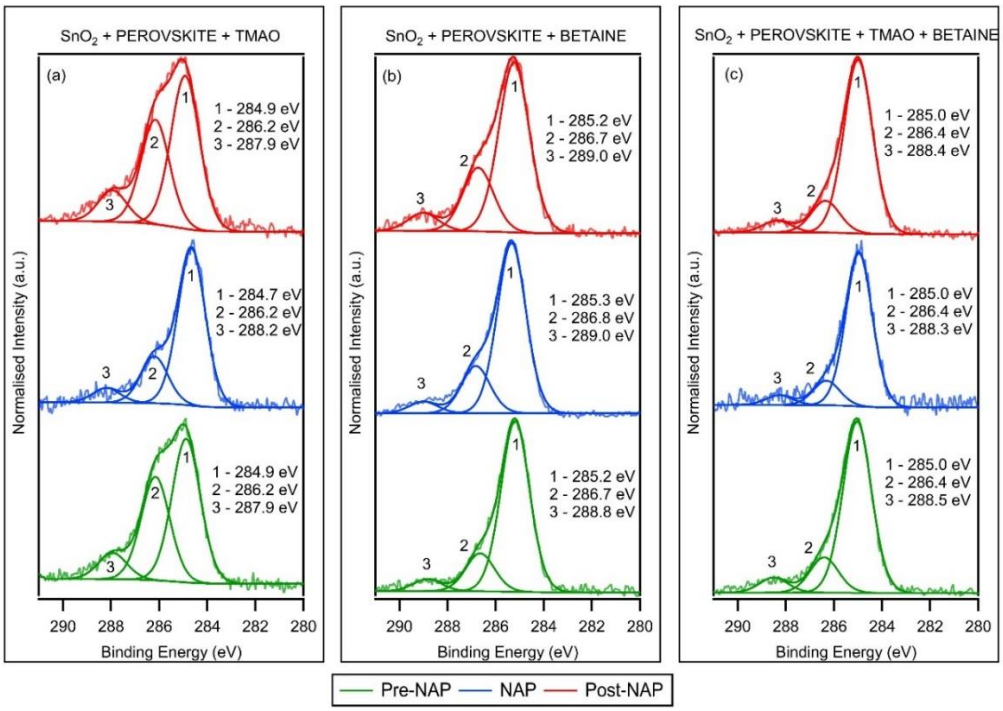

Figure 5.12 High-resolution core level C 1s spectra of the samples measured before exposure, during exposure and after exposure to 4.5 mbar water vapour at room temperature. Spectral intensities are normalised to the intensity of the highest peak.

To enable a more nuanced understanding of the variations in C-N peak intensities (component (2) in Figure 5.12) among the three samples and their changes over the course of water exposure, the C-N peak intensities were normalised by the NAP C-N peak intensity of the TMAO+Betaine sample, which exhibited the least intensity among all samples. This normalisation provided a relative measure of peak intensity across samples, as illustrated in Figure 5.13a.

These areas were then divided by the sum of the C-N peak areas from each sample (i.e. the sum of the pre-exposure, NAP, post-exposure peaks) and converted to percentage changes. The peak intensities during and after water exposure are compared to their intensities before water exposure as depicted in Figure 5.13b.

All samples exhibit a decrease in C-N peak intensities during water exposure compared to intensities observed in the pre-NAP UHV scans. In Figure 5.13a, the TMAO-modified sample demonstrates the highest C-N peak intensity both before and after water

exposure. Notably, while the T+B-modified sample displays a slightly more intense C-N peak before water exposure, the intensity observed after water exposure in the Betaine-modified sample surpasses that of the T+B-modified sample significantly.

Looking at the percentage change in C-N peak intensity relative to the pre-water exposure values for each sample (Figure 5.13b), the Betaine-modified sample exhibits the most considerable increase in C-N intensity post-water exposure, followed by the TMAO-modified sample. This suggests maximum regeneration of the perovskite in the Betaine-modified sample, positioning the TMAO-modified sample as the most stable among the tested composition.

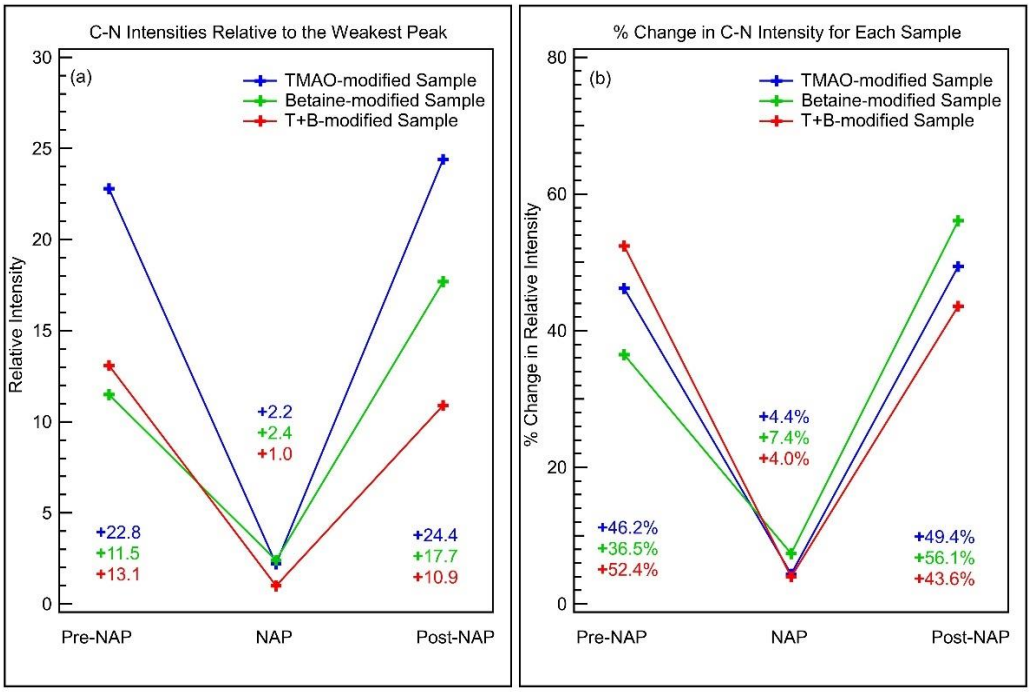

Figure 5.13 (a) Normalised C-N peak intensities relative to the NAP C-N peak intensity of the TMAO+Betaine sample (weakest peak). (b) Percentage changes in the relative C-N peak intensities before, during and after water exposure.

The N 1s core level spectra of the TMAO-modified and Betaine-modified samples are displayed in Figure 5.14 (a-b). Each spectrum can be fitted with two peaks. The low BE peak at 400.5 eV remains constant in all the spectra and can be attributed to the state of nitrogen in the methylamines. This peak also overlaps with the BE of the precursor

MAI. The high BE peaks fitted at 402.6 eV, 402.8 eV and 403.0 eV are consistent with the C-N state in the perovskite. In the TMAO sample the peak at 400.5 eV has much higher intensity than the perovskite peak while in the Betaine sample both the peaks display similar intensities.

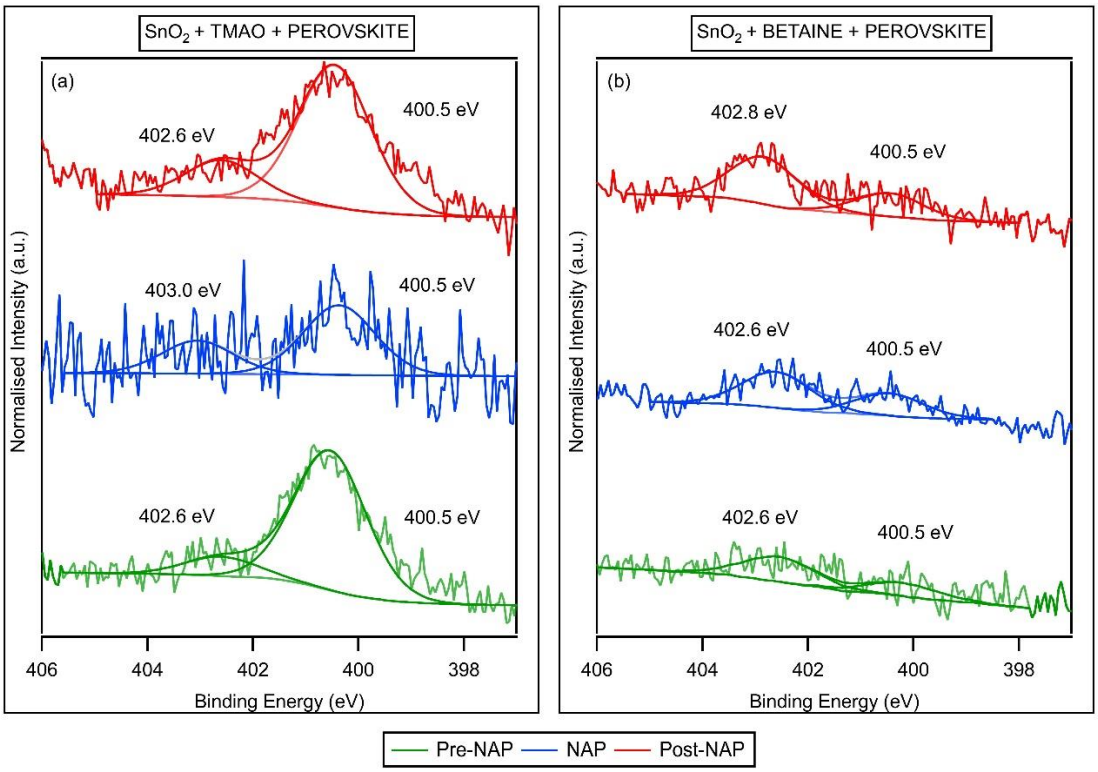

Figure 5.14 High resolution core level N 1s XPS spectra of perovskite modified with (a) TMAO, (b) Betaine, and (c) TMAO & Betaine.

Figure 5.15 (a-c) displays the Pb 4f spectra of the samples. Interestingly, no metallic lead peak is evident in the spectra, except for the Betaine-modified sample during water exposure, where 25 Pb 4f repeated scans were conducted. The absence of metallic lead peaks in the other two samples, where only two scans were taken, supports the idea that the observed metallic lead peaks during XPS analysis are a result of X-ray irradiation. Furthermore, the lack of metallic lead peaks post-water exposure in the Betaine-modified sample (post-NAP scans were recorded from a new position on the sample) suggests that the metallic lead peak was not induced by water exposure.

Every Pb 4f spectrum exhibits a distinct, sharp doublet with the expected spin-orbit splitting energy of 4.87 eV. No binding energy shift is evident in the Pb 4f doublet peaks of the Betaine-modified sample and the TMAO+Betaine-modified sample. However, the TMAO-modified sample exhibits a -0.1 eV BE shift during water exposure, possibly showing a change in the chemical environment on exposure to water. It must be noted that the energy resolution of the instrument might restrict definitive conclusions regarding the actual shifting of this peak.

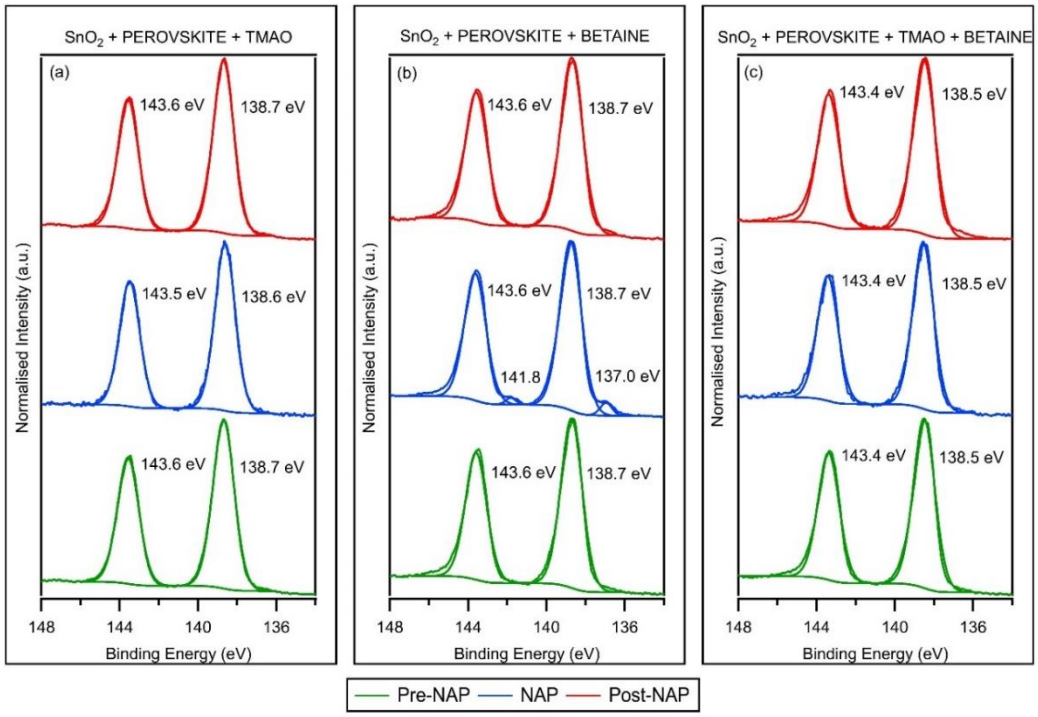

Figure 5.15 High-resolution core level Pb 4f spectra of the samples measured before exposure, during exposure and after exposure to 4.5 mbar water vapour at room temperature.

The I 3d spectra of the samples are shown in Figure 5.16 (a-c). The TMAO-modified sample displays notably noisy and comparatively less intense doublet peaks. Following water exposure, the peak intensity is reduced by a half compared to its pre-water exposure intensity. In contrast, both the Betaine-modified and T+B-modified samples manifest increased peak intensities after water exposure. The Betaine-modified sample

displays a significant 58% intensity surge, while the T+B-modified sample shows a modest 7% increase relative to their respective pre-water exposure intensities.

This could indicate that the TMAO-modified sample undergoes degradation upon water exposure, signifying its susceptibility. The Betaine-modified sample demonstrates promising tolerance to moisture. The proximity of hydrophobic methyl groups to the hydrophilic N^{+}-O^{-} in the TMAO molecule potentially super-hydrates the perovskite crystals, leading to degradation. Contrastingly, the betaine molecule's structure, with its hydrophobic COO^{-} group separated from the hydrophobic $(CH_3)_3N^{+}$ group by an alkyl group, forms a more effective barrier against water. This separation seemingly prevents interaction between the negatively charged iodide ions of the perovskite and the positively charged hydronium ions of water, effectively stabilising the lattice against moisture ingress.

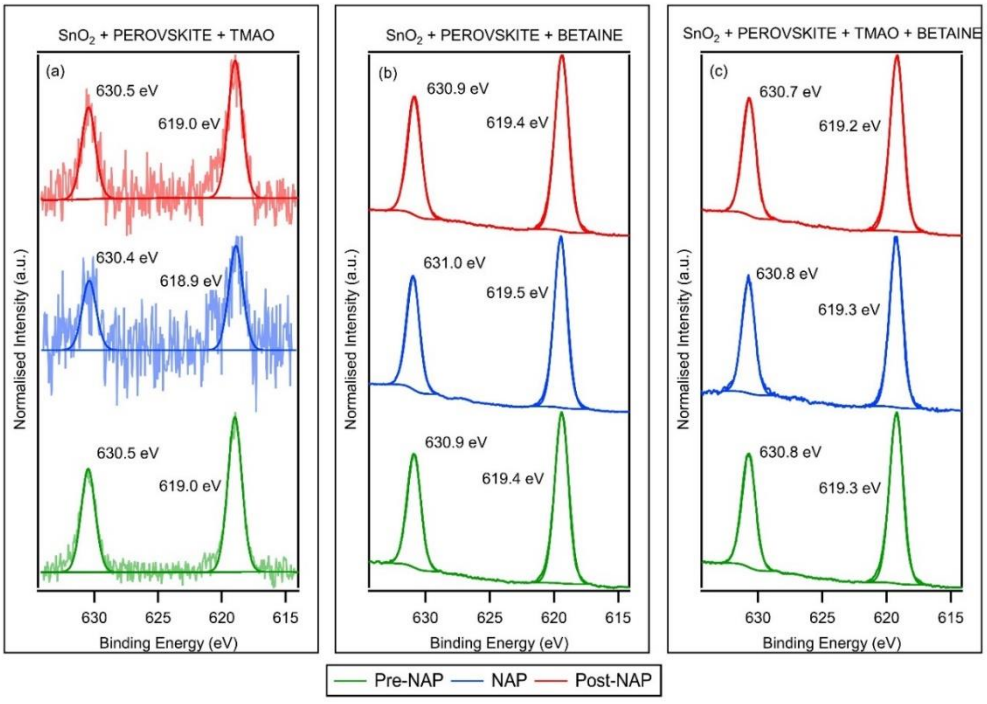

Figure 5.16 High-resolution core level I 3d spectra of the samples measured before exposure, during exposure and after exposure to 4.5 mbar water vapour at room temperature.

5.4. Conclusions

The analysis of perovskite films modified with naturally occurring methylamines, TMAO and betaine, through XPS, AR-HAXPES, and NAP-XPS provides interesting insights into their behaviour under high-temperature and moisture exposure. While the TMAO-modified samples exhibit notable resistance to heat, the Betaine-modified samples show superior moisture endurance. This observation hints at the possibility of achieving enhanced perovskite stability through a delicate optimisation of TMAO and betaine concentrations within the perovskite matrix. Such fine-tuning could serve as a promising avenue for future research.

References

1. Wu, B., et al., *Charge Accumulation and Hysteresis in Perovskite-Based Solar Cells: An Electro-Optical Analysis.* Advanced Energy Materials, 2015. **5**(19): p. 1500829.

2. Jacobsson, T.J., et al., *Unreacted PbI2 as a Double-Edged Sword for Enhancing the Performance of Perovskite Solar Cells.* Journal of the American Chemical Society, 2016. **138**(32): p. 10331-10343.

3. Chen, B., et al., *Origin of J–V Hysteresis in Perovskite Solar Cells.* The Journal of Physical Chemistry Letters, 2016. **7**(5): p. 905-917.

4. Wojciechowski, K., et al., *Heterojunction Modification for Highly Efficient Organic–Inorganic Perovskite Solar Cells.* ACS Nano, 2014. **8**(12): p. 12701-12709.

5. Snaith, H.J., et al., *Anomalous Hysteresis in Perovskite Solar Cells.* The Journal of Physical Chemistry Letters, 2014. **5**(9): p. 1511-1515.

6. Yang, D., et al., *High efficiency planar-type perovskite solar cells with negligible hysteresis using EDTA-complexed SnO2.* Nature Communications, 2018. **9**(1): p. 3239.

7. Li, W., et al., *Enhanced UV-light stability of planar heterojunction perovskite solar cells with caesium bromide interface modification.* Energy & Environmental Science, 2016. **9**(2): p. 490-498.

8. Li, Y., et al., *A Multifunctional Fullerene Derivative for Interface Engineering in Perovskite Solar Cells.* Journal of the American Chemical Society, 2015. **137**: p. 15540−15547.

9. Wang, J.T., et al., *Low-temperature processed electron collection layers of graphene/TiO2 nanocomposites in thin film perovskite solar cells.* Nano Lett, 2014. **14**(2): p. 724-30.

10. Tan, H., et al., *Efficient and stable solution-processed planar perovskite solar cells via contact passivation.* Science, 2017. **355**(6326): p. 722-726.

11. Lee, J.-H., et al., *Introducing paired electric dipole layers for efficient and reproducible perovskite solar cells.* Energy & Environmental Science, 2018. **11**(7): p. 1742-1751.

12. Yancey, P.H., *Organic osmolytes as compatible, metabolic and counteracting cytoprotectants in high osmolarity and other stresses.* J Exp Biol, 2005. **208**(Pt 15): p. 2819-30.

13. Yancey, P.H., *Water Stress, Osmolytes and Proteins.* American Zoologist, 2001. **41**(4): p. 699-709.

14. Yancey, P.H., et al., *Trimethylamine oxide, betaine and other osmolytes in deep-sea animals: depth trends and effects on enzymes under hydrostatic pressure.* Cell Mol Biol (Noisy-le-grand), 2004. **50**(4): p. 371-6.

15. Hunger, J., et al., *Complex Formation in Aqueous Trimethylamine-N-oxide (TMAO) Solutions.* The Journal of Physical Chemistry B, 2012. **116**(16): p. 4783-4795.

16. Rezus, Y.L.A. and H.J. Bakker, *Destabilization of the Hydrogen-Bond Structure of Water by the Osmolyte Trimethylamine N-Oxide.* The Journal of Physical Chemistry B, 2009. **113**(13): p. 4038-4044.

17. Hunger, J., et al., *Water-mediated interactions between trimethylamine-N-oxide and urea.* Physical Chemistry Chemical Physics, 2015. **17**(1): p. 298-306.

18. Chen, Q., et al., *Defect passivation by a betaine-based zwitterionic molecule for high-performance p-i-n methylammonium-based perovskite solar cells.* Solar Energy Materials and Solar Cells, 2024. **264**: p. 112615.

19. Linton, E.P., *The Dipole Moments of Amine Oxides.* Journal of the American Chemical Society, 1940. **62**(8): p. 1945-1948.

20. Ohto, T., et al., *Trimethylamine-N-oxide: its hydration structure, surface activity, and biological function, viewed by vibrational spectroscopy and molecular dynamics simulations.* Physical Chemistry Chemical Physics, 2017. **19**(10): p. 6909-6920.

21. Maniyarasu, S., et al., *Role of Alkali Cations in Stabilizing Mixed-Cation Perovskites to Thermal Stress and Moisture Conditions.* ACS Applied Materials & Interfaces, 2021. **13**(36): p. 43573-43586.

22. Okejiri, F., et al., *Ultrasound-mediated synthesis of nanoporous fluorite-structured high-entropy oxides toward noble metal stabilization.* iScience, 2022. **25**(5): p. 104214.

23. Yang, Y., et al., *Eliminating Charge Accumulation via Interfacial Dipole for Efficient and Stable Perovskite Solar Cells.* ACS Applied Materials & Interfaces, 2019. **11**(38): p. 34964-34972.

24. Calloni, A., et al., *Stability of Organic Cations in Solution-Processed CH3NH3PbI3 Perovskites: Formation of Modified Surface Layers.* The Journal of Physical Chemistry C, 2015. **119**(37): p. 21329-21335.

25. Evangelista, F., et al., *Electronic structure of copper phthalocyanine: An experimental and theoretical study of occupied and unoccupied levels.* The Journal of Chemical Physics, 2007. **126**(12).

26. Brena, B., et al., *Equivalent core-hole time-dependent density functional theory calculations of carbon $1s$ shake-up states of phthalocyanine.* Physical Review B, 2004. **70**(19): p. 195214.

27. Min, H., et al., *Detection of the UV-vis silent biomarker trimethylamine-N-oxide via outer-sphere interactions in a lanthanide metal-organic framework.* Commun Chem, 2022. **5**(1): p. 74.

28. Steirer, K.X., et al., *Defect Tolerance in Methylammonium Lead Triiodide Perovskite.* ACS Energy Letters, 2016. **1**(2): p. 360-366.

29. Conings, B., et al., *Perovskite-Based Hybrid Solar Cells Exceeding 10% Efficiency with High Reproducibility Using a Thin Film Sandwich Approach.* Advanced Materials, 2014. **26**(13): p. 2041-2046.

30. Kot, M., et al., *Room temperature atomic layer deposited Al 2 O 3 on CH 3 NH 3 PbI 3 characterized by synchrotron-based X-ray photoelectron spectroscopy.* 2017.

31. Philippe, B., et al., *Chemical and Electronic Structure Characterization of Lead Halide Perovskites and Stability Behavior under Different Exposures—A Photoelectron Spectroscopy Investigation.* Chemistry of Materials, 2015. **27**(5): p. 1720-1731.

Chapter 6. Conclusions and Further Work

The aim of this thesis is to investigate the stability of perovskite and modified-perovskite films under environmental stresses, specifically heat and moisture, to which they are highly susceptible. We take a fundamental approach to investigate these systems, utilising synchrotron XPS and NEXAFS, as well as relatively new techniques, HAXPES and NAP-XPS. This combination of techniques offers valuable insights into the thermal and moisture resistance of modified perovskite films.

Chapter 3 investigates the thermal stability of two different halide perovskite materials, $MAPbI_3$ and $MAPbBr_3$, employing a comprehensive XPS analysis. This detailed examination involves XPS data acquisition pre- and post- heating, with the samples subjected to temperatures of around 200 °C. The primary objective is to study the response of these perovskite variants to thermal stress and understand the role of halide ions in imparting structural stability to the perovskite lattice. The results suggest that $MAPbBr_3$ shows notably higher thermal stability compared to its $MAPbI_3$ counterpart. The superior stability in $MAPbBr_3$ is substantiated by the absence of distinct perovskite phase peaks in the post-heating spectra of $MAPbI_3$, contrasting the observable persistence of these peaks in the corresponding spectra of $MAPbBr_3$ before and after heating. Additionally, the XPS analysis highlighted the presence of metallic lead species in both sample variants, with intensified peaks observed post-heating. However, the concentration changes in nitrogen, halide, and lead in $MAPbI_3$ were significantly pronounced, while those in $MAPbBr_3$ were comparatively less marked. These findings provide insights into the structural stability of perovskite materials, particularly emphasising the important role played by halide ions in determining their resilience against thermal stress. The comparative analysis aligns with a proposed three-step degradation mechanism and suggests that the higher thermal stability of $MAPbBr_3$ might be attributed to the lower nucleophilic strength of bromide ions and the higher electronegativity of bromine compared to iodine. This understanding holds promise for refining the development of more durable and reliable perovskite-based devices, crucial for advancing the field of solar cell technology.

In Chapter 4, the focus shifts towards improving the stability of the mixed halide perovskite $MAPbI_{3-x}Cl_x$ by modifying the precursor solution using two imidazolium-based ILs: $BMIMBF_4$ and BMIMCl. The effect of these additives on the response of the perovskite samples to heat and moisture is studied using various techniques. To understand the role of the SnO_2 ETL, the samples are divided into two sets: one set is deposited on SnO_2-coated Ti substrate, while the other is deposited on Ti substrate directly. The goal is to understand how SnO_2 and ILs contribute to the thermal stability of these perovskite configurations. The thermal degradation of the films is probed using synchrotron XPS. The results show that the mixed halide perovskite ink is resistant to thermal degradation up to 150 °C. For the IL-modified perovskite samples on SnO_2-coated substrates, perovskite phase peaks are observed even at higher temperatures of 300 °C. This suggests that SnO_2 and ILs (BMIMCl and $BMIMBF_4$) play a crucial role in maintaining stability. The work function results support our findings, showing that pure perovskite samples degrade at 300 °C, while IL-modified perovskite samples show less fluctuation in work function values, especially those deposited on SnO_2. Based on the work function changes, we hypothesise that BMIM cations in $BMIMBF_4$ form a cascade over the perovskite surface, facilitated by the interaction of BF_4^- ions with the hydroxyl groups on the SnO_2 layer. This hypothesis explains the superior thermal stability of the SnO_2/$BMIMBF_4$-Perovskite sample over the $BMIMBF_4$-Perovskite sample. Conversely, for BMIMCl-modified samples, our hypothesis suggests that the limited interaction of the chloride ions with SnO_2 hinders the formation of the dipole layer necessary for the BMIM cascade. Instead, BMIM cations diffuse into the perovskite grain boundaries, enhancing film crystallinity.

Further analysis using NEXAFS supported our findings from XPS and work function analyses, confirm the stability of SnO_2 coated IL-modified perovskite samples. HAXPES measurements helped in understanding the perovskite degradation in terms of depth, showing that IL-modified samples maintain superior thermal stability across different depths compared to pure perovskite samples. It is known that moisture affects the stability of perovskite solar cells, so the endurance of the IL-modified samples against moisture was evaluated using NAP-XPS. Results indicate that IL-modified samples are

more resistant to moisture, with BMIMCl-modified samples showing greater resistance compared to $BMIMBF_4$-modified samples. This aligns with our initial hypothesis about the IL-perovskite interaction mechanisms and help us better interpret the results.

Chapter 5 studies the role of methylamines, TMAO and Betaine, on the stability of the mixed halide perovskite $MAPbI_{3-x}Cl_x$ against high temperature and moisture. The analysis of these modified perovskite films, through XPS, AR-HAXPES, and NAP-XPS provide interesting insights into their behaviour under high-temperature and moisture exposure. While the TMAO-modified samples exhibit notable resistance to heat, the Betaine-modified samples show superior moisture endurance. This observation hints at the possibility of achieving enhanced perovskite stability through a delicate optimisation of TMAO and betaine concentrations within the perovskite matrix. Such fine-tuning could serve as a promising avenue for future research.

This thesis presents a fundamental investigation into the stability of perovskite and modified-perovskite films under environmental stresses. The role of halide ions in preserving the perovskite lattice under high temperatures is demonstrated, with the superior stability of $MAPbBr_3$ over $MAPbI_3$ being shown. Moisture and heat tolerance of the widely used perovskite $MAPbI_{3-x}Cl_x$ is enhanced through modification with ionic liquids $BMIMBF_4$ and BMIMCl. A variety of state-of-the-art techniques such as XPS, NAPXPS, HAXPES, NEXAFS, etc., are employed to elucidate the interaction between the two ionic liquids and the SnO_2 ETL with the perovskite. The impact of methylamines on perovskite stability is also examined, revealing TMAO's resistance to heat and Betaine's superior moisture endurance. These findings provide insights into optimising perovskite stability, which is crucial for the advancement of solar cell technology.

<u>Further work</u>

Our experiments focussed on investigating the thermal and moisture stability of the perovskite films. Further work could include subjecting the films to heat and moisture simultaneously. This could be carried out on the NAP-XPS kit at the Henry Royce

Facilities. A simultaneous exposure to heat and moisture would mirror the real world environment stresses more closely.

The spectroscopic analysis presented in this thesis could be coupled with some imaging techniques such as AFM to investigate the crystallinity of the films. An optimisation of the IL-perovskite concentration could be carried out to enhance the crystallinity of the films and different types of perovskites could be subjected to modification with the ILs with an attempt to improve the stability of the resulting films. Introducing a hole transport layer on top of the modified perovskites could be an interesting future study which would mimic the structure of a real device more closely. This would require HAXPES to give a depth profile through the layers.

A further avenue for future work could be to build devices to test if the observed enhancement in stability in our fundamental studies is replicated in terms of an enhancement in the device performance.

APPENDIX – 1

S.1 XPS survey scans of the pure perovskite and IL-modified perovskite samples deposited on Ti foil substrate, both with and without a SnO_2 layer. It must be noted that survey scans for the $BMIMBF_4$-Perovskite sample without the SnO_2 layer could not be recorded due to encountered problems arising from sample charging.

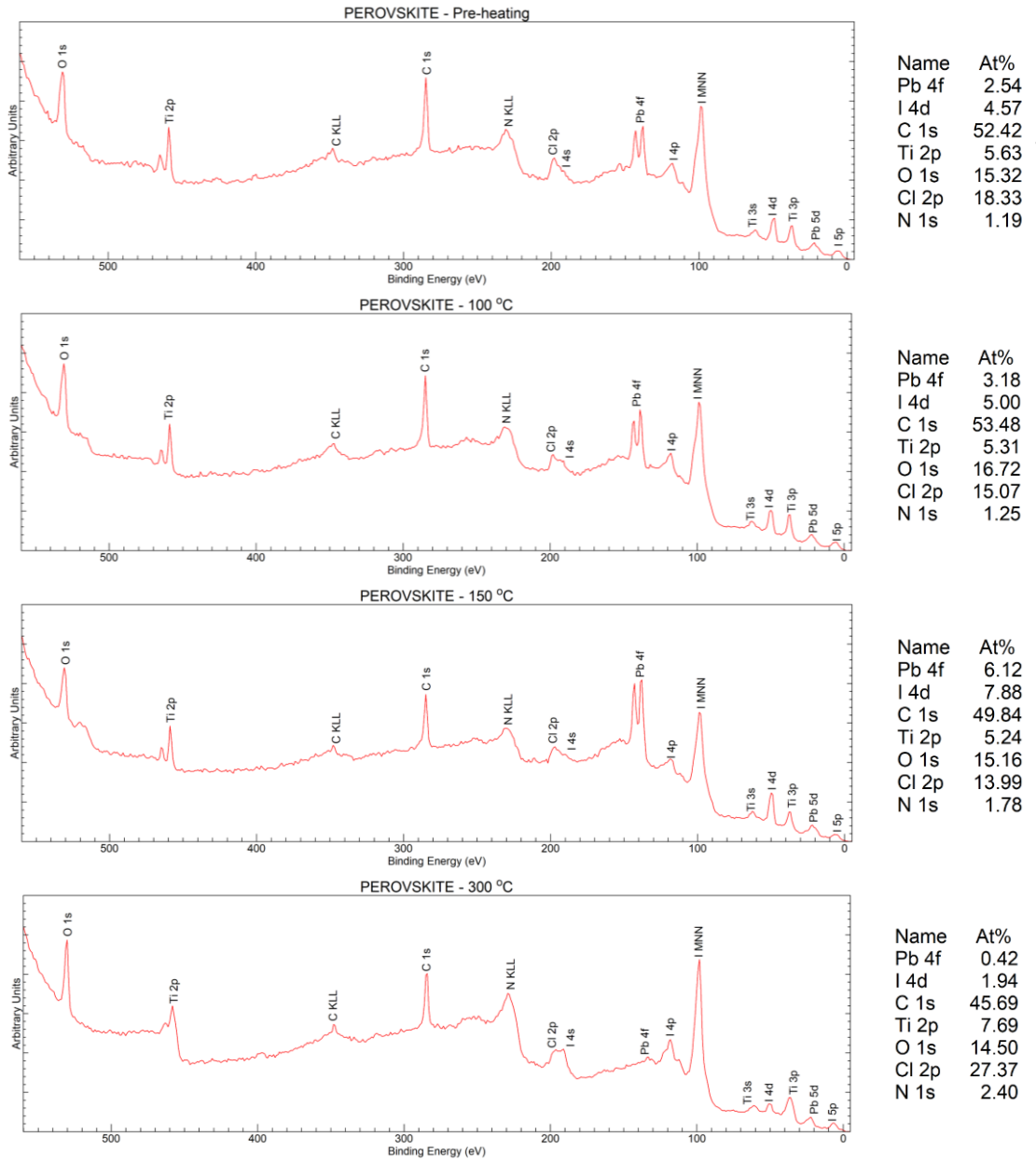

Figure S1: XPS survey spectra of the pure perovskite sample deposited on Ti foil, recorded with an excitation energy of 610 eV at ASTRID-2 synchrotron facility, Denmark.

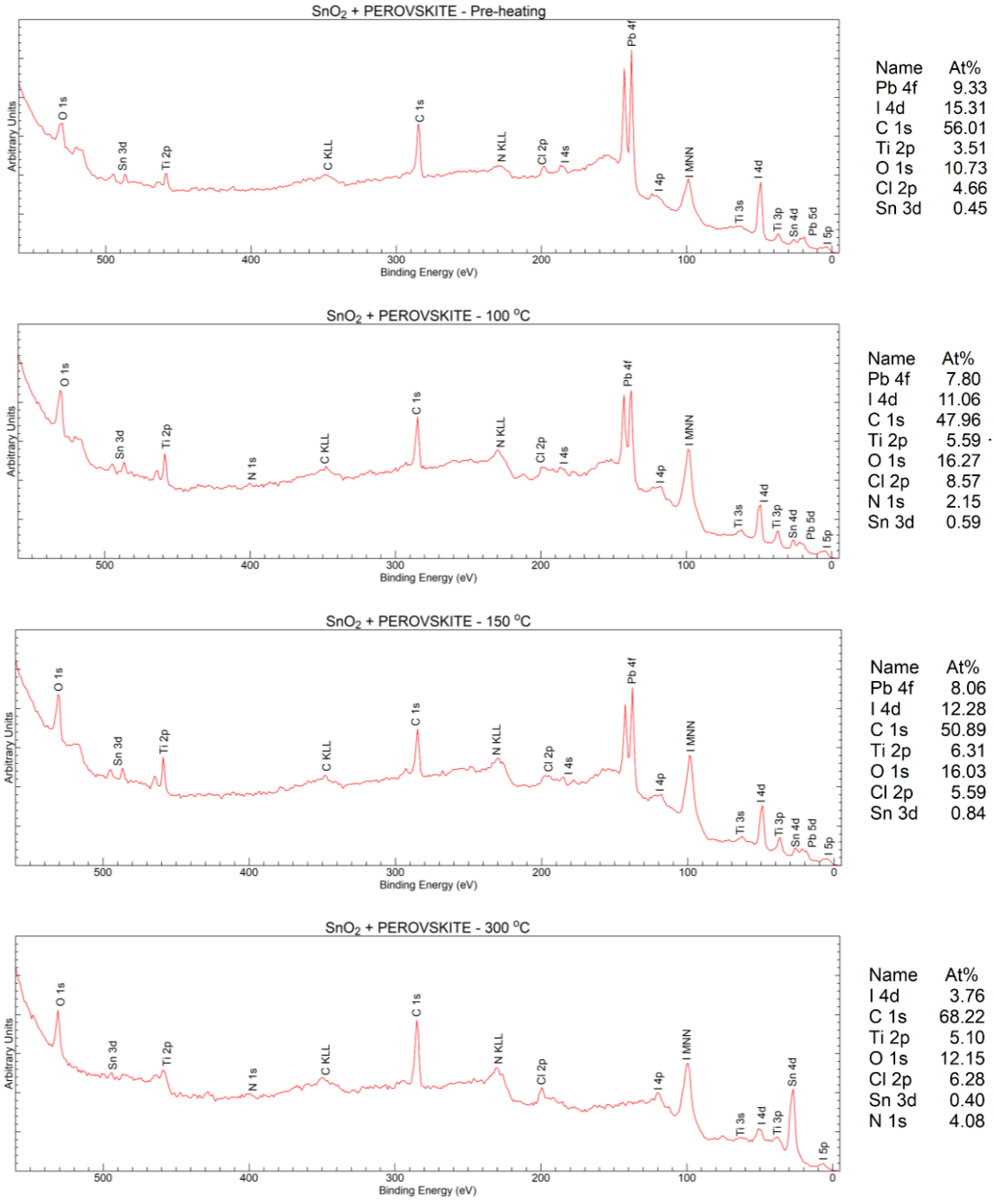

Figure S2: XPS survey spectra of the pure perovskite sample deposited on SnO_2 coated Ti foil, recorded with an excitation energy of 610 eV at ASTRID-2 synchrotron facility, Denmark.

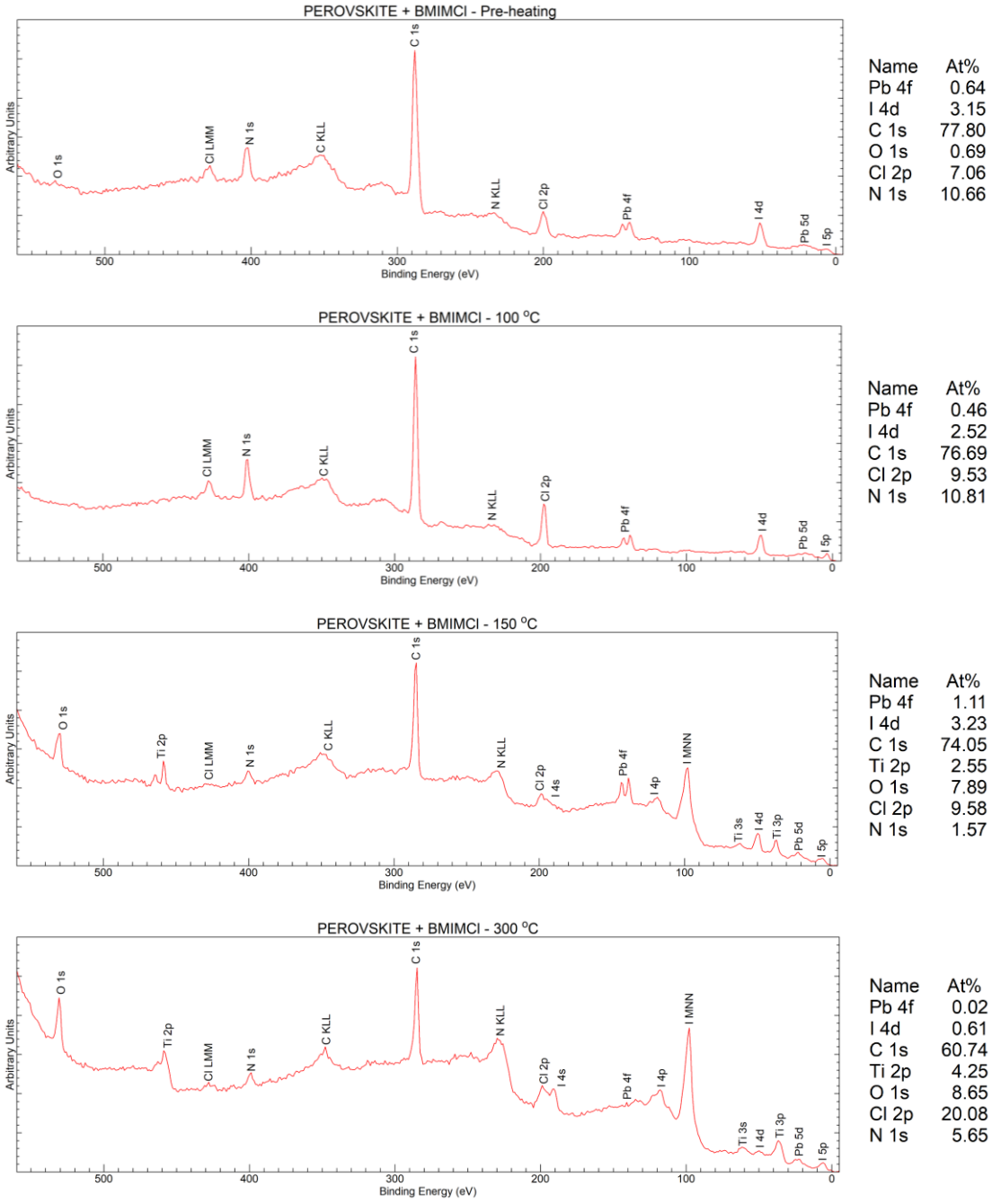

Figure S3: XPS survey spectra of the BMIMCl perovskite sample deposited on Ti foil, recorded with an excitation energy of 610 eV at ASTRID-2 synchrotron facility, Denmark.

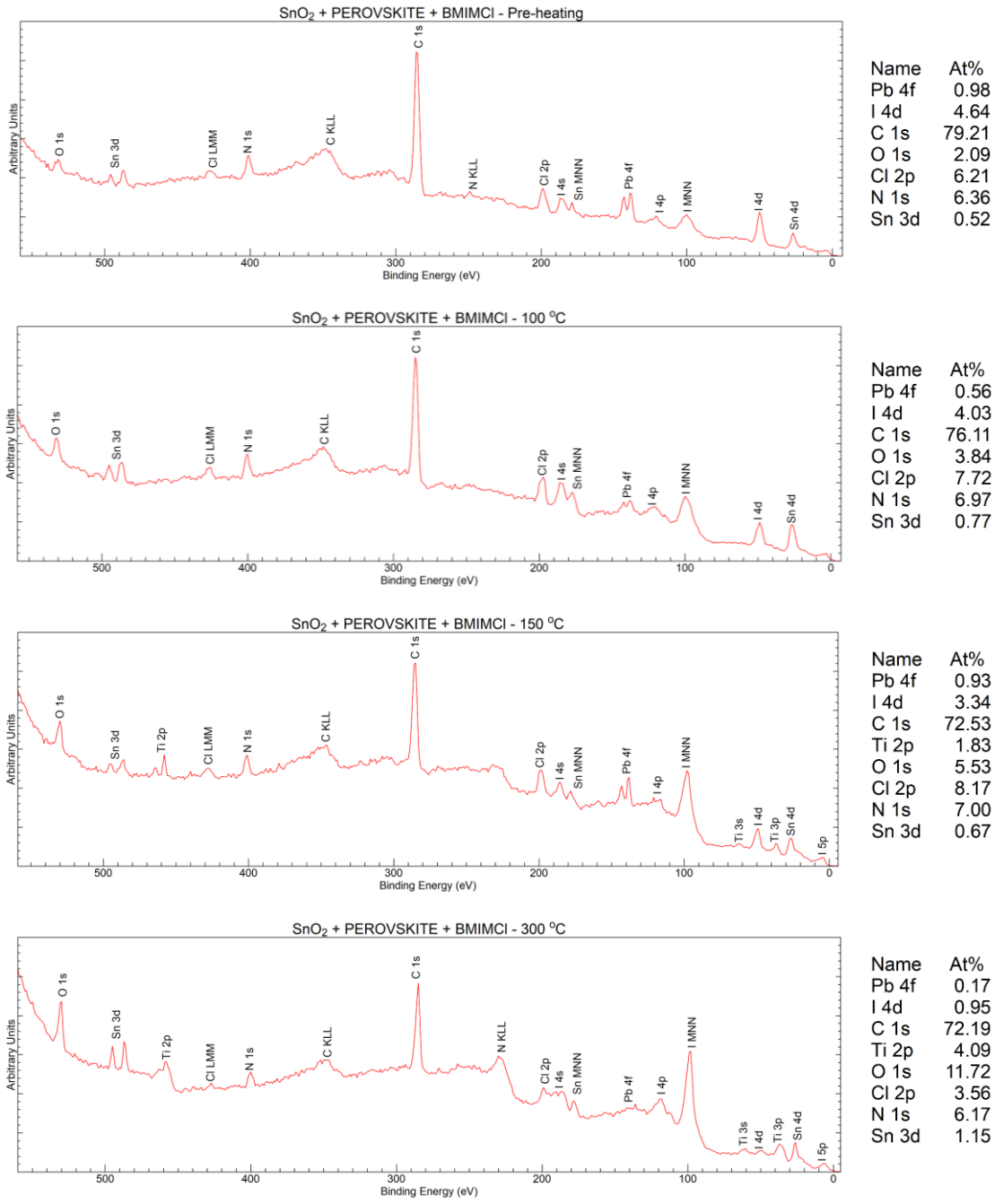

Figure S4: XPS survey spectra of the BMIMCl perovskite sample deposited on SnO_2 coated Ti foil, recorded with an excitation energy of 610 eV at ASTRID-2 synchrotron facility, Denmark.

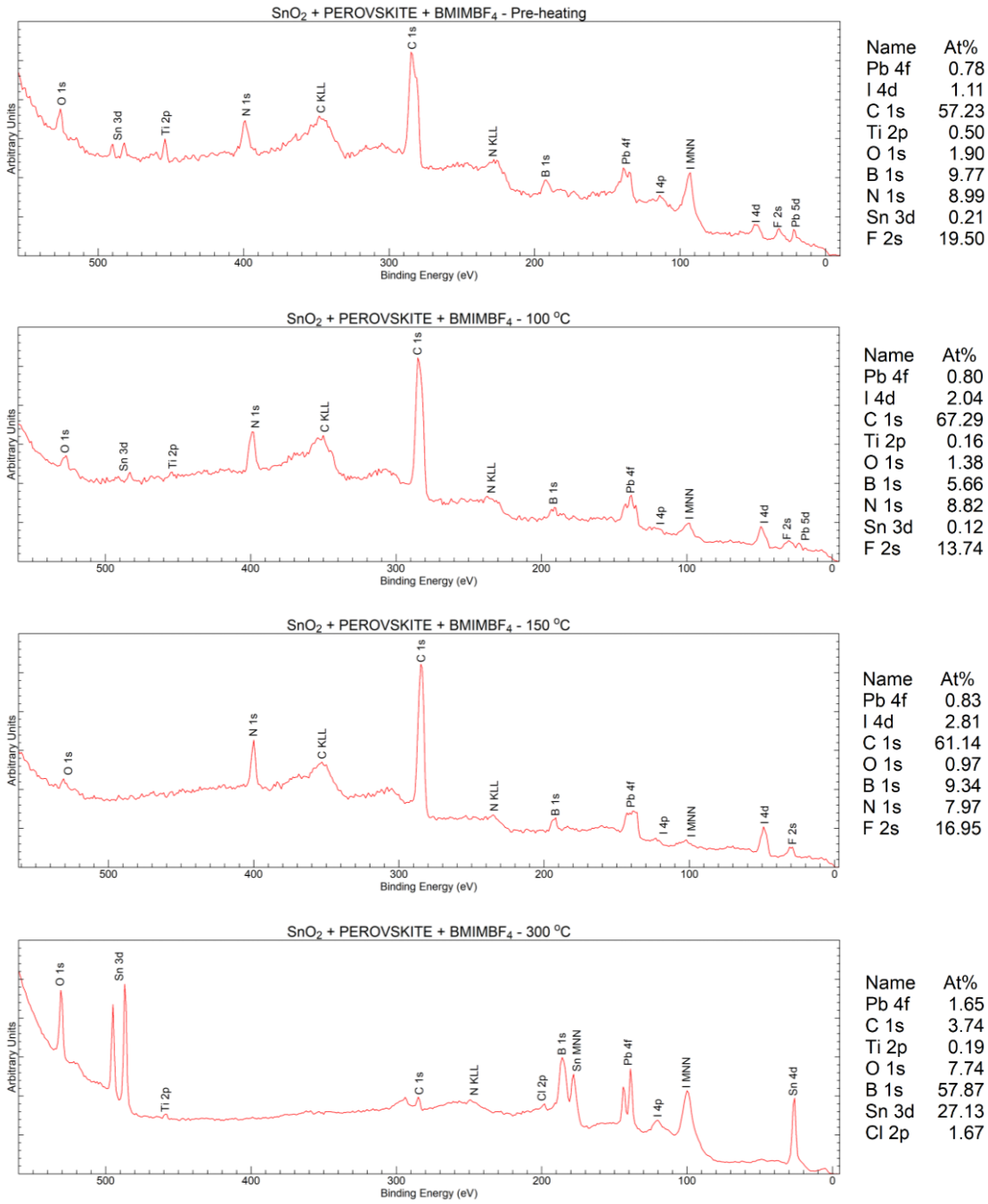

Figure S5: XPS survey spectra of the $BMIMBF_4$ perovskite sample deposited on SnO_2 coated Ti foil, recorded with an excitation energy of 610 eV at ASTRID-2 synchrotron facility, Denmark.

S.2 XPS survey scans of TMAO and Betaine modified perovskite samples deposited on SnO_2 coated Ti foil substrate. It must be noted that survey scan for the TMAO modified Perovskite sample at 150 °C could not be recorded due to encountered problems arising from sample charging.

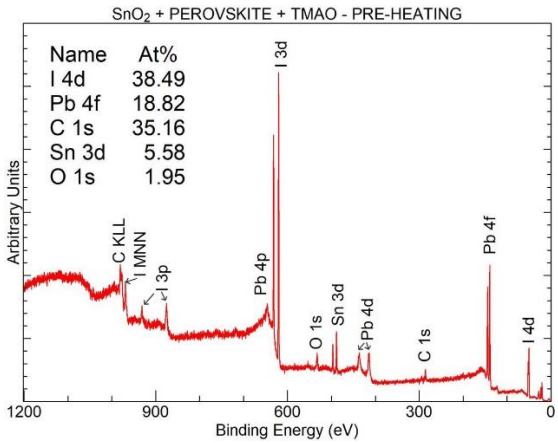

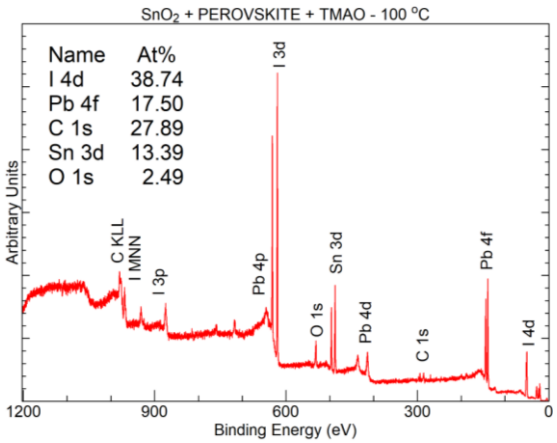

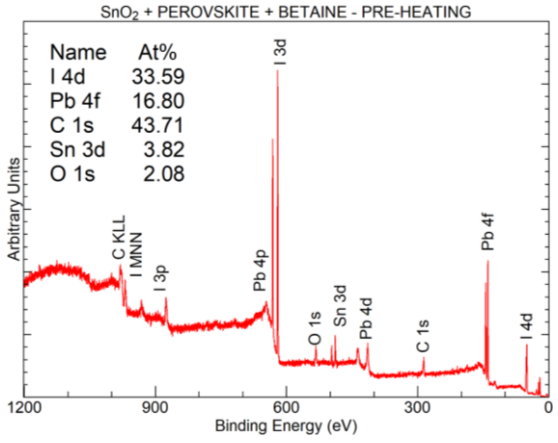

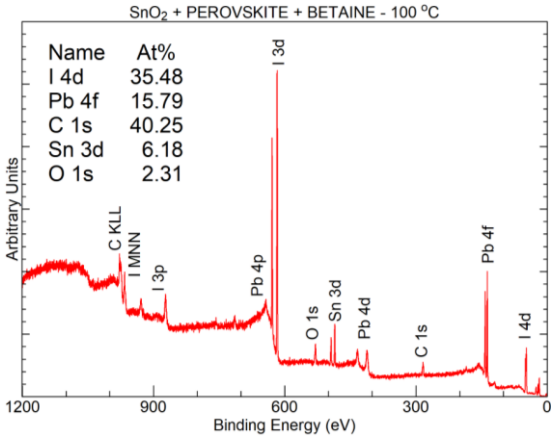

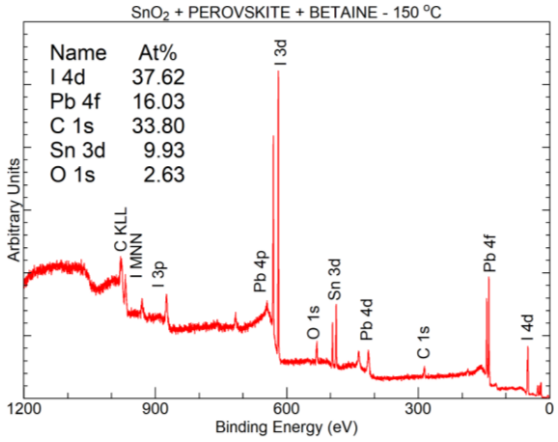

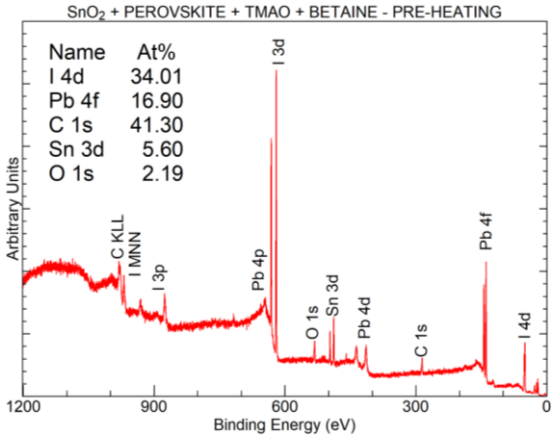

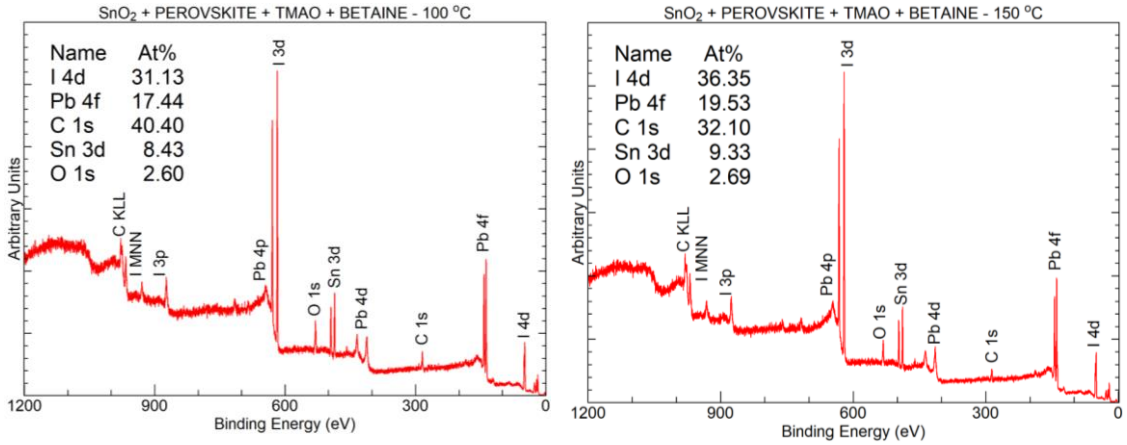

Figure S6: XPS survey spectra of the perovskite samples modified with TMAO and/or Betaine, deposited on SnO_2 coated Ti foil, recorded with an excitation energy of 1486 eV at Henry Royce Facility, Manchester.

S.3 Survey spectra of pure and modified perovskite samples deposited on SnO_2 coated Ti foil substrate measured before, during and after exposure to 4.5 mbar water vapour at room temperature. It must be noted that the atomic percentages are calculated from the integrated peak areas using RSFs from the Scofield library. However, it's important to acknowledge that RSFs are not available for the analyser under NAP conditions. Therefore, these calculations provide only a rough indication of the composition.

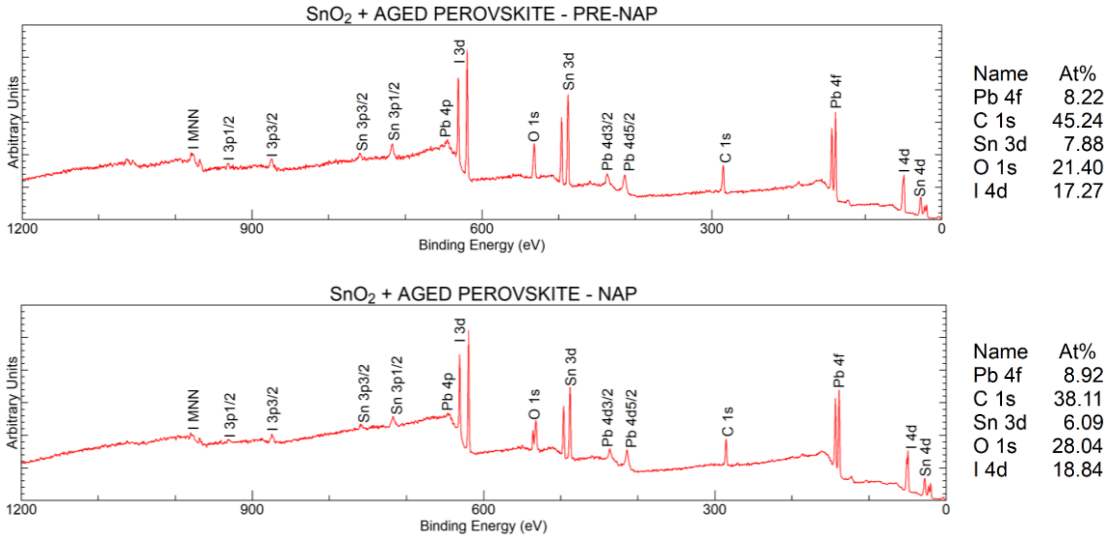

Figure S7: Survey spectra of the aged perovskite samples deposited on SnO_2 coated Ti foil, measured before, during and after exposure to 4.5 mbar water vapour at room

temperature. Spectra were recorded with an excitation energy of 1486 eV at Henry Royce Facility, Manchester.

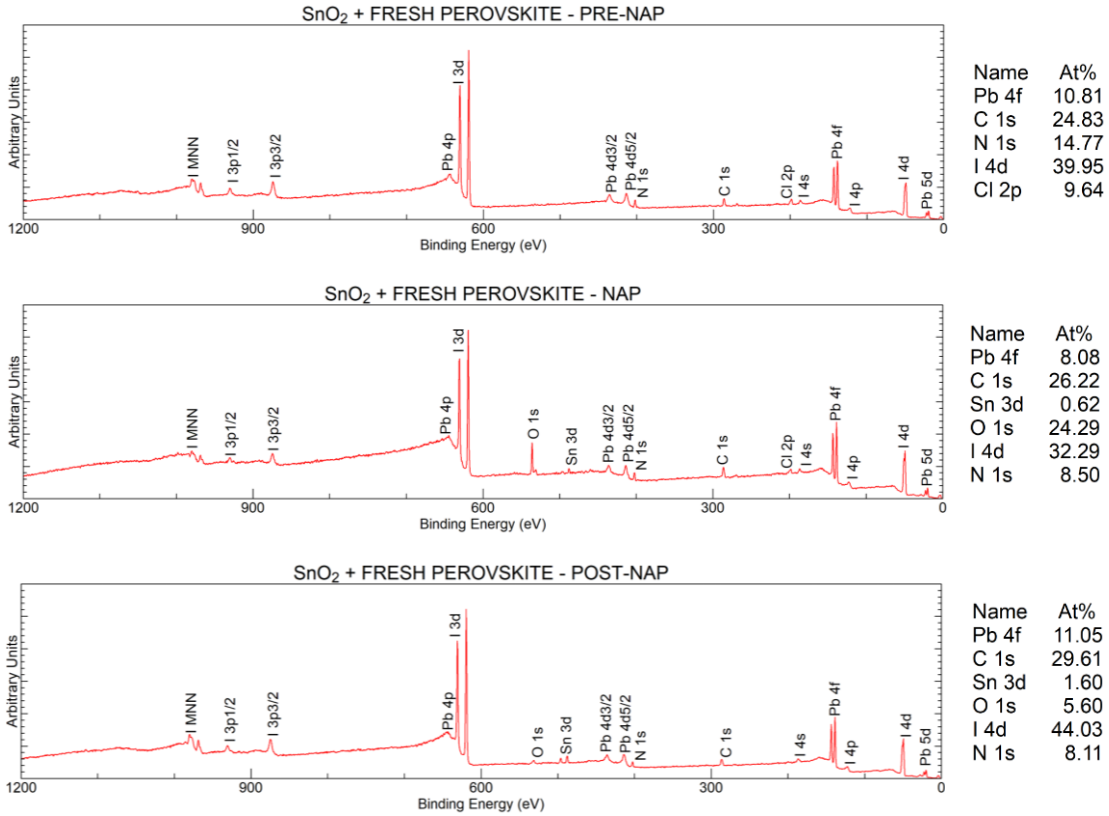

Figure S8: Survey spectra of the fresh perovskite samples deposited on SnO_2 coated Ti foil, measured before, during and after exposure to 4.5 mbar water vapour at room temperature. Spectra were recorded with an excitation energy of 1486 eV at Henry Royce Facility, Manchester.

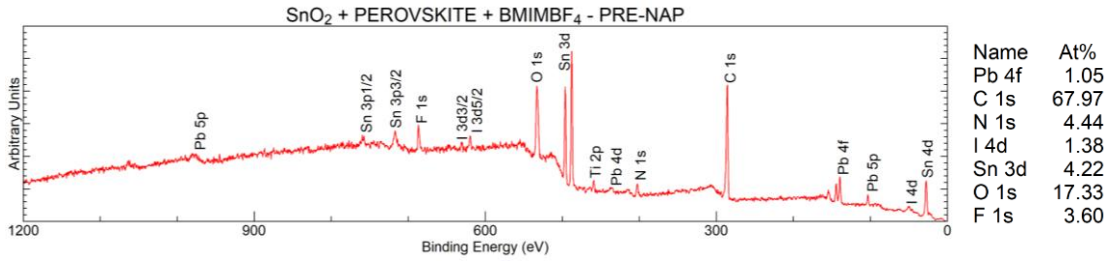

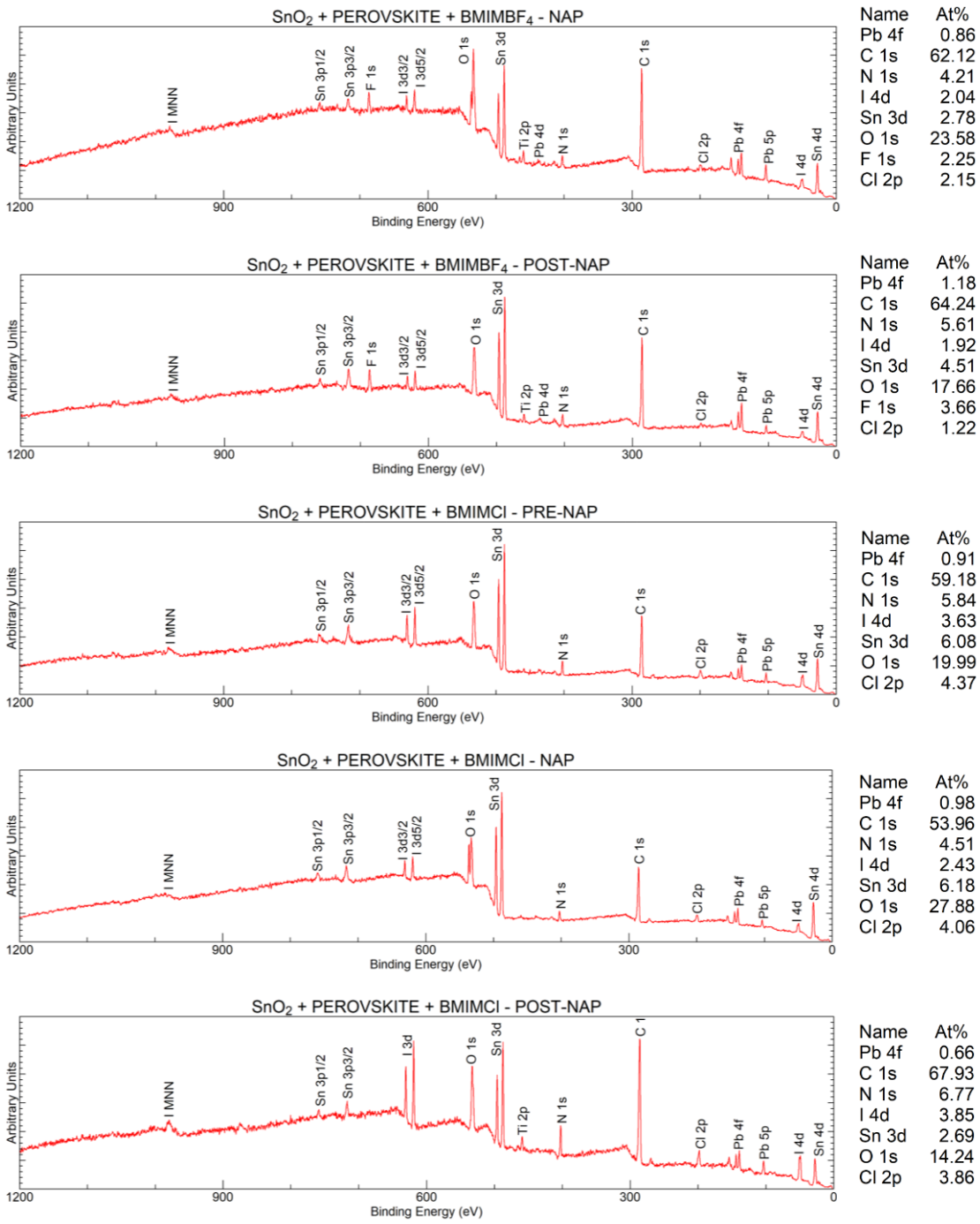

Figure S9: Survey spectra of the IL-modified perovskite samples deposited on SnO_2 coated Ti foil, measured before, during and after exposure to 4.5 mbar water vapour at room temperature. Spectra were recorded with an excitation energy of 1486 eV at Henry Royce Facility, Manchester.

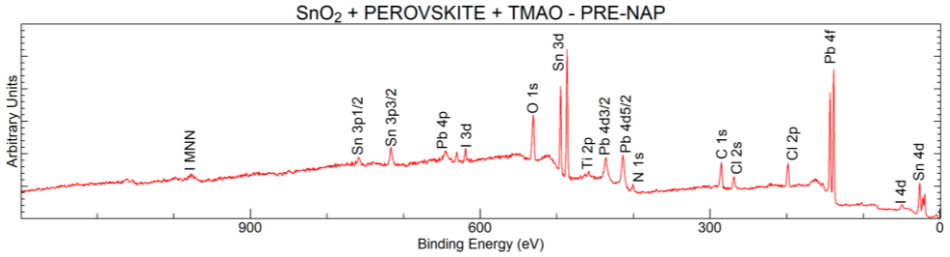

Name	At%
Pb 4f	10.34
C 1s	35.89
N 1s	4.71
Sn 3d	8.24
O 1s	24.27
Cl 2p	14.55
I 4d	1.99

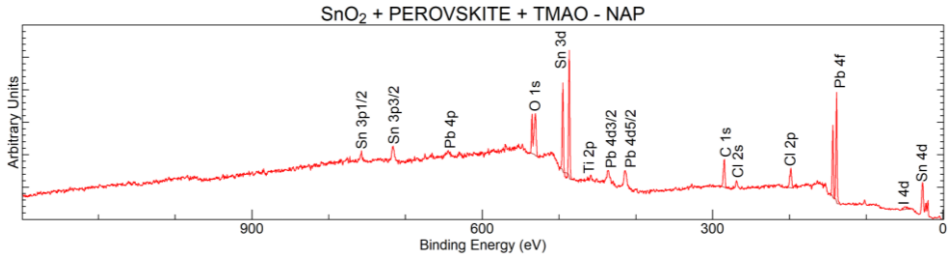

Name	At%
Pb 4f	7.51
C 1s	35.61
Sn 3d	7.82
O 1s	34.69
Cl 2p	12.35
I 4d	2.04

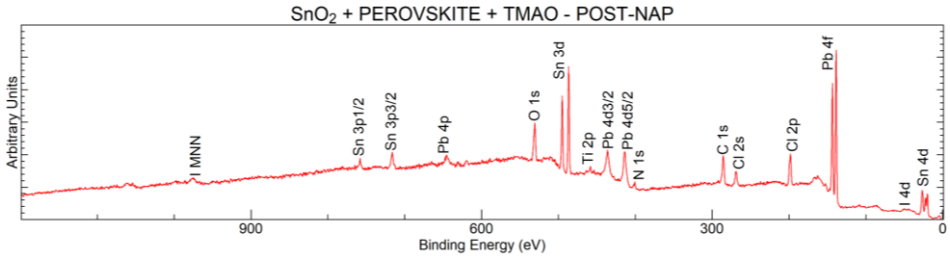

Name	At%
Pb 4f	11.45
C 1s	39.38
N 1s	4.16
Sn 3d	7.03
O 1s	18.46
Cl 2p	18.77
I 4d	0.74

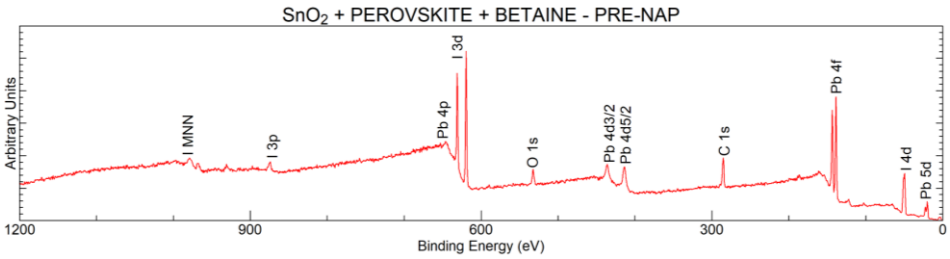

Name	At%
Pb 4f	11.46
C 1s	54.78
O 1s	9.78
Cl 2p	0.94
I 4d	23.04

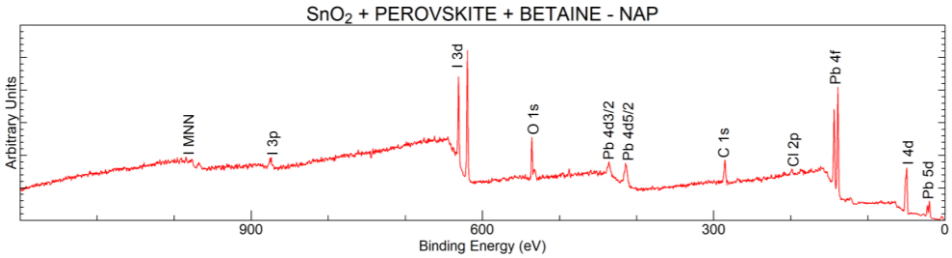

Name	At%
Pb 4f	11.19
C 1s	37.19
O 1s	24.54
Cl 2p	4.55
I 4d	22.53

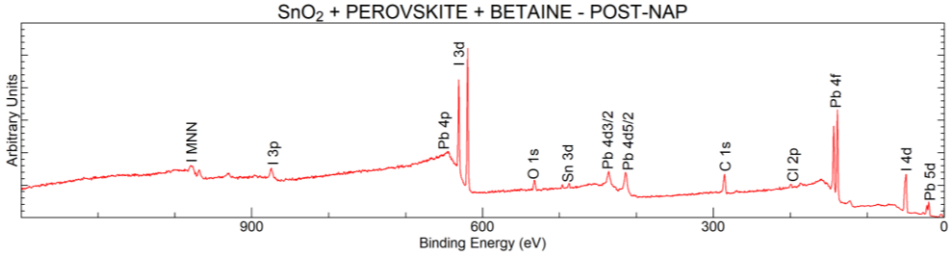

Name	At%
Pb 4f	13.55
C 1s	46.40
O 1s	8.66
Cl 2p	3.33
I 4d	27.45
Sn 3d	0.60

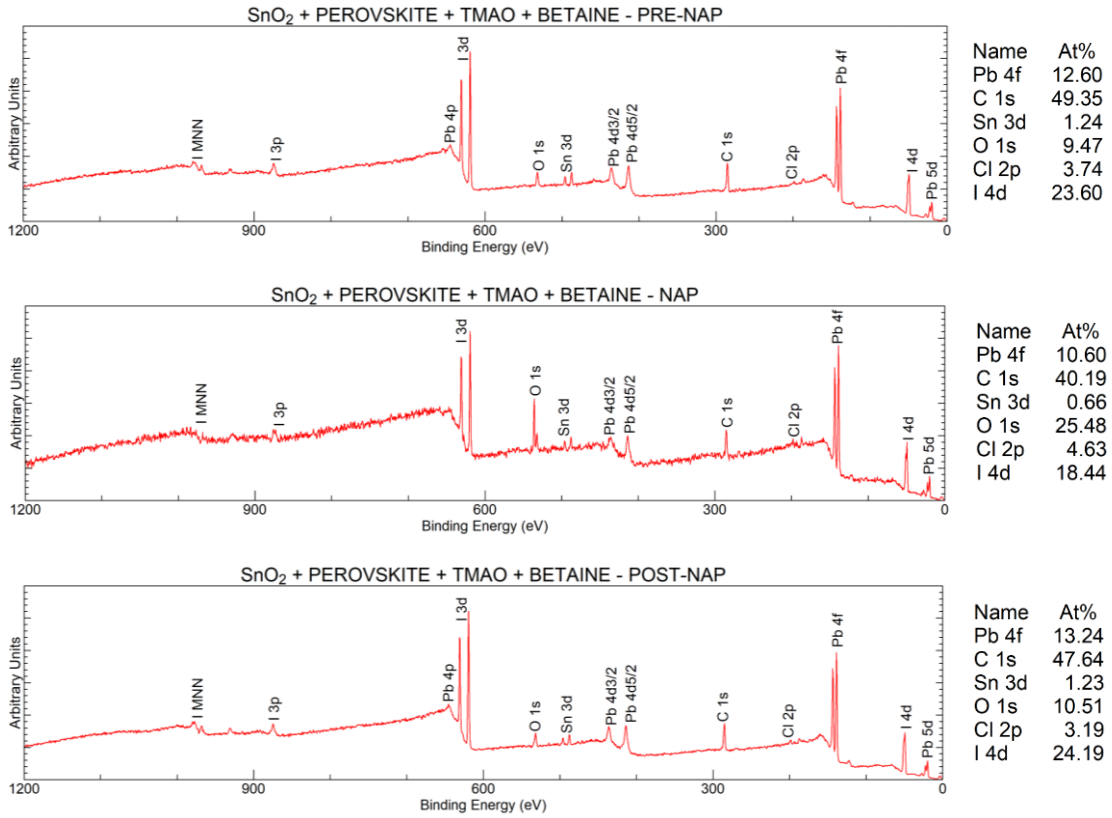

Figure S10: Survey spectra of the perovskite samples modified with TMAO and/or Betaine, deposited on SnO_2 coated Ti foil, measured before, during and after exposure to 4.5 mbar water vapour at room temperature. Spectra were recorded with an excitation energy of 1486 eV at Henry Royce Facility, Manchester.